Titre: Title:	Development of Models and a Unified Platform for Multiphase Load Flow Analysis and Dynamic State Estimation of Large Distribution Systems with Secondary Grids
Auteur: Author:	Baki Emre Cetindag
Date:	2016
Type:	Mémoire ou thèse / Dissertation or Thesis
Référence: Citation:	Cetindag, B. E. (2016). Development of Models and a Unified Platform for Multiphase Load Flow Analysis and Dynamic State Estimation of Large Distribution Systems with Secondary Grids [Ph.D. thesis, École Polytechnique de Montréal]. PolyPublie. https://publications.polymtl.ca/2432/

UNIVERSITÉ DE MONTRÉAL

DEVELOPMENT OF MODELS AND A UNIFIED PLATFORM FOR MULTIPHASE LOAD FLOW ANALYSIS AND DYNAMIC STATE ESTIMATION OF LARGE DISTRIBUTION SYSTEMS WITH SECONDARY GRIDS

BAKI EMRE CETINDAG

DÉPARTEMENT DE GÉNIE ÉLECTRIQUE

ÉCOLE POLYTECHNIQUE DE MONTRÉAL

THÈSE PRÉSENTÉE EN VUE DE L'OBTENTION

DU DIPLÔME DE PHILOSOPHIAE DOCTOR

(GÉNIE ÉLECTRIQUE)

NOVEMBRE 2016

UNIVERSITÉ DE MONTRÉAL

ÉCOLE POLYTECHNIQUE DE MONTRÉAL

Cette thèse intitulée :

DEVELOPMENT OF MODELS AND A UNIFIED PLATFORM FOR MULTIPHASE LOAD FLOW ANALYSIS AND DYNAMIC STATE ESTIMATION OF LARGE DISTRIBUTION SYSTEMS WITH SECONDARY GRIDS

présentée par : CETINDAG Baki Emre

en vue de l'obtention du diplôme de : Philosophiae Doctor

a été dûment acceptée par le jury d'examen constitué de :

M. MAHSEREDJIAN Jean, Ph. D., président

M. KOCAR Ilhan, Ph. D., membre et directeur de recherche

M. KARIMI Houshang, Ph. D., membre

M. SAHIN Cem, Ph. D., membre externe

DEDICATION

To my beloved parents…

ACKNOWLEDGEMENTS

First of all, I would like to express my deepest gratitude to my research supervisor Dr. İlhan Koçar, who is a great mentor, for his extreme patience, technical expertise, continuous guidance, opportunities he created and choosing me as a PhD student. Thank you so much for all your help.

I owe gratitude to Dr. Jean Mahseredjian for the technical insight he gave, his valuable advises and providing all the help I needed. Also, I would like to thank to Dr. Ulas Karaagac for sharing his expert advice and encouragement.

I would like to thank to my father and sister for their tremendous support and constant encouragement. I especially thank my mother for the sacrifice she made the last five months by staying with me while I was writing my thesis. Without their help, I would not be able to finish this PhD.

I also thank to Dr. Akihiro Ametani, for his guidance and insightful talks.

Last but not least, I would like to thank to all my friends in Polytechnique Montreal.

RÉSUMÉ

Cette thèse porte sur la modélisation des différentes composantes des réseaux de distribution pour les études d'écoulement de puissance multiphasé et pour l'estimation d'état. Sans utiliser les modèles appropriés, il n'est pas possible d'obtenir des résultats précis dans l'analyse des réseaux de distribution ou des systèmes électriques en général. La thèse présente aussi un algorithme d'estimation d'état générique pour les réseaux de distribution. La performance de l'algorithme est étudiée en détail en considérant les particularités des réseaux de distribution par opposition aux réseaux de transports.

La thèse commence par la discussion sur la modélisation des régulateurs de tension pour l'écoulement de puissance en utilisant la méthode de Newton. En tenant compte des spécifications techniques de ces appareils, une nouvelle approche de modélisation est présentée en utilisant la formulation d'analyse nodale augmentée modifiée (MANA) et la méthode de Newton. Les résultats obtenus montrent que la technique proposée donne des résultats satisfaisants lorsque les réglages et les spécifications techniques des régulateurs sont considérés. Ensuite, une nouvelle méthode pour modéliser les machines asynchrones (IMs) dans l'écoulement de puissance déséquilibré est démontrée. La nouvelle approche de modélisation est encore basée sur la formulation de MANA et utilise la méthode de Newton. La nouvelle méthode peut être utilisée pour des IMs à cage simple ou double. Il permet de modéliser l'IM avec la puissance électrique, la puissance mécanique ou le couple mécanique comme contrainte. Le glissement de l'IM devient une variable d'écoulement de puissance et il est calculée itérativement. La puissance réactive est fonction de la puissance active et du glissement ou de la puissance active et de la tension de l'IM, donc il n'y a aucun besoin de fixer la puissance réactive. La solution proposée réduit le nombre d'itérations considérablement par rapport aux méthodes de solution à point fixe. La méthode présentée n'est pas actuellement disponible dans la littérature. Finalement, une approche de modélisation systématique est établie pour représenter les éoliennes (WTGs) de Type-III et Type-IV dans l'analyse d'écoulement de puissance multiphasée et déséquilibrée. Les contraintes sont écrites en fonction des composantes symétriques des courants injectés par les WTGs. Le modèle proposé pour les WTGs fonctionne bien dans des conditions déséquilibrées.

La formulation d'écoulement de puissance est ensuite reconduite pour effectuer l'estimation d'état statique des réseaux de distribution dans le domaine de phase à l'aide de la matrice Hachtel

construite à partir des équations de contraintes de MANA. En utilisant des modèles existants et des nouveaux modèles développés dans ce travail dans l'algorithme d'estimation d'état, la contribution du facteur de puissance comme pseudo-mesure sur la précision de l'estimation d'état est étudiée en posant l'hypothèse que la mesure de facteur de puissance est plus précise que la mesure de puissance. Il est remarqué que comme la grandeur du réseau augmente, l'inclusion de facteur de puissance améliore la précision de l'estimation d'état.

Finalement, différentes approches pour l'estimation d'état dynamique des réseaux de distribution sont proposées. Les méthodes sont construites en utilisant le Filtre de Kalman, les prévisions de charge et finalement la matrice Hachtel toujours construite avec la formulation MANA. Deux méthodes pour suivre le comportement dynamique des systèmes d'alimentation sont proposées. La première méthode suit l'évolution des variables d'état du réseau, ce qui est l'objectif principal des estimateurs d'état dynamique. Dans la première méthode, le point clé est de déterminer la matrice de covariance pour les prévisions. Le réglage imprécis de la matrice de covariance affecte sévèrement la performance de l'algorithme. Le réglage est obtenu en faisant de l'estimation d'état statique à plusieurs reprises afin de tenter d'obtenir le poids de chaque variable d'état. Les résultats suggèrent que l'estimateur d'état dynamique est capable de suivre avec précision l'évolution des états dans le réseau aussi longtemps que la matrice de covariance est bien réglée. La deuxième méthode peut être considérée comme une extension de l'estimateur d'état statique qui tient compte de l'évolution dynamique des mesures. Dans cette méthode, les mesures de charge sont suivies de façon indépendante et incorporés dans l'estimateur d'état après avoir été traité dans le Filtre de Kalman à l'aide du profil de charge plus ou moins précis. En absence du profil de charge, les algorithmes de lissage, comme les méthodes de lissage exponentiel, peuvent être utilisés afin d'obtenir une prédiction de mesure dans le bloc de Kalman. Cette méthode est testée sur de très grands réseaux, déséquilibrées et maillés, et une grande amélioration est atteinte dans les résultats par rapport à l'estimateur statique. Grâce à la formulation de Newton, la technique proposée est capable d'analyser de très grands réseaux de distribution, avec plus de vingt mille nœuds, en 3 ou 4 itérations.

Les algorithmes développés fonctionnent bien sur les grands réseaux. Au meilleur de la connaissance de l'auteur, cette thèse est la première à démontrer une solution pour l'estimation d'état de très grands réseaux de distribution avec des topologies maillées du côté basse tension ou secondaire (tels que ceux de New York, Chicago et Toronto).

ABSTRACT

This thesis is on the modeling of various components of distribution systems for multiphase load flow studies and state estimation. Without employing proper models, it is not feasible to obtain accurate results in the analysis of distribution networks or power systems in general. The thesis presents also a generic state estimation solver for distribution networks. The performance of the solver is investigated in detail considering the particularities of distribution networks as opposed to transmission grids.

The thesis starts by discussing the modeling of step voltage regulators for load flow using Newton's method. By taking into account the technical specifications of these devices, a new modeling approach is presented within the modified augmented nodal analysis (MANA) formulation and Newton's method. The results obtained show that the proposed technique gives satisfactory results as far as the settings and technical specifications of the regulators are concerned. Afterwards, a new method to model Induction Machines (IMs) in unbalanced load-flow calculations is demonstrated. The new modeling approach is again based on the MANA formulation and employs Newton's method. The new method can be used for single and double cage IMs. It allows modeling the IM with electrical power input, mechanical power or mechanical torque output. The slip of the IM becomes a load-flow variable computed iteratively. The reactive power is a function of real power constraint and slip or voltage solution of the IM, therefore there is no need to fix the reactive power input. The proposed solution reduces the number of iterations radically as compared to fixed-point solution methods. The presented formulation is not currently available in the literature. Finally, a systematic modeling approach is established to represent Type-IV and Type-III wind turbine generators (WTGs) in multiphase and unbalanced load flow analysis. The proposed approach integrates the constraints based on the sequence components of the injected currents from WTGs. The proposed model for WTGs performs well under unbalanced conditions.

The load flow formulation is then extended to perform static state estimation of distribution networks in phase frame using Hachtel matrix built with MANA constraint equations. By using the existing and new models developed in this work, the contribution of the load power factor pseudo-measurement on the accuracy of state estimation is investigated putting forward the hypothesis that the power factor measurement is more accurate than the power measurement. It is observed that as

the size of the network increases the inclusion of power factor improves the accuracy of state estimation.

Finally, different approaches for the dynamic state estimation of distribution networks are proposed. The formulations are built using Kalman Filter, load forecasting and Hachtel matrix built with MANA formulation. Two methods tracking the dynamic behavior of power systems are proposed. The first method tracks the change of the state variables of the network, which is the main objective of the dynamic state estimators. In the first method, the key point is to determine the covariance matrix for the forecasts. Inaccurate tuning of the covariance matrix, which means poorly defined diagonal elements, affects the performance of the algorithm severely. The tuning is achieved by performing static state estimation repeatedly in order to attempt to obtain the weight of each state variable. The results suggest that the dynamic state estimator is able to accurately track the evolution of states in the network as long as the covariance matrix is well tuned. The second method can be considered as an extension to the static state estimator that considers the dynamic evolution of measurements. In this method, the load measurements are tracked independently and incorporated into state estimator after being processed in Kalman Filter using the load pattern. In the absence of load pattern, smoothing algorithms, such as exponential smoothing methods, can be used to obtain a prediction of measurements in the Kalman block. This method is tested on very large, unbalanced and meshed networks, and a great improvement is attained in the results compared to the static estimator. Thanks to its Newton formulation, the proposed technique is capable of analyzing very large distributing networks with more than twenty thousand nodes within 3 or 4 iterations.

The developed algorithms scale up and work well on large networks. To the best of author’s knowledge, this thesis demonstrates a solution for the state estimation of extremely large scale distribution networks with secondary grid details (such as the ones in New York, Chicago and Toronto) for the first time.

TABLE OF CONTENTS

LIST OF TABLES

LIST OF FIGURES

LIST OF SYMBOLS AND ABBREVIATIONS

$\lvert\ \rvert$	Absolute Value Operator
$\vec{\mathbf{A}}$	System Matrix of a Network in Steady-State
$\vec{\mathbf{A}}_{\mathbf{f}}$	Fortescue Transformation Matrix
$\mathbf{A}_{\mathbf{IL}}$	Adjacency Sub-Matrix of Load Currents
$\mathbf{A}_{\mathbf{IG}}$	Adjacency Sub-Matrix of Generator Currents
$\mathbf{A}_{\mathbf{SM}}$	Jacobian Sub-Matrix of Kirchhoff's Current Law w.r.t IM Slips
$\mathbf{B}_{\mathbf{G}}$	Jacobian Sub-Matrix of Generator Current Constraints w.r.t Generator Currents
ARRSES	Adaptive Rate Response Single Exponential Smoothing
c	Constraint Equations
$\mathbf{C}_{\mathbf{L}}$	Jacobian Sub-Matrix of Load Constraints w.r.t Node Voltages
$\mathbf{C}_{\mathbf{G}}$	Jacobian Sub-Matrix of Generator Constraints w.r.t Node Voltages
$\mathbf{C}_{\mathbf{RV}}$	Jacobian Sub-Matrix of Regulator Constraints w.r.t Node Voltages
$\mathbf{C}_{\mathbf{RI}}$	Jacobian Sub-Matrix of Regulator Constraints w.r.t Branch-Dependent Currents
$\mathbf{C}_{\mathbf{RG}}$	Jacobian Sub-Matrix of Regulator Constraints w.r.t Turns Ratio
$\mathbf{C}_{\mathbf{M}}$	Jacobian Sub-Matrix of IM Constraints w.r.t Node Voltages
$\mathbf{C}_{\mathbf{SM}}$	Jacobian Sub-Matrix of IM Constraints w.r.t IM Slips
$\mathbf{C}_{\mathbf{CG}}$	Jacobian Sub-Matrix of ECG Constraints w.r.t Node Voltages
CT_P	Primary Current Rating of a Current Transformer
CT_S	Secondary Current Rating of a Current Transformer
$\mathbf{D}_{\mathbf{L}}$	Jacobian Sub-Matrix of Load Constraints w.r.t Load Currents

$\mathbf{D_G}$	Jacobian Sub-Matrix of Generator Constraints w.r.t Generator Currents
$\vec{\mathbf{D}}_\mathbf{r}$	Dependency Sub-Matrix of Branch Dependent Devices
$\mathbf{D_{CG}}$	Jacobian Sub-Matrix of ECG Constraints w.r.t ECG Currents
DES	Double Exponential Smoothing
DSE	Dynamic State Estimation
$\vec{\mathbf{E}}_\mathbf{G}$	Vector of Internal Generator Positive Sequence Voltages
ECG	Electronically Coupled Generators
EKF	Extended Kalman Filter
$\mathbf{F}$	State Transition Matrix
$\mathbf{f_n}$	Vector of Kirchhoff's Current Law Constraints
$\mathbf{f_v}$	Vector of Voltage Source Constraints
$\mathbf{f_d}$	Vector of Branch-Dependent Device Constraints
$\mathbf{f_s}$	Vector of Switch Constraints
$\mathbf{f_E}$	Vector of Generator Current Constraints
$\mathbf{f_L}$	Vector of Load Constraints
$\mathbf{f_G}$	Vector of Generator Constraints
$\mathbf{f_{CG}}$	Vector of ECG Constraints
$\mathbf{f_E}$	Vector of Generator Current Constraints
$\mathbf{f_R}$	Vector of Regulator Constraints
$\mathbf{f_M}$	Vector of IM Constraints
$\mathbf{g}$	Vector of Voltage Transformation Ratio
$\mathbf{h}$	Vector of Measurement Functions

$\vec{\mathbf{I}}_{\mathbf{v}}$	Vector of Voltage Source Currents
$\vec{\mathbf{I}}_{\mathbf{d}}$	Vector of Branch-Dependent Devices Currents
$\vec{\mathbf{I}}_{\mathbf{s}}$	Vector of Switch Currents
$\vec{\mathbf{I}}_{\mathbf{n}}$	Vector of Injected Currents at Each Node
$\vec{\mathbf{I}}_{\mathbf{L}}$	Vector of Load Currents
$\vec{\mathbf{I}}_{\mathbf{G}}$	Vector of Generator Currents
$\vec{\mathbf{I}}_{\mathbf{CG}}$	Vector of ECG Currents
IM	Induction Machine
IEKF	Iterated Extended Kalman Filter
GSC	Grid Side Converter
$\mathbf{J}$	Jacobian Matrix
$\mathbf{J}_{\mathbf{c}}$	Jacobian Matrix of Constraints
$\mathbf{J}_{\mathbf{h}}$	Jacobian Matrix of Measurements
$\mathbf{K}$	Kalman Gain Matrix
KF	Kalman filter
LF	Load Flow
MANA	Modified Augmented Nodal Analysis
MSC	Machine Side Converter
N_{PT}	Turns Ratio of a Voltage Transformer
P	Real Power
R'	Compensator Network Resistance Setting
R_{line}	Feeder Resistance

$\mathbf{R}_{\mathbf{cov}}$	Covariance Matrix of Measurements
$\mathbf{Q}$	Covariance Matrix of Process Error
Q	Reactive Power
RLC	Resistance-Inductance-Capacitance
RSC	Rotor Side Converter
$\mathbf{s}_{\mathbf{M}}$	Vector of IM Slips
$\vec{\mathbf{S}}_{\mathbf{r}}$	Adjacency Sub-Matrix of Ideal Switches in Closed Position
$\vec{\mathbf{S}}_{\mathbf{d}}$	Adjacency Sub-Matrix of Ideal Switches in Open Position
SES	Single Exponential Smoothing
SSE	Static State Estimation
$\vec{\mathbf{V}}_{\mathbf{n}}$	Vector of Node Voltages
$\vec{\mathbf{V}}_{\mathbf{r}}$	Adjacency Matrix of Ideal Voltage Sources
$\vec{\mathbf{V}}_{\mathbf{b}}$	Vector of (Voltage) Source Voltages
$\vec{\mathbf{Y}}_{\mathbf{n}}$	Admittance Matrix
$\mathbf{Y}_{\mathbf{G}}$	Jacobian Sub-Matrix of Generator Current Constraints w.r.t Node Voltages
$\mathbf{Y}_{\mathbf{GE}}$	Jacobian Sub-Matrix of Generator Current Constraints w.r.t Internal Voltages
$\mathbf{x}$	State Vector
$\tilde{\mathbf{x}}$	Forecasted State Vector
$\hat{\mathbf{x}}$	True State Vector
X'	Compensator Network Reactance Setting
X_{line}	Feeder Reactance
$\mathbf{z}$	Vector of Measurements

α , γ	Smoothing Multipliers

LIST OF APPENDICES

CHAPTER 1 INTRODUCTION

The smart grid initiatives and increasingly stringent conditions of reliability, sustainability, cost and environmental impacts drive major transformations in distribution networks, not only in terms of infrastructure and circuit topology but also in terms of operation philosophy. In addition to the existing secondary grid networks found in certain urban distribution systems, microgrid integration is becoming more and more common at the distribution level. There are many distribution utilities which are required to operate their networks starting from the subtransmission level. Moreover, the increased integration of distributed generation units in distribution networks has introduced the concept of Active Distribution Networks (ADNs) in power systems. Due to its higher dynamics compared to the conventional distribution networks, an ADN is characterized by the need for voltage control, unique protection schemes, frequency and reactive power control. Therefore, the real-time control of ADNs is an important task and requires reliable state estimation algorithms which need to be fast, at the same time accurate enough to correctly model the distribution system components.

In this thesis, multiphase load flow modeling of various components in modern distribution networks is presented as a first step, since without proper models, it is not feasible to obtain valid results following the analysis of the circuits. Afterwards, dynamic and static state estimation of distribution networks are investigated.

Chapter-2 is the review of the Modified Augmented Nodal Analysis (MANA) approach [1-3] and its applications in steady-state and the load-flow [4, 5] analyses. The linear form of MANA provides the steady-state phasor solution and is obtained by representing the network components with their linear equivalents. The Jacobian form of MANA is used as the basis for performing load flow analysis by transforming the system of equations into Jacobian form and by extending it with nonlinear constraint equations for various components such as generators and loads. The common device models that are already available in the literature are provided here in a compact form both for steady state and load flow analyses using a systematic notation. The objective here is to set the stage for the development of new models and to get the reader familiarize with the methodology and the state-of-the-art in this field. The expandable matrix structure of MANA [1-3]allows the addition of both linear and nonlinear devices in block forms. It has a modular formulation such that addition of a new device does not require modifying the previously defined blocks.

In Chapter-3, the step voltage regulators which are critical for maintaining voltage profile on long distribution feeders are discussed. They are the primary equipment used in Volt/Var optimization. First, their operation and physical structure are explained in detail. Subsequently, the equations that form the constraints for load flow formulation are presented. As is well known, the primary functionality of a voltage regulator is to adjust the voltage of the controlled node given the voltage settings and limits. In the proposed technique, the magnitude of the controlled voltage is therefore the constraint equation.

Chapter-4 describes the integration of the induction machines into load flow formulation. Accurate modelling of the distributed generation units in load-flow solvers is an important criterion when evaluating the performance of the algorithms. The asynchronous induction machines (IM) constitute an important part of a distribution network, and are often modeled as constant PQ devices in the load-flow solution, but there is no direct relation between real and reactive powers of the IM in reality. In the proposed model, MANA approach has been expanded to account for the IMs by considering the slip of each IM as an unknown variable which is to be calculated iteratively. The constraint is the active power and there is no fixation of reactive power. Although the IM has been modeled with active power constraint only in the literature, the published methods rely on fixed point techniques and treat the IM in separate while performing load flow solution. This requires huge number of iterations and the convergence is not guaranteed due to fixed point approach. The integration of IM into Jacobian and the use of a full Newton method are presented for the first time in this work.

In Chapter-5, the electronically coupled generators (ECGs) or distributed energy resources (DERs) are investigated and modeled using MANA load flow formulation. The existing generator model which is explained in the Chapter-2 is not sufficiently accurate. In the classical generator model, a generator is represented by a voltage source behind a Thevenin impedance, which is also the widely used model in the literature [6-14]. On the other hand, the utility scale solar parks or wind parks either control the terminal voltage or reactive power injection. They can have decoupled reactive and active power controls and the grid side converters adjust the power by adjusting the active and reactive current references. Therefore, in multiphase load flow solution under unbalanced conditions, balanced voltage source behind an impedance model, used to represent traditional generators cannot truly represent the full behavior of ECGs. In [15], a technique to represent electronically coupled devices as current injections is presented where the sequence components

are used in constraint equations. In [16], a method based on branch current injection is proposed for radial systems. In [17], the wind parks have been modelled as an impedance as a function of slip assuming it as an induction machine but the most recent wind parks are either Type-III or Type-IV [18] and thus power electronics must be considered in the models. In the proposed model, a current source based model in MANA is presented by taking into account the control circuitry. This is an important contribution since this approach allows integrating different controls into load flow solution in a simple and robust manner.

Chapter-6 investigates the effect of the load power factor in the state estimation and presents a static state estimation [19, 20] algorithm based on the Hachtel formulation [21] by expanding MANA approach for various measurement equations. The method presented is well suited to meshed networks. This is the main advantage over the existing state estimation solvers for distribution networks [22-29] which are mostly designed for radial systems. In this chapter, it is aimed to show when the information related to the power factor available, the state estimation gives better results for distribution networks.

In Chapter-7, the dynamic behavior of the networks is studied and a new approach for the dynamic state estimation of distribution networks is proposed. Unlike its static counterpart described in Chapter-6, the dynamic state estimator also employs the previous estimates of the network to generate virtual measurements. There are numerous advantages of the dynamic state estimation over the static one. It allows longer decision time to the operator of the system, since security assessment, economic dispatching (subtransmission level), etc. can be realized earlier. Most of the dynamic state estimators [30, 31] are based on Kalman filtering [32]. In this thesis, an alternative approach is proposed within the context of the weighted least squares (WLS) method. In this chapter, the Kalman type estimators are reviewed before developing the proposed method which is an extension to the static state estimator obtained by considering the dynamic evolution of measurements. In this method, the load measurements are tracked independently and incorporated into state estimator after being processed in Kalman Filter using the load pattern. In the absence of load pattern, smoothing algorithms, such as exponential smoothing methods are suggested to obtain a prediction of measurements in the Kalman block. This method is tested on very large, unbalanced and meshed networks, and a great improvement is accomplished in the results when compared to the static estimator.

CHAPTER 2 MANA LOAD FLOW

2.1 The Steady-State Form of MANA

The MANA formulation originates from the classical nodal analysis (NA). Its main advantage is to allow independent modeling of devices. The general MANA formulation for a linear network in steady-state has the following form [3]:

$$\underbrace{\begin{bmatrix} \vec{\mathbf{Y}}_n & \vec{\mathbf{V}}_c & \vec{\mathbf{D}}_c & \vec{\mathbf{S}}_c \\ \vec{\mathbf{V}}_r & \vec{\mathbf{V}}_d & \vec{\mathbf{D}}_{vd} & \vec{\mathbf{S}}_{vs} \\ \vec{\mathbf{D}}_r & \vec{\mathbf{D}}_{dv} & \vec{\mathbf{D}}_d & \vec{\mathbf{S}}_{ds} \\ \vec{\mathbf{S}}_r & \vec{\mathbf{S}}_{sv} & \vec{\mathbf{S}}_{sd} & \vec{\mathbf{S}}_d \end{bmatrix}}_{\vec{\mathbf{A}}} \underbrace{\begin{bmatrix} \vec{\mathbf{V}}_n \\ \vec{\mathbf{I}}_v \\ \vec{\mathbf{I}}_d \\ \vec{\mathbf{I}}_s \end{bmatrix}}_{\vec{\mathbf{x}}} = \underbrace{\begin{bmatrix} \vec{\mathbf{I}}_n \\ \vec{\mathbf{V}}_b \\ \vec{\mathbf{d}}_b \\ \vec{\mathbf{s}}_d \end{bmatrix}}_{\vec{\mathbf{b}}} \tag{1.1}$$

The general formulation in (1.1) is the most generic form and contains all device equations. In this thesis, the simplified version of (1.1) is used instead:

$$\underbrace{\begin{bmatrix} \vec{\mathbf{Y}}_n & \vec{\mathbf{V}}_r^T & \vec{\mathbf{D}}_r^T & \vec{\mathbf{S}}_r^T \\ \vec{\mathbf{V}}_r & \mathbf{0} & \mathbf{0} & \mathbf{0} \\ \vec{\mathbf{D}}_r & \mathbf{0} & \mathbf{0} & \mathbf{0} \\ \vec{\mathbf{S}}_r & \mathbf{0} & \mathbf{0} & \vec{\mathbf{S}}_d \end{bmatrix}}_{\vec{\mathbf{A}}} \underbrace{\begin{bmatrix} \vec{\mathbf{V}}_n \\ \vec{\mathbf{I}}_v \\ \vec{\mathbf{I}}_d \\ \vec{\mathbf{I}}_s \end{bmatrix}}_{\vec{\mathbf{x}}} = \underbrace{\begin{bmatrix} \vec{\mathbf{I}}_n \\ \vec{\mathbf{V}}_b \\ \mathbf{0} \\ \mathbf{0} \end{bmatrix}}_{\vec{\mathbf{b}}} \tag{1.2}$$

The equation (1.2), which will be referred as the steady-state form from this point onward is written in the complex domain and is used to find the unknowns in phasor form. The subscript (^{T}) indicates the transpose of a matrix or vector. Throughout this document, the arrow on top of a vector or matrix term indicates that the term can be complex and a transformation into a form of real vectors or matrices is required. For any complex matrix $\vec{\mathbf{C}}$, the real form is given by;

$$\mathbf{C} = \begin{bmatrix} \mathrm{Re}\left(\vec{\mathbf{C}}\right) & -\mathrm{Im}\left(\vec{\mathbf{C}}\right) \\ \mathrm{Im}\left(\vec{\mathbf{C}}\right) & \mathrm{Re}\left(\vec{\mathbf{C}}\right) \end{bmatrix} \tag{1.3}$$

Similarly, the real form of a complex valued vector $\vec{\mathbf{v}}$ is written in a similar way:

$$\mathbf{v} = \begin{bmatrix} \mathrm{Re}\left(\vec{\mathbf{v}}\right) \\ \mathrm{Im}\left(\vec{\mathbf{v}}\right) \end{bmatrix} \tag{1.4}$$

where Re and Im are the real and imaginary part operators, respectively.

In the formulation above, the system matrix $\vec{\mathbf{A}}$ on the left hand-side has the following components:

$\vec{\mathbf{Y}}_\mathbf{n}$: The admittance matrix of the linear network

$\vec{\mathbf{V}}_\mathbf{r}$: The adjacency matrix of the ideal voltage sources

$\vec{\mathbf{D}}_\mathbf{r}$: The voltage dependency matrix of the branch-dependent devices

$\vec{\mathbf{S}}_\mathbf{r}$: The adjacency matrix of the ideal switches (closed)

$\vec{\mathbf{S}}_\mathbf{d}$: The adjacency matrix of the ideal switches (open)

The unknown vector $\vec{\mathbf{x}}$ is composed of the following components:

$\vec{\mathbf{V}}_\mathbf{n}$: The vector containing the node voltage phasors

$\vec{\mathbf{I}}_\mathbf{v}$: The vector containing the current phasors through each ideal voltage source

$\vec{\mathbf{I}}_\mathbf{d}$: The vector containing the current phasors of the branch dependent devices

$\vec{\mathbf{I}}_\mathbf{s}$: The vector containing the current phasors of all switches

The known quantities vector $\vec{\mathbf{b}}$ on the right hand side is formed by the following components:

$\vec{\mathbf{I}}_\mathbf{n}$: The vector of the injected current phasors at each node

$\vec{\mathbf{V}}_\mathbf{b}$: The vector of the voltage source phasors

The system in (1.2) can be solved by direct methods.

2.1.1 The Formation of $\vec{\mathbf{Y}}_\mathbf{n}$ and $\vec{\mathbf{I}}_\mathbf{n}$

The formation of $\vec{\mathbf{Y}}_\mathbf{n}$ is straightforward. Now, assume an impedance indexed with p is connected between the nodes k and ground as shown in Figure 2.1, and $\vec{Z}_p = R_p + jX_p$ in Ω where R_p and X_p are the resistance and reactance of the impedance.

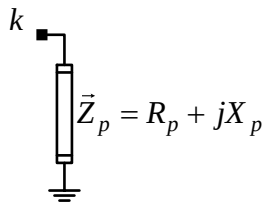

Figure 2.1: RLC Impedance Connected between k and Ground

Its contribution to $\vec{\mathbf{Y}}_\mathbf{n}$ can be expressed with an update equation as follows;

$$\vec{\mathbf{Y}}_\mathbf{n}^{new}(k,k) = \vec{\mathbf{Y}}_\mathbf{n}^{old}(k,k) + \vec{Y}_p \tag{1.5}$$

where $\vec{Y}_p = \vec{Z}_p^{-1}$

If that impedance is connected between the nodes k and m instead, three other parameters need to be updated as well:

$$\begin{aligned}
\vec{\mathbf{Y}}_\mathbf{n}^{new}(m,m) &= \vec{\mathbf{Y}}_\mathbf{n}^{old}(m,m) + \vec{Y}_p \\
\vec{\mathbf{Y}}_\mathbf{n}^{new}(m,k) &= \vec{\mathbf{Y}}_\mathbf{n}^{old}(m,k) - \vec{Y}_p \\
\vec{\mathbf{Y}}_\mathbf{n}^{new}(k,m) &= \vec{\mathbf{Y}}_\mathbf{n}^{old}(k,m) - \vec{Y}_p
\end{aligned} \tag{1.6}$$

If the component to be included in $\vec{\mathbf{Y}}_\mathbf{n}$ is a three phase element such as a 3 phase line, (1.5) and (1.6) are still valid. In that case, $\vec{Y}_p$ becomes a 3 by 3 matrix, and m and k represent the 3 by 1 node vector.

In steady-state form of MANA, the following elements contribute to the construction of $\vec{\mathbf{Y}}_\mathbf{n}$:

- Lines and cables which are represented with PI-model
- PQ loads with their nominal impedance
- Internal impedance of the transformers
- Induction machines with Steinmetz circuit representation
- Any combination of RLC elements

The phasors of the current sources are represented in $\vec{\mathbf{I}}_\mathbf{n}$. Let a current source with the phasor $I_p \angle \theta_p$ be connected at the node k. If the direction is chosen as 'into the node'; then,

$$\vec{\mathbf{I}}_\mathbf{n}(k) = I_p \angle \theta_p \tag{1.7}$$

If there are several current sources are connected to the same node, the sum of current injections must be considered.

2.1.2 The Formation of $\vec{\mathbf{V}}_\mathbf{r}$ and $\vec{\mathbf{V}}_\mathbf{b}$

An ideal voltage source keeps the voltage and the angle of the nodes constant where it is connected. Different configurations of ideal voltage sources can be realized within MANA formulation [5].

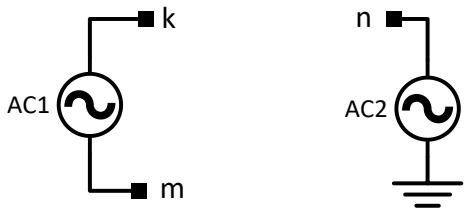

Figure 2.2: Ideal Voltage Source

In Figure 2.2, the first voltage source $AC1$ is connected between the nodes k and m; while the second voltage source $AC2$ is connected between the node n and the ground. Let $V_{AC1}\angle\theta_{AC1}$ and $V_{AC2}\angle\theta_{AC2}$ denote the phasors of the sources $AC1$ and $AC2$ respectively. Then, the formulations of $\vec{\mathbf{V}}_\mathbf{r}$ and $\vec{\mathbf{V}}_\mathbf{b}$ become [3]:

$$\begin{aligned} \vec{\mathbf{V}}_\mathbf{r}(p1, ka) &= 1 & \vec{\mathbf{V}}_\mathbf{r}(p2, n) &= 1 \\ \vec{\mathbf{V}}_\mathbf{r}(p1, kb) &= -1 & \vec{\mathbf{V}}_\mathbf{b}(p2) &= V_{AC2}\angle\theta_{AC2} \\ \vec{\mathbf{V}}_\mathbf{b}(p1) &= V_{AC1}\angle\theta_{AC1} & & \end{aligned} \tag{1.8}$$

where $p1$ and $p2$ are the indices for $AC1$ and $AC2$.

In steady-state form of MANA, the following elements are represented in $\vec{\mathbf{V}}_\mathbf{r}$:

- Single/Three phase ideal voltage sources
- Slack generators can also be included in $\vec{\mathbf{V}}_\mathbf{r}$ as their terminal voltage phasor is a known quantity.

2.1.3 The Formation of $\vec{\mathbf{D}}_{\mathbf{r}}$

The branch related components refer to the elements whose output (or behavior) depends on the state of the system. A single phase ideal transformer can be modeled as a two port device and its hybrid model is demonstrated in Figure 2.3. The matrix containing the hybrid parameters for this model can be expressed as follows [5]:

$$\begin{bmatrix} \vec{V}_2 \\ \vec{I}_1 \end{bmatrix} = \begin{bmatrix} h_{11} & h_{12} \\ h_{21} & h_{22} \end{bmatrix} \begin{bmatrix} \vec{I}_2 \\ \vec{V}_1 \end{bmatrix} \tag{1.9}$$

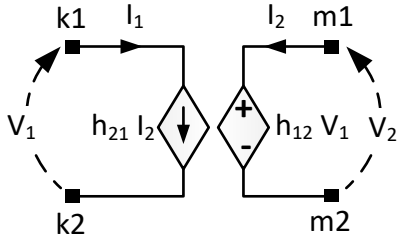

Figure 2.3: Hybrid Model of a Two Port Network

An ideal transformer can be defined by two equations:

$$\frac{\vec{V}_2}{\vec{V}_1} = \frac{N_2}{N_1} = g \tag{1.10}$$

$$N_1\vec{I}_1 = -N_2\vec{I}_2 \quad or \quad \vec{I}_1 = -g\vec{I}_2 \tag{1.11}$$

where N_1 and N_2 are the number of turns, and g is the turns ratio of the transformer. Then, the hybrid parameters of (1.9) become [5]:

$$\vec{V}_{m1} - \vec{V}_{m2} - g\vec{V}_{k1} + g\vec{V}_{k2} = 0 \tag{1.12}$$

The corresponding entries of $\vec{\mathbf{D}}_{\mathbf{r}}$ are given as [5]:

$$\begin{aligned}\vec{\mathbf{D}}_{\mathbf{r}}(p,k1) &= -g \\ \vec{\mathbf{D}}_{\mathbf{r}}(p,k2) &= g \\ \vec{\mathbf{D}}_{\mathbf{r}}(p,m1) &= 1 \\ \vec{\mathbf{D}}_{\mathbf{r}}(p,m2) &= -1\end{aligned} \tag{1.13}$$

The elements that can be modeled using $\vec{\mathbf{D}}_{\mathbf{r}}$ are as follows:

- Three phase transformers can be modeled as a combination of single phase units
- Autotransformers
- Regulators

2.1.4 The Formation of $\vec{\mathbf{S}}_{\mathbf{r}}$ and $\vec{\mathbf{S}}_{\mathbf{d}}$

The switches can be represented in MANA without representing them in $\vec{\mathbf{Y}}_{\mathbf{n}}$ as zero and/or infinite impedance. Consider the two switches in Figure 2.4. The switch $SW1$, which connected between the nodes $k1$ and $m1$, is open and the switch $SW2$, which is connected between the nodes $k2$ and $m2$, is closed. R_{sw} is represents the switch resistance of the non-ideal switches which is quite low.

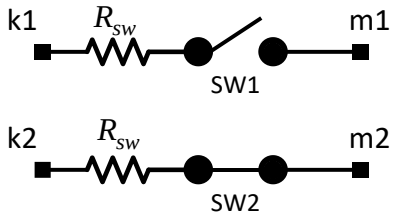

Figure 2.4: (a) Open Switch (b) Closed Switch

Let p denote the index of $SW1$ and q denote the one of $SW2$. Then, p th element of $\vec{\mathbf{I}}_{\mathbf{s}}$ gives the unknown current phasor of $SW1$ and q th element of $\vec{\mathbf{I}}_{\mathbf{s}}$ gives the unknown current phasor of $SW2$.

$$\begin{bmatrix}\vec{I}_{SW1} \\ \vec{I}_{SW2}\end{bmatrix} = \begin{bmatrix}\vec{\mathbf{I}}_{\mathbf{s}}(p) \\ \vec{\mathbf{I}}_{\mathbf{s}}(q)\end{bmatrix} \tag{1.14}$$

An open switch does not allow any current to pass on it. Thus, I_{SW1} must be set to zero. The corresponding entry of $\vec{\mathbf{S}}_{\mathbf{d}}$ is given by the formula [5]:

$$\vec{\mathbf{S}}_{\mathbf{d}}(p,p)=1 \tag{1.15}$$

When the switch is in closed position, the equation which describes its function [5]:

$$\frac{V_{k2}-V_{m2}}{R_{sw}}=I_{SW2} \tag{1.16}$$

Thus, the corresponding entries of $\vec{\mathbf{S}}_{\mathbf{r}}$ and $\vec{\mathbf{S}}_{\mathbf{d}}$ are given as [5]:

$$\begin{aligned}\vec{\mathbf{S}}_{\mathbf{r}}(q,k2)&=1/R_{sw}\\ \vec{\mathbf{S}}_{\mathbf{r}}(q,m2)&=-1/R_{sw}\\ \vec{\mathbf{S}}_{\mathbf{d}}(q,q)&=-1\end{aligned} \tag{1.17}$$

2.2 The Load Flow Analysis in MANA

In the previous section, the solution of a time invariant network is presented where all elements can be expressed with linear equations. The formulation in (1.2) can be expanded for the load flow analysis as well [4].

One of the methods to solve a nonlinear real-valued problem is Newton method. Consider there is a nonlinear function $f(x)$ which is continuously differentiable, the root of $f(x)$ is to be found iteratively [2].

$$x:\ f(x)=0 \tag{1.18}$$

The method linearizes the set of functions around the last known value of x.

$$x^{(i+1)}=x^{(i)}-\frac{f\left(x^{(i)}\right)}{f'\left(x^{(i+1)}\right)} \tag{1.19}$$

$$x^{(i+1)}=x^{(i)}+\Delta x^{(i+1)} \tag{1.20}$$

$$\Delta x^{(i)}=-\frac{f\left(x^{(i)}\right)}{f'\left(x^{(i+1)}\right)} \tag{1.21}$$

where i is the iteration counter, $x^{(i)}$ is the value of x at the i th iteration, and $f'\left(x^{(i)}\right)$ is the first derivative of $f\left(x\right)$ with respect to x. (1.19) is an iterative process which continues until the difference $\Delta x^{(i)}$ between $x^{(i+1)}$ and $x^{(i)}$ becomes sufficiently small.

(1.19) can be applied to a set of functions with several variables as follows:

$$\mathbf{x}:\ \mathbf{f}\left(\mathbf{x}\right)=\mathbf{0} \tag{1.22}$$

$$\mathbf{x}^{(i+1)}=\mathbf{x}^{(i)}+\mathbf{\Delta x}^{(i)} \tag{1.23}$$

$$\Delta\mathbf{x}^{(i)}=-\left(\mathbf{J}\left(\mathbf{x}^{(i)}\right)\right)^{-1}\mathbf{f}\left(\mathbf{x}^{(i)}\right) \tag{1.24}$$

where $\mathbf{J}\left(\mathbf{x}^{(i)}\right)$ is called the Jacobian matrix which is formation is explained as follows. Let us assume there are m unknowns and equations.

$$\mathbf{x}=\begin{bmatrix}x_1\\x_2\\\vdots\\x_m\end{bmatrix}:\quad \mathbf{f}\left(\mathbf{x}^{(i)}\right)=\begin{bmatrix}f_1\left(\mathbf{x}^{(i)}\right)\\f_2\left(\mathbf{x}^{(i)}\right)\\\vdots\\f_m\left(\mathbf{x}^{(i)}\right)\end{bmatrix}=\mathbf{0} \tag{1.25}$$

The Jacobian matrix of $\mathbf{f}\left(\mathbf{x}\right)$ becomes:

$$\mathbf{J}\left(\mathbf{x}\right)=\begin{bmatrix}\frac{\partial f_1}{\partial x_1} & \frac{\partial f_1}{\partial x_2} & \cdots & \frac{\partial f_1}{\partial x_m}\\ \frac{\partial f_2}{\partial x_1} & \frac{\partial f_2}{\partial x_2} & \cdots & \frac{\partial f_2}{\partial x_m}\\ \vdots & \vdots & \ddots & \vdots\\ \frac{\partial f_m}{\partial x_1} & \frac{\partial f_m}{\partial x_2} & \cdots & \frac{\partial f_m}{\partial x_m}\end{bmatrix} \tag{1.26}$$

The Newton method, as aforementioned, requires the system of equations to be solved to be real. Then, the Jacobian formulation of MANA can be written as follows [1-4]:

$$\begin{bmatrix} \mathbf{Y_n} & \mathbf{V_r^T} & \mathbf{D_r^T} & \mathbf{S_r^T} & \mathbf{A_{IL}} & \mathbf{A_{IG}} & \mathbf{0} \\ \mathbf{V_r} & \mathbf{0} & \mathbf{0} & \mathbf{0} & \mathbf{0} & \mathbf{0} & \mathbf{0} \\ \mathbf{D_r} & \mathbf{0} & \mathbf{0} & \mathbf{0} & \mathbf{0} & \mathbf{0} & \mathbf{0} \\ \mathbf{S_r} & \mathbf{0} & \mathbf{0} & \mathbf{S_d} & \mathbf{0} & \mathbf{0} & \mathbf{0} \\ \mathbf{C_L} & \mathbf{0} & \mathbf{0} & \mathbf{0} & \mathbf{D_L} & \mathbf{0} & \mathbf{0} \\ \mathbf{C_G} & \mathbf{0} & \mathbf{0} & \mathbf{0} & \mathbf{0} & \mathbf{D_G} & \mathbf{0} \\ \mathbf{Y_G} & \mathbf{0} & \mathbf{0} & \mathbf{0} & \mathbf{0} & \mathbf{B_G} & \mathbf{Y_{GE}} \end{bmatrix}^{(i)} \begin{bmatrix} \mathbf{\Delta V_n} \\ \mathbf{\Delta I_v} \\ \mathbf{\Delta I_d} \\ \mathbf{\Delta I_s} \\ \mathbf{\Delta I_L} \\ \mathbf{\Delta I_G} \\ \mathbf{\Delta E_G} \end{bmatrix}^{(i)} = - \begin{bmatrix} \mathbf{f_n} \\ \mathbf{f_v} \\ \mathbf{f_d} \\ \mathbf{f_s} \\ \mathbf{f_L} \\ \mathbf{f_G} \\ \mathbf{f_E} \end{bmatrix}^{(i)} \tag{1.27}$$

$$\mathbb{J}\left(\mathbf{x}^{(i)}\right)\mathbf{\Delta x}^{(i)} = -\mathbb{f}\left(\mathbf{x}^{(i)}\right) \tag{1.28}$$

As shown in (1.3), the terms without a bar on top in (1.27) are used to indicate the real valued matrices and vectors.

$\mathbf{A_{IL}}$: The load current adjacency matrix

$\mathbf{A_{IG}}$: The generator current adjacency matrix

$\mathbf{C_L}$: The partial derivatives for the PQ load constraints (w.r.t node voltages)

$\mathbf{D_L}$: The partial derivatives for the PQ load constraints (w.r.t load currents)

$\mathbf{C_G}$: The partial derivatives for the generator constraints (w.r.t node voltages)

$\mathbf{D_G}$: The partial derivatives for the generator constraints (w.r.t generator currents)

$\mathbf{Y_G}$: The partial derivatives for the generator current constraints (w.r.t node voltages)

$\mathbf{B_G}$: The partial derivatives for the generator current constraints (w.r.t generator currents)

$\mathbf{Y_{GE}}$: The partial derivatives for the generator current constraints (w.r.t internal voltage)

$\mathbf{I_L}$: The vector of the load currents

$\mathbf{I_G}$: The vector of the generator currents

$\mathbf{E_G}$: The vector of the generator internal voltages

Given the fact that the formulation (1.2) is linear, the Jacobian form of MANA will employ the real form the matrices presented in (1.2).

2.2.1 The Linear Constraints

The linear constraints in (1.27) are listed as [3];

$\mathbf{f_n}$: The Kirchhoff's Current Law

$\mathbf{f_v}$: The ideal voltage source constraint

$\mathbf{f_d}$: The branch-dependent device constraint

$\mathbf{f_s}$: The switch constraint

$\mathbf{f_E}$: The generator current constraint

Although the generator current constraints are linear, their formulation will be explained under the generator constraints part.

2.2.1.1 The Kirchhoff's Current Law

The algebraic sum of all currents entering and exiting a node must equal zero. The convention of current chosen in MANA formulation is that leaving currents have a positive sign while entering currents have a negative sign. This constraint can be realized by the following equation [4]:

$$\begin{bmatrix} \mathbf{Y_n} & \mathbf{V_r^T} & \mathbf{D_r^T} & \mathbf{S_r^T} & \mathbf{A_{IL}} & \mathbf{A_{IG}} \end{bmatrix} \begin{bmatrix} \mathbf{V_n} \\ \mathbf{I_v} \\ \mathbf{I_d} \\ \mathbf{I_s} \\ \mathbf{I_L} \\ \mathbf{I_G} \end{bmatrix}^{(i)} - \mathbf{I_n} = \mathbf{f_n}^{(i)} \tag{1.29}$$

where $\mathbf{I_n}$ is the real form of the injected current phasors in (1.2).

2.2.1.2 The Ideal Voltage Source Constraint

The ideal voltage constraint can be derived by using (1.8) [3]:

$$\mathbf{V_r}\,\mathbf{V_n}^{(i)} - \mathbf{V_b} = \mathbf{f_v}^{(i)} \tag{1.30}$$

where $\mathbf{V_b}$ is the branch voltage vector in (1.2).

2.2.1.3 The Branch Dependent Device Constraint

The branch dependent device constraint which represents transformers can be found by employing (1.13) [3]:

$$\mathbf{D}_\mathbf{r}\,\mathbf{V}_\mathbf{n}^{(i)} = \mathbf{f}_\mathbf{d}^{(i)} \tag{1.31}$$

2.2.1.4 The Ideal Switch Constraint

Both open and closed switch constraints can be modeled by using (1.15) and (1.17) [3]:

$$\mathbf{S}_\mathbf{r}\mathbf{V}_\mathbf{n} + \mathbf{S}_\mathbf{d}\mathbf{I}_\mathbf{s} = \mathbf{f}_\mathbf{s}^{(i)} \tag{1.32}$$

2.2.2 The Load Constraints

Three types of load are common in a typical distribution networks [3]:

I. Constant power load

II. Constant current load

III. Constant impedance load

Consider the generic load model given in Figure 2.5 where k and m denote the node numbers, and r denote the index of the load. The direction of the load current is chosen as indicated from the node k to the node m.

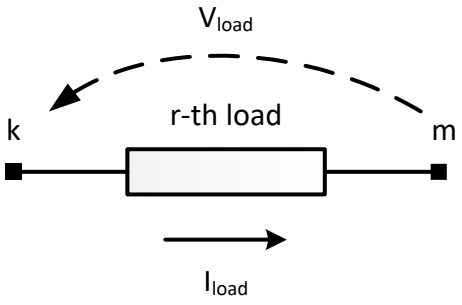

Figure 2.5: Generic Load Model

The equations which define this load are given by:

$$P_r^{(i)} = P_{rated}\left(\frac{\left|\vec{V}_{load}^{(i)}\right|}{V_{rated}}\right)^{N_p} \tag{1.33}$$

$$Q_r^{(i)} = Q_{rated}\left(\frac{\left|\vec{V}_{load}^{(i)}\right|}{V_{rated}}\right)^{N_q} \tag{1.34}$$

where $P_q^{(i)}$ and $Q_q^{(i)}$ give the real and reactive power constraints for the r th load at the i th iteration; P_{rated}, Q_{rated} are the real and reactive power ratings at the nominal voltage V_{rated}. The parameters N_p and N_q define the characteristics of the load [3]:

If $N_p = 0$ and $N_q = 0$, then the type of this load is constant power.

If $N_p = 1$ and $N_q = 1$, then the type of this load is constant current.

If $N_p = 2$ and $N_q = 2$, then the type of this load is constant impedance.

In any case, the constraint equations will be the same. Let r_p and r_q denote the indices for the real and reactive power constraints in $\mathbf{f}_{\mathbf{L}}$.

$$\mathbf{f}_{\mathbf{L}}\left(r_p\right) = P_r^{(i)} - \mathrm{Re}\left(\vec{I}_{load}^{*}\,\vec{V}_{load}\right)^{(i)} \tag{1.35}$$

$$\mathbf{f}_{\mathbf{L}}\left(r_q\right) = Q_r^{(i)} - \mathrm{Im}\left(\vec{I}_{load}^{*}\,\vec{V}_{load}\right)^{(i)} \tag{1.36}$$

where $\vec{I}_{load}$ is the load current phasor, $\vec{V}_{load}$ is the load voltage phasor.

The voltage and current of the load in Figure 2.5 should be expressed in terms of the circuit unknowns:

$$\begin{gathered} \vec{V}_{load} = \vec{V}_k - \vec{V}_m \\ \textit{where} \\ \vec{V}_k = \vec{\mathbf{V}}_{\mathbf{n}}\left(k\right) \\ \vec{V}_m = \vec{\mathbf{V}}_{\mathbf{n}}\left(m\right) \end{gathered} \tag{1.37}$$

Let the real and imaginary parts of V_{load}, V_k and V_m be defined as:

$$
\begin{aligned}
V_{kR} &= \mathrm{Re}\left(\vec{V}_k\right) \\
V_{kI} &= \mathrm{Im}\left(\vec{V}_k\right) \\
V_{mR} &= \mathrm{Re}\left(\vec{V}_m\right) \\
V_{mI} &= \mathrm{Im}\left(\vec{V}_m\right) \\
V_{loadR} &= \mathrm{Re}\left(\vec{V}_{load}\right) = V_{kR} - V_{mR} \\
V_{loadI} &= \mathrm{Im}\left(\vec{V}_{load}\right) = V_{kI} - V_{mI}
\end{aligned}
\tag{1.38}
$$

Similarly, the load current is also an independent variable in MANA.

$$I_{load} = \vec{\mathbf{I}}_{\mathbf{L}}\left(r\right) \tag{1.39}$$

The real and imaginary parts of the load current can be written as:

$$I_{loadR} = \mathrm{Re}\left(\vec{I}_{load}\right) \tag{1.40}$$

$$I_{loadI} = \mathrm{Im}\left(\vec{I}_{load}\right) \tag{1.41}$$

In Figure 2.5, the load is connected between the nodes k and m, and the direction of the current is from k to m. Based on the current convention, the entries of the adjacency matrix become:

$$\vec{\mathbf{A}}_{\mathbf{IL}}\left(k,q\right) = 1 \tag{1.42}$$

$$\vec{\mathbf{A}}_{\mathbf{IL}}\left(m,q\right) = -1 \tag{1.43}$$

Let the matrices $\mathbf{C_L}$ and $\mathbf{D_L}$ be divided into two as follows:

$$\mathbf{C_L} = \begin{bmatrix}\mathbf{C_{L1}} & \mathbf{C_{L2}}\end{bmatrix} \tag{1.44}$$

$$\mathbf{D_L} = \begin{bmatrix}\mathbf{D_{L1}} & \mathbf{D_{L2}}\end{bmatrix} \tag{1.45}$$

$\mathbf{C_{L1}}$: The partial derivatives of $\mathbf{f_L}$ w.r.t the real parts of the node voltages

$\mathbf{C_{L2}}$: The partial derivatives of $\mathbf{f_L}$ w.r.t the imaginary parts of the node voltages

$\mathbf{D_{L1}}$: The partial derivatives of $\mathbf{f_L}$ w.r.t the real parts of the load currents

$\mathbf{D_{L2}}$: The partial derivatives of $\mathbf{f_L}$ w.r.t the imaginary parts of the load currents

2.2.2.1 The Jacobian Terms of the Real Power Constraint

This constraint is defined by (1.35). A generic formulation that holds for all types is contributed here.

$$\mathbf{C_{L1}}\left(r_p,k\right)=\frac{\partial \mathbf{f_L}\left(r_p\right)}{\partial V_{kR}}=\frac{N_p P_{rated} V_{loadR}\left(V_{loadI}^2+V_{loadR}^2\right)^{\frac{N_p}{2}-1}}{\left(V_{rated}\right)^{N_p}}-I_{loadR} \tag{1.46}$$

$$\mathbf{C_{L1}}\left(r_p,m\right)=\frac{\partial \mathbf{f_L}\left(r_p\right)}{\partial V_{mR}}=-\mathbf{C_{L1}}\left(r_p,k\right) \tag{1.47}$$

$$\mathbf{C_{L2}}\left(r_p,k\right)=\frac{\partial \mathbf{f_L}\left(r_p\right)}{\partial V_{kI}}=\frac{N_p P_{rated} V_{loadI}\left(V_{loadI}^2+V_{loadR}^2\right)^{\frac{N_p}{2}-1}}{\left(V_{rated}\right)^{N_p}}-I_{loadI} \tag{1.48}$$

$$\mathbf{C_{L2}}\left(r_p,m\right)=\frac{\partial \mathbf{f_L}\left(r_p\right)}{\partial V_{mI}}=-\mathbf{C_{L2}}\left(r_p,k\right) \tag{1.49}$$

$$\mathbf{D_{L1}}\left(r_p,r\right)=\frac{\partial \mathbf{f_L}\left(r_p\right)}{\partial I_{loadR}}=-V_{loadR} \tag{1.50}$$

$$\mathbf{D_{L2}}\left(r_p,r\right)=\frac{\partial \mathbf{f_L}\left(r_p\right)}{\partial I_{loadI}}=-V_{loadI} \tag{1.51}$$

2.2.2.2 The Jacobian Terms of the Reactive Power Constraint

This constraint is defined by (1.36) [3].

$$\mathbf{C_{L1}}\left(r_q,k\right)=\frac{\partial \mathbf{f_L}\left(r_q\right)}{\partial V_{kR}}=\frac{N_q Q_{rated} V_{loadR}\left(V_{loadI}^2+V_{loadR}^2\right)^{\frac{N_q}{2}-1}}{\left(V_{rated}\right)^{N_p}}+I_{loadI} \tag{1.52}$$

$$\mathbf{C_{L1}}\left(r_q,m\right)=\frac{\partial \mathbf{f_L}\left(r_q\right)}{\partial V_{mR}}=-\mathbf{C_{L1}}\left(r_q,k\right) \tag{1.53}$$

$$\mathbf{C_{L2}}\left(r_q,k\right)=\frac{\partial \mathbf{f_L}\left(r_q\right)}{\partial V_{kI}}=\frac{N_q Q_{rated} V_{loadI}\left(V_{loadI}^2+V_{loadR}^2\right)^{\frac{N_q}{2}-1}}{\left(V_{rated}\right)^{N_p}}-I_{loadR} \tag{1.54}$$

$$\mathbf{C}_{\mathbf{L2}}\left(r_q, m\right) = \frac{\partial \mathbf{f}_{\mathbf{L}}\left(r_q\right)}{\partial V_{mI}} = -\mathbf{C}_{\mathbf{L2}}\left(r_q, k\right) \tag{1.55}$$

$$\mathbf{D}_{\mathbf{L1}}\left(r_q, r\right) = \frac{\partial \mathbf{f}_{\mathbf{L}}\left(r_q\right)}{\partial I_{loadR}} = -V_{loadI} \tag{1.56}$$

$$\mathbf{D}_{\mathbf{L2}}\left(r_q, r\right) = \frac{\partial \mathbf{f}_{\mathbf{L}}\left(r_q\right)}{\partial I_{loadI}} = V_{loadR} \tag{1.57}$$

The formulations from (1.46) to (1.57) are developed for a load connected between two nodes of the circuit. If a load is connected between a node and the ground, the terms above which contain the argument m vanish.

2.2.3 The Conventional Generator Constraints

Any generator constraint can be independently modeled in MANA formulation. The generators can be any of the three types [3]:

I. Slack generator

II. PQ generator

III. PV generator

Consider the generator indexed as r shown in Figure 2.6. The generator is connected to the network at the three phase bus numbered as k. The model described here is called 'voltage source based generator model' as it is modeled with a balanced voltage source behind an impedance. It is important to note that internal nodes of the generator model shown are excluded from $\vec{\mathbf{Y}}_{\mathbf{n}}$.

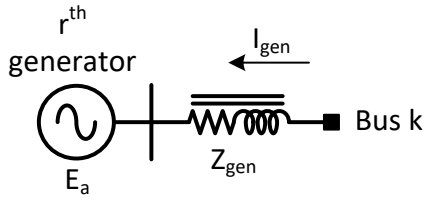

Figure 2.6: Generic Generator Model

where E_a is the phase 'a' component of the internal generator voltage, $\vec{\mathbf{I}}_{\mathbf{gen}}$ is the three phase generator current whose direction is defined as 'into the device', $\vec{\mathbf{Z}}_{\mathbf{gen}}$ is the 3 by 3 internal impedance matrix of this generator.

Let ka, kb, and kc denote the phases 'a', 'b', and 'c' of the bus k. Thus, the terminal voltage phasors of the generator can be in terms of the unknown variables:

$$\vec{\mathbf{V}}_{\mathbf{t}} = \begin{bmatrix} \vec{V}_{ka} \\ \vec{V}_{kb} \\ \vec{V}_{kc} \end{bmatrix} = \begin{bmatrix} \vec{\mathbf{V}}_{\mathbf{n}}(ka) \\ \vec{\mathbf{V}}_{\mathbf{n}}(kb) \\ \vec{\mathbf{V}}_{\mathbf{n}}(kc) \end{bmatrix} \tag{1.58}$$

where V_{ka}, V_{kb}, and V_{kc} are the voltages at nodes ka, kb, and kc, respectively. Their rectangular form become:

$$\begin{bmatrix} \vec{V}_{ka} \\ \vec{V}_{kb} \\ \vec{V}_{kc} \end{bmatrix} = \begin{bmatrix} V_{kaR} + jV_{kaI} \\ V_{kbR} + jV_{kbI} \\ V_{kcR} + jV_{kcI} \end{bmatrix} \tag{1.59}$$

Let $\mathbf{C}_{\mathbf{G}}$ and $\mathbf{D}_{\mathbf{G}}$ be partitioned into two submatrices as follows:

$$\mathbf{C}_{\mathbf{G}} = \begin{bmatrix} \mathbf{C}_{\mathbf{G1}} & \mathbf{C}_{\mathbf{G2}} \end{bmatrix} \tag{1.60}$$

$$\mathbf{D}_{\mathbf{G}} = \begin{bmatrix} \mathbf{D}_{\mathbf{G1}} & \mathbf{D}_{\mathbf{G2}} \end{bmatrix} \tag{1.61}$$

$\mathbf{C}_{\mathbf{G1}}$: The partial derivative of the generator constraint w.r.t the real part of the node voltages

$\mathbf{C}_{\mathbf{G2}}$: The partial derivative of the generator constraint w.r.t the imaginary part of the node voltages

$\mathbf{D}_{\mathbf{G1}}$: The partial derivative of the generator constraint w.r.t the real part of the generator current

$\mathbf{D}_{\mathbf{G2}}$: The partial derivative of the generator constraint w.r.t the imaginary part of the generator current

One of the hypothesis in this generator representation is that the internal source is defined as a balanced three phase voltage source. Based on this, it is enough to define only one unknown for the internal voltage.

$$\vec{\mathbf{E}}_{\mathbf{Int}} = \begin{bmatrix} \vec{E}_a \\ \vec{E}_b \\ \vec{E}_c \end{bmatrix} = \begin{bmatrix} 1 \\ a^2 \\ a \end{bmatrix} E_a \qquad (1.62)$$
$$where\ a = 1\angle 120°$$

where $\vec{\mathbf{E}}_{\mathbf{Int}}$ is the vector of the internal voltage phasors for this generator, E_b and E_c are the voltages of the phases 'b' and 'c' of the internal generator voltage. The voltage of the phase 'a' voltage is the only independent unknown represented in $\vec{\mathbf{E}}_{\mathbf{G}}$. For the r th generator, this unknown is located as follows:

$$\vec{\mathbf{E}}_{\mathbf{G}}(r) = E_a \qquad (1.63)$$

The admittance matrix of this generator can be found by inverting its impedance matrix; given by the formula:

$$\vec{\mathbf{Y}}_{\mathbf{gen}} = \vec{\mathbf{Z}}_{\mathbf{gen}}^{-1}$$
$$where\ \vec{\mathbf{Y}}_{\mathbf{gen}} = \begin{bmatrix} \vec{y}_{11} & \vec{y}_{12} & \vec{y}_{13} \\ \vec{y}_{21} & \vec{y}_{22} & \vec{y}_{23} \\ \vec{y}_{31} & \vec{y}_{31} & \vec{y}_{33} \end{bmatrix} \qquad (1.64)$$

The three current components are independently represented in the generator current vector $\vec{\mathbf{I}}_{\mathbf{G}}$. Let r_1 r_2 and r_3 the indices of the currents of the r^{th} generator under consideration. The elements of $\mathbf{I}_{\mathbf{G}}$ are given by the formula:

$$\begin{bmatrix} \vec{\mathbf{I}}_{\mathbf{G}}(r_1) \\ \vec{\mathbf{I}}_{\mathbf{G}}(r_2) \\ \vec{\mathbf{I}}_{\mathbf{G}}(r_3) \end{bmatrix} = \vec{\mathbf{I}}_{\mathbf{gen}} = \begin{bmatrix} \vec{I}_{gena} \\ \vec{I}_{genb} \\ \vec{I}_{genc} \end{bmatrix} \qquad (1.65)$$

The rectangular form of the generator current can be written as:

$$\begin{bmatrix} \vec{I}_{gena} \\ \vec{I}_{genb} \\ \vec{I}_{genc} \end{bmatrix} = \begin{bmatrix} I_{genaR} + jI_{genaI} \\ I_{genbR} + jI_{gencI} \\ I_{gencR} + jI_{gencI} \end{bmatrix} \qquad (1.66)$$

Noting the direction of the generation current as 'into the device', the elements of $\vec{\mathbf{A}}_{\mathbf{IG}}$ depend on the node numbers of the terminal:

$$\begin{aligned}\vec{\mathbf{A}}_{\mathbf{IG}}\left(ka, r_1\right) &= 1\\ \vec{\mathbf{A}}_{\mathbf{IG}}\left(kb, r_2\right) &= 1\\ \vec{\mathbf{A}}_{\mathbf{IG}}\left(kc, r_3\right) &= 1\end{aligned} \tag{1.67}$$

In total, each generator introduces four new unknowns: three of them being the current and one being the internal voltage.

2.2.3.1 The Generator Current (Linear) Constraint

The first set of constraints for a generator comes from the current equation. The generator current vector $\vec{\mathbf{I}}_{\mathbf{gen}}$ in Figure 2.6 can be written in terms of the internal voltages and terminal voltages of the generator:

$$\vec{\mathbf{Y}}_{\mathbf{gen}}\left(\vec{\mathbf{V}}_{\mathbf{t}} - \vec{\mathbf{E}}_{\mathbf{Int}}\right) = \vec{\mathbf{I}}_{\mathbf{gen}} \tag{1.68}$$

By using (1.58), (1.62),(1.64), (1.65), the constraint equation corresponding to (1.68) can be written as:

$$\begin{bmatrix}\vec{\mathbf{f}}_{\mathbf{E}}\left(r_1\right)\\ \vec{\mathbf{f}}_{\mathbf{E}}\left(r_2\right)\\ \vec{\mathbf{f}}_{\mathbf{E}}\left(r_3\right)\end{bmatrix} = \begin{bmatrix}\vec{y}_{11} & \vec{y}_{12} & \vec{y}_{13}\\ \vec{y}_{21} & \vec{y}_{22} & \vec{y}_{23}\\ \vec{y}_{31} & \vec{y}_{31} & \vec{y}_{33}\end{bmatrix}\begin{bmatrix}\vec{V}_{ka}\\ \vec{V}_{kb}\\ \vec{V}_{kc}\end{bmatrix} - \begin{bmatrix}\vec{y}_{11} & \vec{y}_{12} & \vec{y}_{13}\\ \vec{y}_{21} & \vec{y}_{22} & \vec{y}_{23}\\ \vec{y}_{31} & \vec{y}_{31} & \vec{y}_{33}\end{bmatrix}\begin{bmatrix}1\\ a^2\\ a\end{bmatrix}\vec{E}_a - \begin{bmatrix}1 & 0 & 0\\ 0 & 1 & 0\\ 0 & 0 & 1\end{bmatrix}\begin{bmatrix}\vec{I}_{gena}\\ \vec{I}_{genb}\\ \vec{I}_{genc}\end{bmatrix} \tag{1.69}$$

The entries of matrices $\vec{\mathbf{Y}}_{\mathbf{G}}$, $\vec{\mathbf{Y}}_{\mathbf{GE}}$, and $\vec{\mathbf{D}}_{\mathbf{E}}$ are obtained from (1.69).

For a single generator unit, there are eight unknowns which require eight constraints. The generator current constraint forms six of these constraints which are given in (1.69). The remaining two equations depend on the operation of the generator which will be explained in the next chapter.

2.2.3.2 The Total Injected Real Power Constraint

The total injected real power is a constraint for PQ and PV machines. Based on the model in Figure 2.6, the injected real power by the generator can be written as:

$$P_{injected} = \mathrm{Re}\left(-\vec{\mathbf{I}}^{*}_{\mathbf{gen}}\vec{\mathbf{V}}_{\mathbf{t}}\right) \tag{1.70}$$

The minus is due to the direction of $\vec{\mathbf{I}}_{\mathbf{gen}}$ being out of the node. (1.70) must be rewritten in terms of the circuit unknowns.

By using (1.65) and (1.58), (1.70) can be rewritten as:

$$P_{injected} = \mathrm{Re}\left(-\vec{I}^{*}_{gena}\vec{V}_{ka} - \vec{I}^{*}_{genb}\vec{V}_{kb} - \vec{I}^{*}_{genc}\vec{V}_{kc}\right) \tag{1.71}$$

Let r_p denote the index of this constraint in the vector $\mathbf{f_G}$ in (1.27) and P_r denote the specified power constraint for the r th generator.

$$\mathbf{f_G}\left(r_p\right) = P_r - P_{injected} \tag{1.72}$$

The Jacobian terms corresponding to this constraint are found as follows [3]:

$$\mathbf{C_{G1}}\left(r_p, ka\right) = \frac{\partial \mathbf{f_G}\left(r_p\right)}{\partial V_{kaR}} = I_{genaR} \tag{1.73}$$

$$\mathbf{C_{G1}}\left(r_p, kb\right) = \frac{\partial \mathbf{f_G}\left(r_p\right)}{\partial V_{kbR}} = I_{genbR} \tag{1.74}$$

$$\mathbf{C_{G1}}\left(r_p, kc\right) = \frac{\partial \mathbf{f_G}\left(r_p\right)}{\partial V_{kcR}} = I_{gencR} \tag{1.75}$$

$$\mathbf{C_{G2}}\left(r_p, ka\right) = \frac{\partial \mathbf{f_G}\left(r_p\right)}{\partial V_{kaI}} = I_{genaI} \tag{1.76}$$

$$\mathbf{C_{G2}}\left(r_p, kb\right) = \frac{\partial \mathbf{f_G}\left(r_p\right)}{\partial V_{kbI}} = I_{genbI} \tag{1.77}$$

$$\mathbf{C_{G2}}\left(r_p, kc\right) = \frac{\partial \mathbf{f_G}\left(r_p\right)}{\partial V_{kcI}} = I_{gencI} \tag{1.78}$$

$$\mathbf{D_{G1}}\left(r_p, r_1\right) = \frac{\partial \mathbf{f_G}\left(r_p\right)}{\partial I_{genaR}} = V_{kaR} \tag{1.79}$$

$$\mathbf{D_{G1}}\left(r_p, r_2\right) = \frac{\partial \mathbf{f_G}\left(r_p\right)}{\partial I_{genbR}} = V_{kbR} \tag{1.80}$$

$$\mathbf{D_{G1}}\left(r_p, r_3\right) = \frac{\partial \mathbf{f_G}\left(r_p\right)}{\partial I_{gencR}} = V_{kcR} \tag{1.81}$$

$$\mathbf{D_{G2}}\left(r_p, r_1\right) = \frac{\partial \mathbf{f_G}\left(r_p\right)}{\partial I_{genaI}} = V_{kaI} \tag{1.82}$$

$$\mathbf{D_{G2}}\left(r_p, r_2\right) = \frac{\partial \mathbf{f_G}\left(r_p\right)}{\partial I_{genbI}} = V_{kbI} \tag{1.83}$$

$$\mathbf{D_{G2}}\left(r_p, r_3\right) = \frac{\partial \mathbf{f_G}\left(r_p\right)}{\partial I_{gencI}} = V_{kcI} \tag{1.84}$$

2.2.3.3 The Total Injected Reactive Power Constraint

The total injected reactive power is a constraint only for a PQ machine. For the generator demonstrated in Figure 2.6, the injected reactive power can be defined as:

$$Q_{injected} = \mathrm{Im}\left(-\vec{\mathbf{I}}^{*}_{\mathbf{gen}}\bar{\mathbf{V}}_{\mathbf{t}}\right) \tag{1.85}$$

By using (1.58) and (1.65), the injected reactive power can be expressed as:

$$Q_{injected} = \mathrm{Im}\left(-\vec{I}^{*}_{gena}\vec{V}_{ka} - \vec{I}^{*}_{genb}\vec{V}_{kb} - \vec{I}^{*}_{genc}\vec{V}_{kc}\right) \tag{1.86}$$

Let r_q denote the index of this constraint in the vector $\mathbf{f_G}$ in (1.27) and Q_r denote the specified reactive power constraint for the r th generator.

$$\mathbf{f_G}\left(r_q\right) = Q_r - Q_{injected} \tag{1.87}$$

The Jacobian terms for this constraint are given as follows [3]:

$$\mathbf{C_{G1}}\left(r_q, ka\right) = \frac{\partial \mathbf{f_G}\left(r_q\right)}{\partial V_{kaR}} = -I_{genaI} \tag{1.88}$$

$$\mathbf{C_{G1}}\left(r_q, kb\right) = \frac{\partial \mathbf{f_G}\left(r_q\right)}{\partial V_{kbR}} = -I_{genbI} \tag{1.89}$$

$$\mathbf{C_{G1}}\left(r_q, kc\right) = \frac{\partial \mathbf{f_G}\left(r_q\right)}{\partial V_{kcR}} = -I_{gencI} \tag{1.90}$$

$$\mathbf{C}_{\mathbf{G2}}\left(r_q, ka\right) = \frac{\partial \mathbf{f}_{\mathbf{G}}\left(r_q\right)}{\partial V_{kaI}} = I_{genaR} \tag{1.91}$$

$$\mathbf{C}_{\mathbf{G2}}\left(r_q, kb\right) = \frac{\partial \mathbf{f}_{\mathbf{G}}\left(r_q\right)}{\partial V_{kbI}} = I_{genbR} \tag{1.92}$$

$$\mathbf{C}_{\mathbf{G2}}\left(r_q, kc\right) = \frac{\partial \mathbf{f}_{\mathbf{G}}\left(r_q\right)}{\partial V_{kcI}} = I_{gencR} \tag{1.93}$$

$$\mathbf{D}_{\mathbf{G1}}\left(r_q, r_1\right) = \frac{\partial \mathbf{f}_{\mathbf{G}}\left(r_q\right)}{\partial I_{genaR}} = V_{kaI} \tag{1.94}$$

$$\mathbf{D}_{\mathbf{G1}}\left(r_q, r_2\right) = \frac{\partial \mathbf{f}_{\mathbf{G}}\left(r_q\right)}{\partial I_{genbR}} = V_{kbI} \tag{1.95}$$

$$\mathbf{D}_{\mathbf{G1}}\left(r_q, r_3\right) = \frac{\partial \mathbf{f}_{\mathbf{G}}\left(r_q\right)}{\partial I_{gencR}} = V_{kcI} \tag{1.96}$$

$$\mathbf{D}_{\mathbf{G2}}\left(r_q, r_1\right) = \frac{\partial \mathbf{f}_{\mathbf{G}}\left(r_q\right)}{\partial I_{genaI}} = -V_{kaR} \tag{1.97}$$

$$\mathbf{D}_{\mathbf{G2}}\left(r_q, r_2\right) = \frac{\partial \mathbf{f}_{\mathbf{G}}\left(r_q\right)}{\partial I_{genbI}} = -V_{kbR} \tag{1.98}$$

$$\mathbf{D}_{\mathbf{G2}}\left(r_q, r_3\right) = \frac{\partial \mathbf{f}_{\mathbf{G}}\left(r_q\right)}{\partial I_{gencI}} = -V_{kcR} \tag{1.99}$$

2.2.3.4 The Magnitude Constraint Defined on Phase Voltage

The magnitude of the phase voltage at the terminals of a generator can be a constraint for a PV generator. The formulation here will be given for the phase ‘a’ voltage of the generator shown in Figure 2.6, but it can be generalized for the other phases. The magnitude of the phase ‘a’ is given by the formula:

$$\left|\vec{V}_{ka}\right| = \sqrt{V_{kaR}^2 + V_{kaI}^2} \tag{1.100}$$

Let r_m be the index of this constraint in $\mathbf{f_G}$ vector and V_m be the desired voltage magnitude. Then, the constraint equation becomes:

$$\mathbf{f_G}\left(r_m\right) = V_m - \left|\vec{V}_{ka}\right| \tag{1.101}$$

The Jacobian terms for this constraint are found as follows [3]:

$$\mathbf{C_{G1}}\left(r_m, ka\right) = \frac{\partial \mathbf{f_G}\left(r_m\right)}{\partial V_{kaR}} = \frac{-V_{kaR}}{\left|\vec{V}_{ka}\right|} \tag{1.102}$$

$$\mathbf{C_{G2}}\left(r_m, ka\right) = \frac{\partial \mathbf{f_G}\left(r_m\right)}{\partial V_{kaI}} = \frac{-V_{kaI}}{\left|\vec{V}_{ka}\right|} \tag{1.103}$$

2.2.3.5 The Magnitude Constraint Defined on Positive Sequence Voltage

Instead of the phase voltage, the voltage magnitude constraint can also be defined on the positive sequence component at the terminals of a PV generator. The positive sequence of the voltage at the terminals is written as follows:

$$\vec{V}_{k+} = \frac{1}{3}\left(\vec{V}_{ka} + a\vec{V}_{kb} + a^2\vec{V}_{kc}\right) \tag{1.104}$$

The real and imaginary parts can be expressed in terms of the real unknown quantities as:

$$\mathrm{Re}\left(\vec{V}_{k+}\right) = \frac{V_{kaR}}{3} - \frac{V_{kbR}}{6} - \frac{V_{kcR}}{6} - \frac{\sqrt{3}V_{kbI}}{6} + \frac{\sqrt{3}V_{kcI}}{6} \tag{1.105}$$

$$\mathrm{Im}\left(\vec{V}_{k+}\right) = \frac{V_{kaI}}{3} - \frac{V_{kbI}}{6} - \frac{V_{kcI}}{6} + \frac{\sqrt{3}V_{kbR}}{6} - \frac{\sqrt{3}V_{kcR}}{6} \tag{1.106}$$

Let r_v denote the index of this constraint in $\mathtt{f}_{\mathtt{G}}$ and V_{m+} be the desired magnitude of the positive sequence voltage.

$$\mathbf{f_G}\left(r_v\right) = V_{m+} - \left|\vec{V}_{k+}\right| \tag{1.107}$$

The Jacobian terms for this constraint become [3]:

$$\mathbf{C_{G1}}\left(r_v, ka\right) = \frac{\partial \mathbf{f_G}\left(r_v\right)}{\partial V_{kaR}} = \frac{\mathrm{Re}\left(V_{k+}\right)}{3\left|\vec{V}_{k+}\right|} \tag{1.108}$$

$$\mathbf{C_{G1}}\left(r_v, kb\right) = \frac{\partial \mathbf{f_G}\left(r_v\right)}{\partial V_{kbR}} = -\frac{\mathrm{Re}\left(\vec{V}_{k+}\right) - \sqrt{3}\,\mathrm{Im}\left(\vec{V}_{k+}\right)}{6\left|\vec{V}_{k+}\right|} \tag{1.109}$$

$$\mathbf{C_{G1}}\left(r_v, kc\right) = \frac{\partial \mathbf{f_G}\left(r_v\right)}{\partial V_{kcR}} = -\frac{\mathrm{Re}\left(\vec{V}_{k+}\right) + \sqrt{3}\,\mathrm{Im}\left(\vec{V}_{k+}\right)}{6\left|\vec{V}_{k+}\right|} \tag{1.110}$$

$$\mathbf{C_{G2}}\left(r_v, ka\right) = \frac{\partial \mathbf{f_G}\left(r_v\right)}{\partial V_{kaI}} = \frac{\mathrm{Im}\left(V_{k+}\right)}{3\left|\vec{V}_{k+}\right|} \tag{1.111}$$

$$\mathbf{C_{G2}}\left(r_v, kb\right) = \frac{\partial \mathbf{f_G}\left(r_v\right)}{\partial V_{kbI}} = -\frac{\mathrm{Im}\left(\vec{V}_{k+}\right) + \sqrt{3}\,\mathrm{Re}\left(\vec{V}_{k+}\right)}{6\left|\vec{V}_{k+}\right|} \tag{1.112}$$

$$\mathbf{C_{G2}}\left(r_v, kc\right) = \frac{\partial \mathbf{f_G}\left(r_v\right)}{\partial V_{kcI}} = -\frac{\mathrm{Im}\left(\vec{V}_{k+}\right) - \sqrt{3}\,\mathrm{Re}\left(\vec{V}_{k+}\right)}{6\left|\vec{V}_{k+}\right|} \tag{1.113}$$

2.2.3.6 The Phasor Constraint Defined on the Positive Sequence Voltage Phasor

The phasor value of the positive sequence component at the generator terminals are defined with two constraints. These constraints are defined only for slack generators. Each of the real and imaginary part of the phasor introduces one constraint. The positive sequence component V_{k+} of the terminal voltage of the generator in Figure 2.6 is given in (1.104).

Let r_R and r_I be the indices for the real and imaginary part constraint equations in $\mathtt{f_G}$, and $V_+ = V_m \angle \theta$ be the desired phasor value. Then, the constraint equation becomes:

$$\mathbf{f_G}\left(r_R\right) = \mathrm{Re}\left(V_+ - V_{k+}\right) \tag{1.114}$$

$$\mathbf{f_G}\left(r_I\right) = \mathrm{Im}\left(V_+ - V_{k+}\right) \tag{1.115}$$

Therefore, the Jacobian entries for the real part constraint in (1.114) are written as follows [3]:

$$\mathbf{C_{G1}}\left(r_R, ka\right) = \frac{\partial \mathbf{f_G}\left(r_R\right)}{\partial V_{kaR}} = \frac{-1}{3} \tag{1.116}$$

$$\mathbf{C_{G1}}\left(r_R, kb\right) = \frac{\partial \mathbf{f_G}\left(r_R\right)}{\partial V_{kbR}} = \frac{1}{6} \tag{1.117}$$

$$\mathbf{C_{G1}}\left(r_R, kc\right) = \frac{\partial \mathbf{f_G}\left(r_R\right)}{\partial V_{kcR}} = \frac{1}{6} \tag{1.118}$$

$$\mathbf{C_{G2}}\left(r_R, kb\right) = \frac{\partial \mathbf{f_G}\left(r_R\right)}{\partial V_{kbI}} = \frac{\sqrt{3}}{6} \tag{1.119}$$

$$\mathbf{C_{G2}}\left(r_R, kc\right) = \frac{\partial \mathbf{f_G}\left(r_R\right)}{\partial V_{kcI}} = \frac{-\sqrt{3}}{6} \tag{1.120}$$

Similarly, the Jacobian entries for the imaginary part constraint in (1.115) can be derived as follows [3]:

$$\mathbf{C_{G1}}\left(r_I, kb\right) = \frac{\partial \mathbf{f_G}\left(r_I\right)}{\partial V_{kbR}} = \frac{-\sqrt{3}}{6} \tag{1.121}$$

$$\mathbf{C_{G1}}\left(r_I, kc\right) = \frac{\partial \mathbf{f_G}\left(r_I\right)}{\partial V_{kcR}} = \frac{\sqrt{3}}{6} \tag{1.122}$$

$$\mathbf{C_{G2}}\left(r_I, ka\right) = \frac{\partial \mathbf{f_G}\left(r_I\right)}{\partial V_{kaI}} = \frac{-1}{3} \tag{1.123}$$

$$\mathbf{C_{G2}}\left(r_I, kb\right) = \frac{\partial \mathbf{f_G}\left(r_I\right)}{\partial V_{kbI}} = \frac{1}{6} \tag{1.124}$$

$$\mathbf{C_{G2}}\left(r_I, kc\right) = \frac{\partial \mathbf{f_G}\left(r_I\right)}{\partial V_{kcI}} = \frac{1}{6} \tag{1.125}$$

2.2.4 Convergence Criteria

In order to finalize the iterative load flow algorithm, a convergence criterion is needed. Most often the time, when the difference in the voltage magnitudes $\mathbf{\Delta V_n}^{(i)}$ (which is an element of $\mathbf{\Delta x}^{(i)}$) is sufficiently small, the process is terminated or once the function set is sufficiently close to zero. This condition has been expressed in EMTP-RV [33] with the following inequality:

$$\frac{\left|\mathbf{\Delta V_n}\left(k\right)\right|}{\left|\mathbf{V_n}\left(k\right)\right|} < \varepsilon \quad \vee \quad \left|\mathbf{f}\left(\mathbf{x}\right)\right| < \varepsilon \tag{1.126}$$

where ε is a small number typically smaller than 10^{-4}.

2.3 Summary

This chapter is a review of the existing MANA formulation and presents the MANA approach for phasor solution and load flow analysis. First, the steady state analysis in MANA is presented where all the network components are linearized using linear devices such as RLC branches, branch dependent devices (such as ideal transformers, regulators etc.), voltage sources and switches. Then, the nonlinear form of MANA is presented in which the Jacobian matrix is formed for nonlinear constraints; such as load and generator equations. All the material presented here is the recollection of the literature [1-5]. This chapter will form the basis for the material presented in the following chapters.

CHAPTER 3 STEP VOLTAGE REGULATORS

The step voltage regulators have usually been represented as a variable impedance in load-flow solvers [34-36]. From modelling perspective, this is a workaround in order to integrate an electro-magnetically coupled device into the nodal admittance matrix which has limitations in terms of accommodating different components. Once the tap position is adjusted according to the voltage constraint, the nodal admittance matrix is modified by updating the equivalent variable impedance of the regulator according to the new tap position. The voltage regulators are also represented with hybrid models, as a combination of impedance and current source [37], within again the classical nodal admittance matrix formulation. There exists also a hybrid model which is composed of current and voltage sources together with passive impedances [38].

In this chapter, the integration of the step voltage regulators into the load flow analysis procedure explained in 2.2 will be discussed.

3.1 The Voltage Regulator Model

The typical voltage regulator topology is shown in Figure 3.1. It is composed of two main parts: (1) a tap changing autotransformer and (2) a line drop compensator circuit [22].

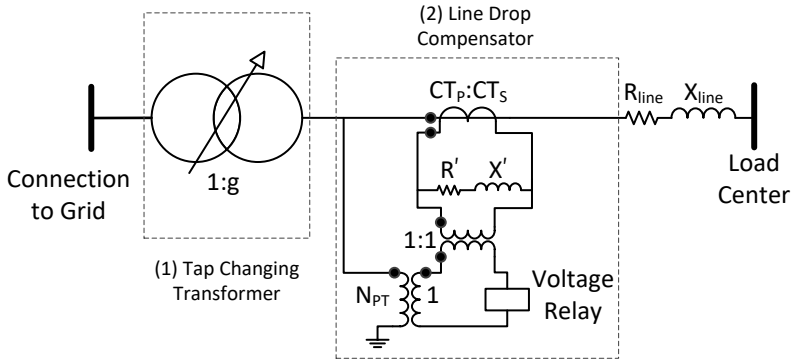

Figure 3.1: Voltage Regulator Circuit Diagram

CT_P : Primary current rating of the current transformer (A)

CT_S : Secondary current rating of the current transformer (A)

N_{PT} : Turns ratio of the voltage transformer

R' : Adjustable compensator circuit resistance (Ω or Volts)

X' : Adjustable compensator circuit reactance (Ω or Volts)

R_{line} : Equivalent resistance of the feeder between regulator and load center (Ω)

X_{line} : Equivalent reactance of the feeder between regulator and load center (Ω)

g : Voltage transformation ratio of the autotransformer

The tap changing transformer change its turns ratio via the tap settings to adjust the voltage on its secondary terminals. It can be either non-ideal with internal impedance or ideal with no impedance. The objective of the line drop compensator circuit is to be able to estimate the voltage at a specified node which is the voltage magnitude at the load center in Figure 3.1. The line drop compensator behaves as a miniature replica of the load feeder between the regulator and the load center. Assuming the voltage relay has a huge input impedance, and the settings R' and X' are given in **Ω**, the voltage on the voltage relay can be expressed as follows:

$$\vec{V}_{relay} = \left(\frac{\vec{V}_{reg}}{N_{PT}} \right) + \vec{I}_D \frac{CT_S}{CT_P} \left(R' + jX' \right) \tag{2.1}$$

$\vec{V}_{relay}$: The voltage appearing on the voltage relay in the line drop compensator circuit

$\vec{V}_{reg}$: The phase to ground voltage on the secondary terminals of the tap changing transformer

$\vec{I}_D$: The current entering the secondary side of the tap changing transformer

The direction of the current I_D is chosen in accordance with the existing ideal transformer model in MANA defined in 2.1.3.

The relation between the output of the tap changing transformer and the load center voltage is given by the formula:

$$\vec{V}_{load} = \vec{V}_{reg} + \vec{I}_D \left(R_{line} + jX_{line} \right) \tag{2.2}$$

$\vec{V}_{load}$: The voltage appearing at the load center

The output voltage of the tap changing transformer can be left at the left hand side for both (2.1) and (2.2):

$$\vec{V}_{reg} = N_{PT}\,\vec{V}_{relay} - \vec{I}_D \frac{N_{PT}\,CT_S}{CT_P}\left(R' + jX'\right) \tag{2.3}$$

$$\vec{V}_{reg} = \vec{V}_{load} - \vec{I}_D \left(R_{line} + jX_{line}\right) \tag{2.4}$$

By combining (2.3) and (2.4), the voltage on the relay and the voltage at the load center can be related as follows:

$$\vec{V}_{relay} = \frac{\vec{V}_{load}}{N_{PT}} \tag{2.5}$$

It is important to note that (2.5) ignores the coupling of the line, thus gives an approximate relation. In other words, the parameters R' and X' are calibrated based on the equivalent impedance of the line. By using (2.3) and (2.4), they can be expressed as a function of the equivalent impedance of the line R_{line} and X_{line}. If the calibration of R' and X' is to be done in Ω , the following formula can be used:

$$R' + jX' = \frac{CT_P}{N_{PT} \cdot CT_S}\left(R_{line} + jX_{line}\right) \quad \textit{where } R' \textit{ and } X' \textit{ are in } \Omega \tag{2.6}$$

However, these settings sometimes are expressed in Volts. In this case, (2.6) becomes:

$$R' + jX' = \frac{CT_P}{N_{PT}}\left(R_{line} + jX_{line}\right) \quad \textit{where } R' \textit{ and } X' \textit{ are in Volts} \tag{2.7}$$

Usually, the positive sequence impedance of the line is used for R_{line} and X_{line} in (2.6) and (2.7). If R' and X' are set to zero, the controlled voltage becomes the one right at the secondary side of the tap changing transformer. This voltage corresponds to V_{reg} in (2.3) and (2.4).

In order to choose the right parameters for the line drop compensator circuit, there is a need for the common base values. In North American distribution networks, the voltage base on the line drop

compensator circuit is chosen as 120 V. Thus, the turn ratio of the voltage transformer N_{PT} is obtained from the division of the nominal line to neutral voltage with 120 Volts.

The nominal current at the primary side of the current transformer in the line drop compensator circuit is calculated by considering the rated apparent power of the feeder. This is the main factor while determining CT_P.

The desired voltage setting $|V_{desired}|$ is adjusted on the voltage relay in the base of the line drop compensator circuit, which is 120 V. The setting transferred to the voltage base of the load center, $|V_{set}|$, is given as follows:

$$|V_{set}| = N_{PT} |V_{desired}| \tag{2.8}$$

The operation of the tap changing transformer is not instantaneous. If the magnitude of the relay voltage is not close to the desired voltage setting within an adjusted bandwidth setting for a certain duration (delay setting), then the regulator controller starts changing the taps one by one until the voltage measured by the relay falls in the bandwidth.

The simplified model of a single phase voltage regulator to be modeled in MANA formulation is presented Figure 3.2, neglecting the reflected impedance of the line drop compensator circuit. The proposed model employs a single phase transformer with a variable turns ratio. A multiphase regulator can be formed as a combination of the single phase units.

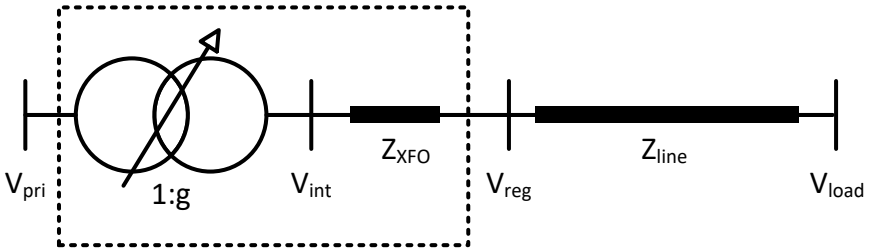

Figure 3.2: Simplified Regulator Model

Z_{line} : The equivalent positive sequence impedance of the feeder between the regulator and the load center $Z_{line} = R_{line} + jX_{line}$

Z_{XFO} : The transformer impedance if the existence of the internal impedance of the tap changing transformer is taken into account

$\vec{V}_{pri}$: The voltage at the primary side of the tap changing transformer

$\vec{V}_{int}$: The internally developed voltage on the secondary side of the tap changing transformer

The model shown in Figure 3.2 can be realized by employing the ideal transformer model described in Figure 2.3. Therefore, the circuit representing the step voltage regulators is demonstrated as Wye grounded-transformer below:

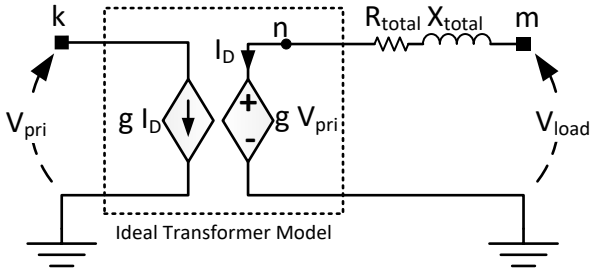

Figure 3.3: Simplified Regulator Circuit

$\vec{Z}_{total}$: The total resistance between the internal node n and the load center $\vec{Z}_{total} = \vec{Z}_{XFO} + \vec{Z}_{line}$

$\vec{V}_{load}$: The voltage at the load center

Although it is not a part of the regulator, the equivalent line impedance is also demonstrated in Figure 3.3, because it directly affects the constraint equation to be solved. The dashed box represents the regulator itself. The objective here is to find the unknown variable, g, iteratively. It is repeated here that g is the turns ratio (or the voltage transformation ratio) of the ideal transformer, and it is equal to the voltage transformation ratio of the autotransformer used in the regulator. Therefore, the unknown vector must be expanded to hold the vector of variable voltage transformation ratios as well.

$$\mathbf{x}^{(i)} = \begin{bmatrix} \mathbf{V_n} \\ \mathbf{I_v} \\ \mathbf{I_d} \\ \mathbf{I_s} \\ \mathbf{I_L} \\ \mathbf{I_G} \\ \mathbf{E_G} \\ \mathbf{g} \end{bmatrix}^{(i)} \tag{2.9}$$

Let r_c and r_g indicate the indices of the regulator current I_D in $\bar{\mathbf{I}}_\mathbf{d}$ and the voltage ratio g of the regulator in $\mathbf{g}$, respectively.

$$\vec{\mathbf{I}}_\mathbf{d}(r_c) = \vec{I}_D = I_{DR} + jI_{DI} \tag{2.10}$$

$$\mathbf{g}(r_g) = g = \frac{\vec{V}_n}{\vec{V}_k} \tag{2.11}$$

Also, the node voltages regarding the regulator are defined as follows:

$$\vec{\mathbf{V}}_\mathbf{n}(k) = \vec{V}_k = V_{kR} + jV_{kI} \tag{2.12}$$

$$\vec{\mathbf{V}}_\mathbf{n}(n) = \vec{V}_n = V_{nR} + jV_{nI} \tag{2.13}$$

$$\vec{\mathbf{V}}_\mathbf{n}(m) = \vec{V}_m = V_{mR} + jV_{mI} \tag{2.14}$$

Thus, the simplified Jacobian matrix in (1.27) needs to be expanded to account for the terms due to $\mathbf{g}$ as well:

$$\begin{bmatrix} \mathbf{Y_n} & \mathbf{V_r^T} & \mathbf{D_r^T} & \mathbf{S_r^T} & \mathbf{A_{IL}} & \mathbf{A_{IG}} & \mathbf{0} & \mathbf{A_{IR}} \\ \mathbf{V_r} & \mathbf{0} & \mathbf{0} & \mathbf{0} & \mathbf{0} & \mathbf{0} & \mathbf{0} & \mathbf{0} \\ \mathbf{D_r} & \mathbf{0} & \mathbf{0} & \mathbf{0} & \mathbf{0} & \mathbf{0} & \mathbf{0} & \mathbf{D_G} \\ \mathbf{S_r} & \mathbf{0} & \mathbf{0} & \mathbf{S_d} & \mathbf{0} & \mathbf{0} & \mathbf{0} & \mathbf{0} \\ \mathbf{C_L} & \mathbf{0} & \mathbf{0} & \mathbf{0} & \mathbf{D_L} & \mathbf{0} & \mathbf{0} & \mathbf{0} \\ \mathbf{C_G} & \mathbf{0} & \mathbf{0} & \mathbf{0} & \mathbf{0} & \mathbf{D_G} & \mathbf{0} & \mathbf{0} \\ \mathbf{Y_G} & \mathbf{0} & \mathbf{0} & \mathbf{0} & \mathbf{0} & \mathbf{B_G} & \mathbf{Y_{GE}} & \mathbf{0} \\ \mathbf{C_{RV}} & \mathbf{0} & \mathbf{C_{RI}} & \mathbf{0} & \mathbf{0} & \mathbf{0} & \mathbf{0} & \mathbf{C_{RG}} \end{bmatrix}^{(i)} \begin{bmatrix} \mathbf{\Delta V_n} \\ \mathbf{\Delta I_v} \\ \mathbf{\Delta I_d} \\ \mathbf{\Delta I_s} \\ \mathbf{\Delta I_L} \\ \mathbf{\Delta I_G} \\ \mathbf{\Delta E_G} \\ \mathbf{\Delta g} \end{bmatrix}^{(i)} = - \begin{bmatrix} \mathbf{f_n} \\ \mathbf{f_v} \\ \mathbf{f_d} \\ \mathbf{f_s} \\ \mathbf{f_L} \\ \mathbf{f_G} \\ \mathbf{f_E} \\ \mathbf{f_R} \end{bmatrix}^{(i)} \tag{2.15}$$

Here, it should be noted that $\mathbf{g}$ is composed of purely real valued unknowns. Thus, the real forms of $\mathbf{A_{IR}}$ and $\mathbf{D_G}$ do not exactly follow the convention used in (1.3).

$$\mathbf{A_{IR}} = \begin{bmatrix} \mathrm{Re}\left(\vec{\mathbf{A}}_{\mathbf{IR}}\right) \\ \mathrm{Im}\left(\vec{\mathbf{A}}_{\mathbf{IR}}\right) \end{bmatrix} \tag{2.16}$$

$$\mathbf{D_G} = \begin{bmatrix} \mathrm{Re}\left(\vec{\mathbf{D}}_{\mathbf{G}}\right) \\ \mathrm{Im}\left(\vec{\mathbf{D}}_{\mathbf{G}}\right) \end{bmatrix} \tag{2.17}$$

The newly added elements of the Jacobian matrix will be explained in the next sections.

3.2 The Constraints and Jacobian Terms

An ideal transformer connected between arbitrary nodes is shown in Figure 3.3 with k, m and n representing nodes. In the MANA load-flow algorithm, a regulator has three types of constraints:

- The current constraint due to the dependent current source
- The voltage constraint due to the dependent voltage source
- $\left|V_{set}\right|$, i.e., the magnitude constraint on the load center voltage V_{load}

3.2.1 Voltage Constraints

The dependent voltage source produces the following constraint:

$$\vec{\mathbf{f}}_{\mathbf{D}}\left(r_c\right) = \vec{V}_n - g\vec{V}_k \tag{2.18}$$

The partial derivative of (2.18) with respect to the node voltage components are already developed previously in (1.13). However, it should be noted that since the turn ratio changes at each iteration, the corresponding entries of $\vec{\mathbf{D}}_{\mathbf{r}}$ must be updated:

$$\vec{\mathbf{D}}_{\mathbf{r}}\left(r_c, k\right) = -g \tag{2.19}$$

The partial derivatives with respect to g are stored in $\vec{\mathbf{D}}_{\mathbf{G}}$:

$$\vec{\mathbf{D}}_{\mathbf{G}}\left(r_c, r_g\right) = -\vec{V}_k \tag{2.20}$$

3.2.2 Current constraints

The currents exiting the two terminals k and n of the ideal transformer unit are given as:

$$\vec{I}_k = -g\vec{I}_D \tag{2.21}$$

$$\vec{I}_n = \vec{I}_D \tag{2.22}$$

These two currents form the constraints for the dependent current source. The calculation of the total current injection constraint in (1.29) remains the same.

The partial derivatives with respect to g which are stored in $\vec{\mathbf{A}}_{\mathbf{IR}}$ are given as:

$$\vec{\mathbf{A}}_{\mathbf{IR}}\left(k, r_g\right) = -\vec{I}_D \tag{2.23}$$

3.2.3 Voltage Magnitude Constraint at the Load Center

The constraint of the regulator can be defined as to keep the voltage on the load center at the set voltage.

$$\mathbf{f}_{\mathbf{R}}\left(r_g\right) = \left|\vec{V}_{load}\right| - \left|V_{set}\right| \tag{2.24}$$

In order to simulate the actual behavior of the regulator, V_{load} can be expressed as a function of the regulator settings as follows:

$$\mathbf{f}_{\mathbf{R}}\left(r_g\right) = \left|g\vec{V}_{pri} + \vec{I}_D\left(\vec{Z}_{XFO} + {N_{PT}}\Big/{CT_P}\left(R' + jX'\right)\right)\right| - \left|V_{set}\right| \tag{2.25}$$

(2.25) can further be simplified to the form below:

$$\mathbf{f}_{\mathbf{R}}\left(r_g\right) = \left|g\vec{V}_{pri} + \vec{I}_D\vec{Z}_{total}\right| - \left|V_{set}\right| \tag{2.26}$$

Let the matrices $\mathbf{C}_{\mathbf{RV}}$ and $\mathbf{C}_{\mathbf{RI}}$ be divided into two as follows:

$$\mathbf{C}_{\mathbf{RV}} = \begin{bmatrix}\mathbf{C}_{\mathbf{RV1}} & \mathbf{C}_{\mathbf{RV2}}\end{bmatrix} \tag{2.27}$$

$$\mathbf{C}_{\mathbf{RI}} = \begin{bmatrix}\mathbf{C}_{\mathbf{RI1}} & \mathbf{C}_{\mathbf{RI2}}\end{bmatrix} \tag{2.28}$$

$\mathbf{C}_{\mathbf{RV1}}$: The partial derivatives of $\mathbf{f}_{\mathbf{R}}$ w.r.t the real parts of the node voltages

$\mathbf{C_{RV2}}$: The partial derivatives of $\mathbf{f_R}$ w.r.t the imaginary parts of the node voltages

$\mathbf{C_{RI1}}$: The partial derivatives of $\mathbf{f_R}$ w.r.t the real parts of the regulator currents

$\mathbf{C_{RI2}}$: The partial derivatives of $\mathbf{f_R}$ w.r.t the imaginary parts of the regulator currents

$$\mathbf{C_{RV1}}\left(r_g,k\right)=\frac{\partial \mathbf{f_R}\left(r_g\right)}{\partial V_{kR}}=\frac{g\,\mathrm{Re}(V_{load})}{\left|V_{load}\right|} \tag{2.29}$$

$$\mathbf{C_{RV2}}\left(r_g,k\right)=\frac{\partial \mathbf{f_R}\left(r_g\right)}{\partial V_{kI}}=\frac{g\,\mathrm{Im}(V_{load})}{\left|V_{load}\right|} \tag{2.30}$$

$$\mathbf{C_{RI1}}\left(r_g,r_c\right)=\frac{\partial \mathbf{f_R}\left(r_g\right)}{\partial I_{DR}}=\frac{R_{total}\,\mathrm{Re}(V_{load})+X_{total}\,\mathrm{Im}(V_{load})}{\left|V_{load}\right|} \tag{2.31}$$

$$\mathbf{C_{RI2}}\left(r_g,r_c\right)=\frac{\partial \mathbf{f_R}\left(r_g\right)}{\partial I_{DI}}=\frac{R_{total}\,\mathrm{Im}(V_{load})-X_{total}\,\mathrm{Re}(V_{load})}{\left|V_{load}\right|} \tag{2.32}$$

$$\mathbf{C_{RR}}\left(r_v,r_v\right)=\frac{\partial \mathbf{f_R}\left(r_g\right)}{\partial g}=\frac{\mathrm{Im}(V_{pri})\,\mathrm{Im}(V_{load})+\mathrm{Re}(V_{pri})\,\mathrm{Re}(V_{load})}{\left|V_{load}\right|} \tag{2.33}$$

3.3 Solution Algorithm and Considerations

Before starting the load-flow algorithm, the elements of $\mathbf{g}$ should be initialized. The initialization is performed by solving the linear system of equations of by representing loads with equivalent impedances evaluated at their nominal voltages. For a voltage regulator, the initial transformation ratio is assumed to be the ratio of the set voltage $\left|V_{set}\right|$ to the nominal primary voltage.

After finding the linear solution for initialization, the load-flow algorithm is run. The existing approach for the load-flow solution using MANA formulation utilizes Newton's method which is defined for real valued, differentiable, continuous functions[4]. On the other hand, a regulator can only have discrete voltage transformation ratios due to its tap settings. Thus, the resultant ratio given by the load flow solution should be rounded to the closest discrete value. It is therefore proposed to split the overall solution into two parts:

- Load-Flow with variable ratio

- Verification of load flow solution with fixed and discrete ratio, and minor adjustment of tap positions if necessary (plus or minus one tap change if necessary)

3.3.1 Load Flow with "g" Being Variable

The difference vector $\mathbf{\Delta g}$ of voltage transformation ratio is present in the unknown vector $\mathbf{\Delta x}$ and thus g is considered as a continuous variable. The Jacobian matrix has the form in (2.15). The ratio g is calculated iteratively for all regulators

Once the iterative process is complete, each element of $\mathbf{g}$ should be rounded to the closest possible value since the tap positions are discrete. For each tap position, there is a corresponding voltage transformation ratio (or turns ratio).

Now let's consider the regulator model given in Figure 3.3. When the tap is at the lowest position, the voltage transformation ratio is called $g_{\min}$ and when it is at the maximum, it is defined as $g_{\max}$. For N_{Tap} number of tap positions, there are $2\times N_{Tap}+1$ possible discrete ratio available. Thus, the discrete turn ratio vector of this regulator is given as (in MATLAB notation):

$$g_{discrete} = linspace\left(g_{\min}, g_{\max}, 2\times N_{Tap}+1\right) \tag{2.34}$$

3.3.2 Load Flow After Fixing "g"

Due to the modification in the turns ratios, the voltage profile must be recalculated. However this time, $\mathbf{g}$ is not represented in the unknown vector $\mathbf{x}$. Thus, the submatrices $\mathbf{J_{TV}}$, $\mathbf{J_{TI}}$, $\mathbf{J_{TD}}$, $\mathbf{A_{TV}}$ and $\mathbf{A_{TI}}$ disappear from the Jacobian matrix. The Jacobian matrix shrinks to the original form described in (1.27). Since the load flow already converged previously and $\mathbf{g}$ is modified slightly, this part usually takes 1 or 2 iterations. At this stage, it is important to check if the magnitudes of the node voltages controlled by the regulators are within the bandwidth. Rather than directly using (2.25), the inequality in (2.35) must be used.

$$\begin{aligned} V_{\min} < \left|\vec{V}_{load}\right| < V_{\max} \\ where\ \vec{V}_{load} = \left|g\vec{V}_{pri} + \vec{I}_D\left(\vec{Z}_{XFO} + {N_{PT}}/{CT_P}\left(R' + jX'\right)\right)\right| \end{aligned} \tag{2.35}$$

where $V_{\min}$ and $V_{\max}$ shows the limits corresponding to the set voltage and the bandwidth of the regulator. If $|V_{load}|$ is less than $V_{\min}$, the tap position must be increased by 1 unless it is at the maximum position. If $|V_{load}|$ is less than $V_{\max}$, then the tap position must be decreased by 1 unless it is at the minimum position. If $|V_{load}|$ is already within the limits, no action is necessary for this regulator. The flow chart indicating the stages of the algorithm is demonstrated in Figure 3.4.

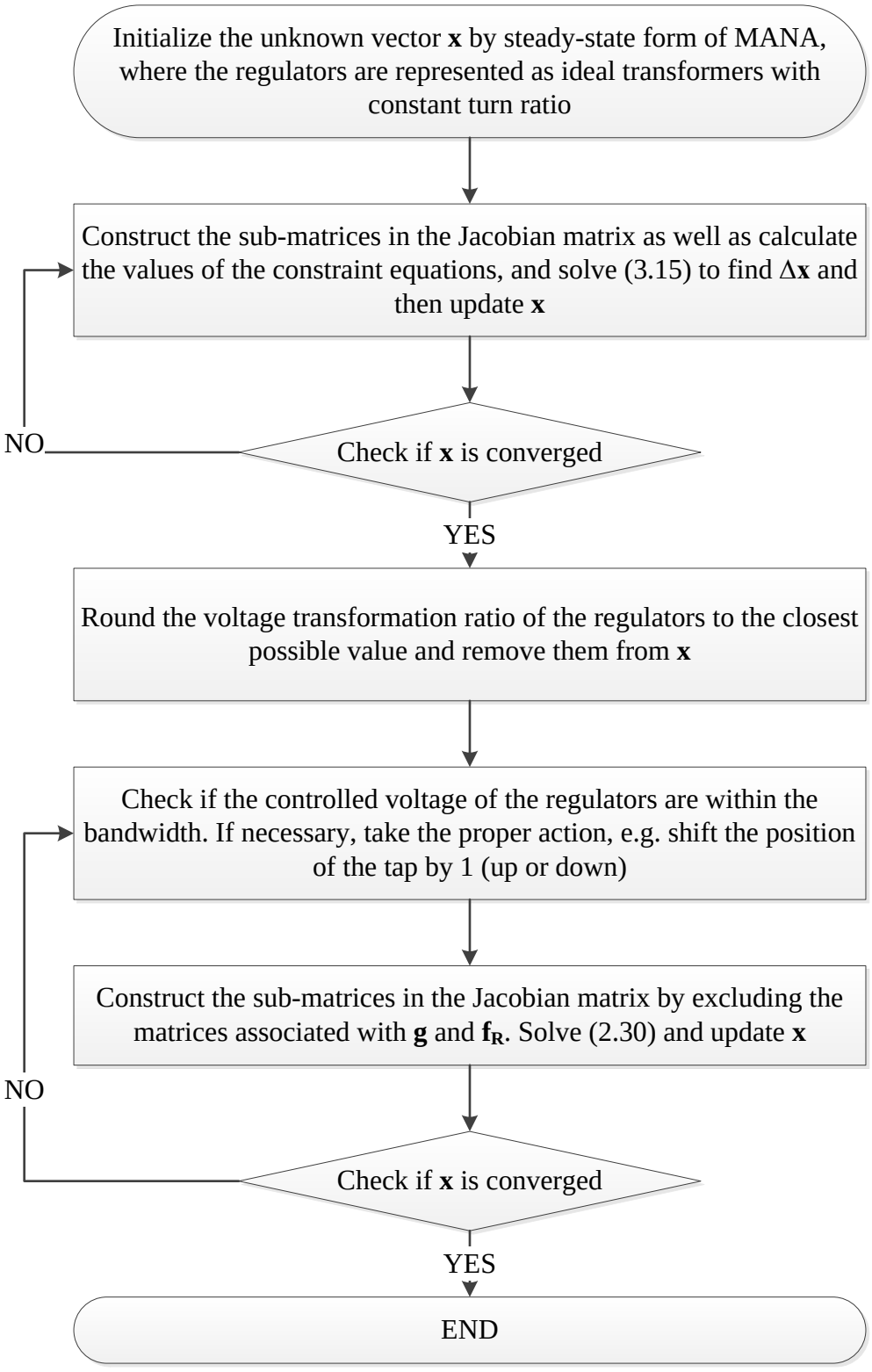

Figure 3.4: Flowchart of the Load Flow with the insertion of Regulators

3.4 Study Cases

The algorithm presented in Figure 3.4 is applied to the standard IEEE test circuits to evaluate the performance.

3.4.1 Study Case-1: Remote Location Voltage Control

The IEEE 13 Node Test Feeder [39] is a small but typical distribution network with a radial structure. The network has an unbalanced nature due to its unbalanced load and untransposed line configurations in the system. This network is presented to serve as a common benchmark to verify the correctness of the algorithms.

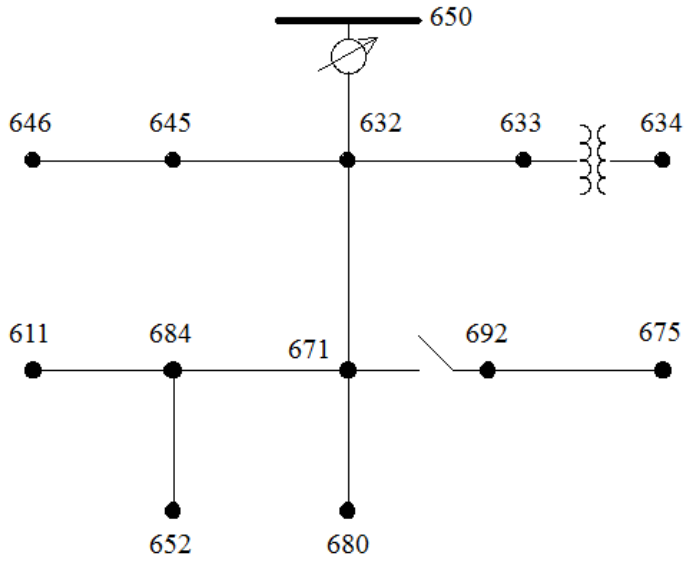

Figure 3.5: IEEE 13 Node Test Feeder

In Figure 3.5, the voltage regulator is placed at the substation bus “650”. It is adjusted to control the voltage at the end of the line segment to which it is connected, i.e., Bus “632”.

The regulator relay settings are given in Table 3.1.

Table 3.1: Regulator Relay data

Monitoring Phase	A-B-C
Bandwidth	2 V
N_{PT}	20
CT_P	700 A
R'	3 V
X'	9 V
V_{set}	122 V

The transformer employed in the regulator has no internal impedance, i.e., $Z_{XFO} = 0$. As R' and X' are given in Volts, (2.7) can be used to form the constraint equation. The regulator is assumed to have 16 tap positions, so there are 33 (2×16+1; 1 neutral, 16 high, 16 low positions) discrete turns ratios possible.

The distribution network is connected to the substation at the bus 650 which is assumed to be the slack bus. The voltage magnitude is kept at 1 pu at the slack bus

By using the parameters of the relay in Table 3.1, the set voltage on the load center in Figure 3.5 is calculated as:

$$\left|V_{set}\right| = 20 \times 122 = 2440 \; Volts \tag{2.36}$$

The bandwidth is set to 2 V. Thus, the acceptable voltage band ranges from 2420 V to 2460 V.

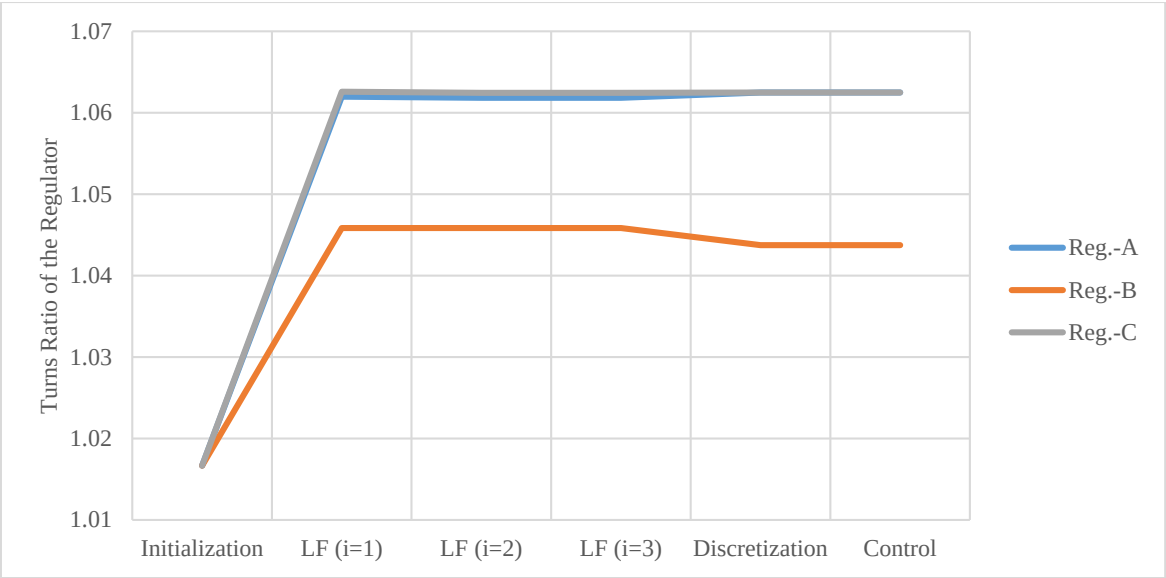

Figure 3.6: The evolution of the voltage transformation ratio of the regulators

The variation of the voltage transformation ratio is demonstrated in Figure 3.6. In the initialization part, the turns ratios are assumed to be equal to the ratio of the set voltage to the nominal voltage (2440/2400=1.06777). The load-flow section is shown with the letters “LF” where turn ratios are represented as variables. In the discretization stage, the turns ratios are rounded to the closest discrete value possible. No load flow solution is performed at this stage. One more load flow iteration is performed in the control stage for convergence with fixed turns ratios.

The calculated tap positions corresponding to the ratios demonstrated in Figure 3.6 are presented in Table 3.2 together with the published results taken from [40]. There is one position difference between the proposed and published tap positions. However, in this regulator, one tap change corresponds to ±0.75 V difference. As the bandwidth is 2 V, a difference of one or two tap position is acceptable.

Table 3.2: Tap Positions

	Proposed	Published
Reg.-A	10	10
Reg.-B	7	8
Reg.-C	10	11

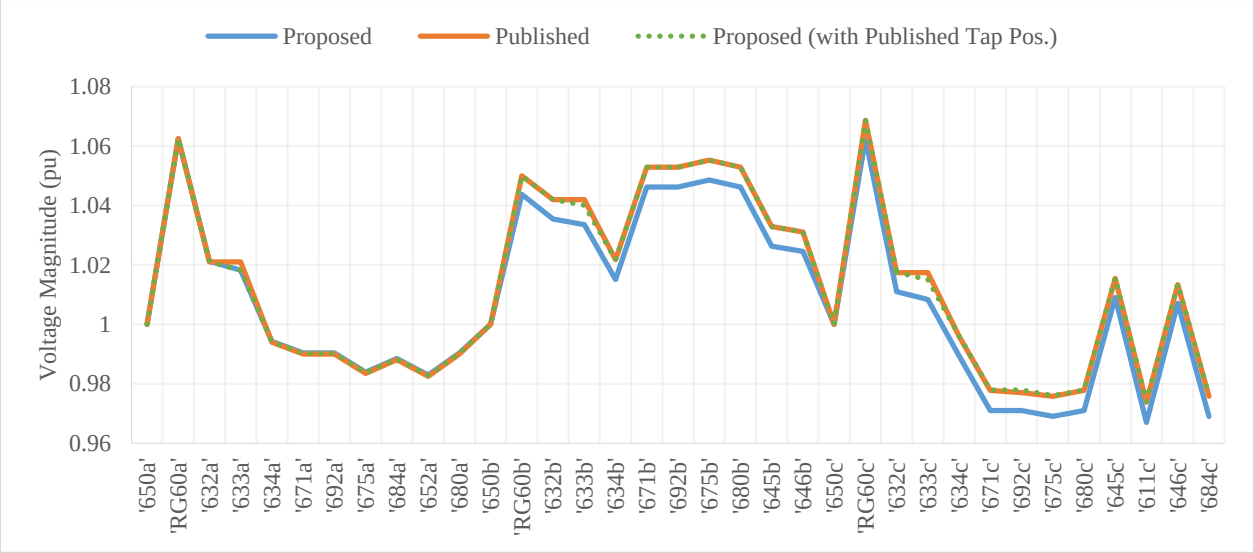

Figure 3.7: The Voltage Profile of the Network

In Figure 3.6: The evolution of the voltage transformation ratio of the regulators, the proposed and published voltage profiles are presented. Although the solutions are close, they do not overlap due to the difference of one tap position.

One of the aspects that needs attention is the voltage on the voltage relay, as it is related to the desired voltage setting. As seen in Table 3.1, the desired voltage is set to 122 V and the relay voltage should be in the vicinity of this setting within the bandwidth. Due to the discrete tap positions, the turns ratio is rounded to the closest value. Therefore, it is normal to have a difference between the relay voltage magnitudes and the desired voltage setting (122 V) as seen in Figure 3.8.

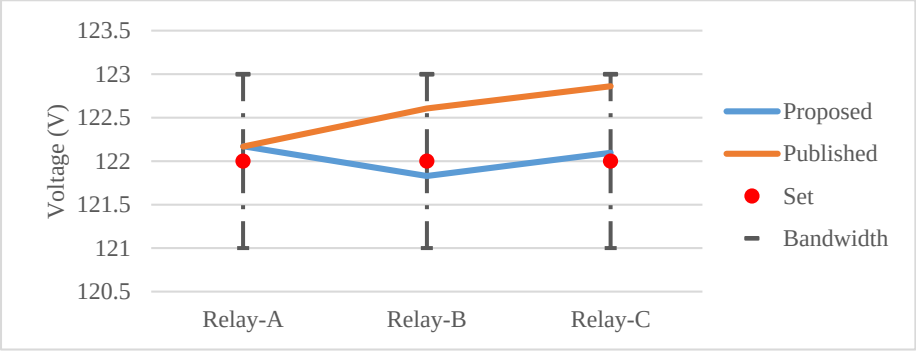

Figure 3.8: The Voltage on the Relay

3.4.2 Study Case-2: Terminal Voltage Control

The second test case is the single line diagram of IEEE 8500 Node Test-Feeder [40] illustrated in Figure 3.9. It is a large, radial and realistic network having both MV and LV levels and containing most components available in a typical North American medium voltage distribution feeder; such as, multiphase voltage regulators, single and three phase capacitor banks, and load service transformers. This network is designed to challenge the algorithms to the limit. As it is described in [41], if any algorithm performs well for the IEEE 8500 node test feeder, it is more likely that it will perform well in actual networks. The original test feeder has both balanced and unbalanced loading cases. In this study case, the unbalanced loading state is considered.

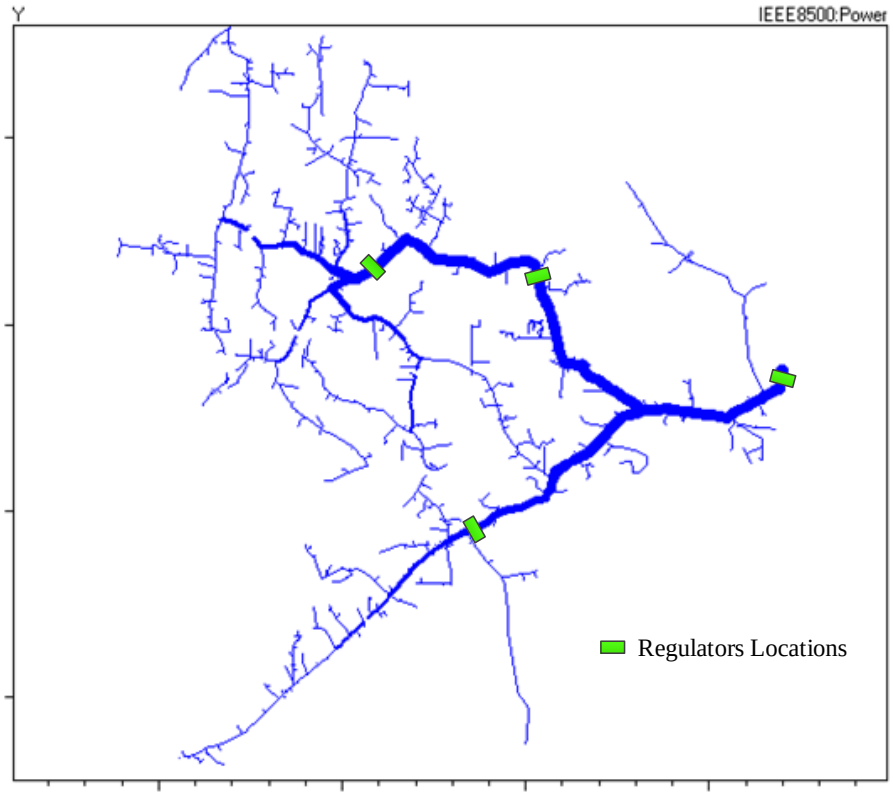

Figure 3.9: IEEE 8500-Node Test Feeder

In the circuit modelled in MANA, there are 12065 nodes (including the internal nodes for the transformers), 3703 lines, 1 transformer, 2354 single phase loads, 9 single phase and 1 three phase capacitor banks, 1177 load service transformer and 4 three phase voltage regulators.

The regulators are modelled as ideal transformers and they control their secondary terminal voltages. Therefore, the R' and X' settings are set to zero. Each regulator has 16 taps. The

minimum and maximum off-load per-unit voltage that can be controlled for all regulators are given as 0.9 and 1.1 pu, respectively. The bandwidth is set to 2 V.

In Figure 3.9, 4 three phase voltage regulators at different locations which result in 12 single phase regulator units are shown with green rectangle shapes. The set values $|V_{desired}|$ of the regulators are given as; 126.5 V for the regulator located at the substation and 125 V for the other three regulators

The evolution of the voltage transformation ratios of the regulators is shown in Figure 3.10. Despite the huge size of the network, the load-flow with turns ratios being variables take only 4 iterations. After the load flow is completed and the turns ratios are rounded to the closest discrete setting (the discretization stage), it requires just one iteration to update the voltage profile (the control stage).

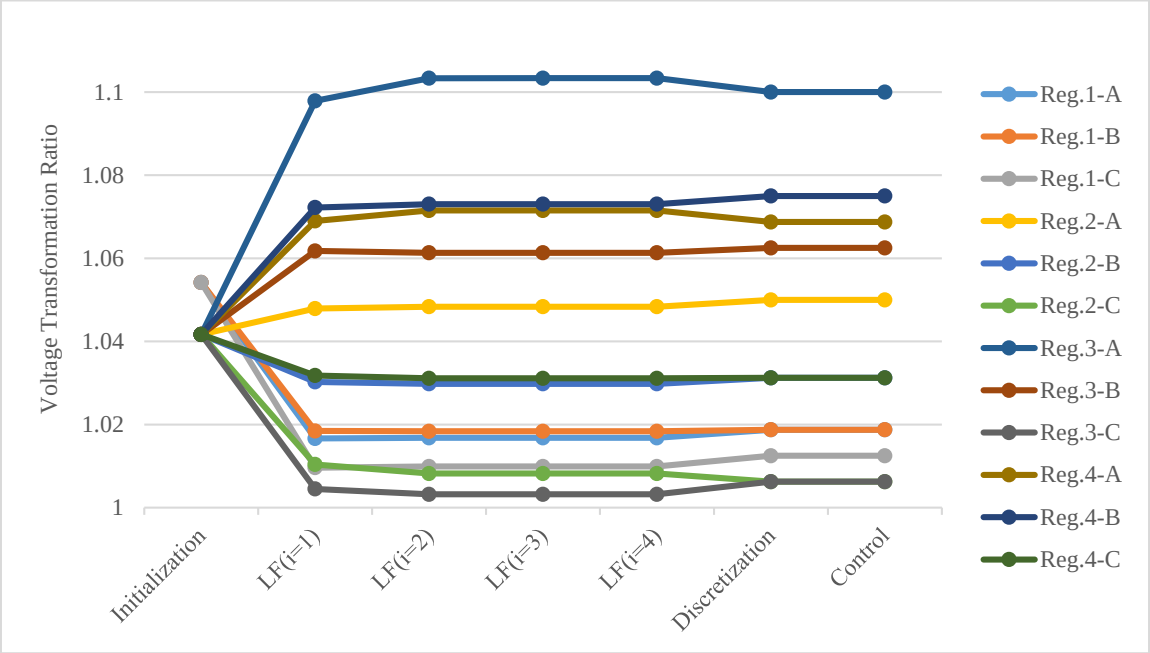

Figure 3.10: The Evolution of the Voltage Transformation Ratio of the Regulators

When a fixed point technique is used as the load flow algorithm, and the regulators are adjusted with control iterations at the end of each load flow solution, the number of iterations significantly increase. The fixed point solution algorithm of OpenDSS requires a maximum of 16 iterations to solve the power flow at a given set of regulator tap positions. The regulator taps are changed 5 times during the initial solution, resulting a total of 62 iterations through the solver [40]. Moreover, the change in regulator tap positions from one load flow solution to another is not always smooth as discussed in [4] and this is independent of the load flow solution algorithm, i.e., Newton or fixed

point. This increases the risk of well-known “fighting” problem between regulators through control iterations. Note that the proposed approach provides turns ratios close to the final solution in just one iteration and the convergence characteristics is smooth as seen Figure 3.10.

Table 3.3: Tap Positions

	Proposed	**Published**
Reg.1-a	3	2
Reg.1-b	3	2
Reg.1-c	2	1
Reg.2-a	8	11
Reg.2-b	5	6
Reg.2-c	1	2
Reg.3-a	16	16
Reg.3-b	10	11
Reg.3-c	1	1
Reg.4-a	11	12
Reg.4-b	12	12
Reg.4-c	5	5

In Table 3.3., it appears that the tap position for the phase A of the regulator 2 is quite different than the published result. One of the reasons, is the sequential connection of the regulators. The regulator 1 is the closest to the substation. Thus, even a single tap position difference creates a chain effect on the voltage profile and the tap positions of the other regulators. Moreover, from Figure 3.11, it is seen that the proposed algorithm performs better as far as the bandwidth settings are concerned. Consider the phase-A of the regulator 3. For that unit, the set voltage $|V_{set}|$ is 7.5 kV and the bandwidth is 2 V (on a scale of 120 V). Therefore, the acceptable voltage range is from 7440 V to 7560 V. The published voltage magnitude is not within the limits, while the proposed result is within the acceptable band.

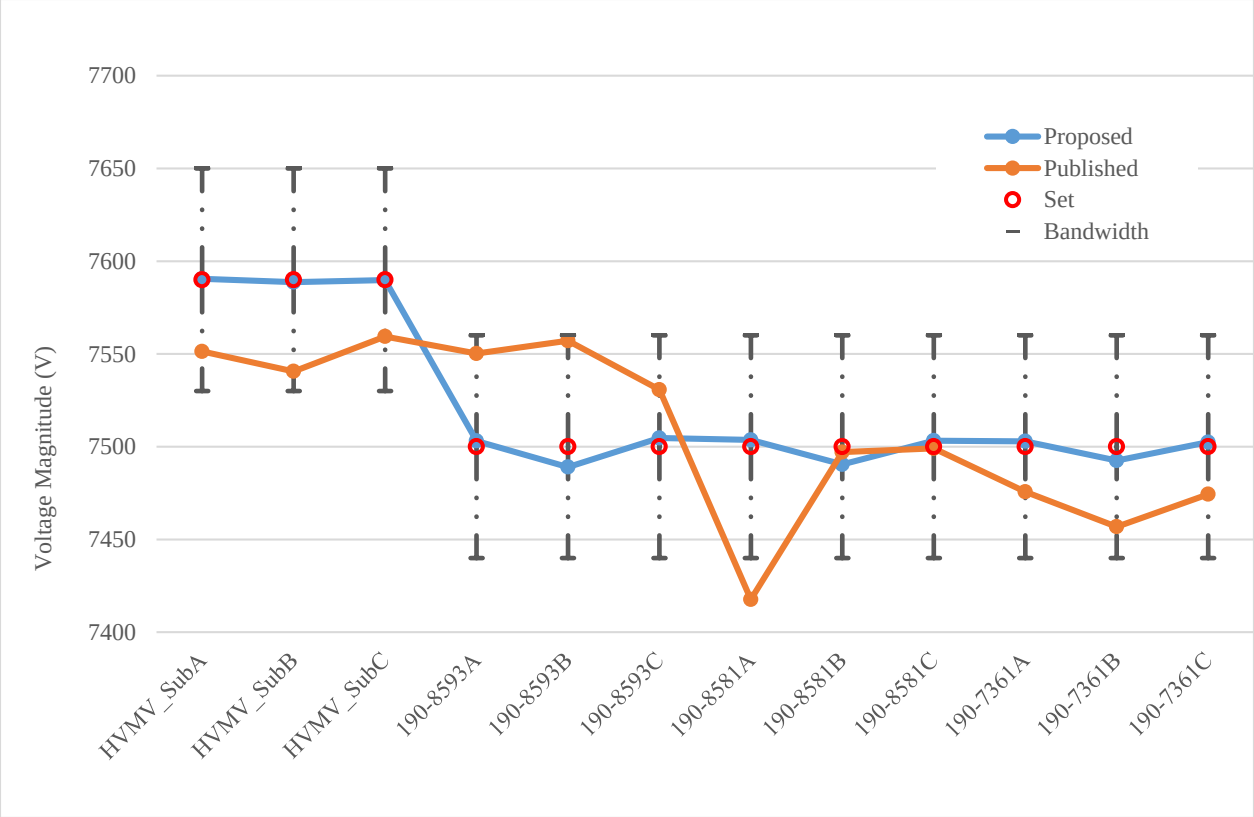

Figure 3.11: Magnitudes of the Voltages at the Controlled Nodes

3.5 Summary

In this chapter, the step voltage regulators are inserted in the MANA load flow formulation. The proposed method is tested on two published networks. The difference between the proposed and published results are due to the bandwidth settings of the regulators and the existence of more than one correct solution. It is however noted that when the tap positions are forced to be the same with the published ones, the voltage profile is identical for the proposed and published results; this constitutes a validation for the method.

CHAPTER 4 ASYNCHRONOUS MACHINES

This chapter is on the load flow modeling of the IM using MANA formulation. The machine model which is based on the Steinmetz circuit is presented and afterwards, the Jacobian terms and constraints are developed. The load flow model uses the real power as the constraint and the reactive power is not fixed. In this approach, the slip becomes a variable in the unknown vector and iteratively corrected using Newton's method. The presented approach is a novel approach and significantly outperforms the existing fixed point approaches in terms of convergence characteristics and iteration number [42]. The proposed modeling approach allows smooth transition between load flow solution and electromagnetic transient analysis in time domain. This is an important validation of the proposed approach for the modeling of IMs.

4.1 Induction Machine Model

It is useful to resort to sequence networks of an IM in order to develop load-flow equations. The Steinmetz equivalent circuit Figure 4.1 is directly used as the positive sequence network. The negative sequence network differs only in the value of the slip, because it creates a rotating flux in an opposite direction and thus the slip becomes negative [43].

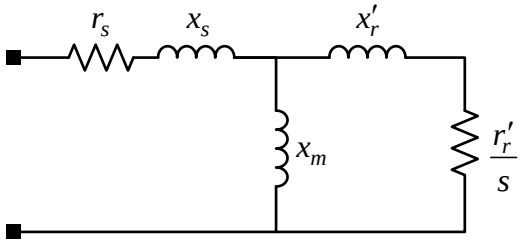

Figure 4.1: Single Cage Squirrel Machine Model

r_s : The stator resistance (Ω)

x_s : The stator reactance (Ω)

x_m : The magnetizing branch reactance (Ω)

x'_r : The rotor reactance reflected on stator (Ω)

r'_r : The rotor resistance reflected to stator (Ω)

s : The slip of the machine

The Steinmetz circuit can also be expanded to the double cage induction machines as well:

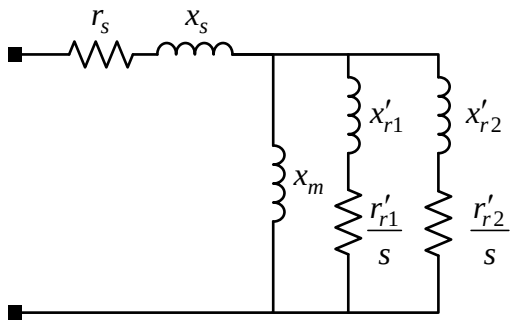

Figure 4.2: Double Cage Squirrel Machine Model

r'_{r1} : The resistance of the first cage reflected to stator (Ω)

r'_{r2} : The resistance of the second cage reflected to stator (Ω)

x'_{r1} : The reactance of the first cage reflected to stator (Ω)

x'_{r2} : The reactance of the second cage reflected to stator (Ω)

Let the synchronous speed be denoted by ω_s which is in rad/s and the actual rotational speed be denoted by ω_r. Then, positive sequence slip s_p is found as follows:

$$s_p = \frac{\omega_s - \omega_r}{\omega_s} \tag{3.1}$$

The positive slip is defined with respect to the deviation from the synchronous speed, while the negative sequence slip is defined with respect to the deviation from the negative of the synchronous speed.

$$\begin{aligned} s_n &= \frac{\omega_s + \omega_r}{\omega_s} \\ &= \frac{2\omega_s - (\omega_s - \omega_r)}{\omega_s} \\ &= 2 - s_p \end{aligned} \tag{3.2}$$

From this point onwards, whenever the slip s is mentioned, the positive slip s_p will be meant, since the negative slip is a function of the positive slip.

$$s = s_p \tag{3.3}$$

The next step is to write the positive Z_1 and negative Z_2 sequence impedances at the terminals of the machine. Since the IMs are typically connected in delta or ungrounded wye configuration, the zero sequence current (and so the admittance) is taken as zero.

The sequence impedances of the single cage machines are simply given as;

$$\vec{Z}_{pos} = r_s + jx_s + \frac{jx_m\left(\frac{r_r}{s} + jx_r\right)}{\frac{r_r}{s} + j\left(x_m + x_r\right)} \tag{3.4}$$

$$\vec{Z}_{neg} = r_s + jx_s + \frac{jx_m\left(\frac{r_r}{s} + jx_r\right)}{\frac{r_r}{2-s} + j\left(x_m + x_r\right)} \tag{3.5}$$

Let us consider an IM connected to the power network at the nodes k_a, k_b, and k_c with the direction of the machine currents as indicated with arrows in Figure 4.3

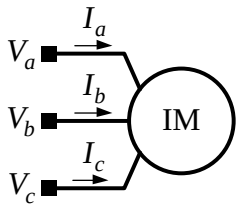

Figure 4.3: The Direction of the Machine Currents

$\vec{I}_a$, $\vec{I}_b$, and $\vec{I}_c$ are the phase currents of the machine defined as into the IM and V_a, V_b, and V_c are the terminal phase voltages. The real power delivered to the IM P_{IM} can be given by the expression:

$$P_{IM} = \mathrm{Re}\left(\vec{\mathbf{I}}^{*}_{\mathbf{abc}}\vec{\mathbf{V}}_{\mathbf{abc}}\right)$$
$$\textit{where}\ \ \vec{\mathbf{I}}_{\mathbf{abc}} = \begin{bmatrix} I_a \\ I_b \\ I_c \end{bmatrix} \qquad \vec{\mathbf{V}}_{\mathbf{abc}} = \begin{bmatrix} V_a \\ V_b \\ V_c \end{bmatrix} = \begin{bmatrix} \vec{\mathbf{V}}_{\mathbf{n}}(k_a) \\ \vec{\mathbf{V}}_{\mathbf{n}}(k_b) \\ \vec{\mathbf{V}}_{\mathbf{n}}(k_c) \end{bmatrix} \tag{3.6}$$

(3.6) can be written as function of sequence components as follows:

$$\begin{aligned} P_{IM} &= \mathrm{Re}\left(\vec{\mathbf{I}}^{*}_{\mathbf{abc}}\vec{\mathbf{V}}_{\mathbf{abc}}\right) \\ &= \mathrm{Re}\left(\left(\vec{\mathbf{A}}_{\mathbf{f}}\vec{\mathbf{I}}_{\mathbf{012}}\right)^{*}\left(\vec{\mathbf{A}}_{\mathbf{f}}\vec{\mathbf{V}}_{\mathbf{012}}\right)\right) \\ &= \mathrm{Re}\left(\vec{\mathbf{I}}^{*}_{\mathbf{012}}\vec{\mathbf{A}}^{*}_{\mathbf{f}}\vec{\mathbf{A}}_{\mathbf{f}}\vec{\mathbf{V}}_{\mathbf{012}}\right) \\ &= \mathrm{Re}\left(3\vec{\mathbf{I}}^{*}_{\mathbf{012}}\vec{\mathbf{V}}_{\mathbf{012}}\right) \end{aligned} \tag{3.7}$$
$$\textit{where}\ \ \vec{\mathbf{I}}_{\mathbf{012}} = \begin{bmatrix} \vec{I}_{zero} \\ \vec{I}_{pos} \\ \vec{I}_{neg} \end{bmatrix} \quad \vec{\mathbf{V}}_{\mathbf{012}} = \begin{bmatrix} \vec{V}_{zero} \\ \vec{V}_{pos} \\ \vec{V}_{neg} \end{bmatrix}$$

In order to avoid confusion with the system matrix notation, the Fortescue matrix is represented by $\vec{\mathbf{A}}_{\mathbf{f}}$ instead of $\vec{\mathbf{A}}$. In (3.7), I_{zero}, I_{pos}, and I_{neg} are the zero, positive, and negative sequence current phasor components, and V_{zero}, V_{pos}, and V_{neg} are the zero, positive, and negative sequence voltage phasor components of the IM. The machine currents are not represented as unknown variable in the proposed model in MANA. Let $\vec{\mathbf{Y}}_{\mathbf{012}}$ be the three by three diagonal admittance matrix representing the IM. Then, (3.7) becomes;

$$\begin{aligned} P_{IM} &= 3\ \mathrm{Re}\left(\left(\vec{\mathbf{Y}}_{\mathbf{012}}\vec{\mathbf{V}}_{\mathbf{012}}\right)^{*}\vec{\mathbf{V}}_{\mathbf{012}}\right) \\ &= 3\ \mathrm{Re}\left(\vec{\mathbf{V}}^{*}_{\mathbf{012}}\vec{\mathbf{Y}}^{*}_{\mathbf{012}}\vec{\mathbf{V}}_{\mathbf{012}}\right) \end{aligned} \tag{3.8}$$
$$\textit{where}\ \ \vec{\mathbf{Y}}_{\mathbf{012}} = \begin{bmatrix} \vec{Y}_{zero} & 0 & 0 \\ 0 & \vec{Y}_{pos}(s) & 0 \\ 0 & 0 & \vec{Y}_{neg}(s) \end{bmatrix}$$

One of the main assumption in the formulation was only to consider wye-grounded and delta connections for the IMs. Thus, the term Y_{zero} which represents zero sequence admittance of the IM

becomes 0. The positive and negative admittance components of the IM are found by inverting (3.4) and (3.5):

$$\vec{Y}_{pos} = 1 \big/ \vec{Z}_{pos} \tag{3.9}$$

$$\vec{Y}_{neg} = 1 \big/ \vec{Z}_{neg} \tag{3.10}$$

(3.8) can be simplified as:

$$\begin{aligned} P_{IM} &= 3\ \mathrm{Re}\left(\vec{\mathbf{V}}_{\mathbf{012}}^{*}\vec{\mathbf{Y}}_{\mathbf{012}}^{*}\vec{\mathbf{V}}_{\mathbf{012}}\right) \\ &= 3\ \mathrm{Re}\left(\left|\vec{V}_{pos}\right|^{2}\vec{Y}_{pos} + \left|\vec{V}_{neg}\right|^{2}\vec{Y}_{neg}\right) \\ &= 3\left(\left|\vec{V}_{pos}\right|^{2}G_{pos} + \left|\vec{V}_{neg}\right|^{2}G_{neg}\right) \\ &\textit{where } G_{pos} = \mathrm{Re}\left(\vec{Y}_{pos}\right) \quad G_{neg} = \mathrm{Re}\left(\vec{Y}_{neg}\right) \end{aligned} \tag{3.11}$$

(3.11) is a function depending only on the node voltages and the slip of the IM. In other words, it is possible to define a real power constraint for an IM only by considering its slip as an unknown variable.

4.2 The Constraints and Jacobian Terms

The electrical power input P_{IM} is the only constraint associated with an IM. If the sign of P_{IM} is positive, then the IM is to be considered operating in motor mode; while in case the sign is negative, it is operating in generator mode. The vector of unknown variables is expanded to hold the slip of the IMs.

$$\mathbf{x}^{(i)} = \begin{bmatrix} \mathbf{V_n} \\ \mathbf{I_v} \\ \mathbf{I_d} \\ \mathbf{I_s} \\ \mathbf{I_L} \\ \mathbf{I_G} \\ \mathbf{E_G} \\ \mathbf{s_M} \end{bmatrix}^{(i)} \tag{3.12}$$

where $\mathbf{s_M}$ is the vector composed of the real valued slips. Also, the simplified form of the Jacobian matrix in (1.27) must be expanded for the IM constraints:

$$\begin{bmatrix} \mathbf{Y_n} & \mathbf{V_r^T} & \mathbf{D_r^T} & \mathbf{S_r^T} & \mathbf{A_{IL}} & \mathbf{A_{IG}} & \mathbf{0} & \mathbf{A_{SM}} \\ \mathbf{V_r} & \mathbf{0} & \mathbf{0} & \mathbf{0} & \mathbf{0} & \mathbf{0} & \mathbf{0} & \mathbf{0} \\ \mathbf{D_r} & \mathbf{0} & \mathbf{0} & \mathbf{0} & \mathbf{0} & \mathbf{0} & \mathbf{0} & \mathbf{0} \\ \mathbf{S_r} & \mathbf{0} & \mathbf{0} & \mathbf{S_d} & \mathbf{0} & \mathbf{0} & \mathbf{0} & \mathbf{0} \\ \mathbf{C_L} & \mathbf{0} & \mathbf{0} & \mathbf{0} & \mathbf{D_L} & \mathbf{0} & \mathbf{0} & \mathbf{0} \\ \mathbf{C_G} & \mathbf{0} & \mathbf{0} & \mathbf{0} & \mathbf{0} & \mathbf{D_G} & \mathbf{0} & \mathbf{0} \\ \mathbf{Y_G} & \mathbf{0} & \mathbf{0} & \mathbf{0} & \mathbf{0} & \mathbf{B_G} & \mathbf{Y_{GE}} & \mathbf{0} \\ \mathbf{C_M} & \mathbf{0} & \mathbf{0} & \mathbf{0} & \mathbf{0} & \mathbf{0} & \mathbf{0} & \mathbf{C_{SM}} \end{bmatrix}^{(i)} \begin{bmatrix} \mathbf{\Delta V_n} \\ \mathbf{\Delta I_v} \\ \mathbf{\Delta I_d} \\ \mathbf{\Delta I_s} \\ \mathbf{\Delta I_L} \\ \mathbf{\Delta I_G} \\ \mathbf{\Delta E_G} \\ \mathbf{\Delta s_M} \end{bmatrix}^{(i)} = - \begin{bmatrix} \mathbf{f_n} \\ \mathbf{f_v} \\ \mathbf{f_d} \\ \mathbf{f_s} \\ \mathbf{f_L} \\ \mathbf{f_G} \\ \mathbf{f_E} \\ \mathbf{f_M} \end{bmatrix}^{(i)} \tag{3.13}$$

Here, it should be noted that $\mathbf{s_M}$ is composed of purely real valued unknowns. Thus, the real forms of $\mathbf{A_{SM}}$ does not exactly follow the convention used in (1.3):

$$\mathbf{A_{SM}} = \begin{bmatrix} \mathrm{Re}\left(\vec{\mathbf{A}}_{\mathbf{SM}}\right) \\ \mathrm{Im}\left(\vec{\mathbf{A}}_{\mathbf{SM}}\right) \end{bmatrix} \tag{3.14}$$

4.2.1 Contributions to Current Injection Constraint

The phase current of the IM shown in Figure 4.3 are given in terms node voltages and machine currents in (3.6):

$$\vec{\mathbf{I}}_{\mathbf{abc}} = \vec{\mathbf{Y}}_{\mathbf{abc}} \vec{\mathbf{V}}_{\mathbf{abc}} \tag{3.15}$$

where $\vec{\mathbf{Y}}_{\mathbf{abc}}$ denotes the admittance of the p^{th} IM and is a function of the slip values. It can be calculated by using the sequence admittance matrix in (3.8):

$$\vec{\mathbf{Y}}_{\mathbf{abc}} = \vec{\mathbf{A}}_{\mathbf{f}} \vec{\mathbf{Y}}_{\mathbf{012}} \vec{\mathbf{A}}_{\mathbf{f}}^{\mathbf{-1}} \tag{3.16}$$

Since the current of the IMs are not included in the vector of unknowns $\mathbf{x}$, the IMs are represented as a variable admittance. Thus, the corresponding section of the admittance matrix $\vec{\mathbf{Y}}_{\mathbf{n}}$ must be updated by the most recent IM admittances $\vec{\mathbf{Y}}_{\mathbf{abc}}$. Let the p^{th} IM be connected to the bus $\mathbf{k}$ which contains the node numbers for the three phases: k_a, k_b, and k_c, and $\vec{\mathbf{Y}}_{\mathbf{n},self}$ denote the admittance

matrix of the overall network before the inclusion of any IM admittances which is formed by the all impedances in the network but the ones belong to the IMs. The corresponding entries of $\vec{\mathbf{Y}}_{\mathbf{n}}$ are updated as:

$$\vec{\mathbf{Y}}_{\mathbf{n}}^{(i)}(\mathbf{k},\mathbf{k}) = \vec{\mathbf{Y}}_{\mathbf{n},self}(\mathbf{k},\mathbf{k}) + \vec{\mathbf{Y}}_{\mathbf{abc}} \tag{3.17}$$

Also, since the slip is not constant, the partial derivative of (3.15) with respect to the slip values must be considered as well:

$$\begin{aligned} \vec{\mathbf{A}}_{\mathbf{IM}}(\mathbf{k}, p) &= \frac{\partial \vec{\mathbf{Y}}_{\mathbf{abc}}}{\partial \mathbf{s}_{\mathbf{M}}(p)} \vec{\mathbf{V}}_{\mathbf{abc}} \\ \textit{where } \frac{\partial \vec{\mathbf{Y}}_{\mathbf{abc}}}{\partial \mathbf{s}_{\mathbf{M}}(p)} &= \vec{\mathbf{A}}_{\mathbf{f}} \frac{\partial \vec{\mathbf{Y}}_{\mathbf{012}}}{\partial \mathbf{s}_{\mathbf{M}}(p)} \vec{\mathbf{A}}_{\mathbf{f}}^{\mathbf{-1}} \end{aligned} \tag{3.18}$$

By using (3.8)-(3.10):

$$\frac{\partial \vec{\mathbf{Y}}_{\mathbf{012}}}{\partial s} = \begin{bmatrix} 0 & 0 & 0 \\ 0 & \dfrac{\partial \vec{Y}_{pos}}{\partial s} & 0 \\ 0 & 0 & \dfrac{\partial \vec{Y}_{neg}}{\partial s} \end{bmatrix} \tag{3.19}$$

And finally;

$$\frac{\partial \vec{Y}_{pos}}{\partial s} = -\frac{r_r\, x_m^2}{\left(r_s + jx_s + \dfrac{jx_m (r_r + jx_r\, s)}{r_r + jx_m\, s + jx_r\, s} \right)^2 (r_r + jx_m\, s + jx_r\, s)^2} \tag{3.20}$$

$$\frac{\partial \vec{Y}_{neg}}{\partial s} = \frac{\dfrac{jx_m r_r}{s^2\left(jx_m + jx_m - \dfrac{r_r}{2-s}\right)} + \dfrac{jx_m r_r\left(jx_r + \dfrac{r_r}{2}\right)}{(2-s)^2 (q_1)^2}}{\left(r_s + jx_s + \dfrac{jx_m\left(\dfrac{r_r}{s} + jx_r\right)}{q_1}\right)^2} \tag{3.21}$$

$$where\ q_1 = jx_r - \frac{r_r}{s-2} + jx_m$$

4.2.2 Electrical Power Constraint

The electrical power input of an IM is the only constraint needed in this formulation. From (3.11), the power constraint for the p^{th} IM becomes:

$$\mathbf{f_M}(p) = P_{in} - 3\left(\left|\vec{V}_1\right|^2 G_{pos} + \left|\vec{V}_2\right|^2 G_{neg}\right) \tag{3.22}$$

where P_{in} is the specified input electrical power of the p^{th} IM.

The submatrices $\mathbf{C_M}$ and $\mathbf{C_{SM}}$ are formed by taking the partial derivatives of (3.22) with respect to the node voltages and the slip, respectively. For the sake of simplicity, $\mathbf{C_M}$ can be partitioned into two parts as shown below:

$$\mathbf{C_M} = \begin{bmatrix}\mathbf{C_{M1}} & \mathbf{C_{M2}}\end{bmatrix} \tag{3.23}$$

$\mathbf{C_{M1}}$: The partial derivatives of $\mathbf{f_M}$ w.r.t to the real part of the node voltages

$\mathbf{C_{M2}}$: The partial derivatives of $\mathbf{f_M}$ w.r.t to the imaginary part of the node voltages

Let the terminal voltages of the p^{th} IM be expressed in terms of the Cartesian form as follows:

$$\vec{\mathbf{V}}_{\mathbf{abc}} = \begin{bmatrix}\vec{V}_a \\ \vec{V}_b \\ \vec{V}_c\end{bmatrix} = \begin{bmatrix}V_{aR} + jV_{aI} \\ V_{bR} + jV_{bI} \\ V_{cR} + jV_{cI}\end{bmatrix} \tag{3.24}$$

$$\mathbf{C_{M1}}\left(p,k_a\right)=\frac{\partial \mathbf{f_{IM}}\left(p\right)}{\partial V_{aR}}=2V_{posR}\,G_{pos}+2V_{negR}\,G_{neg} \tag{3.25}$$

$$\mathbf{C_{M1}}\left(p,k_b\right)=\frac{\partial \mathbf{f_{IM}}\left(p\right)}{\partial V_{bR}}=\left(-V_{posR}+\sqrt{3}V_{posI}\right)G_{pos}+\left(-V_{negR}-\sqrt{3}V_{negI}\right)G_{neg} \tag{3.26}$$

$$\mathbf{C_{M1}}\left(p,k_c\right)=\frac{\partial \mathbf{f_{IM}}\left(p\right)}{\partial V_{cR}}=\left(-V_{posR}-\sqrt{3}V_{posI}\right)G_{pos}+\left(-V_{negR}+\sqrt{3}V_{negI}\right)G_{neg} \tag{3.27}$$

$$\mathbf{C_{M2}}\left(p,k_a\right)=\frac{\partial \mathbf{f_{IM}}\left(p\right)}{\partial V_{aI}}=2V_{posI}\,G_{pos}+2V_{negR}\,G_{neg} \tag{3.28}$$

$$\mathbf{C_{M2}}\left(p,k_b\right)=\frac{\partial \mathbf{f_{IM}}\left(p\right)}{\partial V_{bI}}=\left(-\sqrt{3}V_{posR}-V_{posI}\right)G_{pos}+\left(\sqrt{3}V_{negR}-V_{negI}\right)G_{neg} \tag{3.29}$$

$$\mathbf{C_{M2}}\left(p,k_c\right)=\frac{\partial \mathbf{f_{IM}}\left(p\right)}{\partial V_{cI}}=\left(\sqrt{3}V_{posR}-V_{posI}\right)G_{pos}+\left(-\sqrt{3}V_{negR}-V_{negI}\right)G_{neg} \tag{3.30}$$

$$\mathbf{C_{SM}}\left(p,p\right)=\frac{\partial \mathbf{f_{IM}}\left(p\right)}{\partial s}=3\left(\left(V_{posR}^2+V_{posI}^2\right)\frac{\partial G_{pos}}{\partial s}+\left(V_{negR}^2+V_{negI}^2\right)\frac{\partial G_{neg}}{\partial s}\right) \tag{3.31}$$

where V_{posR}, V_{posI}, V_{negR}, and V_{negI} indicate the real and imaginary parts of the positive and negative sequence voltage at the machine terminals.

4.3 Study Cases

This solution technique has been tested on different scenarios. Two cases are demonstrated below. The study case-1 utilizes a test case specifically developed to validate new IM models. The study case-2 is a modified version of IEEE 34-BUS Test Feeder [40] and allows testing the performance characteristics of the convergence of the proposed technique on a realistic network.

4.3.1 Study Case-1: Induction Machine Test Case

The aim of the test case shown in Figure 4.4 is developed to form a benchmark for the new IM models, as stated in [44].

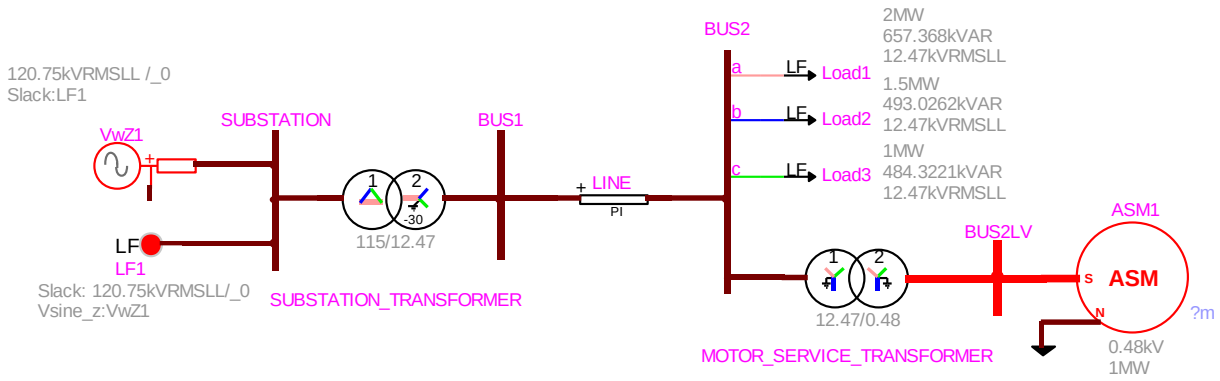

Figure 4.4: Network Schematic for the Study Case-1

The test case is small unbalanced network with only four buses, three loads, one-line segment and two transformers as shown in Figure 4.4 where the single cage IM is indicated as “ASM1”.

The parameters of the test case are presented in Appendix-A section. The IM is operating in motor mode and its electrical power input is given as 1 MW: $P_{in} = 1MW$.

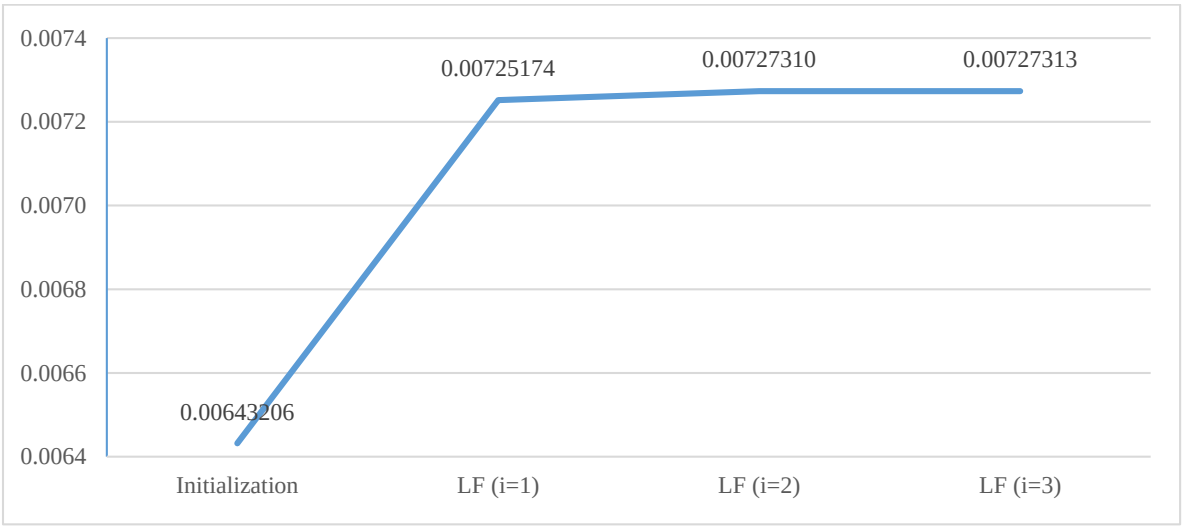

Figure 4.5: Evolution of the Slip of the IM

In Figure 4.5, the evolution of the slip is demonstrated. In the initialization, it is assumed that the reactive power consumption of the IM is half the scalar value of the input real power. Although this is a simple approximation, it is enough as far as the initialization is concerned.

Using the proposed load-flow technique, the final slip of the IM is found as 0.0072731344 in 3 iterations only. This is very close to the published result of 0.00727714.

The results for the proposed IM model which is presented in Table 4.1 are rather close to the published ones. Moreover, the voltage magnitude and angle for the proposed model are compared with the published ones in Figure 4.6 and Figure 4.7. The difference between the node voltage magnitudes do not exceed 0.2 % at the bus where the IM is connected.

Table 4.1: Induction Motor Solution

Quantity	**Published**	**Proposed**
$I_s\left(+seq.\right)$ (A)	1416.6	1416.2
$I_s\left(-seq.\right)$ (A)	80.6557	80.6296
$I_r\left(+seq.\right)$ (A)	1339.32	1338.93
$I_r\left(-seq.\right)$ (A)	78.3065	78.2812
Stator Loss (W)	6146.05	6142.9
Rotor Loss (W)	7251.21	7253.07
Shaft Power (kW)	986.6	986.6
Slip	0.00727714	0.00727313

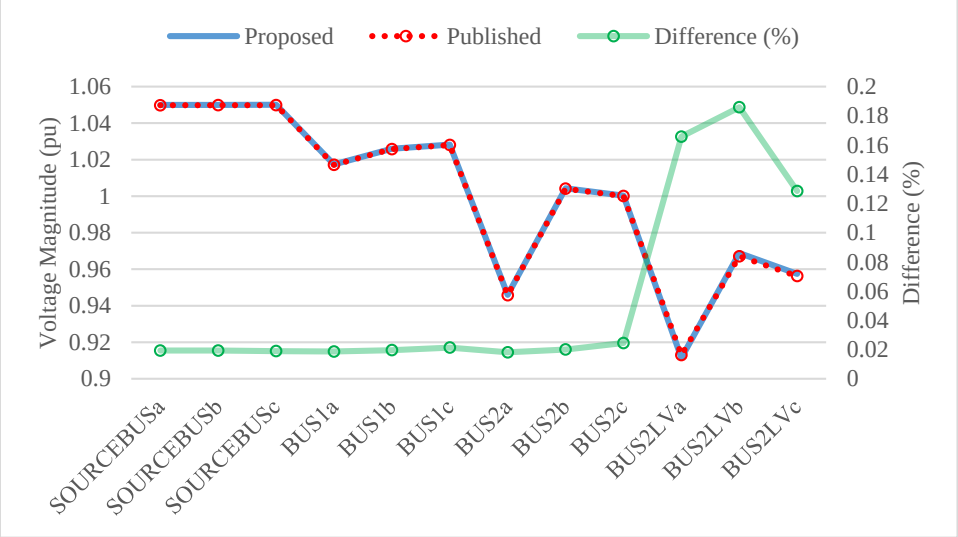

Figure 4.6: Voltage Magnitude

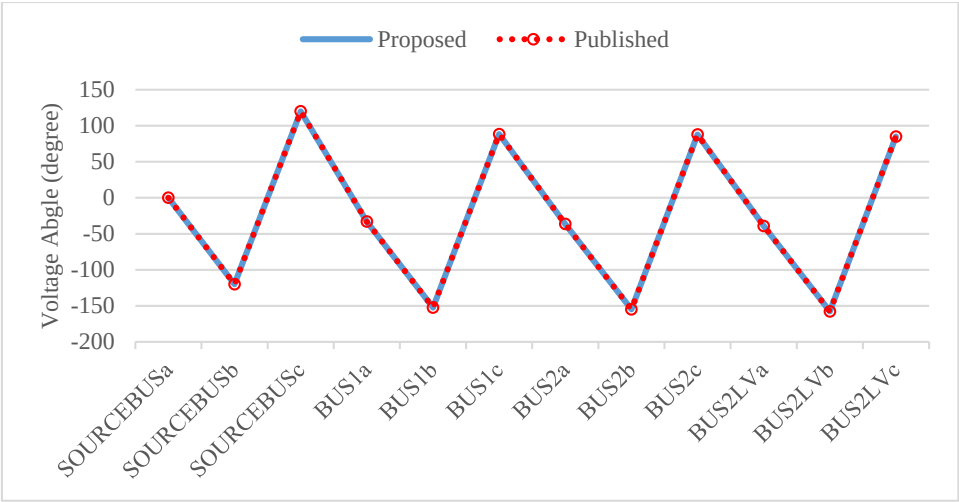

Figure 4.7: Voltage Angle

In EMTP [1], it is possible to specify an IM in the load-flow solution as a PQ device with the nominal PQ parameters being the constraints (by fixing Q). Then, the slip of the IM is initialized using the voltage solution and nominal power. This approach, which will be tagged as the "existing initialization method", miscalculates the slip whenever the voltage is apart from the nominal voltage. The inaccuracy is due to fixing of Q in the load-flow solution. As a result, the time-domain solution of the machine will not be accurate.

Consider again the 4-BUS system of Figure 4.4 but now with a balanced line and balanced 3-phase load, in order to focus on the initialization of the IM:

Line R positive sequence: 0.9 Ω

Line X positive sequence: 2.0 Ω

Line C positive sequence: 10^{-5} S

Load at BUS2: 1500 kW + 490.03 kvar per phase

Using the proposed load-flow solution, the input electrical power of the IM is fixed to 1000 kW and the slip is evaluated as 0.76792763. The proposed technique allows flawless transition from load-flow to time-domain, as shown in Figure 4.8.

Simulation results for the original unbalanced 4-BUS system of Figure 4.4 are presented in Figure 4.9. This demonstrates the accuracy of the proposed load-flow solution for the time-domain initialization of unbalanced networks. The time-domain IM equations are initialized in EMTP [1],

using the new proposed load flow solution. It is noticed that the instantaneous power has a slight small variation at the beginning of the simulation, this is due to the fact that the load-flow solution calculates and imposes average power, not instantaneous. The network is unbalanced and that is why the power now oscillates around its average.

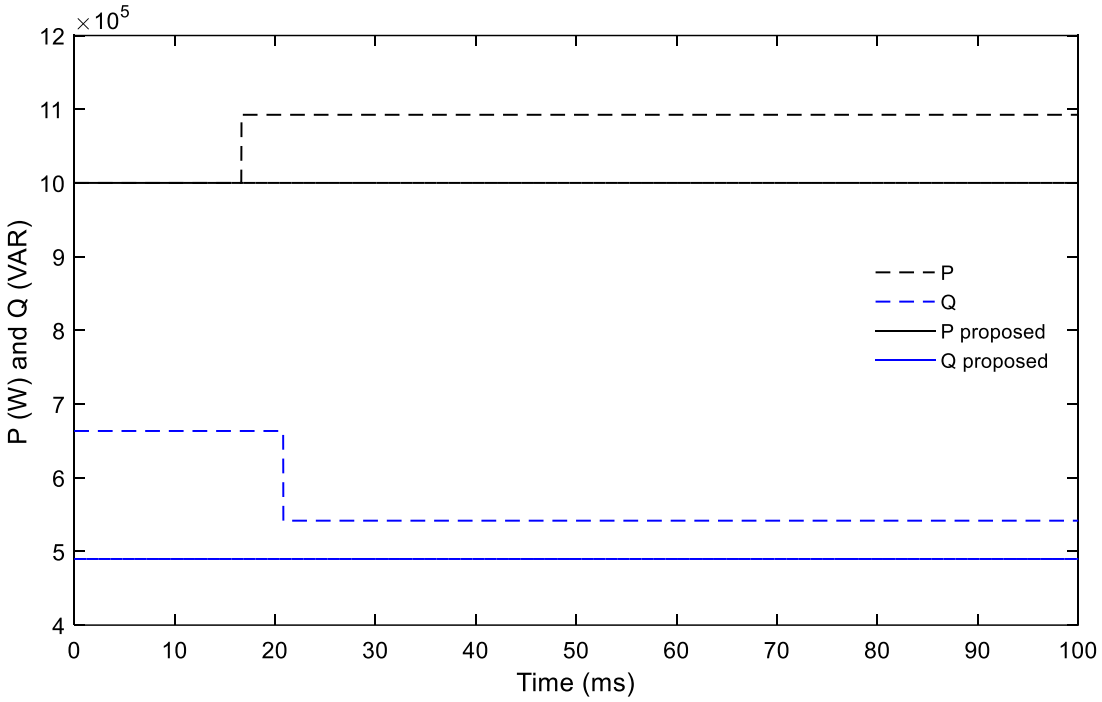

Figure 4.8: PQ input of IM from Load-Flow to Time-Domain

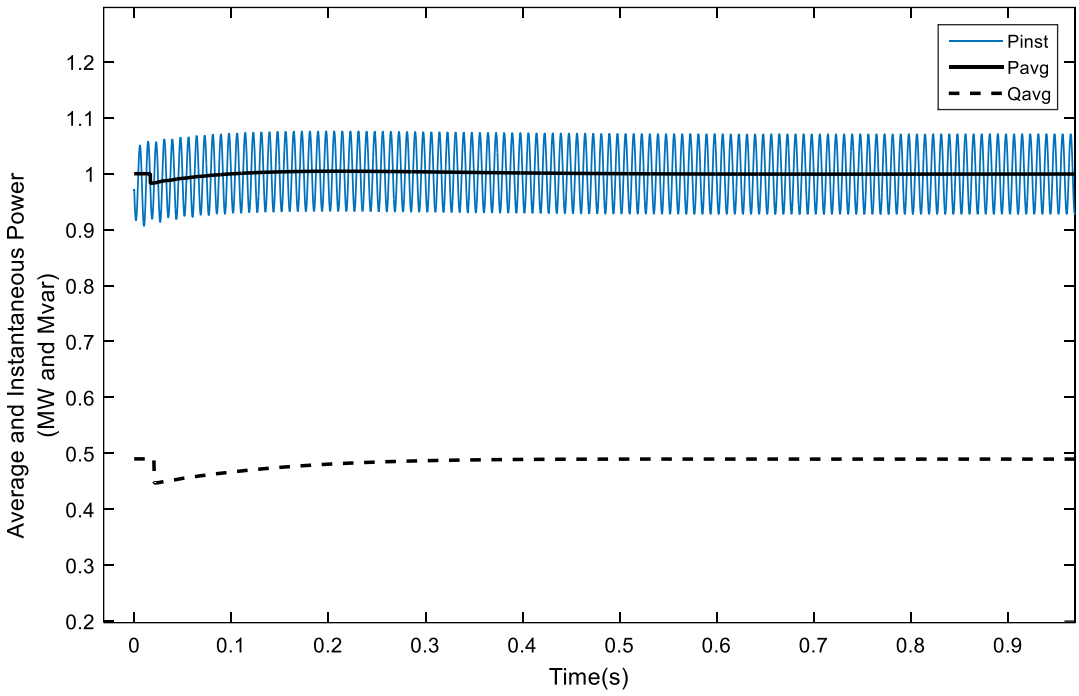

Figure 4.9: PQ input initialization of IM, unbalanced 4-BUS

4.3.2 Study Case-2: Induction Machine Test Case for the 34-Bus Test Feeder

This network case has been developed by the Distribution System Analysis Subcommittee of the Power Systems Analysis, Computing and Economics Committee [45]. In this test case, the original IEEE 34-Bus Test Feeder has been modified by adding two IMs rated at 480 V, 660 kW together with their power transformers as shown in Figure 4.10.

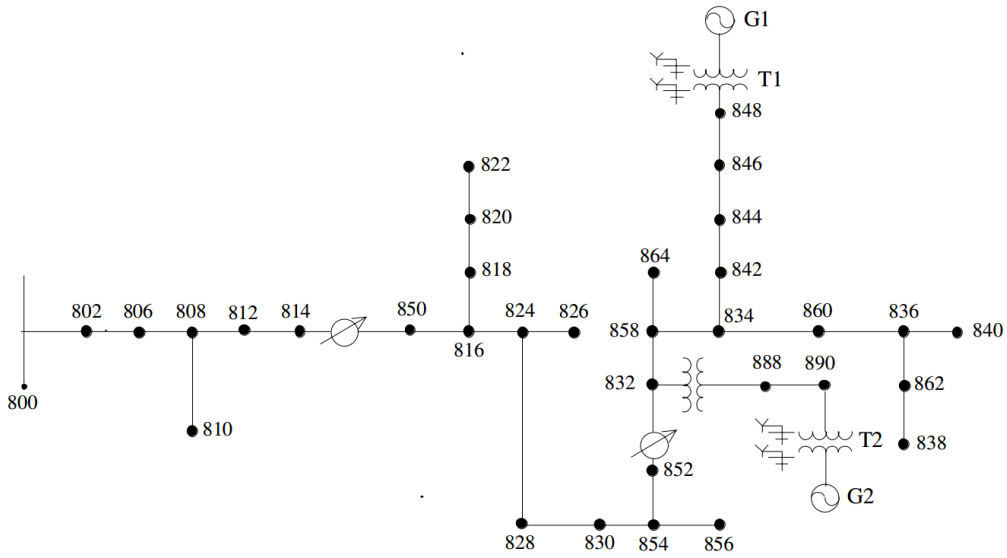

Figure 4.10: Network Schematic for the Study Case-2

In the circuit modelled in MANA, there are 110 nodes (including the internal nodes for the transformers), 30 lines segments, 15 single phase transformer, 78 single phase loads, and 6 single phase capacitor banks.

The two IMs are identical with the characteristics as tabulated in Appendix-B.

Both G1 and G2 are operating in the generator mode and each generating 660 kW: $P_{in} = -660\ kW$

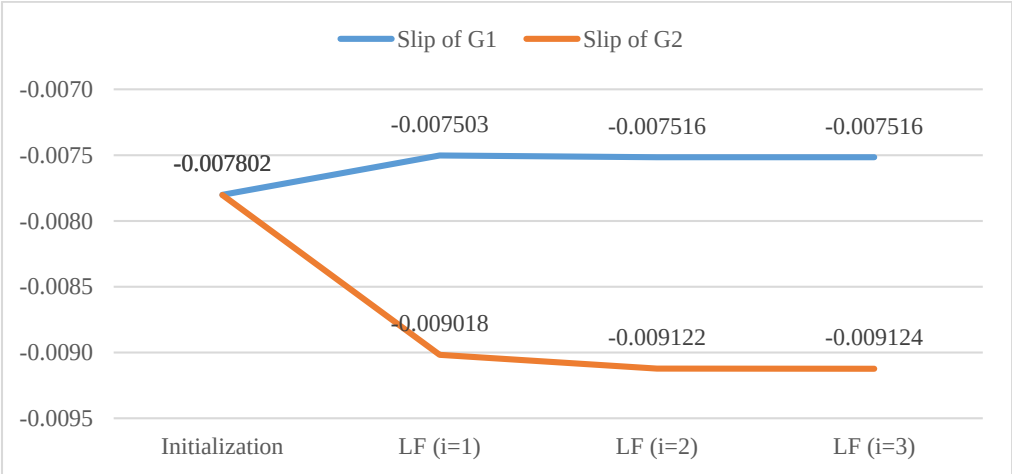

Figure 4.11: Evolution of the Slip of the IM

Similar to the one in the Study Case-1, an initial slip is ‘assumed’ by assuming that the IMs are consuming half the scalar value of the real power at nominal voltage.

Table 4.2: Slip Values

	Proposed	**Published**
G1	-0.007515888	-0.00751
G2	-0.009123541	-0.00912

The slip values with proposed technique show an agreement with the published results. Also, the parameters related to the IMs are compared in Table 4.3 with the published results and also close to each other. In Figure 4.12 and Figure 4.13, the voltage magnitude and angle are shown, respectively. The maximum deviation from the published magnitudes is 0.103 % for the magnitude; while the maximum difference in the angle is 0.058 degrees. This proves the validity and accuracy of the proposed algorithm.

Table 4.3: Generator Solution

Quantity	**Published**		**Proposed**	
	G1	G2	G1	G2
$\vec{I}_s\left(+seq.\right)$ (A)	871.371	953.413	871.418	953.167
$I_s\left(-seq.\right)$ (A)	21.2034	21.9022	20.9935	21.5359
$I_r\left(+seq.\right)$ (A)	825.162	909.999	825.214	909.764
$I_r\left(-seq.\right)$ (A)	20.5858	21.2643	20.3820	20.9086
Stator Loss (W)	4216.96	5048.09	4217.36	5045.4
Rotor Loss (W)	4994.67	6074.03	4995.24	6070.78

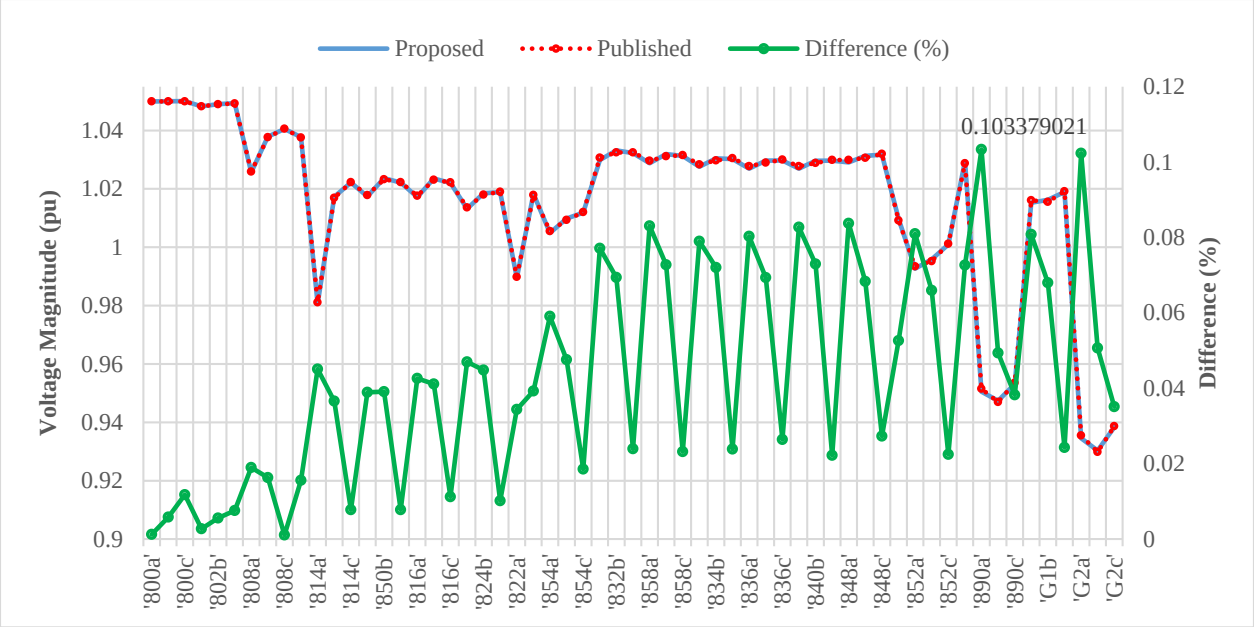

Figure 4.12: Voltage Magnitude

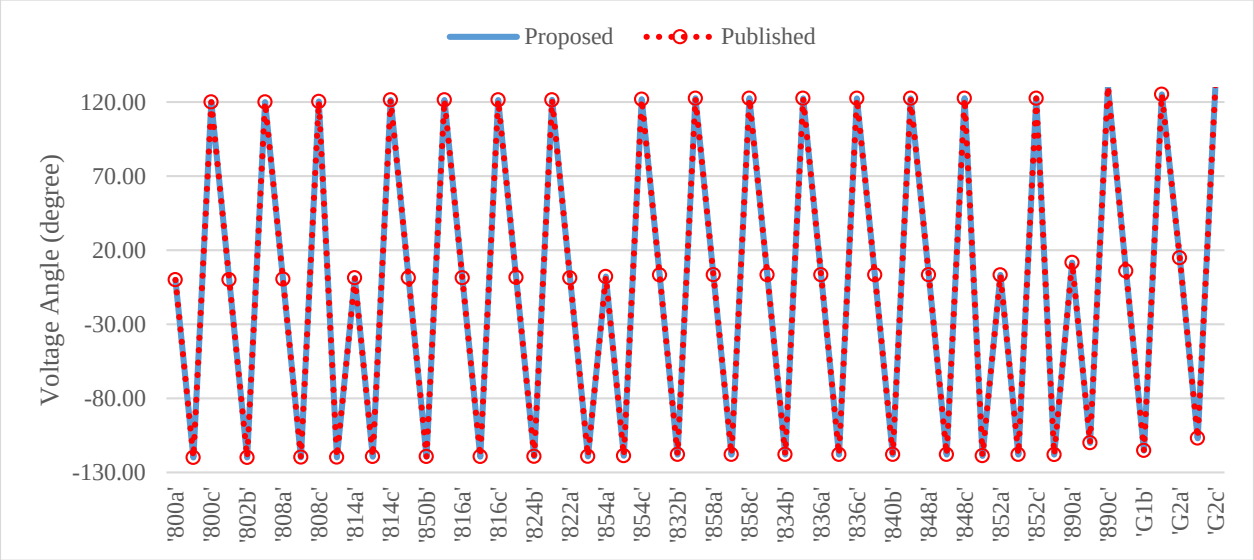

Figure 4.13: Voltage Angle

Consider again the unbalanced IEEE 34-Bus Test Feeder with the two IMs of Figure 4.10. The EMTP initialization solution starts with the slips found in Table 4.2 and the specified P values. At 300 milliseconds a short circuit is triggered at BUS 888 on phase A. The short circuit is removed at 400 ms.

In Figure 4.14, the initialized phase currents and following time-domain solutions of the IM named G1 is shown.

Figure 4.15 and Figure 4.16 show the electrical power inputs of the IMs G1 and G2 respectively. The oscillations in real power are due to the unbalanced network. As explained above, this is also the cause for not being able to achieve perfect initialization (the power increases only slightly from the initial value), but this is acceptable from a practical point of view.

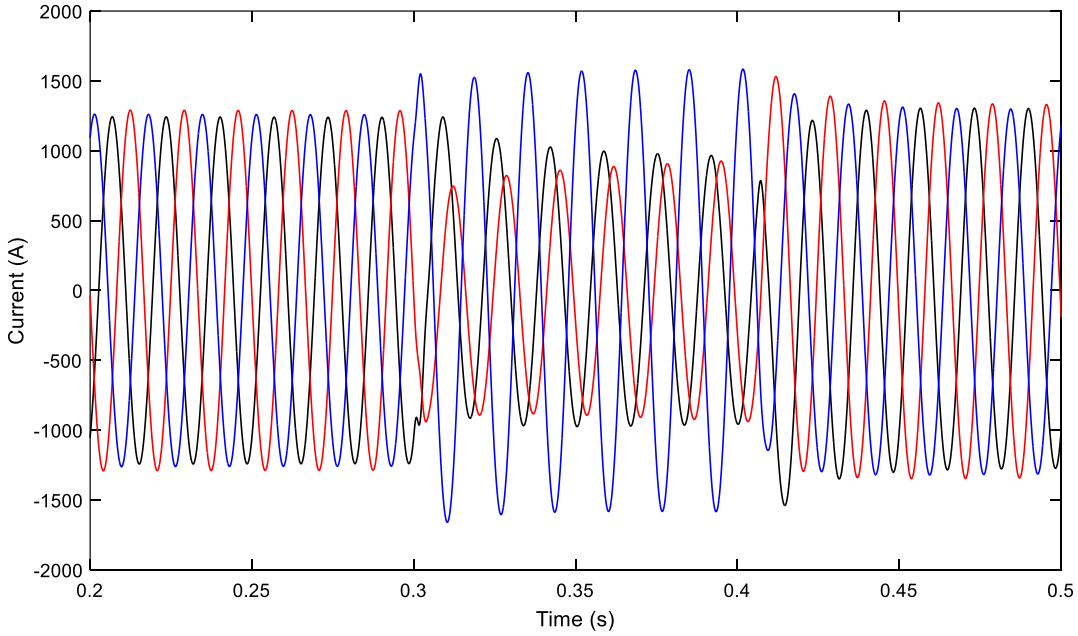

Figure 4.14: G1 IM-G1 Currents, Phases A, B and C

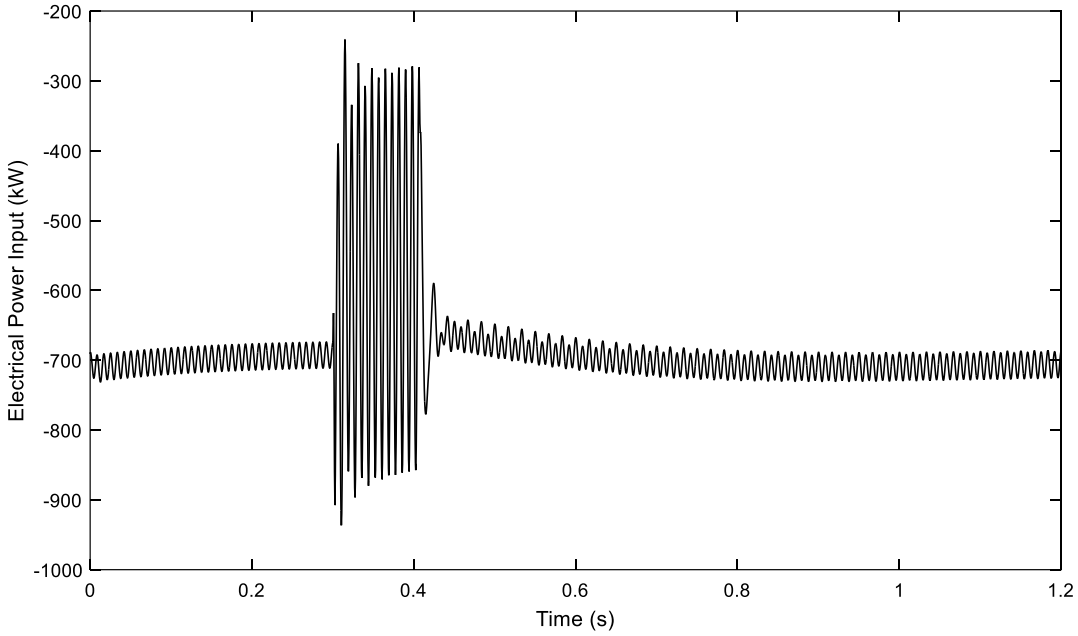

Figure 4.15: Electrical Instantaneous Power Input of G1

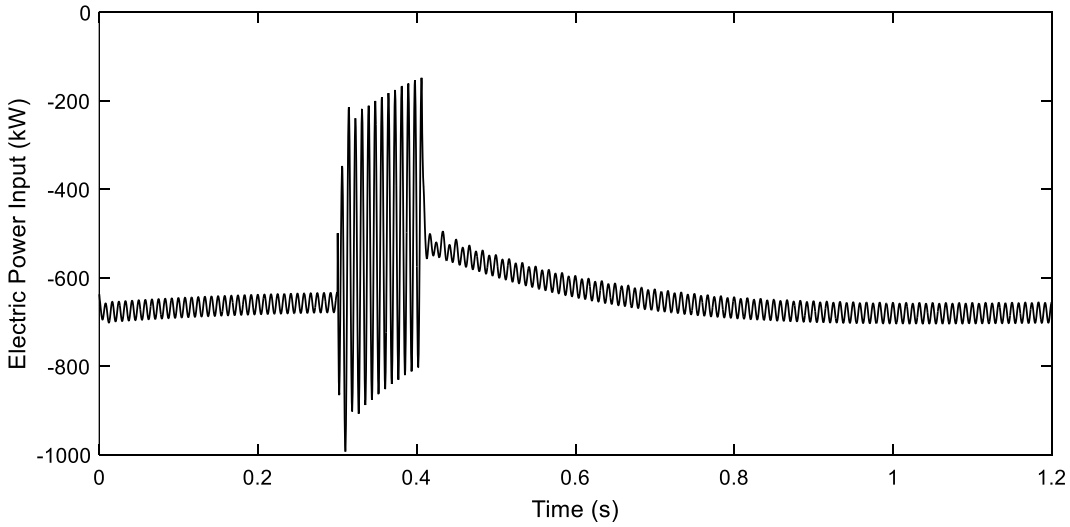

Figure 4.16: Electrical Instantaneous Power Input of G2

4.4 Summary

This chapter presented the inclusion of the induction machines into MANA load-flow [4, 5]. Within this Newton solution method of nonlinear load-flow equations, the induction machines can be specified with electrical power input, mechanical power output or mechanical torque.

The proposed new approach is robust, can be applied to arbitrary networks without limitations and its Jacobian matrix based formulation is straightforward.

The proposed load-flow solution has been validated with published benchmarks. It has been demonstrated that for the 4-BUS test system the new method is capable of converging with only 3 iterations, whereas the published fixed-point approach uses 21 iterations. In the 34-BUS benchmark case, the new method requires only 4 iterations and the published fixed-point solution uses 81 iterations.

In addition to contributing to the unbalanced load-flow solution of induction machines, this work demonstrates that the load-flow solution can be used to directly initialize its time-domain counterpart for the simulation of electromagnetic transients. The accuracy of time-domain initialization is a powerful approach for validating load-flow solutions. There is a seamless transition between load-flow and time-domain solutions when average IM powers are considered.

CHAPTER 5 ELECTRONICALLY COUPLED GENERATORS

In this chapter, a novel approach to model ECGs (specifically, the wind turbine generators-WTGs) in the load flow studies is discussed in MANA platform. After the introduction of the necessary physical model for the power electronic devices, the constraints and corresponding Jacobian entries are developed. Finally, the proposed model is tested on a test network and the comparative results are presented.

5.1 The Electronically Coupled Generator Model

Most commercially available power system tools represent ECGs as conventional synchronous machines whose model is explained in CHAPTER 2. The control mechanism of the ECGs is different than the one of synchronous machines. The classical synchronous model explained in CHAPTER 2 does not take into account the complex power electronic controls. Recently proposed models represent the ECGs as variable impedance [46-48]. In [49, 50], a hybrid voltage/current source model is presented and each sequence component is treated independently.

5.1.1 Type-III Wind Turbine Model

The Type-III wind turbines are doubly fed induction generators (DFIGs) where the stator of a wound rotor induction machine is directly coupled to the grid and the rotor network is connected through a back to back converter at the POI (point of interconnection) as seen in Figure 5.1. The converter is composed of the rotor side converter (RSC), and the grid side converter (GSC) circuits. The GSC and RSC are coupled through a DC link capacitor. The line inductance together with the capacitor bank connected next to the GSC helps to increase the power quality by eliminating the high order harmonics. The crowbar is used to protect the RSC against over-currents. The DC chopper provides protection against the over-voltages. During crowbar ignition, the RSC is blocked and the machine consumes reactive power.

The control of the wind turbine is realized by controlling the RSC and GSC by means of vector control techniques which allow the control of real and reactive powers independently. The currents are projected on a rotating reference frame based on either flux or voltage. The projections are named d and q components of their respective currents. The changes in the q-component cause to real power change output and the ones in the d-component cause to reactive power changes in flux

based reference frame. The situation is the opposite when the voltage based reference frame is chosen.

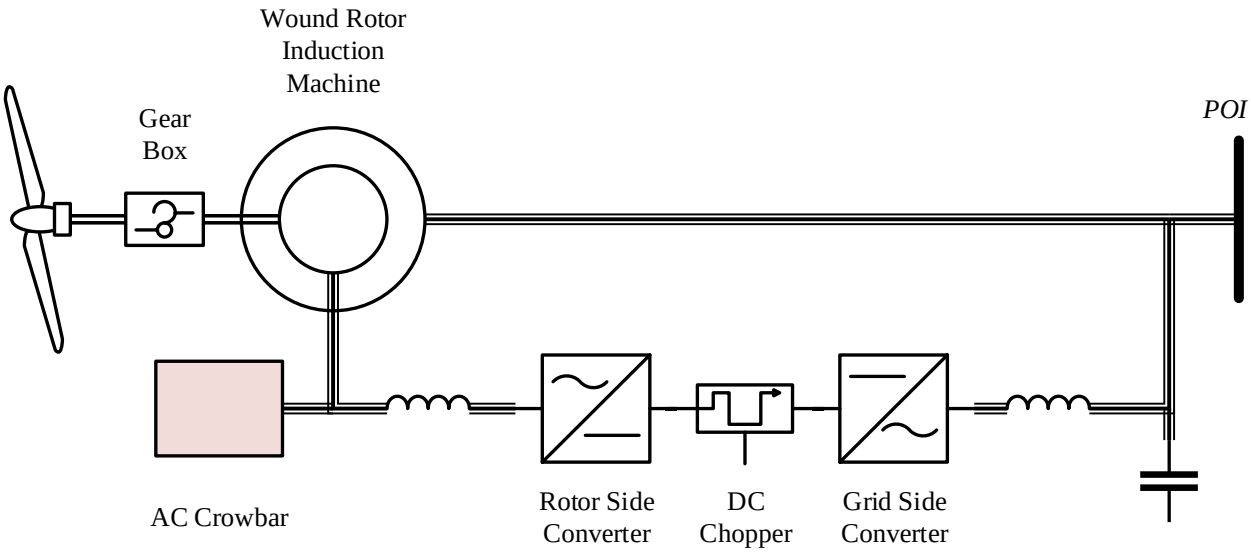

Figure 5.1: Circuit Diagram of a Single DFIG

5.1.2 Type-IV Wind Turbine Model

The Type-IV wind turbines are composed of a permanent magnet synchronous machine and power electronics equipment. Unlike Type-III counterparts, the Type-IV generators are isolated from the grid via the two back to back converters and connected to the grid at POI as shown in Figure 5.2. The back to back converters have two parts: machine side converter (MSC) and grid side converter (GSC). Also, a line inductor is employed to improve the power quality.

As in the case of the Type-III wind turbines, the vector control techniques are employed to control the MSC and GSC in a Type-IV wind turbine generator. The MSC adjusts the active power delivered by the permanent magnet synchronous machine, while the GSC maintains the DC bus voltage by transmitting the active power delivered by the MSC. Moreover, depending on the mode operation, the GSC is also used to control the voltage at POI or the reactive power injected to the grid.

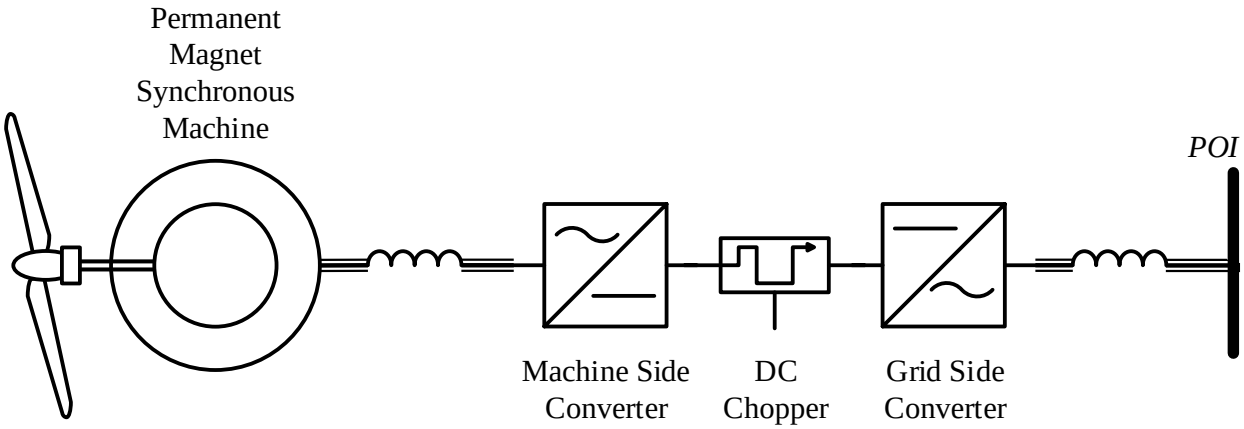

Figure 5.2: Circuit Diagram of a Type-IV WTG

5.1.3 The Proposed Model

The control circuitry of Type-III and IV wind turbine generators adjusts the power injected to the network at POI based on (as aforementioned) the dq components of the currents. Representing the ECGs as current sources rather than voltage source behind a Thevenin impedance gives the possibility of defining the constraints on the sequence components of the machine. Thus, the current source based generator model for the ECGs for load flow studies is shown in Figure 5.3 with the direction of the generator current indicated.

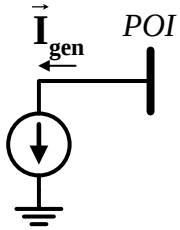

Figure 5.3: Current Source Representation of ECGs

$\vec{\mathbf{I}}_{\mathbf{gen}}$ stands for the generator current in the proposed model and is composed of the phase currents of the machine whose direction is defined as 'into the device'. The bus where the ECG is connected to the network is marked as *POI*. Although $\vec{\mathbf{I}}_{\mathbf{gen}}$ is the quantity actually represented in the unknown vector $\mathbf{x}$, the constraints of the ECGs are defined in terms of the sequence components because the control philosophy of the ECGs is based on the sequence parameters as explained in

the previous section. As a matter of fact, this is the main driving force behind replacing the conventional voltage source based generator model with the current based one. Now, let us consider the phase currents of the generator in Figure 5.3 are defined as in (3.32).

$$\vec{\mathbf{I}}_{\mathbf{gen}} = \begin{bmatrix} \vec{I}_a \\ \vec{I}_b \\ \vec{I}_c \end{bmatrix} = \begin{bmatrix} I_{aR} + jI_{aI} \\ I_{bR} + jI_{bI} \\ I_{cR} + jI_{cI} \end{bmatrix} \tag{3.32}$$

As seen from (3.32), a single ECG introduces six unknowns and therefore there is a need for six constraint equations representing the ECG. For the sake of simplicity, the subscript **gen** is removed from the notation.

Let k_a, k_b, and k_c be the node indices at the terminals of the generator. The voltage at *POI* is defined as in (3.33).

$$\vec{\mathbf{V}}_{\mathbf{POI}} = \begin{bmatrix} \vec{\mathbf{V}}_{\mathbf{n}}(k_a) \\ \vec{\mathbf{V}}_{\mathbf{n}}(k_b) \\ \vec{\mathbf{V}}_{\mathbf{n}}(k_c) \end{bmatrix} = \begin{bmatrix} \vec{V}_a \\ \vec{V}_b \\ \vec{V}_c \end{bmatrix} = \begin{bmatrix} V_{aR} + jV_{aI} \\ V_{bR} + jV_{bI} \\ V_{cR} + jV_{cI} \end{bmatrix} \tag{3.33}$$

5.2 The Constraints and Jacobian Terms

The phase currents of each generator is an unknown in MANA and by inserting the generator currents to the vector unknowns $\mathbf{x}$, the simplified version of the system of equations in (1.27) becomes:

$$\begin{bmatrix} \mathbf{Y_n} & \mathbf{V_r}^{\mathrm{T}} & \mathbf{D_r}^{\mathrm{T}} & \mathbf{S_r}^{\mathrm{T}} & \mathbf{A_{IL}} & \mathbf{A_{IG}} & \mathbf{0} & \mathbf{A_{CG}} \\ \mathbf{V_r} & \mathbf{0} & \mathbf{0} & \mathbf{0} & \mathbf{0} & \mathbf{0} & \mathbf{0} & \mathbf{0} \\ \mathbf{D_r} & \mathbf{0} & \mathbf{0} & \mathbf{0} & \mathbf{0} & \mathbf{0} & \mathbf{0} & \mathbf{0} \\ \mathbf{S_r} & \mathbf{0} & \mathbf{0} & \mathbf{S_d} & \mathbf{0} & \mathbf{0} & \mathbf{0} & \mathbf{0} \\ \mathbf{C_L} & \mathbf{0} & \mathbf{0} & \mathbf{0} & \mathbf{D_L} & \mathbf{0} & \mathbf{0} & \mathbf{0} \\ \mathbf{C_G} & \mathbf{0} & \mathbf{0} & \mathbf{0} & \mathbf{0} & \mathbf{D_G} & \mathbf{0} & \mathbf{0} \\ \mathbf{Y_G} & \mathbf{0} & \mathbf{0} & \mathbf{0} & \mathbf{0} & \mathbf{B_G} & \mathbf{Y_{GE}} & \mathbf{0} \\ \mathbf{C_{CG}} & \mathbf{0} & \mathbf{0} & \mathbf{0} & \mathbf{0} & \mathbf{0} & \mathbf{0} & \mathbf{D_{CG}} \end{bmatrix}^{(i)} \begin{bmatrix} \mathbf{\Delta V_n} \\ \mathbf{\Delta I_v} \\ \mathbf{\Delta I_d} \\ \mathbf{\Delta I_s} \\ \mathbf{\Delta I_L} \\ \mathbf{\Delta I_G} \\ \mathbf{\Delta E_G} \\ \mathbf{\Delta I_{CG}} \end{bmatrix}^{(i)} = - \begin{bmatrix} \mathbf{f_n} \\ \mathbf{f_v} \\ \mathbf{f_d} \\ \mathbf{f_s} \\ \mathbf{f_L} \\ \mathbf{f_G} \\ \mathbf{f_E} \\ \mathbf{f_{CG}} \end{bmatrix}^{(i)} \tag{3.34}$$

The subscript "$\mathbf{C}$" under $\mathbf{I_{CG}}$ indicates the "current based generator model" and is used to differentiate it from the original generator current vector $\mathbf{I_G}$.

The submatrices $\mathbf{C}_{\mathbf{CG}}$ and $\mathbf{D}_{\mathbf{CG}}$ contain the Jacobian entries of $\mathbf{f}_{\mathbf{CG}}$ and can be partitioned into two parts:

$$\mathbf{C}_{\mathbf{CG}} = \begin{bmatrix} \mathbf{C}_{\mathbf{CG1}} & \mathbf{C}_{\mathbf{CG2}} \end{bmatrix} \tag{3.35}$$

$$\mathbf{D}_{\mathbf{CG}} = \begin{bmatrix} \mathbf{D}_{\mathbf{CG1}} & \mathbf{D}_{\mathbf{CG2}} \end{bmatrix} \tag{3.36}$$

$\mathbf{C}_{\mathbf{CG1}}$: The partial derivatives of $\mathbf{f}_{\mathbf{CG}}$ w.r.t the real parts of the voltages

$\mathbf{C}_{\mathbf{CG2}}$: The partial derivatives of $\mathbf{f}_{\mathbf{CG}}$ w.r.t the imaginary parts of the voltages

$\mathbf{D}_{\mathbf{CG1}}$: The partial derivatives of $\mathbf{f}_{\mathbf{CG}}$ w.r.t the real parts of the generator currents

$\mathbf{D}_{\mathbf{CG2}}$: The partial derivatives of $\mathbf{f}_{\mathbf{CG}}$ w.r.t the imaginary parts of the generator currents

As mentioned above, the generator current $\vec{\mathbf{I}}_{\mathbf{gen}}$ is located in $\vec{\mathbf{I}}_{\mathbf{CG}}$. Let $p1$, $p2$, and $p3$ represent the position indices of $\vec{\mathbf{I}}_{\mathbf{gen}}$ in $\vec{\mathbf{I}}_{\mathbf{CG}}$. By using (3.32);

$$\begin{bmatrix} I_a \\ I_b \\ I_c \end{bmatrix} = \begin{bmatrix} \vec{\mathbf{I}}_{\mathbf{CG}}(p1) \\ \vec{\mathbf{I}}_{\mathbf{CG}}(p2) \\ \vec{\mathbf{I}}_{\mathbf{CG}}(p3) \end{bmatrix} \tag{3.37}$$

Also, the sequence components for both voltage and current shall be defined by using (3.32) and (3.33) as:

$$\vec{\mathbf{I}}_{\mathbf{012}} = \vec{\mathbf{A}}_{\mathbf{f}}^{-1}\vec{\mathbf{I}}_{\mathbf{gen}} = \begin{bmatrix} \vec{I}_{zero} \\ \vec{I}_{pos} \\ \vec{I}_{neg} \end{bmatrix} = \begin{bmatrix} I_{zeroR} + jI_{zeroI} \\ I_{posR} + jI_{posI} \\ I_{negR} + jI_{negI} \end{bmatrix} \tag{3.38}$$

$$\vec{\mathbf{V}}_{\mathbf{012}} = \vec{\mathbf{A}}_{\mathbf{f}}^{-1}\vec{\mathbf{V}}_{\mathbf{POI}} = \begin{bmatrix} \vec{V}_{zero} \\ \vec{V}_{pos} \\ \vec{V}_{neg} \end{bmatrix} = \begin{bmatrix} V_{zeroR} + jV_{zeroI} \\ V_{posR} + jV_{posI} \\ V_{negR} + jV_{negI} \end{bmatrix} \tag{3.39}$$

In the next section, various constraint equations will be derived where the letter r will always indicate the constraint under investigation.

5.2.1 The Negative Sequence Constraints

The inner controller generates controlled converter voltages by using dq frame DC current references, and voltage and current measurements at the POI terminals. The measurements are filtered as mentioned before and transformed into dq domain. As opposed to reference currents, they contain oscillations when the network is unbalanced and these oscillations are not suppressed. Because of the phase shift introduced by the filter, the negative sequence component at the converter voltages are not identical to the negative sequence voltage at the POI and therefore negative sequence current will circulate in the converter. The amount of this current is very low compared to positive sequence current (around a few percent even if the network is heavily unbalanced) but it exists. The linear dependency between the negative sequence voltage at the POI and the negative sequence current can be expressed as follows:

$$\vec{K}_{neg}\,\vec{V}_{neg} = \vec{I}_{neg} \tag{3.40}$$

where $\vec{K}_{neg} = K_{negR} + jK_{negI}$ is a complex quantity which is in the order of admittance. Since the sequence parameters are complex, (3.40) creates two constraints.

The real part of (3.40) is the first negative sequence constraint for this generator;

$$\mathbf{f_{CG}}\left(r\right) = \mathrm{Re}\left(\vec{K}_{neg}\,\vec{V}_{neg} - \vec{I}_{neg}\right) = \mathbf{0} \tag{3.41}$$

Then, the corresponding Jacobian terms are found as;

$$\mathbf{C_{CG1}}\left(r,k_a\right) = \frac{\partial \mathbf{f_{CG}}\left(r\right)}{\partial V_{aR}} = \frac{K_{negR}}{3} \tag{3.42}$$

$$\mathbf{C_{CG1}}\left(r,k_b\right) = \frac{\partial \mathbf{f_{CG}}\left(r\right)}{\partial V_{bR}} = \frac{\sqrt{3}\,K_{negI}}{6} - \frac{K_{negR}}{6} \tag{3.43}$$

$$\mathbf{C_{CG1}}\left(r,k_c\right) = \frac{\partial \mathbf{f_{CG}}\left(r\right)}{\partial V_{cR}} = -\frac{\sqrt{3}\,K_{negI}}{6} - \frac{K_{negR}}{6} \tag{3.44}$$

$$\mathbf{C_{CG2}}\left(r,k_a\right) = \frac{\partial \mathbf{f_{CG}}\left(r\right)}{\partial V_{aI}} = -\frac{K_{negI}}{3} \tag{3.45}$$

$$\mathbf{C}_{\mathbf{CG2}}(r,k_b)=\frac{\partial \mathbf{f}_{\mathbf{CG}}(r)}{\partial V_{bI}}=\frac{K_{negI}}{6}+\frac{\sqrt{3}\,K_{negR}}{6} \tag{3.46}$$

$$\mathbf{C}_{\mathbf{CG2}}(r,k_c)=\frac{\partial \mathbf{f}_{\mathbf{CG}}(r)}{\partial V_{cI}}=\frac{K_{negI}}{6}-\frac{\sqrt{3}\,K_{negR}}{6} \tag{3.47}$$

$$\mathbf{D}_{\mathbf{CG1}}(r,p1)=\frac{\partial \mathbf{f}_{\mathbf{CG}}(r)}{\partial I_{aR}}=-1/3 \tag{3.48}$$

$$\mathbf{D}_{\mathbf{CG1}}(r,p2)=\frac{\partial \mathbf{f}_{\mathbf{CG}}(r)}{\partial I_{bR}}=1/6 \tag{3.49}$$

$$\mathbf{D}_{\mathbf{CG1}}(r,p3)=\frac{\partial \mathbf{f}_{\mathbf{CG}}(r)}{\partial I_{cR}}=1/6 \tag{3.50}$$

$$\mathbf{D}_{\mathbf{CG2}}(r,p2)=\frac{\partial \mathbf{f}_{\mathbf{CG}}(r)}{\partial I_{bI}}=-\sqrt{3}/6 \tag{3.51}$$

$$\mathbf{D}_{\mathbf{CG2}}(r,p3)=\frac{\partial \mathbf{f}_{\mathbf{CG}}(r)}{\partial I_{cI}}=\sqrt{3}/6 \tag{3.52}$$

The imaginary part of (3.40) also becomes a constraint:

$$\mathbf{f}_{\mathbf{CG}}(r)=\mathrm{Im}\left(\vec{K}_{neg}\,\vec{V}_{neg}-\vec{I}_{neg}\right)=\mathbf{0} \tag{3.53}$$

The Jacobian entries of (3.53) are given as;

$$\mathbf{C}_{\mathbf{CG1}}(r,k_a)=\frac{K_{negI}}{3} \tag{3.54}$$

$$\mathbf{C}_{\mathbf{CG1}}(r,k_b)=-\frac{\sqrt{3}\,K_{negR}}{6}-\frac{K_{negI}}{6} \tag{3.55}$$

$$\mathbf{C}_{\mathbf{CG1}}(r,k_c)=\frac{\sqrt{3}\,K_{negR}}{6}-\frac{K_{negI}}{6} \tag{3.56}$$

$$\mathbf{C}_{\mathbf{CG2}}(r,k_a)=\frac{K_{negR}}{3} \tag{3.57}$$

$$\mathbf{C}_{\mathbf{CG2}}\left(r,k_b\right)=-\frac{K_{negR}}{6}+\frac{\sqrt{3}\,K_{negI}}{6} \tag{3.58}$$

$$\mathbf{C}_{\mathbf{CG2}}\left(r,k_c\right)=-\frac{K_{negR}}{6}-\frac{\sqrt{3}K_{negI}}{6} \tag{3.59}$$

$$\mathbf{D}_{\mathbf{CG1}}\left(r,p2\right)=\sqrt{3}/6 \tag{3.60}$$

$$\mathbf{D}_{\mathbf{CG1}}\left(r,p3\right)=-\sqrt{3}/6 \tag{3.61}$$

$$\mathbf{D}_{\mathbf{CG2}}\left(r,p1\right)=-1/6 \tag{3.62}$$

$$\mathbf{D}_{\mathbf{CG2}}\left(r,p2\right)=1/6 \tag{3.63}$$

$$\mathbf{D}_{\mathbf{CG2}}\left(r,p3\right)=1/6 \tag{3.64}$$

5.2.2 The Zero Sequence Constraints

Due to the topology of converters, the wind park does not contribute to zero sequence current. In other words, the sum of phase currents of the wind park is zero. However, the transformers where the wind park is connected to the grid, may allow the zero sequence current to circulate on their windings. Thus, the zero sequence current equation must consider this circulating zero sequence current as well.

A similar relation to (3.40) can be defined for the zero sequence components:

$$\vec{K}_{zero}\,\vec{V}_{zero}=\vec{I}_{zero} \tag{3.65}$$

where $\vec{K}_{zero}=K_{zeroR}+jK_{zeroI}$ is in the order of zero sequence admittance of the transformer.

As in the negative sequence constraint case, the real and imaginary parts constitute a constraint.

$$\mathbf{f}_{\mathbf{CG}}\left(r\right)=\mathrm{Re}\left(\vec{K}_{zero}\,\vec{V}_{zero}-\vec{I}_{zero}\right)=\mathbf{0} \tag{3.66}$$

The Jacobian entries are simply found as:

$$\mathbf{C}_{\mathbf{CG1}}\left(r,k_a\right)=\frac{K_{zeroR}}{3} \tag{3.67}$$

$$\mathbf{C}_{\mathbf{CG1}}\left(r,k_b\right)=\frac{K_{zeroR}}{3} \tag{3.68}$$

$$\mathbf{C}_{\mathbf{CG1}}\left(r,k_c\right)=\frac{K_{zeroR}}{3} \tag{3.69}$$

$$\mathbf{C}_{\mathbf{CG2}}\left(r,k_a\right)=-\frac{K_{zeroI}}{3} \tag{3.70}$$

$$\mathbf{C}_{\mathbf{CG2}}\left(r,k_b\right)=-\frac{K_{zeroI}}{3} \tag{3.71}$$

$$\mathbf{D}_{\mathbf{CG1}}\left(r,p1\right)=-1/3 \tag{3.72}$$

$$\mathbf{D}_{\mathbf{CG1}}\left(r,p2\right)=-1/3 \tag{3.73}$$

$$\mathbf{D}_{\mathbf{CG1}}\left(r,p3\right)=-1/3 \tag{3.74}$$

Also, the imaginary part of (3.65) forms the second zero sequence constraint.

$$\mathbf{f}_{\mathbf{CG}}\left(r\right)=\mathrm{Im}\left(\vec{K}_{zero}\vec{V}_{zero}-\vec{I}_{zero}\right)=\mathbf{0} \tag{3.75}$$

Thus, the Jacobian entries of (3.75) are given as:

$$\mathbf{C}_{\mathbf{CG1}}\left(r,k_a\right)=\frac{K_{zeroI}}{3} \tag{3.76}$$

$$\mathbf{C}_{\mathbf{CG1}}\left(r,k_b\right)=\frac{K_{zeroI}}{3} \tag{3.77}$$

$$\mathbf{C}_{\mathbf{CG1}}\left(r,k_c\right)=\frac{K_{zeroI}}{3} \tag{3.78}$$

$$\mathbf{C}_{\mathbf{CG2}}\left(r,k_a\right)=\frac{K_{zeroR}}{3} \tag{3.79}$$

$$\mathbf{C}_{\mathbf{CG2}}\left(r,k_b\right)=\frac{K_{zeroR}}{3} \tag{3.80}$$

$$\mathbf{C}_{\mathbf{CG2}}\left(r,k_c\right)=\frac{K_{zeroR}}{3} \tag{3.81}$$

$$\mathbf{D}_{\mathbf{CG2}}\left(r,p1\right)=-1/3 \tag{3.82}$$

$$\mathbf{D}_{\mathbf{CG2}}\left(r, p2\right) = -1/3 \tag{3.83}$$

$$\mathbf{D}_{\mathbf{CG2}}\left(r, p3\right) = -1/3 \tag{3.84}$$

5.2.3 The Positive Sequence Constraints

As explained in the previous section, the WTGs control the positive sequence current to adjust the injected power. Thus, for a WTG in PQ mode, the positive sequence real and reactive powers are the constrains. Also, a WTG in PV mode has the positive sequence component of the injected real power and the magnitude of the positive sequence voltage as constraints.

Thus, in this section, the three constraint equations related to the positive sequence will be developed:

- The positive sequence real power P_{pos}
- The positive sequence reactive power Q_{pos}
- The magnitude of the positive sequence voltage $\left|\vec{V}_{pos}\right|$

The total injected apparent power of the generator in Figure 5.3 can be written as;

$$S_{inj} = -\vec{\mathbf{I}}^{*}_{\mathbf{gen}}\vec{\mathbf{V}}_{\mathbf{POI}} \tag{3.85}$$

The negative sign is due to the direction of the current. By using (3.38) and (3.39), (3.85) can be written as:

$$\begin{aligned}
\vec{S}_{inj} &= -\left(\vec{\mathbf{A}}_{\mathbf{f}}\vec{\mathbf{I}}_{\mathbf{012}}\right)^{*}\left(\vec{\mathbf{A}}_{\mathbf{f}}\vec{\mathbf{V}}_{\mathbf{012}}\right) \\
&= -\vec{\mathbf{I}}^{*}_{\mathbf{012}}\vec{\mathbf{A}}^{*}_{\mathbf{f}}\vec{\mathbf{A}}_{\mathbf{f}}\vec{\mathbf{V}}_{\mathbf{012}} \\
&= -3\left(\vec{I}^{*}_{zero}\vec{V}_{zero} + \vec{I}^{*}_{pos}\vec{V}_{pos} + \vec{I}^{*}_{neg}\vec{V}_{neg}\right) \\
&= -\left(\vec{S}_{zero} + \vec{S}_{pos} + \vec{S}_{neg}\right)
\end{aligned} \tag{3.86}$$

5.2.3.1 The Positive Sequence Real Power

Let P_r denote the positive sequence injected power. The constraint equation is given as;

$$\mathbf{f}_{\mathbf{CG}}\left(r\right) = P_r + \mathrm{Re}\left(\vec{S}_{pos}\right) \tag{3.87}$$

The Jacobian terms corresponding to (3.87) are found as follows;

$$\mathbf{C}_{\mathbf{CG1}}\left(r,k_a\right)=I_{posR} \tag{3.88}$$

$$\mathbf{C}_{\mathbf{CG1}}\left(r,k_b\right)=\frac{\sqrt{3}\,I_{posI}}{2}-\frac{I_{posR}}{2} \tag{3.89}$$

$$\mathbf{C}_{\mathbf{CG1}}\left(r,k_c\right)=-\frac{\sqrt{3}\,I_{posI}}{2}-\frac{I_{posR}}{2} \tag{3.90}$$

$$\mathbf{C}_{\mathbf{CG2}}\left(r,k_a\right)=I_{posI} \tag{3.91}$$

$$\mathbf{C}_{\mathbf{CG2}}\left(r,k_b\right)=-\frac{\sqrt{3}\,I_{posR}}{2}-\frac{I_{posI}}{2} \tag{3.92}$$

$$\mathbf{C}_{\mathbf{CG2}}\left(r,k_c\right)=\frac{\sqrt{3}\,I_{posR}}{2}-\frac{I_{posI}}{2} \tag{3.93}$$

$$\mathbf{D}_{\mathbf{CG1}}\left(r,p1\right)=V_{posR} \tag{3.94}$$

$$\mathbf{D}_{\mathbf{CG1}}\left(r,p2\right)=\frac{\sqrt{3}V_{posI}}{2}-\frac{V_{posR}}{2} \tag{3.95}$$

$$\mathbf{D}_{\mathbf{CG1}}\left(r,p3\right)=-\frac{\sqrt{3}V_{posI}}{2}-\frac{V_{posR}}{2} \tag{3.96}$$

$$\mathbf{D}_{\mathbf{CG2}}\left(r,p1\right)=V_{posI} \tag{3.97}$$

$$\mathbf{D}_{\mathbf{CG2}}\left(r,p2\right)=-\frac{\sqrt{3}V_{posR}}{2}-\frac{V_{posI}}{2} \tag{3.98}$$

$$\mathbf{D}_{\mathbf{CG2}}\left(r,p3\right)=\frac{\sqrt{3}V_{posR}}{2}-\frac{V_{posI}}{2} \tag{3.99}$$

5.2.3.2 The Positive Sequence Reactive Power

Let Q_r denote the positive sequence injected power. The constraint equation is given as;

$$\mathbf{f}_{\mathbf{CG}}\left(r\right)=Q_r+\mathrm{Im}\left(\vec{S}_{pos}\right) \tag{3.100}$$

The Jacobian terms corresponding to (3.100) are found as follows;

$$\mathbf{C}_{\mathbf{CG1}}\left(r,k_a\right)=-I_{posI} \tag{3.101}$$

$$\mathbf{C}_{\mathbf{CG1}}\left(r,k_b\right)=\frac{\sqrt{3}\,I_{posR}}{2}+\frac{I_{posI}}{2} \tag{3.102}$$

$$\mathbf{C}_{\mathbf{CG1}}\left(r,k_c\right)=-\frac{\sqrt{3}\,I_{posR}}{2}+\frac{I_{posI}}{2} \tag{3.103}$$

$$\mathbf{C}_{\mathbf{CG2}}\left(r,k_a\right)=I_{posR} \tag{3.104}$$

$$\mathbf{C}_{\mathbf{CG2}}\left(r,k_b\right)=\frac{\sqrt{3}\,I_{posI}}{2}-\frac{I_{posR}}{2} \tag{3.105}$$

$$\mathbf{C}_{\mathbf{CG2}}\left(r,k_c\right)=-\frac{\sqrt{3}\,I_{posI}}{2}-\frac{I_{posR}}{2} \tag{3.106}$$

$$\mathbf{D}_{\mathbf{CG1}}\left(r,p1\right)=V_{posI} \tag{3.107}$$

$$\mathbf{D}_{\mathbf{CG1}}\left(r,p2\right)=-\frac{\sqrt{3}V_{posR}}{2}-\frac{V_{posI}}{2} \tag{3.108}$$

$$\mathbf{D}_{\mathbf{CG1}}\left(r,p3\right)=\frac{\sqrt{3}V_{posR}}{2}-\frac{V_{posI}}{2} \tag{3.109}$$

$$\mathbf{D}_{\mathbf{CG2}}\left(r,p1\right)=-V_{posR} \tag{3.110}$$

$$\mathbf{D}_{\mathbf{CG2}}\left(r,p2\right)=-\frac{\sqrt{3}V_{posI}}{2}+\frac{V_{posR}}{2} \tag{3.111}$$

$$\mathbf{D}_{\mathbf{CG2}}\left(r,p3\right)=\frac{\sqrt{3}V_{posI}}{2}+\frac{V_{posR}}{2} \tag{3.112}$$

5.2.3.3 The Magnitude of the Positive Sequence Voltage

Let V_r denote the desired magnitude of positive sequence voltage where $V_r>0$. The constraint equation is given as;

$$\mathbf{f}_{\mathbf{CG}}\left(r\right)=V_r-\left|\vec{V}_{pos}\right| \tag{3.113}$$

The Jacobian terms of (3.113) are given as;

$$\mathbf{C_{CG1}}\left(r,k_a\right)=-\frac{\left(2V_{aR}-V_{bR}-V_{cR}-\sqrt{3}V_{bI}+\sqrt{3}V_{cI}\right)}{18\left|V_{pos}\right|} \tag{3.114}$$

$$\mathbf{C_{CG1}}\left(r,k_b\right)=\frac{\left(V_{aR}-2V_{bR}+V_{cR}-\sqrt{3}V_{aI}+\sqrt{3}V_{cI}\right)}{18\left|V_{pos}\right|} \tag{3.115}$$

$$\mathbf{C_{CG1}}\left(r,k_c\right)=\frac{\left(V_{aR}+V_{bR}-2V_{cR}+\sqrt{3}V_{aI}-\sqrt{3}V_{bI}\right)}{18\left|V_{pos}\right|} \tag{3.116}$$

$$\mathbf{C_{CG2}}\left(r,k_a\right)=-\frac{\left(2V_{aI}-V_{bI}-V_{cI}+\sqrt{3}V_{bI}-\sqrt{3}V_{cI}\right)}{18\left|V_{pos}\right|} \tag{3.117}$$

$$\mathbf{C_{CG2}}\left(r,k_b\right)=\frac{\left(V_{aI}-2V_{bI}+V_{cI}+\sqrt{3}V_{aR}-\sqrt{3}V_{cR}\right)}{18\left|V_{pos}\right|} \tag{3.118}$$

$$\mathbf{C_{CG2}}\left(r,k_c\right)=-\frac{\left(-V_{aI}-V_{bI}+2V_{cI}+\sqrt{3}V_{aR}-\sqrt{3}V_{bR}\right)}{18\left|V_{pos}\right|} \tag{3.119}$$

Since (3.113) has no current component, it does not contribute to the matrices $\mathbf{D_{CG1}}$, $\mathbf{D_{CG2}}$.

5.3 Study Cases

The proposed model is tested on several networks and here two typical examples will be demonstrated. In the first test case, the IEEE 34 Bus network [40] has been modified by adding a single unit of DFIG unit in PQ mode. In the second case, the IEEE 39 Bus (also known as "New England test system") [51] is used to test the proposed model. In both cases, the parameters K_{neg} and K_{zero} were taken from the time domain simulation of EMTP software [33] whose results also form the reference for the proposed model.

5.3.1 Study Case-1: IEEE 34 Bus Network

The aim of this study case is to show the effect of the proposed model on a typical distribution network. A single ECG unit is added to the bus "828" shown in Figure 5.4. The network parameters are given in [40].

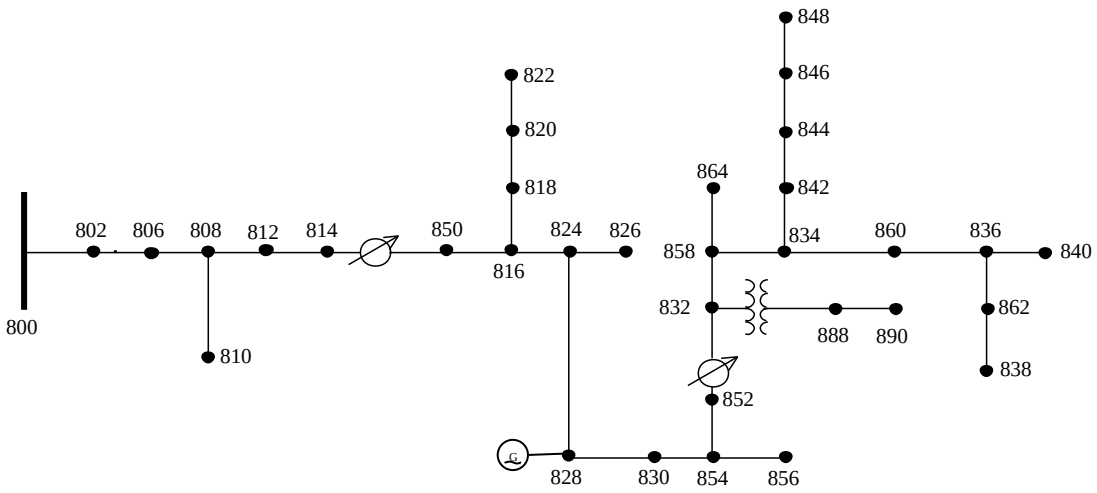

Figure 5.4: IEEE 34 Bus with a Generator Unit

The generator is operating in PQ mode and injecting 500 kW with 0 VAR to the network. The rest of the network parameters remains the same as is in the original IEEE 34 Bus system. The model based parameters are obtained from the time-domain simulation as follows:

Table 5.1: The Generator Parameters

K_{negR} (S)	147.623
K_{negI} (S)	555.802
K_{zeroR} (S)	5.699
K_{zeroI} (S)	139.614

In Figure 5.5, the results obtained by the proposed model are compared with the results obtained by EMTP [33]. The green line demonstrates the discrepancy between the proposed results and EMTP time-domain results. Moreover, the same network has been simulated with the classical generator model. In Figure 5.6, the voltage profile has been presented if the classical generator model presented in Chapter-2 were employed. In each graph, the green line shows the difference

in the magnitude in percentage. In the proposed model in Figure 5.5, the maximum difference is 0.0436 % in the voltage magnitude and the average difference is 0.03 %; while in the classical model in Figure 5.6, the maximum difference is 0.164 % and the average is 0.05 %. Furthermore, the generator sequence currents are compared for the three simulations in Table 5.2 and it can be seen that there is a strong agreement between the time-domain results of EMTP and the proposed model.

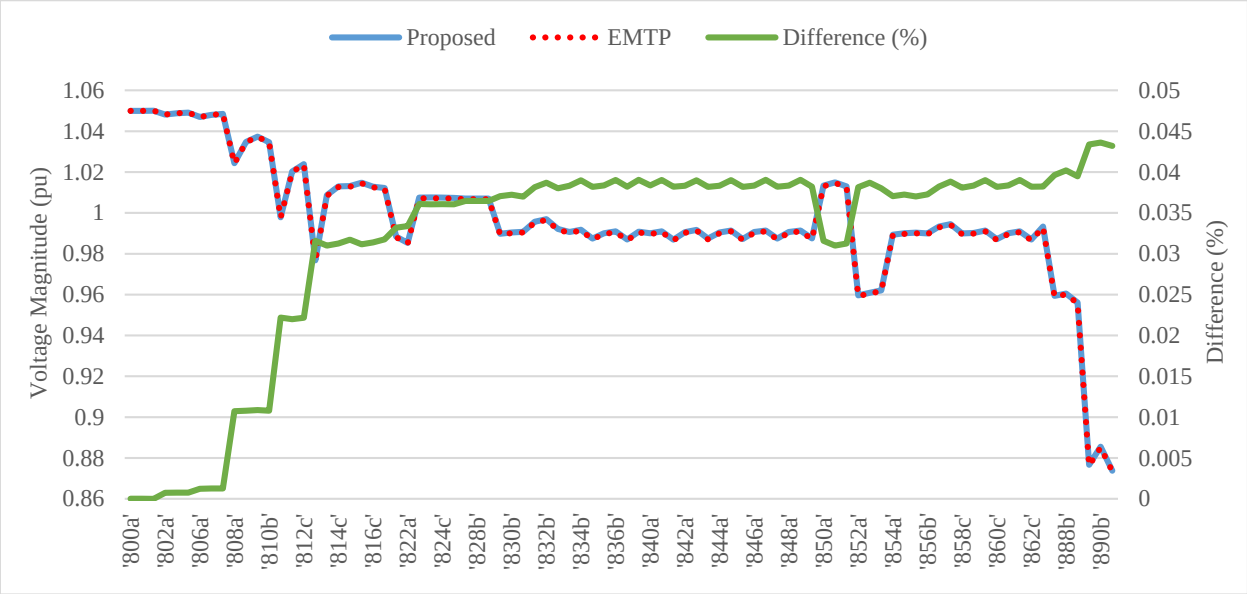

Figure 5.5: Voltage Profile of the Network (Proposed Model)

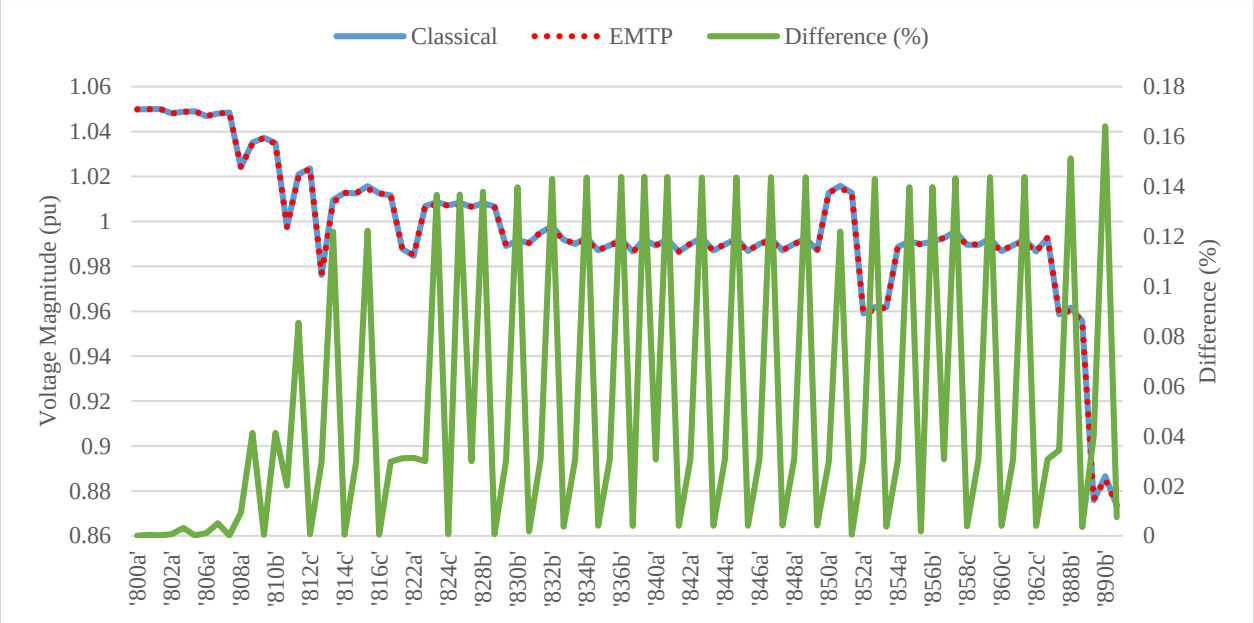

Figure 5.6: Voltage Profile of the Network (Classical Model)

Table 5.2: The Generator Sequence Currents

	Classical		Proposed		EMTP	
	Mag. (A)	**Ang. (degree)**	**Mag. (A)**	**Ang. (degree)**	**Mag. (A)**	**Ang. (degree)**
$\vec{I}_{zero}$	1.103264	126.1404	1.337038	125.4638	1.341525	125.5637
$\vec{I}_{pos}$	11.51378	178.4695	11.31216	178.4198	11.30907	178.3968
$\vec{I}_{neg}$	1.037724	19.71885	1.510935	22.66425	1.510917	23.04078

5.3.2 Study Case-2: IEEE 39 Bus Test Case

In this study case, the IEEE 10 Generator 39 Bus System [40] is employed which is a balanced transmission network. In this network, there are 10 generators: 1 of them being the slack generator, the remaining 9 generators are modeled as Type-IV WTGs. Since the network is balanced, the negative and zero sequence voltage and current components are trivial. Thus, the aim of this study case is to prove that in case of balanced networks, the proposed model and classical generator model should agree. In Figure 5.7, the single line diagram of this case is shown with the bus numbers indicated.

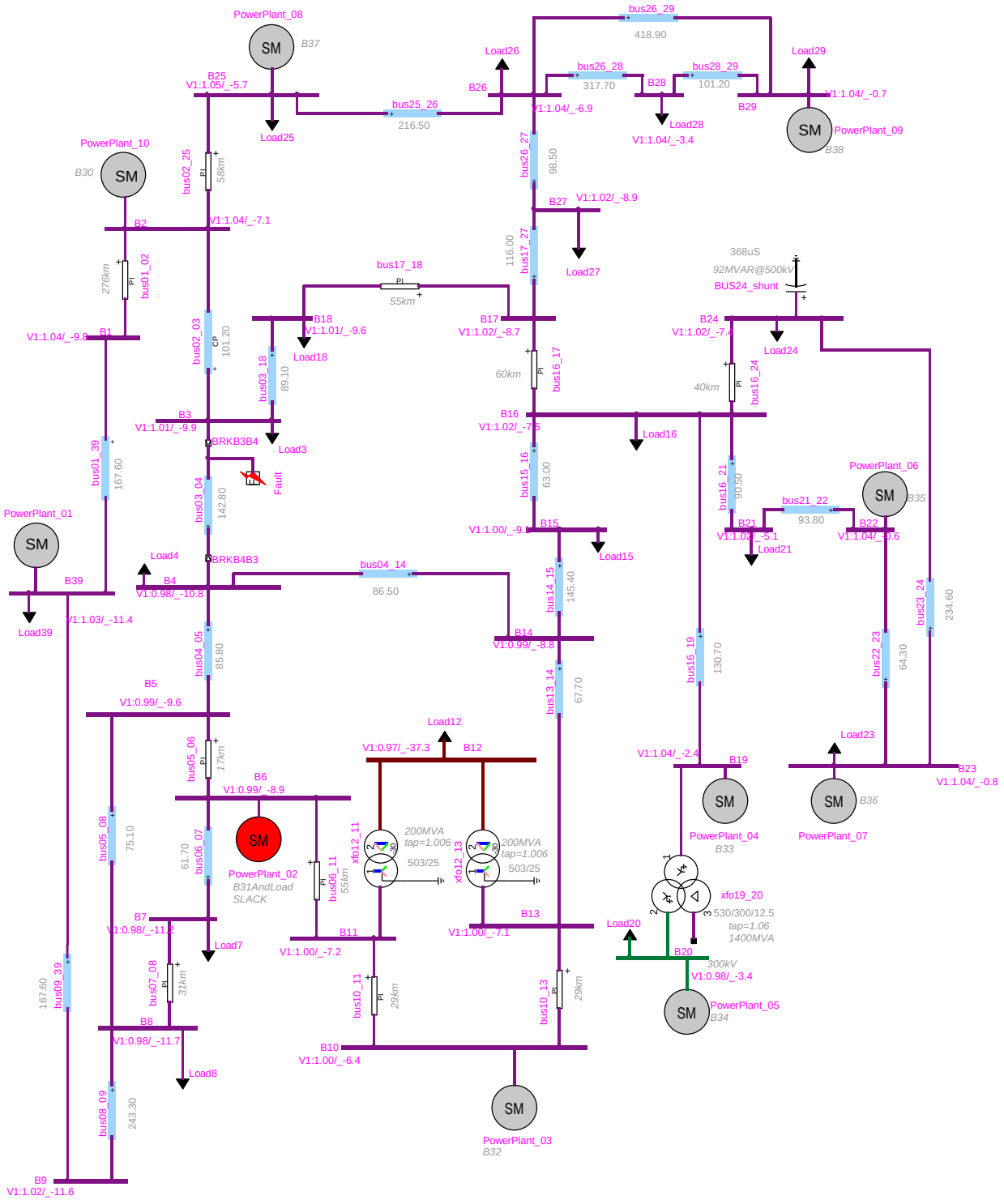

Figure 5.7: Network Schematic of IEEE 39 Bus Test Case

The single line diagram of the test case in Figure 5.7. “G2” represents the slack generator. As, aforementioned, the system is balanced; the generator parameters K_{neg} and K_{zero} are expected to have no effect on the solution.

The specifications related of the generators are tabulated in Table 5.3. The line voltage column defines the positive sequence voltage magnitude and the injected power column defines the real power constraint.

Table 5.3: The Generator Constraints

Generator	Bus	Line Voltage (kV)	Injected Power (MW)
G10	B30	20	270
G1	B39	515	1000
G9	B38	20.53	800
G3	B32	19.662	650
G5	B34	20.15	508
G4	B33	19.944	632
G6	B35	20.986	650
G7	B36	21.27	560
G8	B37	20.556	540

The comparison of the voltage magnitudes is presented below in Figure 5.8 for the proposed and classical approaches together with the difference. It can be observed that the difference is negligibly small for the two cases as expected. This further proves the validity of the concept.

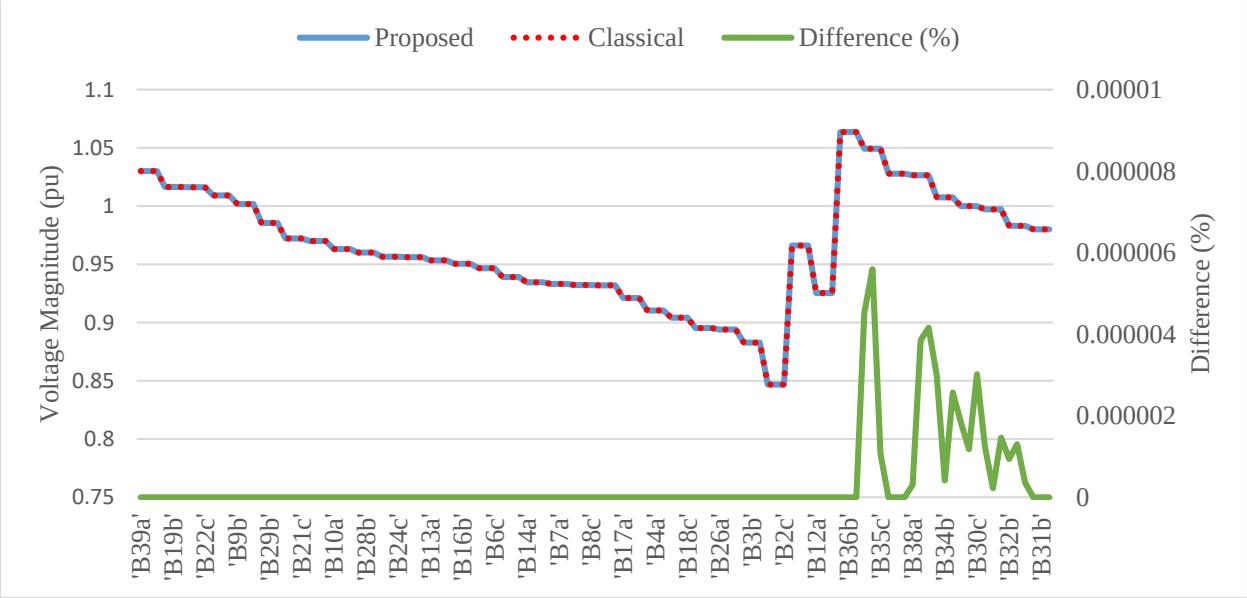

Figure 5.8: Voltage Profile of the Network

5.3.3 Study Case-3: The Comprehensive Test Case

The objective of this study case is to create a test network which includes all the load flow models presented in this thesis and thus, to test the convergence characteristics of the MANA solver. The proposed models will be tested against their fixed-point representations. The unbalanced version of the original IEEE 8500 Node test feeder [41] is modified to include ECGs and IMs at several locations of the network. Also, single phase generator units are added on the LV grid to represent the distributed generation units.

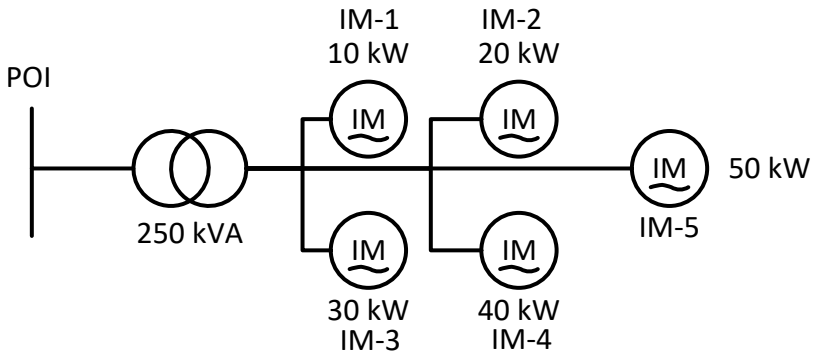

Figure 5.9: Induction Machine Group

In order to resemble a more realistic case, five identical IMs with different power generation output are connected to the original network at the bus “POI” via a transformer shown in Figure 5.9. There

are four IM groups at different locations in this test case. Thus, the total power injected by a single group of IMs is 150 kW. The parameters of the IMs which are obtained from [52] are presented in Table5.4:

Table 5.4: The IM Generator Parameters

Type	Nom. V.	Nom. P.	$r_s(pu)$	$x_s(pu)$	$x_m(pu)$	$r_{r1}(pu)$	$x_{r1}(pu)$	$r_{r2}(pu)$	$x_{r2}(pu)$
Single Cage	400 V	45 kW	0.043	0.0684	1.8564	0.0153	0.0684	#	#
Double Cage	400 V	45 kW	0.043	0.0366	2.1718	0.017	0.1205	0.1474	0.0366

The IM-1 is a single cage IM, and the IM-2 is a double cage IM. The characteristics of the transformer in Figure 5.9 are given in Table 5.5:

Table 5.5: The Transformer Parameters

Voltage Ratings	$12.47kV/400V$
Connection	Delta-Wye Grounded
Apparent Power Rating	250 kVA
X	5 %
R	1 %

The POI and types of each wind-park are presented in Table 5.6:

Table 5.6: The IM Groups

Group Number	Type	POI
1	IM-1	M1026986
2	IM-1	E193509
3	IM-2	L2822877
4	IM-2	P850083

The overall real power injection of the IMs is 600 kW. In addition to the IMs, there are 10 ECGs operating in PQ mode. The parameters K_{neg} and K_{zero} are assumed to be zero. In order to diversify the production, a different injected electrical power is assigned to each ECG as demonstrated in Table 5.7:

Table 5.7: The ECG Parameters

ECG Number	POI	$P_{inj.}$ (kW)	$Q_{inj.}$ (VAR)
1	N1138604	100	0
2	M1026997	120	0
3	196-31070	140	0
4	M1186063	160	0
5	L3235255	180	0
6	M1009784	200	0
7	M1026834	220	0
8	N1144668	240	0
9	M1125914	260	0
10	L3197646	280	0

The power total generation of the ECGs is 1.9 MW.

The distributed energy resources are added to the secondary LV grid. The secondary grid contains a center tapped transformer, two line segments and two loads as demonstrated in Figure 5.10. The single phase generators which are connected to the 240 V level are highlighted by the red rectangle. Each single phase generator injects 1.2 kW at power factor 1. There are 500 single phase generators.

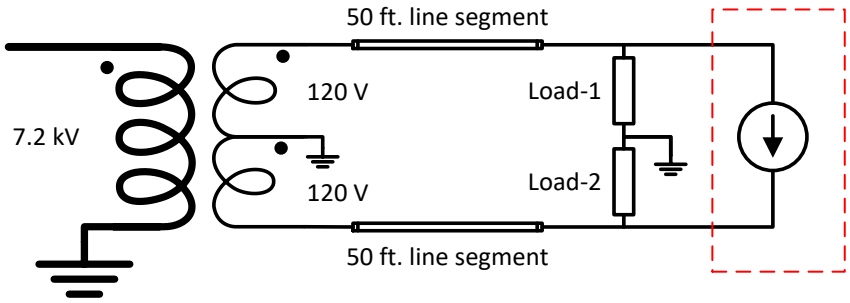

Figure 5.10: Secondary LV Grid with Single Phase Generator

The solver-1 refers to the one where all devices are represented in the Jacobian matrix. On the other hand, the solver-2 refers to the fixed-point method. Unlike the classical fixed-point techniques, turn ratio and slip variables are updates at each iteration. Both solvers are subject to the same convergence criteria:

$$\frac{\left|\Delta\vec{\mathbf{V}}_{\mathbf{n}}(i)\right|}{\left|\vec{\mathbf{V}}_{\mathbf{n}}(i)\right|} < 10^{-3} \quad for\ all\ i \tag{3.120}$$

There is a huge difference between the iteration numbers for the two solvers: It takes 4+2 iterations for the solver-1 to converge, while the solver-2 requires 32 iterations for convergence.

In table 5.8, the resultant slip values for two solvers are presented. There is a close resemblance between the two. The tap positions and the controlled voltages are presented in Table 5.9 and 5.10, respectively. The difference of 1 tap position is acceptable as far as the controlled voltages are within the bandwidth. From Figure 5.11 to Figure 5.15, the evolutions of slips for IMs with different output power are demonstrated. The Figure 5.16 and Figure 5.17 show the evolution of the turn ratio. It can be seen from the figures that the Jacobian based solver has no oscillation around the solution point and has faster convergence rate compared to the fixed-point solver.

Table 5.8: The Resultant Slip Values for the IMs

IM name	**Slip (Solver-1)**	**Slip (Solver-2)**
Gr. 1-IM 1	-0.00383	-0.00385
Gr. 1-IM 2	-0.00743	-0.00747
Gr. 1-IM 3	-0.01102	-0.01107
Gr. 1-IM 4	-0.01462	-0.01469
Gr. 1-IM 5	-0.01827	-0.01836
Gr. 2-IM 1	-0.00378	-0.00378
Gr. 2-IM 2	-0.00733	-0.00733
Gr. 2-IM 3	-0.01088	-0.01088
Gr. 2-IM 4	-0.01443	-0.01443
Gr. 2-IM 5	-0.01803	-0.01803
Gr. 3-IM 1	-0.00364	-0.00366
Gr. 3-IM 2	-0.00709	-0.00713
Gr. 3-IM 3	-0.01052	-0.01057
Gr. 3-IM 4	-0.01396	-0.01403
Gr. 3-IM 5	-0.01743	-0.01752
Gr. 4-IM 1	-0.00368	-0.00368
Gr. 4-IM 2	-0.00717	-0.00717
Gr. 4-IM 3	-0.01065	-0.01065
Gr. 4-IM 4	-0.01414	-0.01414
Gr. 4-IM 5	-0.01766	-0.01767

Table 5.9: The Resultant Tap Positions

Regulator Name	Tap Position (Solver-1)	Tap Position (Solver-2)
Reg. 1-a	19	19
Reg. 1-b	19	19
Reg. 1-c	18	18
Reg. 2-a	23	23
Reg. 2-b	20	21
Reg. 2-c	18	17
Reg. 3-a	28	28
Reg. 3-b	24	23
Reg. 3-c	17	17
Reg. 4-a	24	24
Reg. 4-b	25	25
Reg. 4-c	20	20

Table 5.10: The Resultant Controlled Voltages

Regulator Name	Cont. Voltage (V) (Solver-1)	Cont. Voltage (V) (Solver-2)
Reg. 1-a	7606.69	7607.07
Reg. 1-b	7600.81	7599.38
Reg. 1-c	7591.23	7591.219
Reg. 2-a	7511.33	7516.76
Reg. 2-b	7511.84	7497.787
Reg. 2-c	7528.72	7484.709
Reg. 3-a	7509.97	7514.276
Reg. 3-b	7528.7	7474.788
Reg. 3-c	7515.68	7516.664
Reg. 4-a	7501.59	7504.059
Reg. 4-b	7493.57	7488.035
Reg. 4-c	7489.12	7489.706

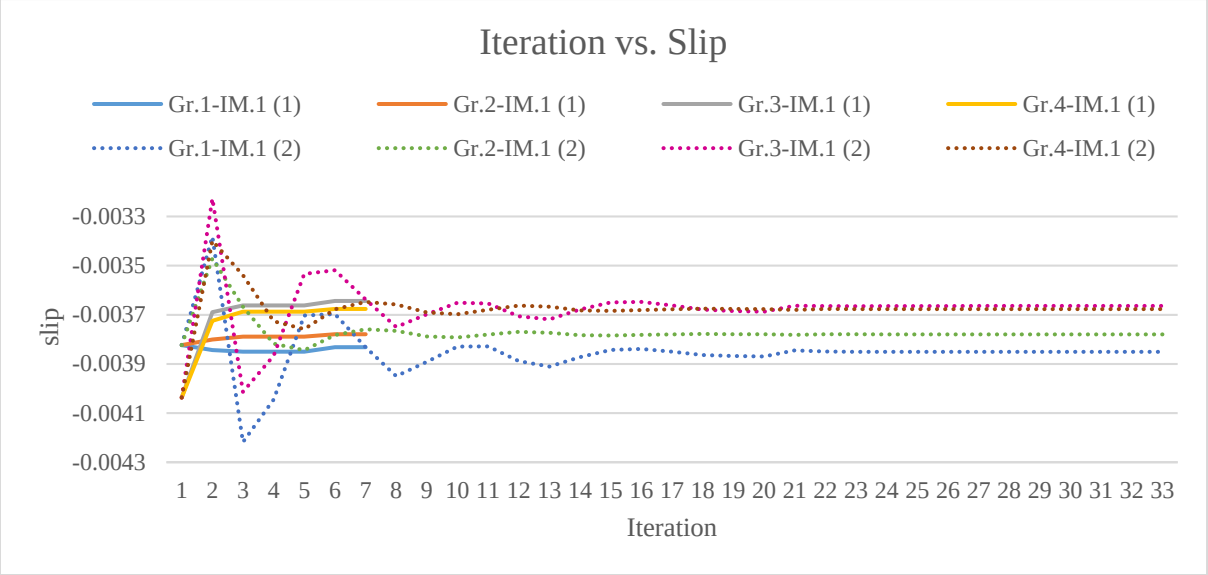

Figure 5.11: Iteration vs. Slip for All Groups (IM-1)

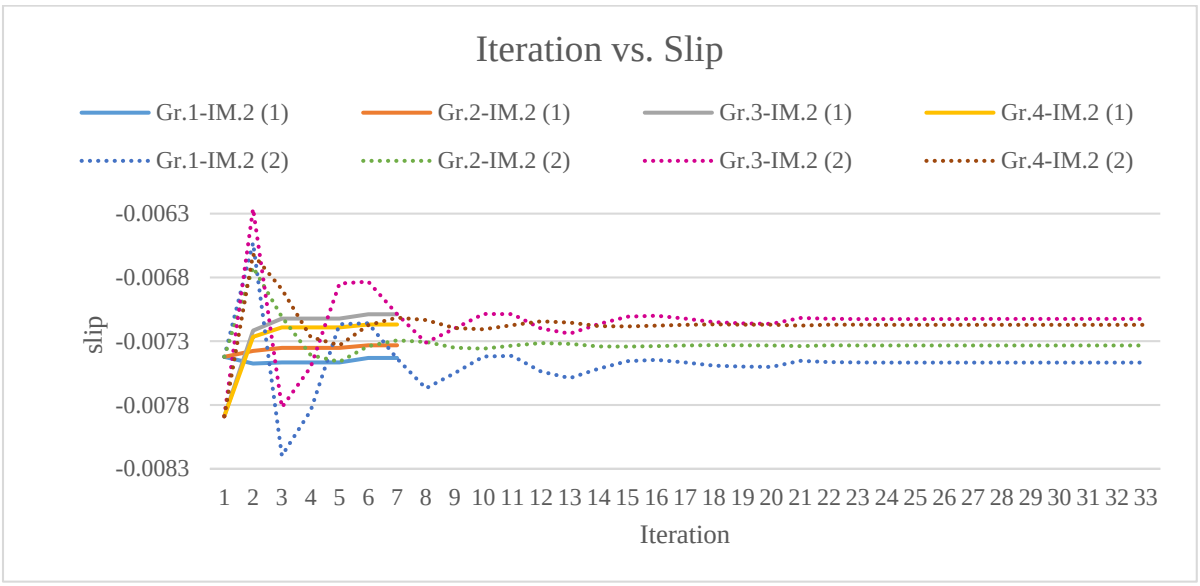

Figure 5.12: Iteration vs. Slip for All Groups (IM-2)

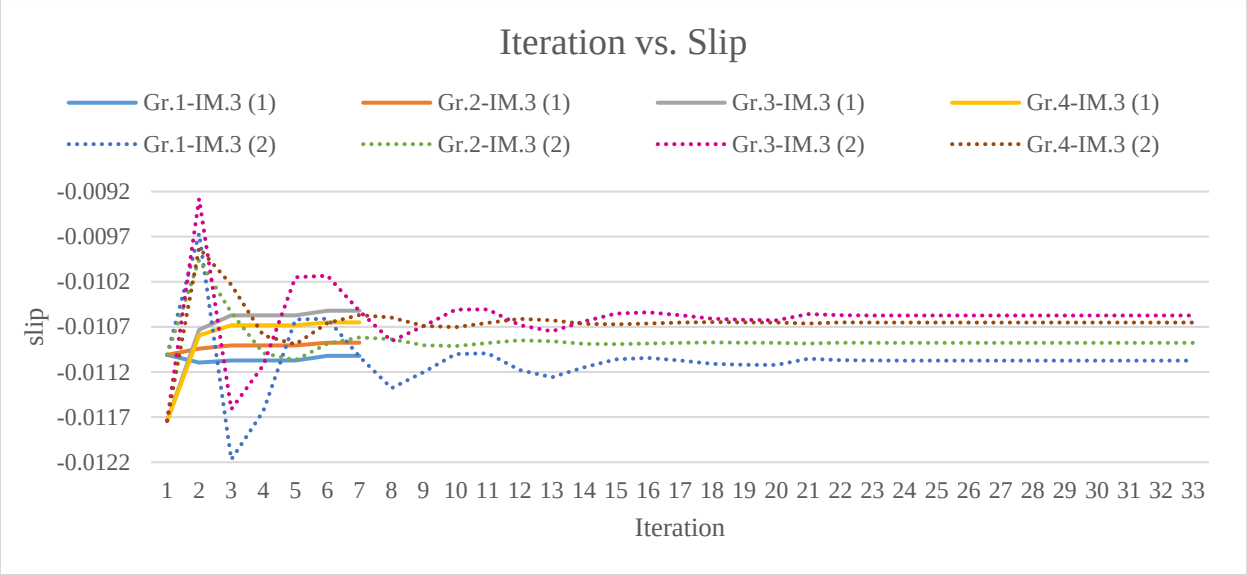

Figure 5.13: Iteration vs. Slip for All Groups (IM-3)

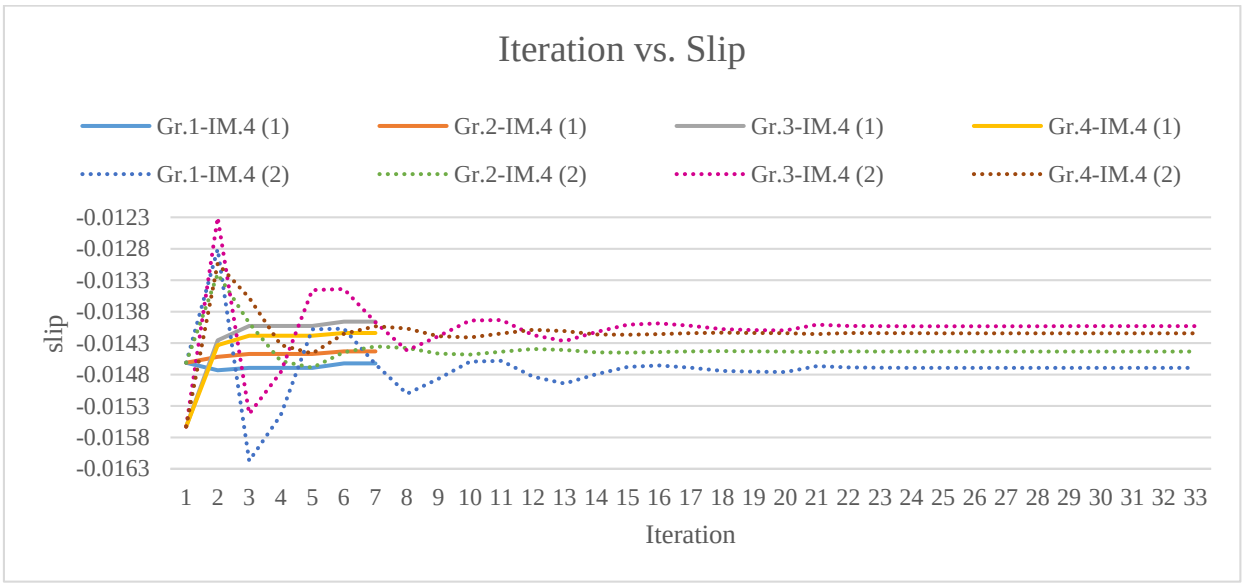

Figure 5.14: Iteration vs. Slip for All Groups (IM-4)

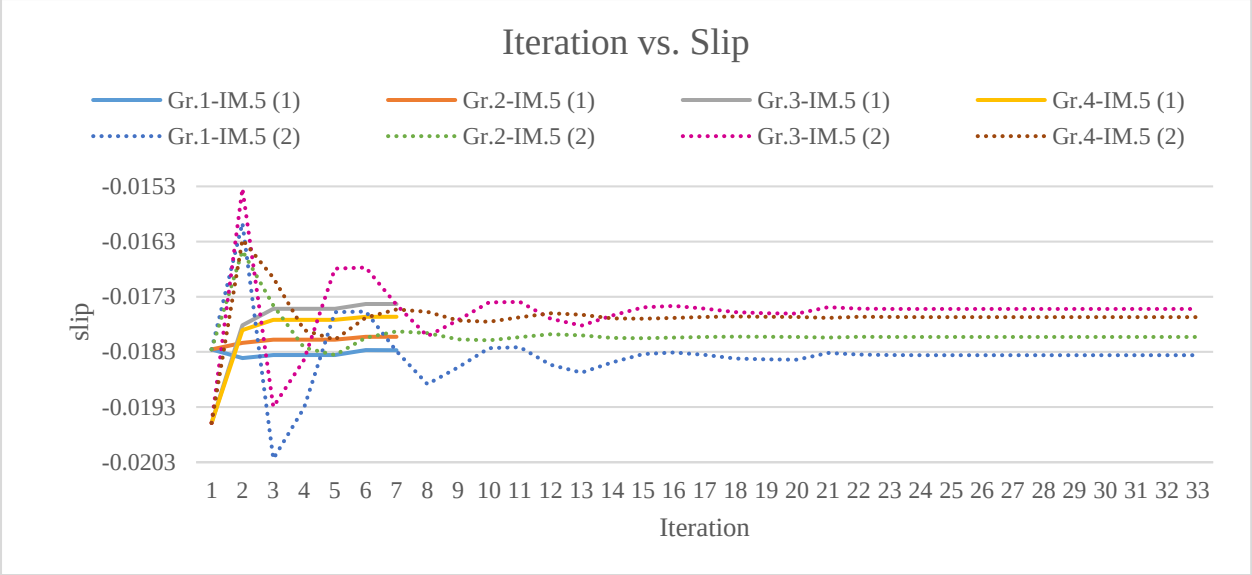

Figure 5.15: Iteration vs. Slip for All Groups (IM-5)

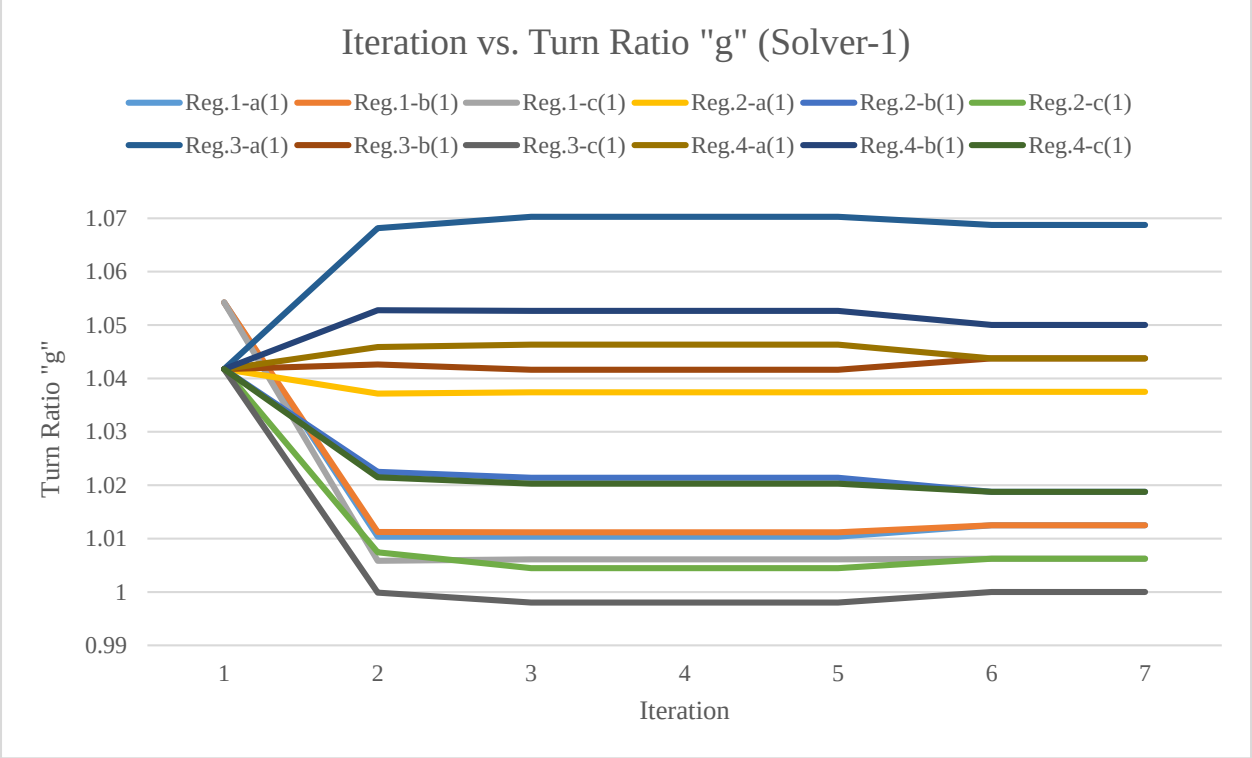

Figure 5.16: Iteration vs. Turn Ratio (Solver-1)

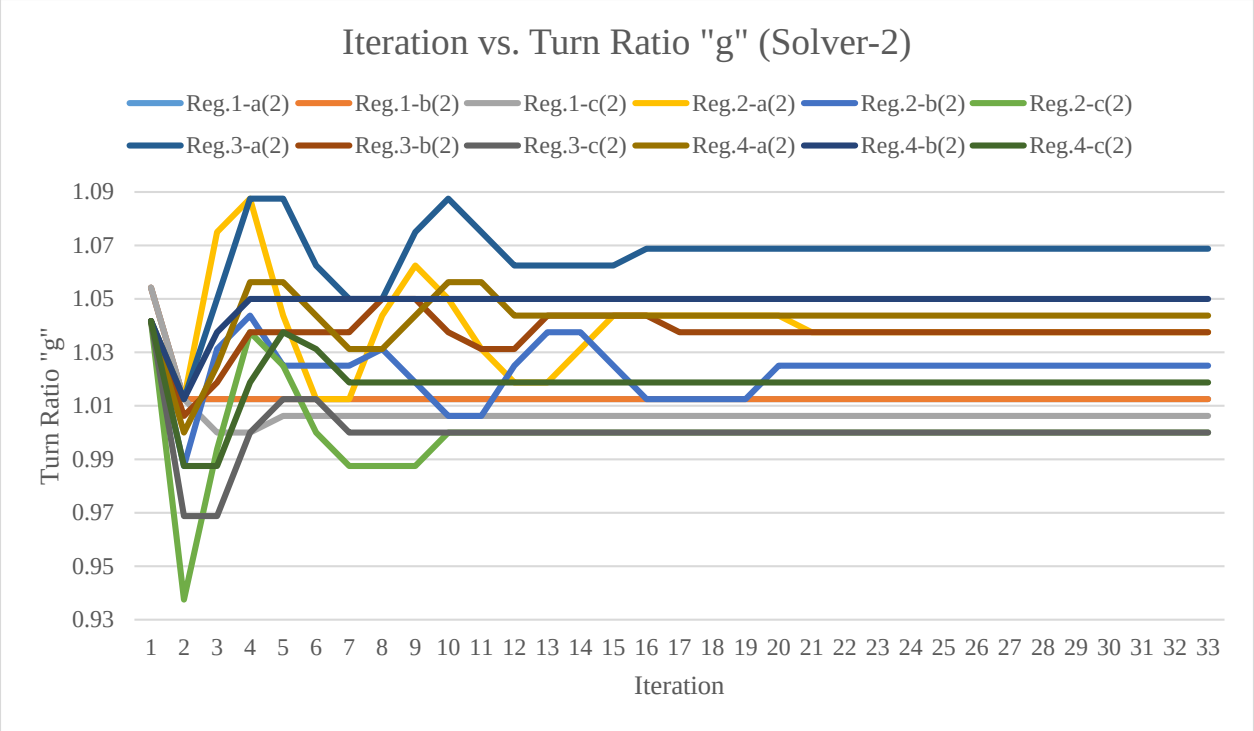

Figure 5.17: Iteration vs. Turn Ratio (Solver-2)

5.4 Summary

In this chapter, a new and precise load flow model is presented to account for various ECGs. The proposed generator model is basically a controlled current source and the constraints are defined on the sequence components of this source. The positive sequence component of the current is utilized to define the power injection to the grid. The generator behaves as a constant impedance to the negative and zero sequence voltages appearing at its terminals. The proposed model is tested on two study cases (both balanced and unbalanced), and the results are compared with precise time-domain EMTP simulations. The results obtained by the proposed method match the time-domain results.

CHAPTER 6 MULTIPHASE STATIC STATE ESTIMATION AND THE EFFECT OF THE LOAD POWER FACTOR PSEUDOMEASUREMENT ON ITS ACCURACY

The introduction of state estimation (SE) algorithms for transmission networks dates back to 1970's [19, 20]. The application of SE to the distribution network, however, has gained interest starting form 1990's. Most algorithms are based on the load allocation scheme [22]. Given that it is not practical to process all the load consumptions in real-time for the time being due to the huge size of distribution networks and the number of loads, the load-allocation tool is a pragmatic approach that is aimed to provide the distribution operators with an overview of network state that will allow them to take better decisions as opposed to having no other estimation [53]. However, the distribution networks are becoming "smarter" with the introduction of emerging technologies; such as online metering, monitoring of distributed energy resources (DER), smart automation, proliferation of SCADA (Supervisory Control and Data Acquisition) systems and also distribution level PMUs (Phasor Management Units). Especially, after the introduction of the DER units in distribution networks, the real-time state estimation has become a key concern in distribution management systems. In the light of these advancements, a reliable and accurate SE algorithm is needed for distribution systems [54, 55].

The state estimation algorithms proposed for distribution systems need to take into account the particularities of distribution systems. The distinct features are summarized as follows [53, 56]:

- The number of real time measurements is limited and is not sufficient to maintain observability.
- The load data have limited accuracy.
- Many measurements are current measurements rather than power.
- The distribution networks are unbalanced, have high R/X rations (making the decoupled SE not suitable) and have tens of thousands of nodes.

The existing SE algorithms for distribution networks are technically categorized in two groups. The branch current based state estimation algorithms constitute the first group [23-25, 57, 58]. The second group is the nodal admittance matrix based state estimation methods [26, 29, 59, 60]. The branch current based state estimation algorithms originally designed for radial systems or weakly

meshed networks [61], and does not perfectly fit to the networks with DER units. Moreover, as the size of the network increases, the formulation of these algorithms gets more complex. Also, given the fact that the general tendency of interconnecting several feeders once operated radially [55], there are already better distribution system analysis tools which are topology independent [1, 4, 62-64]. The nodal admittance matrix based state estimation methods are more systematic and based on the admittance matrix of the network. In the nodal admittance matrix based state estimation methods, the power flows and injection measurements should be expressed as a function of node voltages and device currents. The nodal analysis technique however has certain limitations. For example, in the classical nodal analysis, the Norton representation of the sources must be considered and it is not always straightforward to represent all devices in the nodal admittance matrix (such as transformers). These limitations are overcome by MANA method.

In the next section, first the MANA formulation will be expanded to account for the measurements which are associated with SE. The term measurement will both refer to statistical measurements as well as real-time telemetered measurements. When the statistical data is considered, it will be assumed that the measurements have a lower accuracy compared to the telemetered measurements. The statistical measurements essentially refer to load data obtained from historical load profiles and automated meter readings. They are also known as pseudo-measurements. The term accuracy used for measurements will also be clarified in the coming sections. Then, the effect of the load power factor on the accuracy of state estimation is investigated. In SE, the load measurements are formed by considering real and reactive powers independently. The hypothesis used in this work is that the power factor measurement is more precise than the power measurements. Therefore, adjusting the reactive power measurement in terms of the power factor can minimize the discrepancy between active and reactive power measurements in SE, and improve the accuracy of the SE solution.

6.1 General Formulation

The general objective of an SE algorithm is to relate the state of the network to the observed measurements [65].

From this point onwards, the bold letter $\mathbf{z}$ will always imply the measurement vector. The vector $\mathbf{h}$ is the set of nonlinear functions which relates the vector of unknowns $\mathbf{x}$ to the measurement vector $\mathbf{z}$. Thus, the relation between $\mathbf{x}$ and $\mathbf{z}$ can be expressed as follows;

$$\mathbf{z} = \mathbf{h}(\mathbf{x}) + \mathbf{e} \tag{4.1}$$

In (4.1), the term $\mathbf{e}$ denotes the measurement errors. Let m denote the number of measurement; then, each element of (4.1) can written as;

$$\begin{bmatrix} z_1 \\ z_2 \\ \vdots \\ z_m \end{bmatrix} = \begin{bmatrix} h_1(\mathbf{x}) \\ h_2(\mathbf{x}) \\ \vdots \\ h_m(\mathbf{x}) \end{bmatrix} + \begin{bmatrix} e_1 \\ e_2 \\ \vdots \\ e_m \end{bmatrix} \tag{4.2}$$

The $\mathbf{e}$ vector satisfies two conditions:

1) The measurement error is Gaussian distributed white signal. Therefore, the expected value (or the mean) of each element of $\mathbf{e}$ is zero:

$$E(e_j) = 0 \qquad \forall\ j = 1, 2, ..., m \tag{4.3}$$

2) The elements of $\mathbf{e}$ are uncorrelated; thus, all measurements are independent:

$$E(e_k\, e_l) = \begin{cases} 0 & if\ k \neq l \\ \sigma_k^2 & if\ k = l \end{cases} \tag{4.4}$$

The equation (4.4) can also be expressed as:

$$Cov(\mathbf{e}) = E[\mathbf{e} \cdot \mathbf{e}^{\mathrm{T}}] = \mathbf{R}_{\mathbf{cov}} = diag(\sigma_1^2, ..., \sigma_m^2) \tag{4.5}$$

where σ_j is the standard deviation to reflect the accuracy of the j th measurement and $\mathbf{R}_{\mathbf{cov}}$ is the covariance matrix. As the measurements are uncorrelated, the covariance matrix is always diagonal.

The main purpose of an SE algorithm is to find a solution that minimizes the norm of the error vector $\mathbf{e}$. The weighted least squares (WLS) is the mostly used method to find the optimal state vector [24, 66]. The objective of the WLS is to minimize the error between $\mathbf{z}$ and $\mathbf{h}(\mathbf{x})$. Thus, the objective function for the WLS problem $F(\mathbf{x})$ can be expressed as;

$$\begin{aligned} & F(\mathbf{x}) = \min\left(\left(\mathbf{z}-\mathbf{h}(\mathbf{x})\right)^{\mathrm{T}} \mathbf{R}_{\mathbf{cov}}^{-1}\left(\mathbf{z}-\mathbf{h}(\mathbf{x})\right)\right) \\ & s.t.\ \mathbf{c}(\mathbf{x}) = \mathbf{0} \end{aligned} \tag{4.6}$$

In (4.6), $F(\mathbf{x})$ denotes the minimization function of the SE algorithm, and $\mathbf{c}(\mathbf{x})$ is the set of network constraints.

There are two most commonly used techniques to solve (4.6); namely normal equations with constraints (NEC) [67] and Hachtel's method [21].

The NEC method for (4.6) can be formulated as follows:

$$\begin{bmatrix} \mathbf{J}_{\mathbf{h}}^{\mathrm{T}}(\mathbf{x})\mathbf{R}_{\mathbf{cov}}\mathbf{J}_{\mathbf{h}}(\mathbf{x}) & \mathbf{J}_{\mathbf{c}}^{\mathrm{T}}(\mathbf{x}) \\ \mathbf{J}_{\mathbf{c}}(\mathbf{x}) & \mathbf{0} \end{bmatrix} \begin{bmatrix} \Delta\mathbf{x} \\ \boldsymbol{\lambda} \end{bmatrix} = \begin{bmatrix} \mathbf{J}_{\mathbf{h}}^{\mathrm{T}}(\mathbf{x})\mathbf{R}_{\mathbf{cov}}\left(\mathbf{z}-\mathbf{h}(\mathbf{x})\right) \\ -\mathbf{c}(\mathbf{x}) \end{bmatrix} \tag{4.7}$$

$\mathbf{J}_{\mathbf{c}}(\mathbf{x}) = \dfrac{\partial \mathbf{c}(\mathbf{x})}{\partial \mathbf{x}}$: The Jacobian matrix of the constraints

$\mathbf{J}_{\mathbf{h}}(\mathbf{x}) = \dfrac{\partial \mathbf{h}(\mathbf{x})}{\partial \mathbf{x}}$: The Jacobian matrix of the measurements

$\boldsymbol{\lambda}$ contains the Lagrange multipliers.

The Hachtel's formulation for (4.6) can be expressed as follows;

$$\begin{bmatrix} \mathbf{R}_{\mathbf{cov}} & \mathbf{J}_{\mathbf{h}}(\mathbf{x}) & \mathbf{0} \\ \mathbf{J}_{\mathbf{h}}^{\mathrm{T}}(\mathbf{x}) & \mathbf{0} & \mathbf{J}_{\mathbf{c}}^{\mathrm{T}}(\mathbf{x}) \\ \mathbf{0} & \mathbf{J}_{\mathbf{c}}(\mathbf{x}) & \mathbf{0} \end{bmatrix} \begin{bmatrix} \mathbf{r} \\ \Delta\mathbf{x} \\ \boldsymbol{\lambda} \end{bmatrix} = \begin{bmatrix} \mathbf{z}-\mathbf{h}(\mathbf{x}) \\ \mathbf{0} \\ -\mathbf{c}(\mathbf{x}) \end{bmatrix} \tag{4.8}$$

In (4.8), $\mathbf{r}$ is the residual vector for the measurements.

The two methods were investigated and compared in several papers in terms of robustness, stability, and accuracy [21, 68-70]. The Hachtel formulation provides a technique that is numerically more stable. The size of the system matrix and the number of non-zero elements are greater in the Hachtel formulation; however, due to its robustness and more systematical formulation, the Hachtel formulation is the preferred technique in most algorithms.

6.2 State Estimation Algorithm in MANA

The expandable formulation of MANA allows the realization of the SE algorithm defined in (4.8) . In this chapter, the base form of MANA in (1.27) will be considered for the development of constraint and measurement equations. The formulation in [60] is expanded for several other measurements.

6.2.1 Covariance Matrix $\mathbf{R_{cov}}$

In SE analysis, the measurements have a random error. Any Gaussian random signal x has a probability density function expressed as;

$$pdf\left(x \mid \mu_x, \sigma_x^2\right) = \frac{1}{\sqrt{2\sigma_x^2 \pi}} e^{-\frac{(x-\mu_x)^2}{2\sigma_x^2}} \tag{4.9}$$

μ_x : The mean (or expected) value of x

σ_x : The standard deviation of the signal x

σ_x^2 : The covariance of the signal x

The white Gaussian signals have zero mean $\left(\mu_x = 0\right)$ and the graphical representation of any white signal is illustrated in Figure 6.1. On the x-axis, the origin shows the most probable value of the signal x which is $\mu_x = 0$. The x-axis shows the deviation of x from the expected value. It can be stated that the probability of a selected sample of x being within the region bounded by $-\sigma$ and σ is 68.2 %.

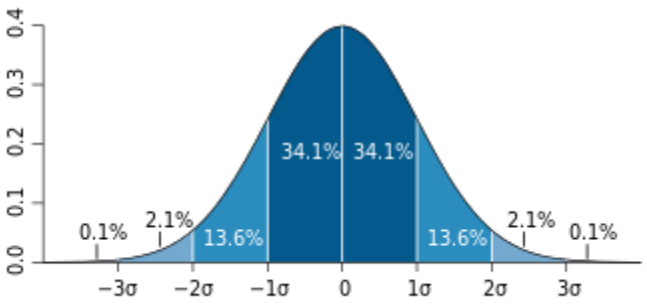

Figure 6.1: Probability Distribution Function of a White Signal

In (4.8), as aforementioned, the diagonal entries of $\mathbf{R}_{\mathbf{cov}}$ are formed by the covariance of the associated error. In the SE, the measured quantities have an unknown 'true' value and again an unknown 'random' error. The true value of the quantity can be obtained by using the statistical tools. It is a common practice to define the standard deviation (or covariance) as the percentage of the true value. Thus, in this chapter, the standard deviation will always be expressed in terms of percentage. In the SE algorithms, the real-time measurements have a higher accuracy; meaning that their covariance is small; usually between 1-5 %. On the other hand, the statistical measurements; such as load allocation, are less precise. Their standard variation can be as great as 30 % depending on the variations in the load profile in the network.

6.2.2 Network Constraints

The network constraints $\mathbf{c}(\mathbf{x})$ which can be extracted from (1.27) are given as;

$$\mathbf{c}(\mathbf{x}) = \begin{bmatrix} \mathbf{f}_{\mathbf{n}} \\ \mathbf{f}_{\mathbf{v}} \\ \mathbf{f}_{\mathbf{d}} \\ \mathbf{f}_{\mathbf{s}} \\ \mathbf{f}_{\mathbf{E}} \end{bmatrix} \tag{4.10}$$

In (4.10), it can be seen that the terms related with the load constraints $\mathbf{f}_{\mathbf{L}}$ and the generator constraints $\mathbf{f}_{\mathbf{G}}$ have vanished. The reason is that in the SE, the load power consumptions as well as generator power injections must be treated as measurements rather than constraints. Thus, the Jacobian matrix of $\mathbf{c}(\mathbf{x})$ in (4.8) is given as;

$$\mathbf{J}_{\mathbf{c}}(\mathbf{x}) = \begin{bmatrix} \mathbf{Y}_{\mathbf{n}} & \mathbf{V}_{\mathbf{r}}^{\mathrm{T}} & \mathbf{D}_{\mathbf{r}}^{\mathrm{T}} & \mathbf{S}_{\mathbf{r}}^{\mathrm{T}} & \mathbf{A}_{\mathbf{IL}} & \mathbf{A}_{\mathbf{IG}} & \mathbf{0} \\ \mathbf{V}_{\mathbf{r}} & \mathbf{0} & \mathbf{0} & \mathbf{0} & \mathbf{0} & \mathbf{0} & \mathbf{0} \\ \mathbf{D}_{\mathbf{r}} & \mathbf{0} & \mathbf{0} & \mathbf{0} & \mathbf{0} & \mathbf{0} & \mathbf{0} \\ \mathbf{S}_{\mathbf{r}} & \mathbf{0} & \mathbf{0} & \mathbf{S}_{\mathbf{d}} & \mathbf{0} & \mathbf{0} & \mathbf{0} \\ \mathbf{Y}_{\mathbf{G}} & \mathbf{0} & \mathbf{0} & \mathbf{0} & \mathbf{0} & \mathbf{B}_{\mathbf{G}} & \mathbf{Y}_{\mathbf{GE}} \end{bmatrix} \tag{4.11}$$

The formation of the terms of $\mathbf{J}_{\mathbf{c}}$ as well as the constraint equations $\mathbf{c}(\mathbf{x})$ can be found in Chapter 2.2.

6.2.3 Measurement Equations

In the SE analysis, there are various measurements associated with a power network. In this section, the most commonly used measurements will be presented within MANA formulation.

The measurements can be categorized into three groups:

$$\mathbf{z} = \begin{bmatrix} \mathbf{z_L} \\ \mathbf{z_G} \\ \mathbf{z_A} \end{bmatrix} \tag{4.12}$$

$\mathbf{z_L}$: The measurement vector related with the loads

$\mathbf{z_G}$: The measurement vector related with the generators

$\mathbf{z_A}$: The vector of auxiliary measurements

Similarly, $\mathbf{h}(\mathbf{x})$ can be written in the same order as $\mathbf{z}$:

$$\mathbf{h}(\mathbf{x}) = \begin{bmatrix} \mathbf{h_L}(\mathbf{x}) \\ \mathbf{h_G}(\mathbf{x}) \\ \mathbf{h_A}(\mathbf{x}) \end{bmatrix} \tag{4.13}$$

The Jacobian matrix of the measurements $\mathbf{J_h}$ has the form as follows;

$$\mathbf{J_h} = \begin{bmatrix} \mathbf{C_L} & \mathbf{0} & \mathbf{0} & \mathbf{0} & \mathbf{D_L} & \mathbf{0} & \mathbf{0} \\ \mathbf{C_G} & \mathbf{0} & \mathbf{0} & \mathbf{0} & \mathbf{0} & \mathbf{D_G} & \mathbf{0} \\ \mathbf{J_{V_n}} & \mathbf{0} & \mathbf{0} & \mathbf{J_{I_s}} & \mathbf{0} & \mathbf{0} & \mathbf{0} \end{bmatrix} \tag{4.14}$$

The submatrices $\mathbf{C_L}$, $\mathbf{D_L}$, $\mathbf{C_G}$, and $\mathbf{D_G}$ are formed in the same way as explained in the sections 2.2.2 and 2.2.3. $\mathbf{J_{V_n}}$ and $\mathbf{J_{I_s}}$ are the submatrices associated with the auxiliary measurements. For simplicity, each of the matrices $\mathbf{J_{V_n}}$ and $\mathbf{J_{I_s}}$ can be partitioned into two parts:

$$\mathbf{J_{V_n}} = \begin{bmatrix} \mathbf{J_{V_{n1}}} & \mathbf{J_{V_{n2}}} \end{bmatrix} \tag{4.15}$$

$$\mathbf{J_{I_s}} = \begin{bmatrix} \mathbf{J_{I_{s1}}} & \mathbf{J_{I_{s2}}} \end{bmatrix} \tag{4.16}$$

$\mathbf{J_{V_{n1}}}$: The partial derivatives of $\mathbf{h_A}(\mathbf{x})$ w.r.t to the real parts of the node voltages

$\mathbf{J}_{\mathbf{V_{n2}}}$: The partial derivatives of $\mathbf{h_A}(\mathbf{x})$ w.r.t to the imaginary parts of the node voltages

$\mathbf{J}_{\mathbf{I_{s1}}}$: The partial derivatives of $\mathbf{h_A}(\mathbf{x})$ w.r.t to the real parts of the switch currents

$\mathbf{J}_{\mathbf{I_{s2}}}$: The partial derivatives of $\mathbf{h_A}(\mathbf{x})$ w.r.t to the imaginary parts of the switch currents

6.2.3.1 Node Voltage Measurement

The voltage measurement is amongst the mostly used measurement in a power system. The voltage magnitude at different buses is monitored in real-time with high accuracy. Now, let us consider that the magnitude of the voltage at the k th node is monitored. Then, the measurement equation becomes:

$$\begin{aligned} &\mathbf{h_A}(r) = \sqrt{V_{kR}^2 + V_{kI}^2} \\ &\textit{where } \bar{\mathbf{V}}_{\mathbf{n}}(k) = V_{kR} + jV_{kI} \end{aligned} \tag{4.17}$$

The Jacobian terms for this measurement becomes:

$$\mathbf{J}_{\mathbf{V_{n1}}}(r,k) = \frac{V_{kR}}{\sqrt{V_{kR}^2 + V_{kI}^2}} \tag{4.18}$$

$$\mathbf{J}_{\mathbf{V_{n2}}}(r,k) = \frac{V_{kI}}{\sqrt{V_{kR}^2 + V_{kI}^2}} \tag{4.19}$$

The assumed standard deviation for voltage magnitude measurement is 3 %.

6.2.3.2 Branch Current Measurement

The magnitude of the current is one of the most common measurement types. The current of circuit breakers is a measured quantity in distribution networks and it is possible to monitor this quantity. The circuit breakers are simply modeled with an ideal switch model in MANA presented in Section 2.1.4. Now, let us consider a closed switch (indexed as s) connected between the nodes k and m with the direction of the switch current I_{sw} indicated by the arrow.

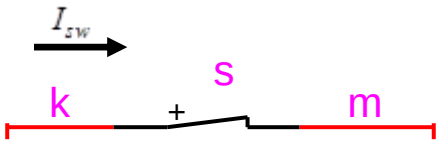

Figure 6.2: Closed Switch between k and m

The current magnitude for this switch can be expressed in terms of the unknowns as follows;

$$\begin{aligned} &\mathbf{h}_{\mathbf{A}}(r) = \sqrt{I_{swR}^2 + I_{swI}^2} \\ &\textit{where } \bar{\mathbf{I}}_{\mathbf{s}}(s) = I_{sw} = I_{swR} + jI_{swI} \end{aligned} \tag{4.20}$$

Thus, the Jacobian terms are found as follows;

$$\mathbf{J}_{\mathbf{I}_{s1}}(r,s) = \frac{I_{swR}}{\sqrt{I_{swR}^2 + I_{swI}^2}} \tag{4.21}$$

$$\mathbf{J}_{\mathbf{I}_{s2}}(r,s) = \frac{I_{swI}}{\sqrt{I_{swR}^2 + I_{swI}^2}} \tag{4.22}$$

6.2.3.3 Branch Power Measurement

As an alternative to the current measurement, the real power flowing through a feeder can also be a measurement. Let us again consider the switch model in Figure 6.2. By using the sign direction indicated, the real power passing through it can be written as;

$$\begin{aligned} &\mathbf{h}_{\mathbf{A}}(r) = \mathrm{Re}\left(I_{sw}^{*} V_k\right) \\ &\textit{where } \vec{\mathbf{V}}_{\mathbf{n}}(k) = V_k = V_{kR} + jV_{kI} \end{aligned} \tag{4.23}$$

The corresponding Jacobian terms become;

$$\mathbf{J}_{\mathbf{V}_{n1}}(r,k) = I_{swR} \tag{4.24}$$

$$\mathbf{J}_{\mathbf{V}_{n2}}(r,k) = I_{swI} \tag{4.25}$$

$$\mathbf{J}_{\mathbf{I}_{s1}}(r,s) = V_{kR} \tag{4.26}$$

$$\mathbf{J}_{\mathbf{I}_{s2}}(r,s) = V_{kI} \tag{4.27}$$

6.2.3.4 Phasor Measurement Unit (PMU)

One of the newest trends in power distribution systems is to install PMUs at different locations in the network. They provide both the magnitude and the angle of the node voltages. Due to the rectangular formulation of MANA approach, it is easier to form node voltages in real and imaginary parts rather than in magnitude and angle.

Let us consider that a PMU is installed at the k th node of the network. The measurement equations are simply formed as follows;

$$\mathbf{h_A}\left(r_1\right) = \mathrm{Re}\left(\vec{\mathbf{V}}_\mathbf{n}\left(k\right)\right) \tag{4.28}$$

$$\mathbf{h_A}\left(r_2\right) = \mathrm{Im}\left(\vec{\mathbf{V}}_\mathbf{n}\left(k\right)\right) \tag{4.29}$$

By using (4.28) and (4.29), the Jacobian terms are found as;

$$\mathbf{J}_{\mathbf{V_{n1}}}\left(r_1, k\right) = 1 \tag{4.30}$$

$$\mathbf{J}_{\mathbf{V_{n2}}}\left(r_2, k\right) = 1 \tag{4.31}$$

6.3 The Load Power Factor

In the SE analysis, the load measurements are formed by considering real and reactive powers independently. In other words, the relation between the real and reactive powers for a load is ignored.

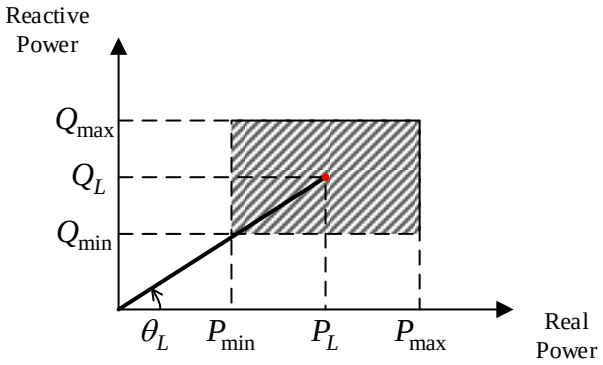

Figure 6.3: Load Power in Rectangular Form

In Figure 6.3, the power consumption of a load is illustrated in rectangular form where the x-axis denotes the real power and the y-axis is the reactive power. The real power consumption is marked

with P_L; while the reactive power consumption is denoted by Q_L; and the red point shows the true operating condition of the load. The bold line can be considered as the impedance of the load. Due to the measurements errors, the measured values for the real and reactive powers lie within the intervals $[P_{\min}, P_{\max}]$ and $[Q_{\min}, Q_{\max}]$, respectively. Therefore, any point in the shaded rectangle in Figure 6.3 might represent a possible measurement pair for this load.

Now, let us take a closer look at the angle θ_L which at the same time happens to be the impedance angle of the load. The load angle gives the explicit relation between the real and reactive powers of the load. The load power factor pf_L is a characteristics used to define loads in power networks. Its formula is simply;

$$pf_L = \begin{cases} \cos\theta_L & if\ Q_L \geq 0 \\ -\cos\theta_L & if\ Q_L < 0 \end{cases} \tag{4.32}$$

Or, equivalently;

$$pf_L = \frac{Q_L}{\sqrt{P_L^2 + Q_L^2}} \tag{4.33}$$

The hypothesis claimed here is that, the power factor of loads is more precise than the power measurements. In other words, the percentage error in the measurement of the load power factor is smaller. Here, The variations in the load power factor measurement is considered to be less than 0.5 %.

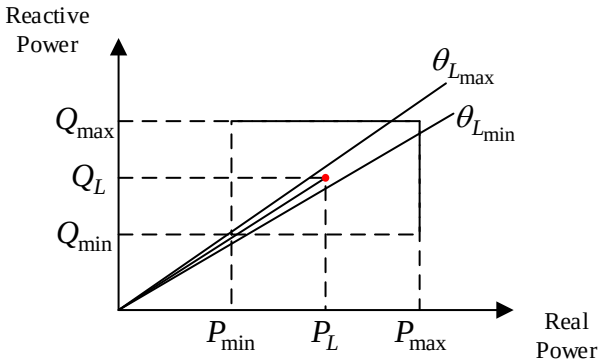

Figure 6.4: The Limits for the Load Angle

In Figure 6.4, the limits for the load angle are indicated with $\theta_{L_{\min}}$ and $\theta_{L_{\max}}$. It suggests that if there is a small disturbance on the power factor, the load angle will not refract from its true value. This conclusion is very useful in forming the measurements of the loads; because the shaded area in Figure 6.3 which shows the possible measurement pairs for this load has shrunk to the one demonstrated in Figure 6.4. Therefore, it can be stated that, considering the relation between the real and reactive power consumptions of a load, can improve the performance of SE algorithms. This method is especially useful for the cases with the load allocation schemes where the standard deviation of a load is quite large.

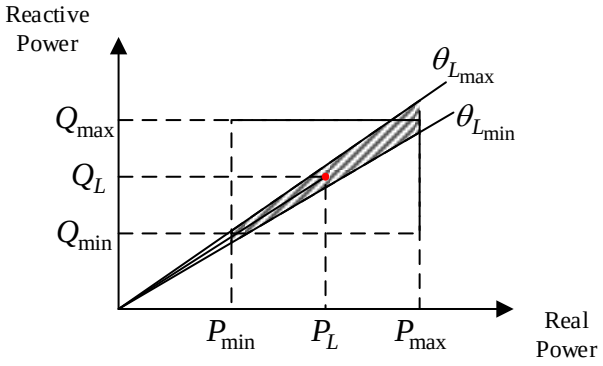

Figure 6.5: Load Power in Rectangular Form

In the next section, the performance of the SE algorithm will be compared for the two methods. In the first method (named as Method-I), the reactive and real power measurements are treated independently. And in the second method (named hereinafter as Method-II), the reactive power measurement will be obtained as a function of the real power and the power factor. To prove the validity of this concept, various distribution networks will be subjected to tests using the two methods. The algorithms are to be tried for hundred times consecutively to obtain a reliable set of data. Then, the results of the SE analyses will be compared to the load flow results which give the true state of the system.

6.4 Study Cases

In the literature, there exist various distribution networks. The results for four different size distribution networks will be presented.

6.4.1 Study Case-1: IEEE 13 Bus Network:

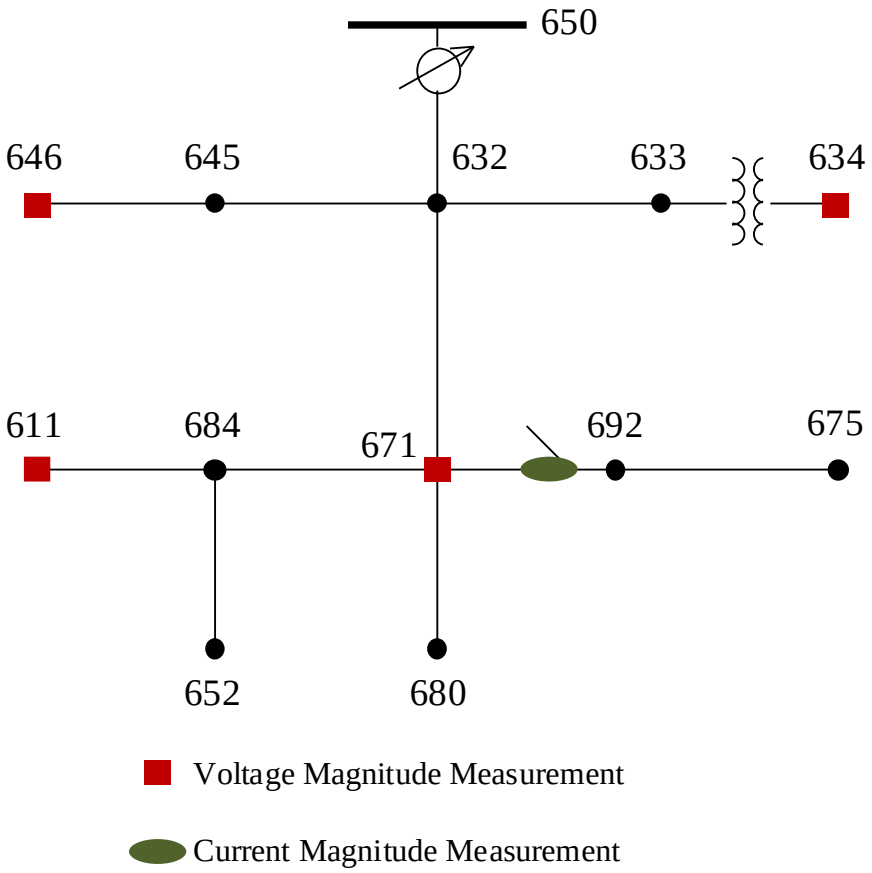

Figure 6.6: IEEE 13 Bus Test Feeder with the Positions of Measurements

This network is a micro distribution IEEE distribution test case which was also used in CHAPTER 3. Although the circuit is small in size (with only 35 nodes and 20 loads), it contains the essential components in a typical distribution network.

In Figure 6.6, the network schematic together with the locations of the measurement units. The voltages are measured at 5 different locations. Also, the current passing through the switch between the buses 671 and 692 is measured.

The assumed standard deviation for the measurements are given in Table 6.1.

Table 6.1: Standard Deviation of the Measurements

Measurement Type	Standard Deviation
Magnitude of the Switch Current	1 %
Magnitude of the Node Voltage	5 %
Load Real Power	20 %
Load Reactive Power (only for Method-I)	20 %

The methods have been tested with 100 different set of measurements. As aforementioned, the load flow results are the reference. The average values of the errors for each node voltage are demonstrated in Figure 6.7 with blue and orange lines. Also, the worst trial is marked on the same graph where gray line shows the results of the Method-I and yellow one shows the results of the Method-II. It can be stated that the use of the power factor slightly improved the performance of the SE algorithm for this small system.

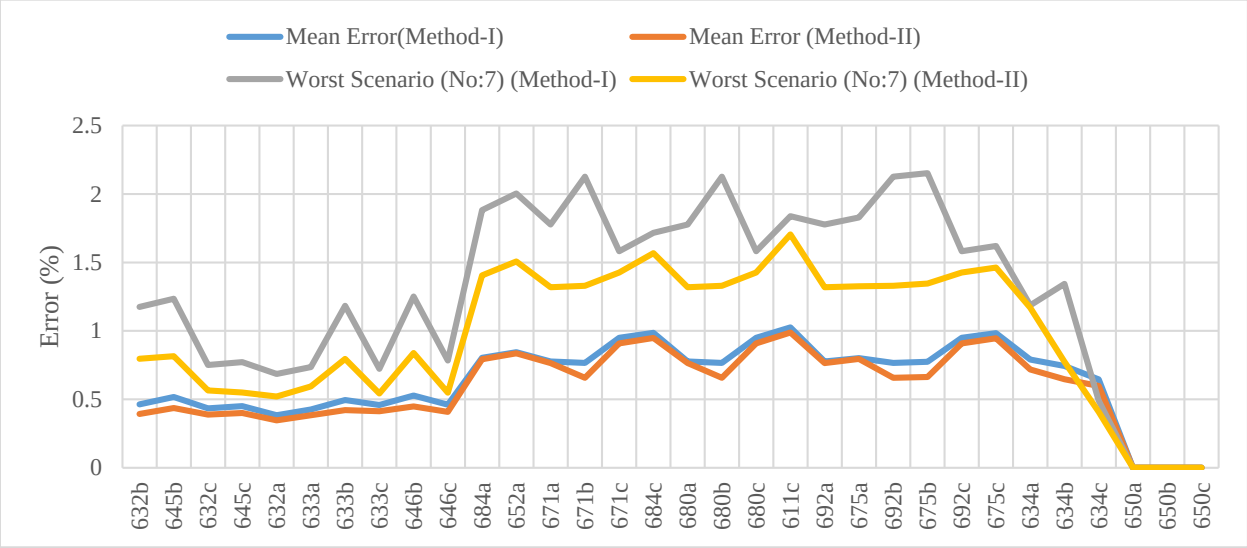

Figure 6.7: Comparison of Method-I and Method-II

6.4.2 Study Case-2: IEEE 34 Bus Test Case

In this study case, the IEEE 34 Bus system is subject to the SE algorithm with the two methods. The characteristics of the network was given in the section 4.3.2.

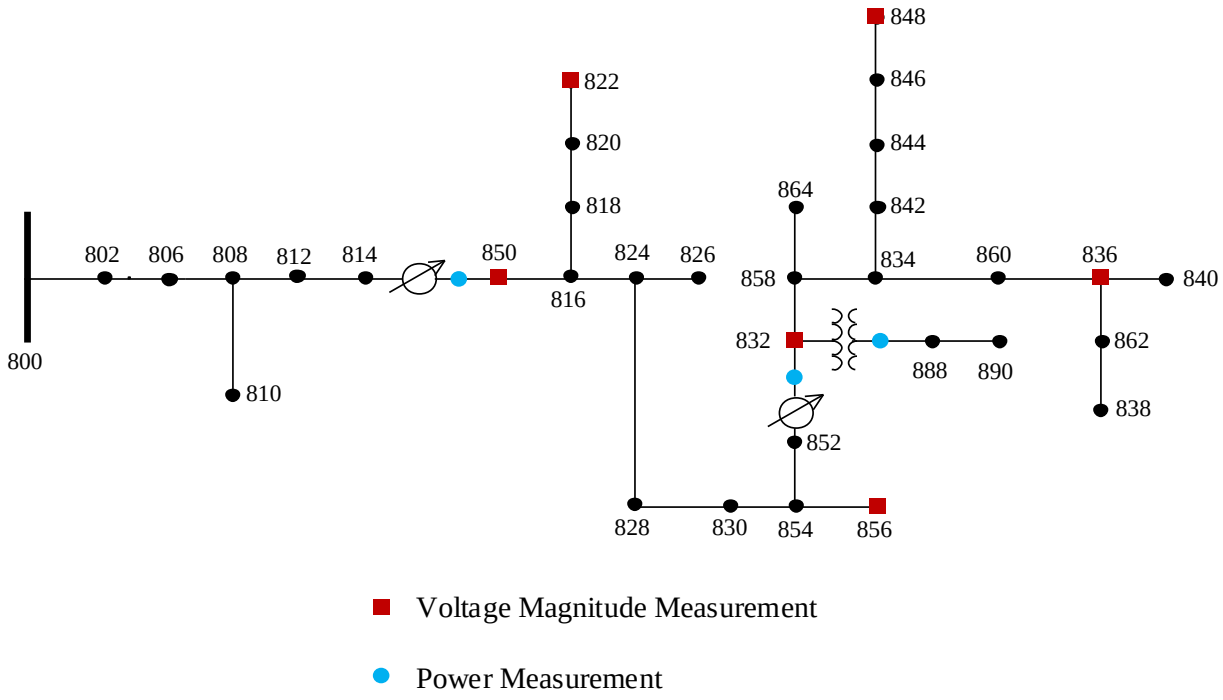

Figure 6.8: IEEE 34 Bus Test Network with Measurements

This small distribution network has long line segments which makes it a typical suburban network. In this scenario, the network voltage is measured at six different locations. Moreover, the power is monitored at the output of transformers and regulators.

The assumed standard deviation for the measurements are tabulated as follows;

Table 6.2: Standard Deviation of the Measurements

Measurement Type	Standard Deviation
Branch Power	2 %
Magnitude of the Node Voltage	5 %
Load Real Power	25 %
Load Reactive Power (only for Method-I)	25 %

The mean error for the node voltage magnitudes in percentage are shown in Figure 6.9. On the average, the performance of the SE algorithm is better: In the Method-I, the overall mean error 0.797 % while this parameter is 0.59 % for the Method-II. An alternative representation of the results in Figure 6.10 shows the density of the error. Furthermore, as seen from Figure 6.9, there is huge improvement in the worst case scenario. In the Method-I, the peak difference reaches up to 7

%; while in the Method-II, the maximum difference is as great as 1.8 %. The use of the power factor greatly improved the results for this network.

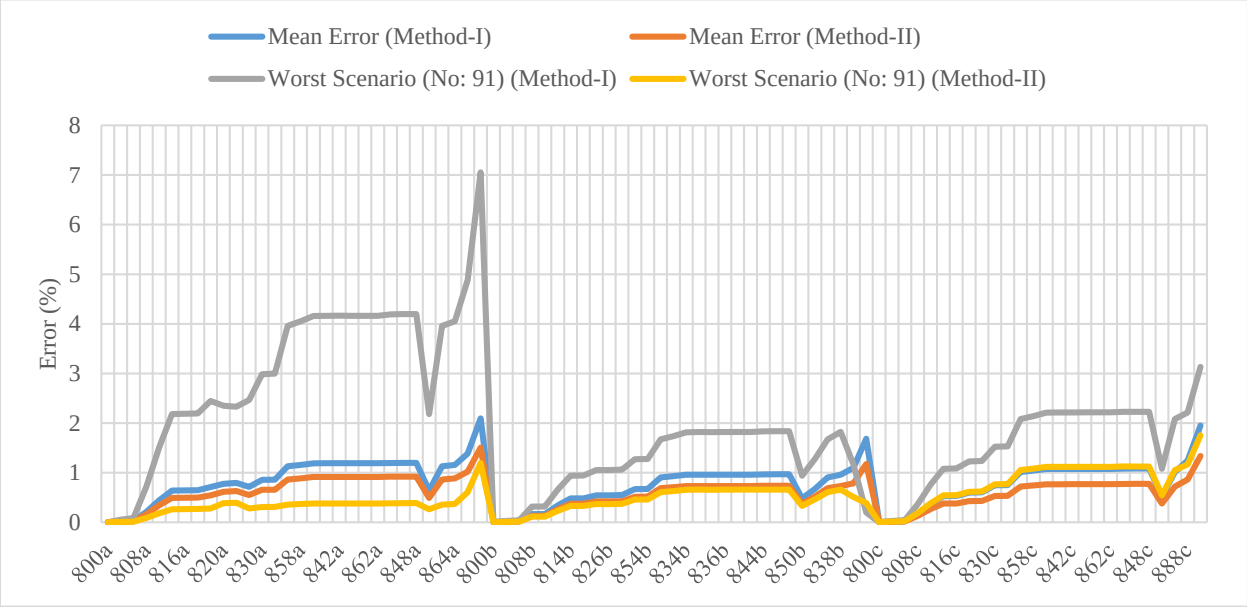

Figure 6.9: Comparison of Method-I and Method-II for the Study Case-II

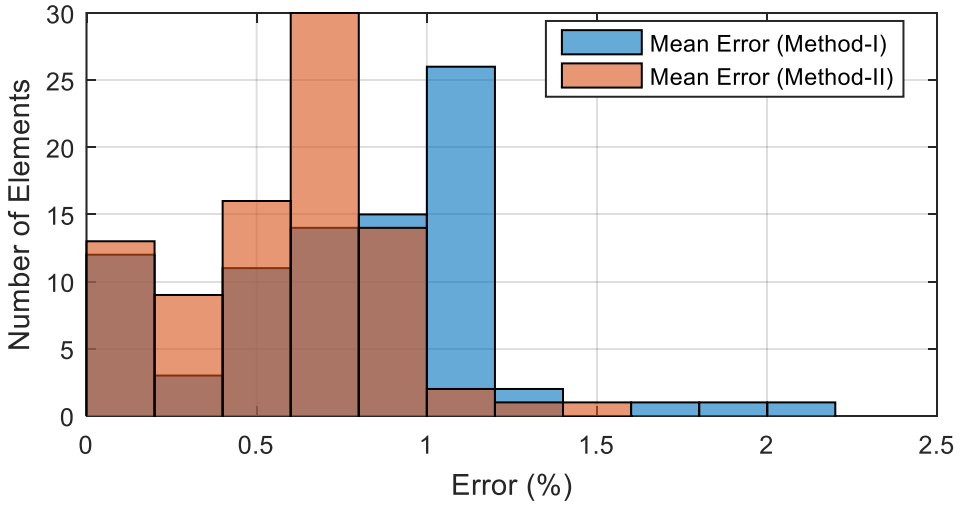

Figure 6.10: Comparison of Method-I and Method-II for the Study Case-II

6.4.3 Study Case-3: IEEE 342 Node Distribution Network

The IEEE 342 Node network [71] is a moderate size, heavily meshed (unlike classical ones), unbalanced distribution network with several transformers connected in parallel. This type of meshed distribution networks is used in dense populated areas in North America.

Due to its complexity, this network is analyzed in three parts, namely; (1) primary feeders, (2) grid network, and (3) spot networks.

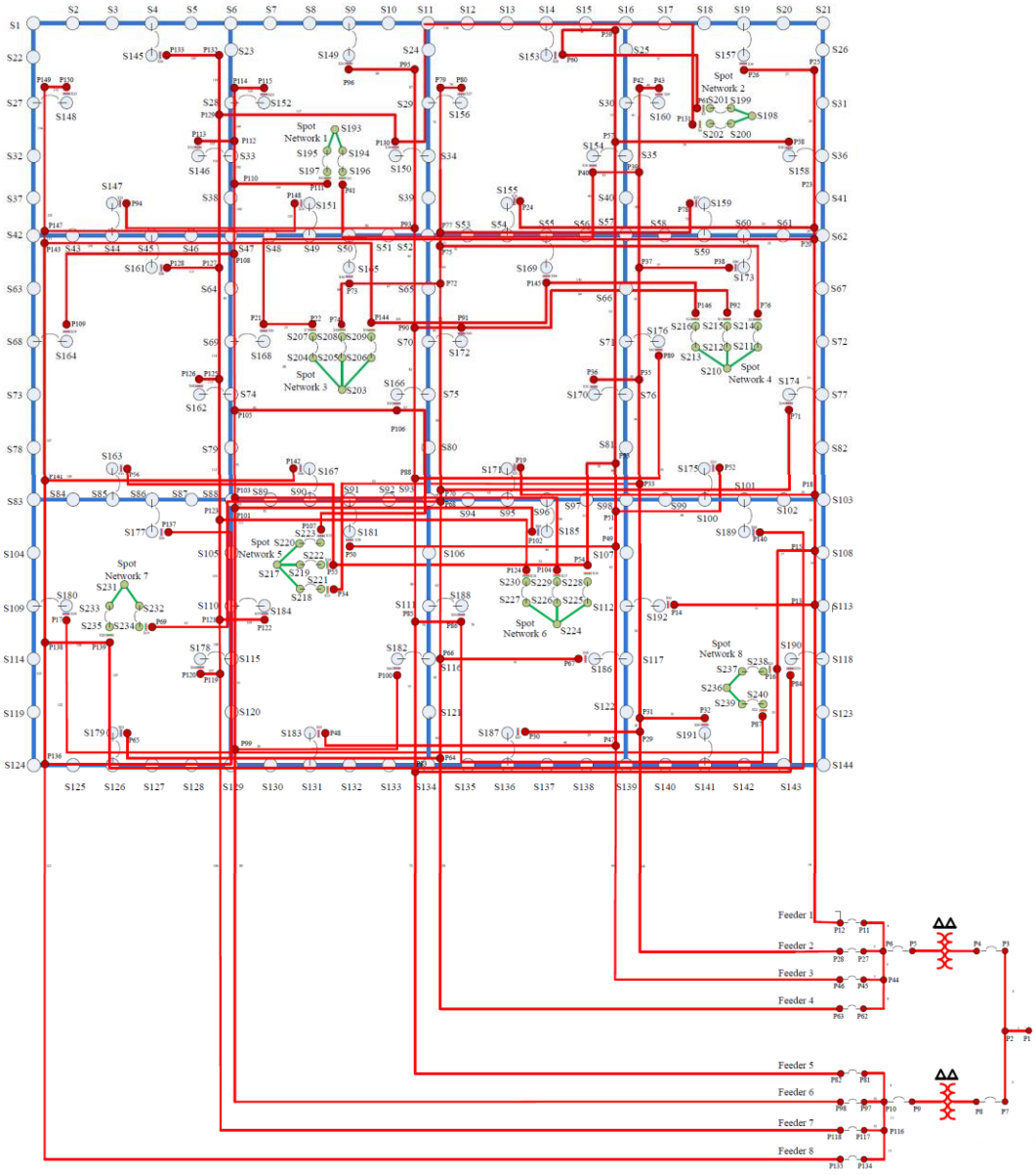

Figure 6.11: Single Line Diagram of IEEE 342 Node Distribution Network

The single line diagram of the distribution network is shown Figure 6.11 where the red, blue, and green lines indicate the primary feeders, the grid network, and the spot networks, respectively. The network is connected to the 230 kV transmission network (at the bus “P1”) with two delta connected transformers each rated at 50 MVA. The primary feeder circuit is composed of eight

feeders rated at 13.2 kV. The grid network contains 48 transformers each rated at 1 MVA. There are 8 spot networks in total. Further specification related to the network can be obtained from [40].

In this study case, the voltage magnitude is measured on the grid network at the11 bus whose names are; S134, S129, S139, S47, S52, S57, S62, S16, S11, S88, S93. Furthermore, the real power on the eight primary feeders is also monitored.

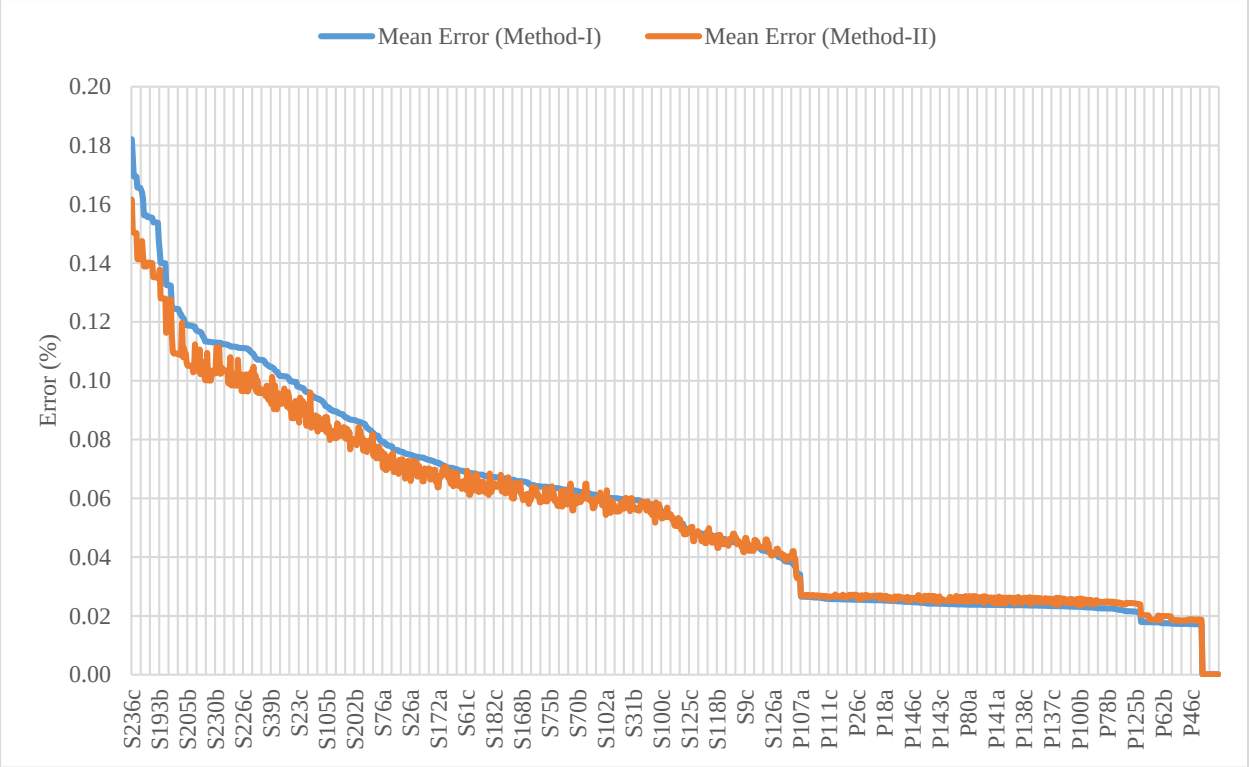

Figure 6.12: Comparison of Method-I and Method-II

The results obtained by the two methods are presented in Figure 6.12. One interesting observation is the performance of the algorithm is greatly affected by the location of the nodes. In other words, the nodes distant to the substation have the highest mean error as expected. The effect of the power factor is much more visible for the distant nodes than the closer ones. The Method-II produces better results for the distant nodes and has no significant advantage over the nodes closer to the substation.

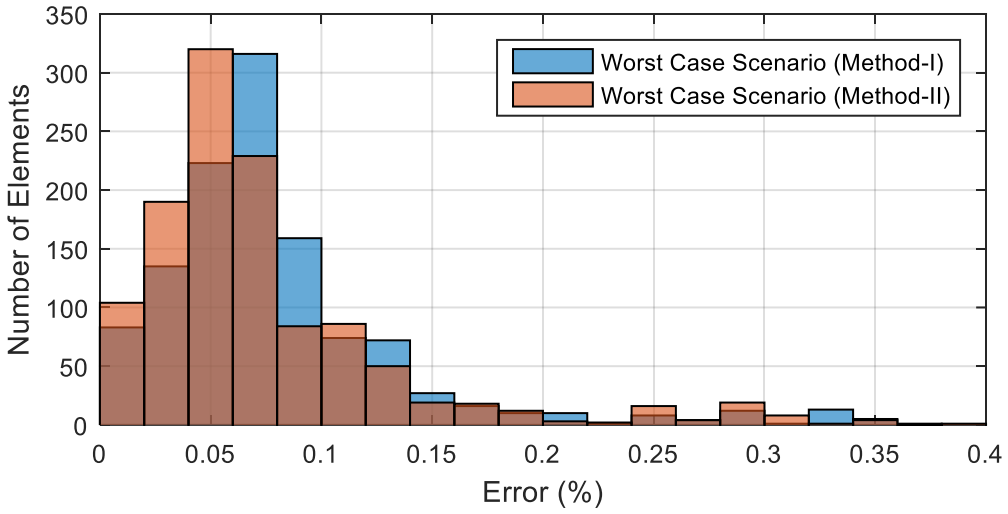

Figure 6.13: Worst Case Scenario for the Study Case-3

In Figure 6.13, the simulation where the maximum deviation of error occurs is presented with a histogram. The average error is 0.08 % and 0.073 % for the Methods I and II, respectively. Even in the worst case scenario, the healing effect of the power factor can be observed.

6.4.4 Study Case-4: Large Scale Distribution Network

This study case is based on the real distribution network of a downtown area in a North American urban city which covers approximately an area of $3.2 km^2$. The network is balanced, meshed and has more than 5500 buses. There are 33 feeders connected to the substation which is connected to 138 kV transmission network. Also, there are two PQ-type generator units each rated at 20 MW and 12 MVAR. The total load demand is 292.96 MW and 152.39 MVAR.

The network modeled in MANA has the properties as tabulated in Table 6.3.

Table 6.3: Network Parameters

Quantity	Number
Nodes (including internal ones)	16674
Loads	4440
Line Segments	6175
Single Phase Transformer Units	1326

In the SE analysis, the voltage is measured at 62 locations with the accuracy of 5 %. The load allocation scheme is used to represent the loads in the SE and the standard deviation for the loads is 20 %.

In Figure 6.14, the histogram shows the mean error comparison for the two methods. The most nodes are in the percentage error band [0.2, 0.22]. The average error of all nodes are 0.276 % and 0.272 % for the Method-I and II, respectively.

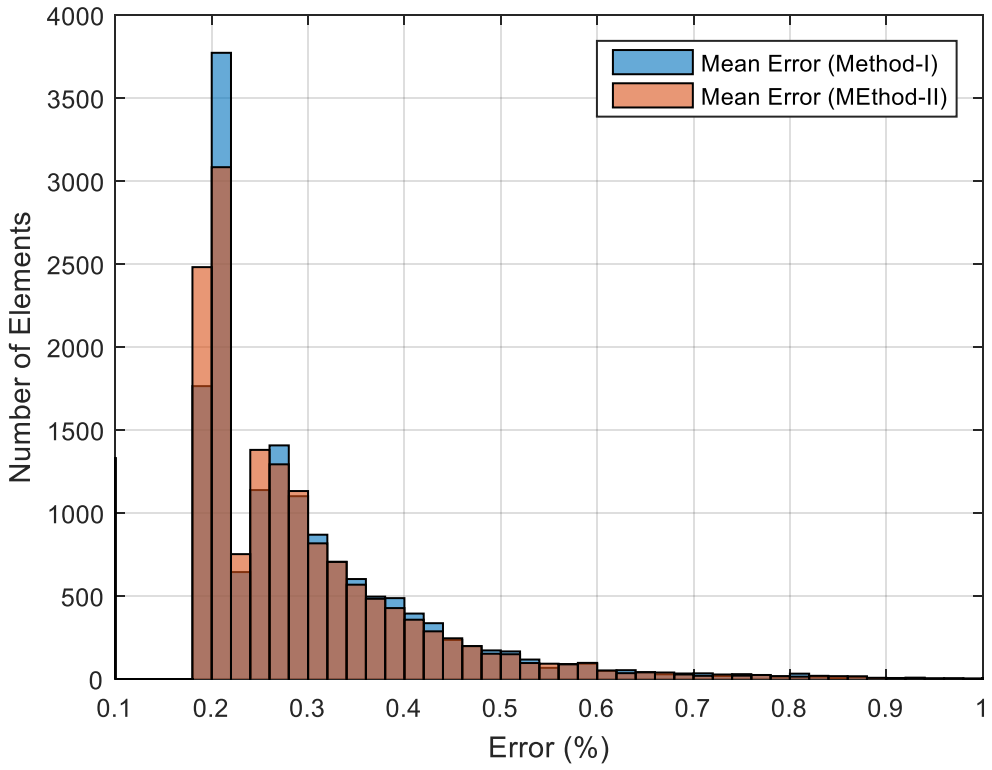

Figure 6.14: Comparison of Mean Error for Method-I and II

The worst case scenario is presented in Figure 6.15. It can be seen from the graph that the power factor has tremendously increased the performance of the SE algorithm. The average error for the Method-I is obtained as 0.661 % while this number is 0.496 % for the Method-II. This study case proves that even for large scale networks the power factor can still affect the outcome of the SE algorithms.

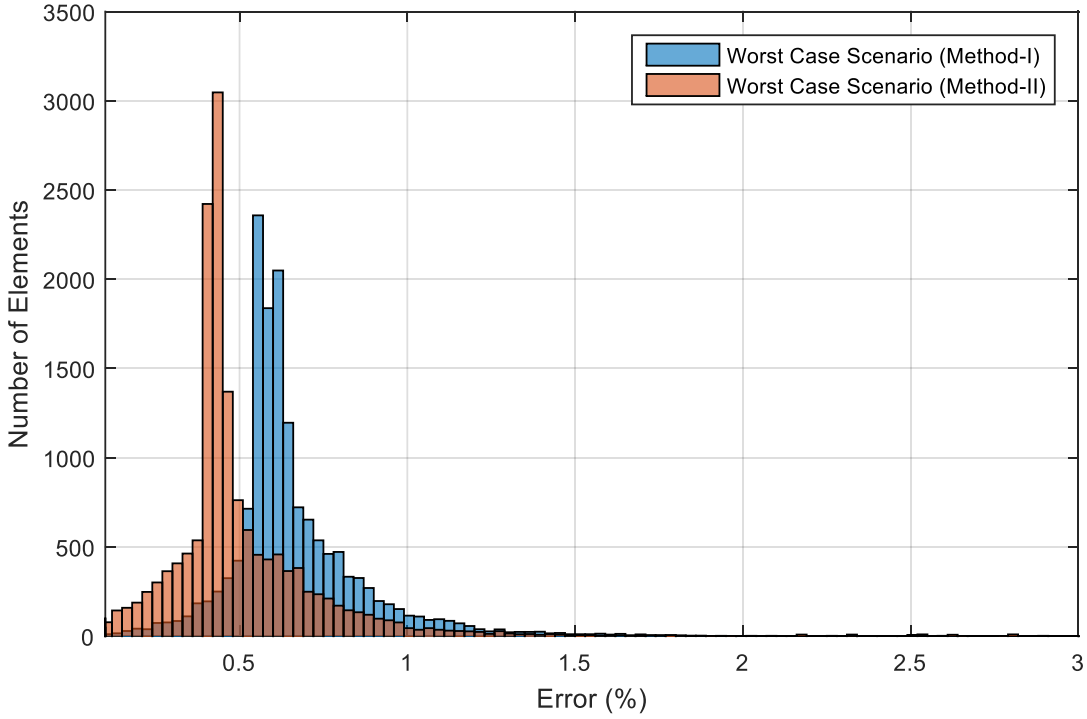

Figure 6.15: Comparison of Worst Case Scenario for Method-I and II

6.5 Summary

In this chapter, the effect of the load power factor on the accuracy of state estimation is investigated. In SE, the load measurements are formed by considering real and reactive powers independently. In other words, the relation between the real and reactive powers for a load is ignored. The hypothesis used in this work is that the power factor measurement has more precision than the power measurements. Therefore, adjusting the reactive power measurement in terms of the power factor will minimize the discrepancy between active and reactive power measurements in SE, and this may improve the accuracy of the SE solution. Four test cases with different sizes are tested with two different approaches, i.e. with independent active and reactive power measurements, and with active and adjusted reactive power measurement using load power factor. It is observed that the effect of the load power factor depends on a number of factors. Firstly, as the size of the network and the number of loads increase, the power factor has more impact on the accuracy of the solution. The difference between the two approaches is the minimum in case of a small network. Secondly, the nodes with different proximity to the substation can have different percentage error. On the overall, the power factor of the loads improves the accuracy of the solution.

CHAPTER 7 DYNAMIC STATE ESTIMATION IN MANA

Static SE ignores the evolution of network state through measurement instants. On the other hand, a dynamic state estimator provides a recursive update of state taking into account the forecast and/or previous measurement instant. There are several studies using Kalman filter based approaches done so far [30, 31, 72]. Through the application of the Kalman filter techniques and the most recent measurement vector, the state vector is first 'predicted' and then, in the data assimilation section, 'corrected'. The first stage is also defined as 'state forecasting' and the second stage is defined as 'state filtering'. In the first stage, the forecast state vector and its covariance are usually evaluated by employing linear exponential smoothing techniques [73]. In the second stage, when the new measurements are available, the state vector is filtered based on a WLS method. After the first stage, it is common to run a routine to detect the possible bad data due to the forecast state variables [30, 74]. The challenge in the application of Kalman Filter techniques for the dynamic SE of distribution systems is the solution of the resulting matrix that is full and large.

In this chapter, two different dynamic state estimation algorithms are presented using the augmented matrix formulation. The first algorithm presented is a non Kalman, WLS technique in which forecasted state are used as measurements. There are certain advantages and disadvantages of this approach. The advantage is that, unlike the Kalman based techniques, the resulting matrix that needs to be solved is not a full matrix, so that the sparse matrix techniques can still be used. This enables the dynamic state estimation of larger scale networks, as in the case of distribution networks. Another advantage is that, the unknowns written as a combination of other unknowns in the MANA formulation need not to be forecasted. The main disadvantage is that the formation of covariance matrix for the forecasts requires a prior statistical analysis and fine-tuning for further precision. In the Kalman based methods, the process of tuning is done automatically. The second proposed algorithm originates from the statistical state estimation and employs Kalman filter techniques in a different way than the classical dynamic state estimators. In this technique Kalman filter and linear exponential techniques if applicable are applied to measurements only in order to smooth them. Afterwards, these measurements are fed to the static SE. This approach is found to be more suitable for real distribution networks.

The outline of this chapter is as follows: first the linear smoothing techniques which are the essential component of dynamic SE are reviewed in detail; then, the generic Extended Kalman

Filter process is given in detail. Afterwards, the first proposed algorithm is explained. Finally, the second algorithm is presented and comparative results are provided for large scale distribution networks.

7.1 State Forecasting

Holt's linear exponential smoothing technique is a simple method used for short-term forecasting [73]. According to Kalekar [75], the main motivation behind the exponential smoothing is to assign exponentially decaying weights as the observation gets older. In other words, the more recent the observation is, the higher weight in forecasting the next state it has. The salient advantage of the exponential smoothing techniques is that it obviates the storage of all historical data of an observed variable, as opposed to moving average techniques. There are several variations of linear exponential smoothing techniques, the mostly used types will be presented in the next sections.

7.1.1 Single Exponential Smoothing (SES)

Single exponential smoothing (also known as simple exponential smoothing) is used for short-range forecasting. In this model, no trend or pattern of growth is assumed. A detailed reading on the derivation of the formula can be found in [73]. The general formula is given as:

$$\tilde{x}_{t+1} = \alpha\, x_t + (1-\alpha)\,\tilde{x}_t \tag{5.1}$$

In (5.1), the variable x_t is the observation at the present time t. The symbol $\sim$ is used to indicate the forecast value. The parameter α reflects the significance of the effect the last observation has on the forecast value. Therefore, (5.1) suggests that when it is used recursively to each consecutive observation in the time series, the new forecast is computed as the weighted average of the last observation and the previous forecast value. If α equals to 1, then the previous observations are ignored entirely; and if α equals to zero, the forecast value will be equal to the previous forecast value, thus all the forecasts will be equal to the initial value of the forecast. Therefore, α must be chosen between 0 and 1 to produce intermediate results.

7.1.2 Adaptive Response Rate Single Exponential Smoothing (ARRSES)

In the SES forecasting method, α is fixed for the whole process. The ARRSES has an obvious advantage over SES in the sense that it allows α to change in a controlled way, as the data pattern

changes over time. This property is useful when dealing with great number of variables to be forecasted. The technique is called adaptive due to the automatic update of the α at each time. The general formulation is given as follows:

$$\tilde{x}_{t+1} = \alpha_t \, x_t + (1-\alpha_t)\,\tilde{x}_t \tag{5.2}$$

Where

$$\alpha_{t+1} = \left| \frac{A_t}{M_t} \right| \tag{5.3}$$

$$A_t = \beta E_t + (1-\beta) A_{t-1} \tag{5.4}$$

$$M_t = \beta |E_t| + (1-\beta) M_{t-1} \tag{5.5}$$

$$E_t = x_t - \tilde{x}_t \tag{5.6}$$

In (5.4), A_t represents the smoothed estimate of forecast error and is found by the weighted summation of A_{t-1} and the most recent forecasting error E_t; M_t is the smoothed estimate of the absolute forecast error; and β is the weight of the error smoothing which can vary between 0 and 1. In terms of behavior, the ARRSES is much more sensitive to the changes in the observations.

7.1.3 Double Exponential Smoothing: Holt's Two Parameter Method (DES)

Holt [76] extended SES to allow the data forecasting with trends. The forecast for Holt's linear DES technique requires two smoothing constants, α and γ (with values between 0 and 1) and three equations:

$$S_{t+1} = \alpha x_t + (1-\alpha)(S_t + b_t) \tag{5.7}$$

$$b_{t+1} = \gamma (S_{t+1} - S_t) + (1-\gamma) b_t \tag{5.8}$$

$$\tilde{x}_{t+1} = S_{t+1} + b_{t+1} \tag{5.9}$$

In (5.7), S_t denotes an estimate of the level of the series at the time t and in (5.8), b_t is called the 'trend' which represents the slope of the series at the time t. The further discussion on the smoothing methods can be obtained in [73].

7.2 Dynamic Mathematical Model

In Kalman filter based algorithms, in order to form the mathematical model for the dynamic behavior of the state vector, a two-stage algorithm is utilized. The first stage is called parameter identification. Let the true state vector at time t be denoted by $\mathbf{x}_t$. The state transition model for a dynamic system is usually expressed with the formula below:

$$\mathbf{x}_{t+1} = \mathbf{F}_t \mathbf{x}_t + \mathbf{G}_t + \mathbf{w}_t \tag{5.10}$$

In (5.10), $\mathbf{F}_t$ is a non-zero diagonal matrix with dimension $(r \times r)$; $\mathbf{G}_t$ is a non-zero vector with dimension $(r \times 1)$; $\mathbf{w}_t$ is a white Gaussian process noise with zero mean due to the state transition function with the covariance matrix $\mathbf{Q}_t$, and the subscript t is the time index. Now, what is needed is to identify the parameters $\mathbf{F}_t$, $\mathbf{G}_t$ for all forecasting schemes discussed in Chapter 7.1.

7.2.1 Parameter Identification for SES

Let $y_{j,t}$ be the jth element of the true state vector $\mathbf{x}_t$. The SES (5.1) gives the forecast value for $y_{j,t}$ as follows:

$$\tilde{x}_{j,t+1} = \alpha_j x_{j,t} + (1-\alpha_j)\tilde{x}_{j,t} \tag{5.11}$$

where

$$x_{j,t} = \mathbf{x}_t(j) \tag{5.12}$$

In (5.11), α_j is the weight associated with $x_{j,t}$. By using (5.11), the entries of $\mathbf{F}_t$, $\mathbf{G}_t$ are found as:

$$\mathbf{F}_t(j,j) = \alpha_j \tag{5.13}$$

$$\mathbf{G}_t(j,1) = (1-\alpha_j)\tilde{x}_{j,t} \tag{5.14}$$

7.2.2 Parameter Identification for ARRSES

The formulation of the case of ARRSES is similar to the one of SES. By using (5.2), the forecast value of an unknown is given by;

$$\tilde{x}_{j,t+1} = \alpha_{j,t} x_{j,t} + \left(1-\alpha_{j,t}\right)\tilde{x}_{j,t} \tag{5.15}$$

In (5.15), the weighting factors are time-dependent. The entries of $\mathbf{F}_t$ and $\mathbf{G}_t$ are found as;

$$\mathbf{F}_t\left(j, j\right) = \alpha_{j,t} \tag{5.16}$$

$$\mathbf{G}_t\left(j,1\right) = \left(1-\alpha_{j,t}\right)\tilde{x}_{j,t} \tag{5.17}$$

7.2.3 Parameter Identification for DES

The forecast value for $x_{j,t}$ is given by the formulae in (5.7)-(5.9):

$$\tilde{x}_{j,t+1} = S_{j,t+1} + b_{j,t+1} \tag{5.18}$$

By replacing $S_{j,t}$ and $b_{j,t}$ with (5.7) and (5.8), the forecast $\tilde{y}_{j,t+1}$ can be expressed as:

$$\begin{aligned} \tilde{x}_{j,t+1} \quad &= \alpha_j x_{j,t} + \left(1-\alpha_j\right)\left(S_{j,t} + b_{j,t}\right) \\ &\quad + \gamma_j\left(\alpha_j x_{j,t} + \left(1-\alpha_j\right)\left(S_{j,t} + b_{j,t}\right) - S_{j,t}\right) \\ &\quad + \left(1-\gamma_j\right) b_{j,t} \end{aligned} \tag{5.19}$$

The term $\left(S_{j,t} + b_{j,t}\right)$ in fact gives the previous estimate for $x_{j,t}$:

$$\tilde{x}_{j,t} = S_{j,t} + b_{j,t} \tag{5.20}$$

By putting (5.20) into (5.19);

$$\begin{aligned} \tilde{x}_{j,t+1} \quad &= \alpha_j x_{j,t} + \left(1-\alpha_j\right)\tilde{x}_{j,t} \\ &\quad + \gamma_j\left(\alpha_j x_{j,t} + \left(1-\alpha_j\right)\tilde{x}_{j,t} - S_{j,t}\right) \\ &\quad + \left(1-\gamma_j\right) b_{j,t} \\ &= \alpha_j\left(1+\gamma_j\right) x_{j,t} + \left(1+\gamma_j\right)\left(1-\alpha_j\right)\tilde{x}_{j,t} \\ &\quad - \gamma_j S_{j,t} + \left(1-\gamma_j\right) b_{j,t} \end{aligned} \tag{5.21}$$

Thus, the terms of $\mathbf{F}_t$ and $\mathbf{G}_t$ given by (5.21);

$$\mathbf{F}_t\left(j, j\right) = \alpha_j\left(1+\gamma_j\right) \tag{5.22}$$

$$\mathbf{G}_t(j,1) = (1+\gamma_j)(1-\alpha_j)\tilde{x}_{j,t} - \gamma_j S_{j,t} + (1-\gamma_j) b_{j,t} \tag{5.23}$$

7.3 Extended Kalman Filter Algorithm

In 1960, R. E. Kalman [77] published his revolutionary technique which recursively solved the discrete data linear fitting problem. Since then, the Kalman filter has seen a tremendous interest in different disciplines; including power systems. Bishop [78] defines Kalman filter as a set of mathematical equations which provides a recursive means to estimate the state of a system, in such a way that the mean squared error is minimized. The Kalman filter can consider past, present, as well as future states; it can do so even when the precise nature of the modeled system is unknown which allows the use of forecast techniques. An iterative version of the Kalman filter (known as Iterated Extended Kalman Filter –IEKF) was also developed to hold the nonlinear measurements. In [79], Lefebvre explains the detailed theoretical analysis of the IEKF. Here, the derivation of the IEKF itself will be omitted.

For a state vector $\hat{\mathbf{x}}_t$ denoting the optimal (true) state at time t; the IEKF algorithm can be summarized in a nutshell as in Figure 7.1.

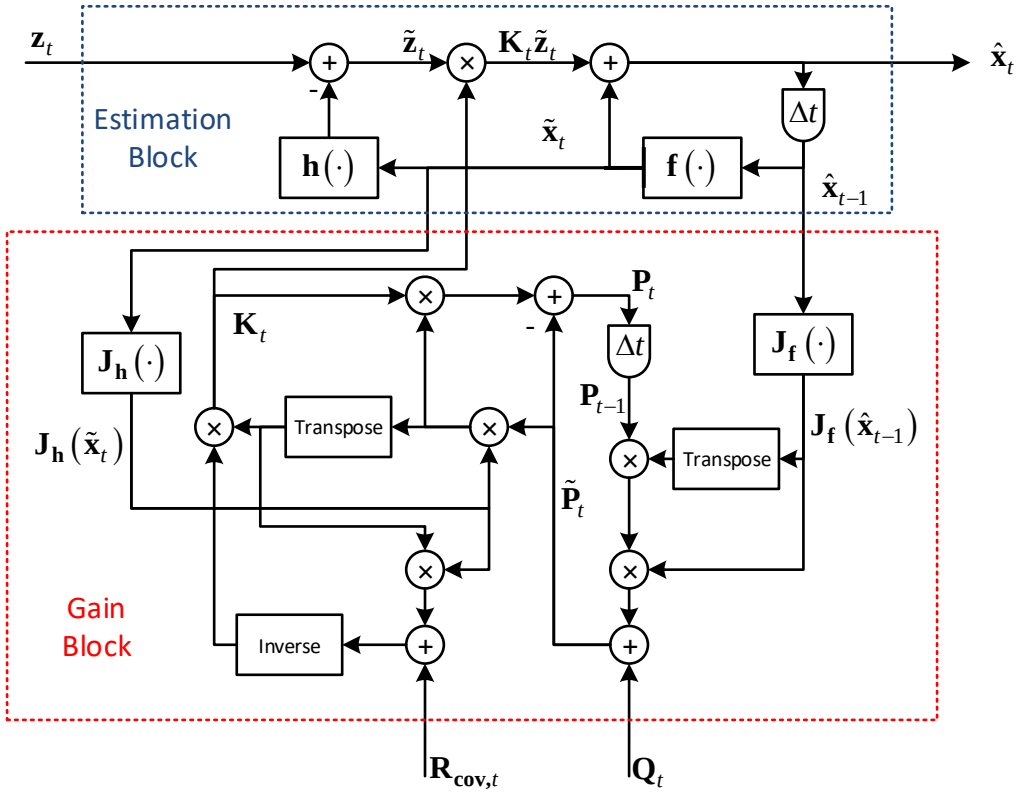

Figure 7.1: The Flow Chart of Iterated Extended Kalman Filter

In Figure 7.1, in the estimation block, the block $\mathbf{f}(\cdot)$ represents the state transition function which creates the forecast state vector and the block $\mathbf{h}(\cdot)$ is the measurement function. In the gain block, $\mathbf{K}_\mathbf{k}$ is called Kalman gain; $\mathbf{R}_{\mathbf{cov},t}$ is the covariance matrix of the measurements at time t; $\mathbf{P}_t$ is the forecast error covariance; and $\mathbf{Q}_t$ is the error covariance matrix due to the state transition function. The IEKF offers a two stage solution: in the estimation block, the state vector at the next time instant is 'predicted'; and in the gain block, the 'predicted' state vector is filtered with the latest arriving measurements.

The gain block is the iterated part where two successive state vectors are close enough. The overall algorithm of IEKF is presented in Figure 7.2.

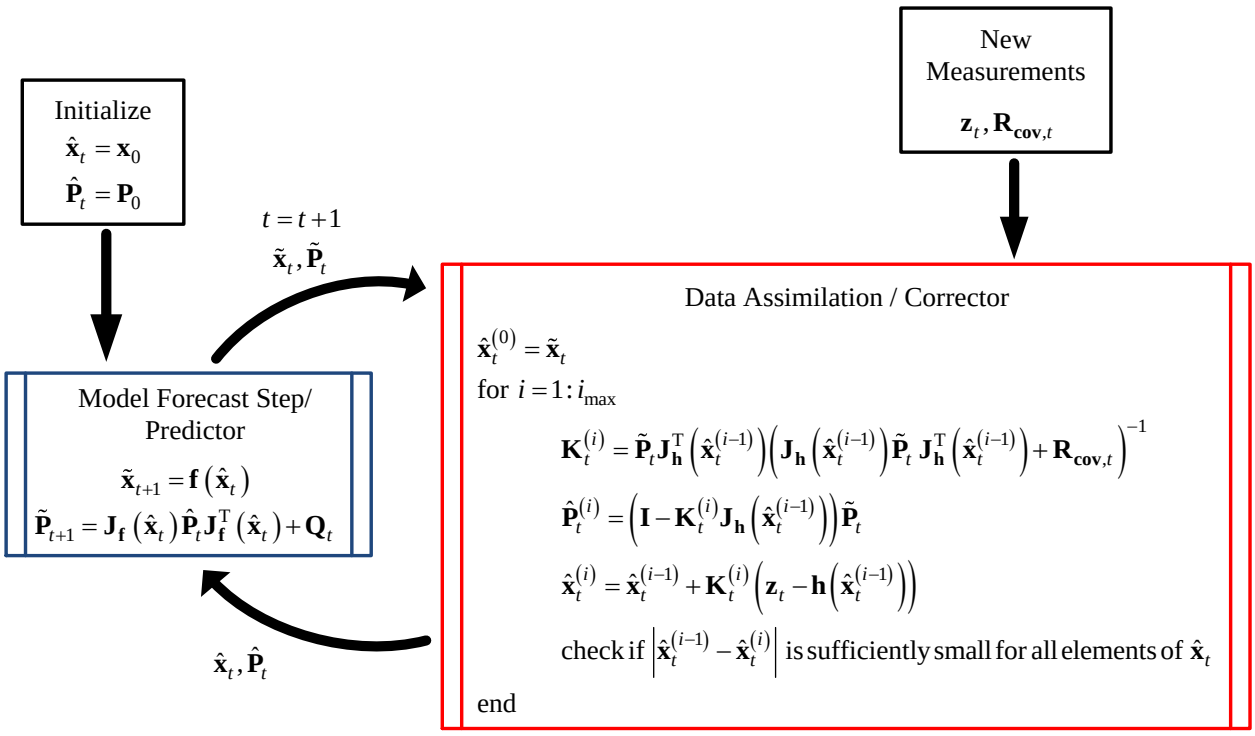

Figure 7.2: The Overall Algorithm of Iterated Extended Kalman Filter

7.4 Objective Function of Dynamic State Estimation

The objective function for the dynamic state estimation is formulated as follows;

$$L\left(\mathbf{x}_t\right) = \min\left(\left(\mathbf{z}_t - \mathbf{h}\left(\mathbf{x}_t\right)\right)^{\mathrm{T}}\mathbf{R}_{\mathbf{cov}}^{-1}\left(\mathbf{z}_t - \mathbf{h}\left(\mathbf{x}_t\right)\right) + \left(\tilde{\mathbf{x}}_t - \mathbf{x}_t\right)^{\mathrm{T}}\mathbf{P}_t^{-1}\left(\tilde{\mathbf{x}}_t - \mathbf{x}_t\right)\right) \quad s.t.\ \mathbf{c}\left(\mathbf{x}_t\right) = \mathbf{0} \tag{5.24}$$

The vector $\hat{\mathbf{x}}_t$ is the optimal solution which minimizes (5.24).

In [30], this problem is solved by the IEKF algorithm presented in Figure 7.2 together with the use of DES as state transition function. However, in this approach three problems may appear.

First, modelling the constraints is an important problem. Most often the time, they are modeled in the measurement vector $\mathbf{h}(\cdot)$ as highly accurate measurements. This is due to the fact that Kalman filter was not originally designed for systems with constraint equations.

Secondly, in the algorithm presented in Figure 7.2, all the elements of the state vector must be predicted individually. However, thanks to the constraint equations available, most of the state

variables can be expressed as a function of other variables. Therefore, it is not necessary to forecast all variables and include them in $\tilde{\mathbf{x}}_t$.

Finally, a major issue with Kalman based algorithms is that they require the factorization of a full matrix.

$$\mathbf{K}_t^{(i)} = \tilde{\mathbf{P}}_t \mathbf{J}_\mathbf{h}^\mathrm{T}\left(\hat{\mathbf{x}}_t^{(i-1)}\right)\left(\mathbf{J}_\mathbf{h}\left(\hat{\mathbf{x}}_t^{(i-1)}\right)\tilde{\mathbf{P}}_t\,\mathbf{J}_\mathbf{h}^\mathrm{T}\left(\hat{\mathbf{x}}_t^{(i-1)}\right)+\mathbf{R}_{\mathbf{cov},t}\right)^{-1} \tag{5.25}$$

At the very beginning, $\tilde{\mathbf{P}}_t$ is a diagonal matrix. However, at the end of the first time instant, the matrix $\hat{\mathbf{P}}_t$ becomes 100 % full, thus in the time instant $\tilde{\mathbf{P}}_t$ becomes full as well. Thus, starting from the second time instant, a full matrix solution is needed.

7.5 Proposed Method I: Hachtel Based Dynamic State Estimator

As mentioned in CHAPTER 6, the Hachtel formulation has shown great stability for the static state estimator when employed in MANA approach [60]. The objective function for the static case is similar to (5.24) except the fact that it does not account for the forecast variables. Thus, (5.24) can be formulated as;

$$\begin{gathered} L\left(\mathbf{x}_t\right)=\min\left(\mathbf{y}^\mathrm{T}\begin{bmatrix}\mathbf{R}_{\mathbf{cov}}^{-1} & \mathbf{0}\\ \mathbf{0} & \mathbf{P}_t^{-1}\end{bmatrix}\mathbf{y}\right)\\ s.t.\ \mathbf{c}\left(\mathbf{x}_t\right)=\mathbf{0}\\ where\ \mathbf{y}=\begin{bmatrix}\mathbf{z}_t-\mathbf{h}\left(\mathbf{x}_t\right)\\ \tilde{\mathbf{x}}_t-\mathbf{x}_t\end{bmatrix}\end{gathered} \tag{5.26}$$

The formulation in (5.26) can easily be constructed in Hachtel approach. In (5.26), due to the existence of the constraints $\mathbf{c}(\cdot)$, all elements of $\mathbf{x}_t$ are not needed to be forecast. As a matter of fact, if the node voltages are predicted; other MANA related unknown state variables, such as transformer current, switch current, are determined through the device equations.

The Hachtel formulation presented in CHAPTER 6 has the form as follows;

$$\begin{bmatrix}\mathbf{R}_{\mathbf{cov}} & \mathbf{J}_\mathbf{h}\left(\mathbf{x}\right) & \mathbf{0}\\ \mathbf{J}_\mathbf{h}^\mathrm{T}\left(\mathbf{x}\right) & \mathbf{0} & \mathbf{J}_\mathbf{c}^\mathrm{T}\left(\mathbf{x}\right)\\ \mathbf{0} & \mathbf{J}_\mathbf{c}\left(\mathbf{x}\right) & \mathbf{0}\end{bmatrix}^{(i)}\begin{bmatrix}\mathbf{r}\\ \Delta\mathbf{x}\\ \boldsymbol{\lambda}\end{bmatrix}^{(i)}=\begin{bmatrix}\mathbf{z}-\mathbf{h}\left(\mathbf{x}\right)\\ \mathbf{0}\\ -\mathbf{c}\left(\mathbf{x}\right)\end{bmatrix}^{(i)} \tag{5.27}$$

(5.27) is designed for the static SE algorithm; thus it does not account for the state transition. The objective function (5.26) also accounts for the forecast unknowns. Therefore, it is possible to modify the Hachtel formulation as follows:

$$\begin{bmatrix} \mathbf{R}_{cov} & \mathbf{0} & \mathbf{J}_{h} & \mathbf{0} \\ \mathbf{0} & \tilde{\mathbf{P}} & \mathbf{I}_{F} & \mathbf{0} \\ \mathbf{J}_{h}^{T} & \mathbf{I}_{F}^{T} & \mathbf{0} & \mathbf{J}_{C}^{T} \\ \mathbf{0} & \mathbf{0} & \mathbf{J}_{C} & \mathbf{0} \end{bmatrix}^{(i)} \begin{bmatrix} \mathbf{r}_{h} \\ \mathbf{r}_{F} \\ \Delta\hat{\mathbf{x}} \\ \boldsymbol{\lambda} \end{bmatrix}^{(i)} = \begin{bmatrix} \mathbf{z}-\mathbf{h}(\hat{\mathbf{x}}) \\ \tilde{\mathbf{x}}_{F}-\hat{\mathbf{x}}_{F} \\ \mathbf{0} \\ -\mathbf{c}(\hat{\mathbf{x}}) \end{bmatrix}^{(i)} \tag{5.28}$$

$\tilde{\mathbf{P}}$: The forecast covariance matrix for $\tilde{\mathbf{x}}_{F}$

$\mathbf{I}_{F}$: The Jacobian matrix of forecast values

The dynamic SE algorithm in Figure 7.2 can be modified as follows.

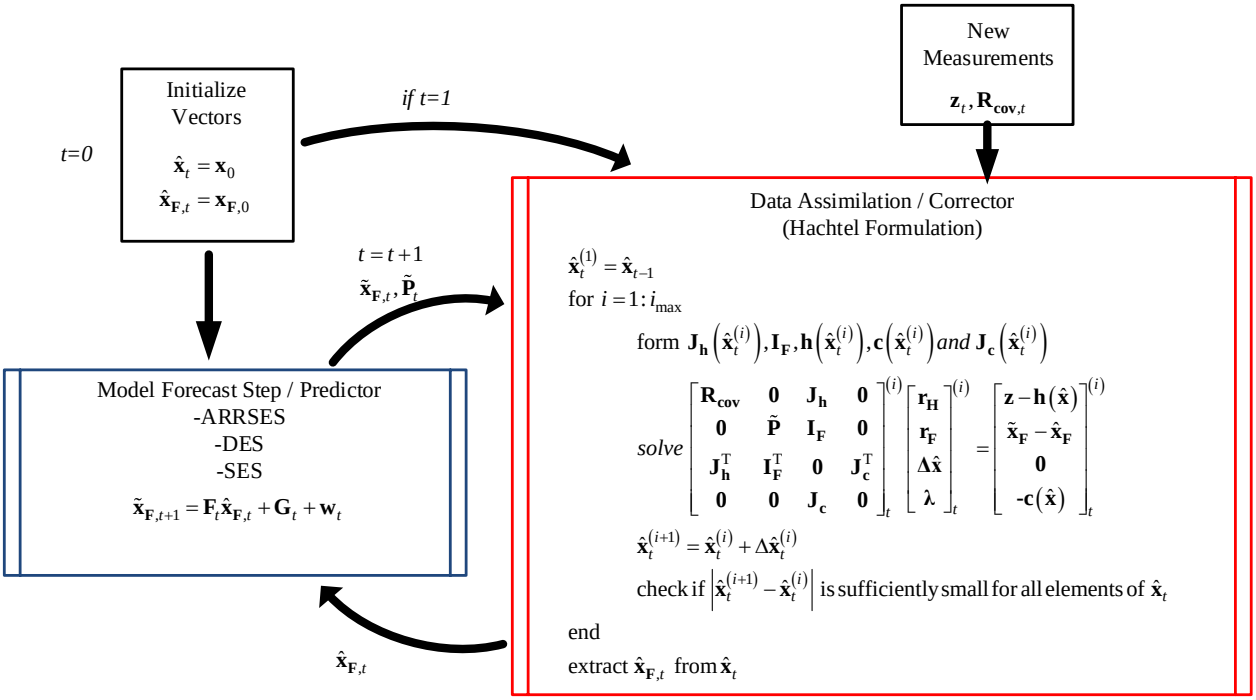

Figure 7.3: Hachtel based Dynamic State Estimator

Since forecasts are also measurements, the Jacobian matrix $\mathbf{I}_{F}$ for the forecasts, which is formed by taking the partial derivatives of $\tilde{\mathbf{x}}$ with respect to the vector of unknowns $\hat{\mathbf{x}}$; thus, composed of 1's and 0's only.

To have a smooth start, it is assumed that the initial state of the system is well known. Therefore, when $t = 0$, the forecast vector $\tilde{\mathbf{x}}_{\mathbf{F},0}$ and true state vector $\hat{\mathbf{x}}_0$ are obtained by considering the load flow solution of the network. The forecast covariance matrix $\tilde{\mathbf{P}}$ can be initialized with identity matrix since the forecast vector is the true state.

In the data assimilation part, with the arrival of new set of measurements, the iterative part starts. The true state vector $\hat{\mathbf{x}}_t$ is initialized by its value at previous time instant $\hat{\mathbf{x}}_{t-1}$. When the data assimilation part ends, the true state vector is fed to the "Model Forecast" (or Predictor) part where the forecast vector is formed for the next time instant. In the Predictor part, any smoothing technique, presented in section 7.1 (such as SES, DES or ARRSES) can be used. Although in the forecast aided SE algorithms [30, 72], the DES is the method of choice; the ARRSES is more suitable technique for the systems with many variables, as the need for tuning of parameters is the minimum. Furthermore, the oscillation of forecasts in case of a sudden change is minimum. Therefore, the ARRSES is the perfect candidate to form the station transition matrix in the Predictor part.

The formation of $\tilde{\mathbf{P}}$ is also done at the Predictor part. $\tilde{\mathbf{P}}$ is formed by three matrices;

$$\tilde{\mathbf{P}} = \mathbf{R}_{\mathbf{F}} + \mathbf{Q}_t + \mathbf{C} \tag{5.29}$$

In (5.29), $\mathbf{Q}_t$ is the process noise which also appears in IEKF in Figure 7.2 due to the forecast formula which is associated with $\mathbf{w}_t$. $\mathbf{R}_{\mathbf{F}}$ is the covariance of $\tilde{\mathbf{x}}$ and indicates the standard deviation of the unknowns. In order to be able to form $\mathbf{R}_{\mathbf{F}}$, a prior statistical analysis needs to be done by considering the static SE algorithm. This process is not shown in the algorithm in Figure 7.3 as it can be considered as a separate process. The last term $\mathbf{C}$ is the constant term matrix. The object of employing $\mathbf{C}$ is to introduce relaxation to the system of equations. The fine tuning of $\tilde{\mathbf{P}}$ is an important step in the algorithm. If it is not well not tuned, the algorithm will converge to a wrong solution.

7.6 Proposed Method II: Semi-Dynamic State Estimator

Although tracking the states is the main objective of DSE algorithms, the increased size of the Jacobian matrix may decrease the speed of the algorithm for extremely big networks (even if the

Jacobian is mostly sparse). Also, global tuning of the state variables might be cumbersome. Furthermore, in distribution networks, it is easier to obtain the pattern of the loads than the state variables. Thus, it is asserted here that tracking measurements instead of state variables has the potential to improve precision and numerical stability of SSE. The SSE algorithm presented in CHAPTER 6 can be extended for the DSE studies by featuring the load pattern as well. An approximate load pattern can be used to employ the KF techniques.

In this method, the measurements are predicted by means of KF where it is assumed that the load pattern is known. It must be noted that the state variables of the network are not directly used in the KF algorithm, but the measurements themselves form another state vector. Let $\breve{\mathbf{x}}$ denote the state vector composed of the measurements:

$$\mathbf{z} = \breve{\mathbf{x}} + \mathbf{e} \tag{5.30}$$

In (5.30), all measurements are independent and represented as a variable in $\breve{\mathbf{x}}$. (5.30) can be rewritten as:

$$\begin{bmatrix} z_1 \\ z_2 \\ \vdots \\ z_m \end{bmatrix} = \begin{bmatrix} \breve{x}_1 \\ \breve{x}_2 \\ \vdots \\ \breve{x}_m \end{bmatrix} + \begin{bmatrix} e_1 \\ e_2 \\ \vdots \\ e_3 \end{bmatrix} \tag{5.31}$$

(5.31) implies that since the measurements are represented by a single unknown, the Jacobian matrix of the measurements equals to identity matrix. Therefore, there is no more need for inverting a full matrix. By doing so, any number of measurements can be tracked in KF algorithm without performing costly calculations. Concerning the measurements of which the patterns are not known, the smoothing equations are used to extract their trend. The overall algorithm is summarized in Figure 7.4.

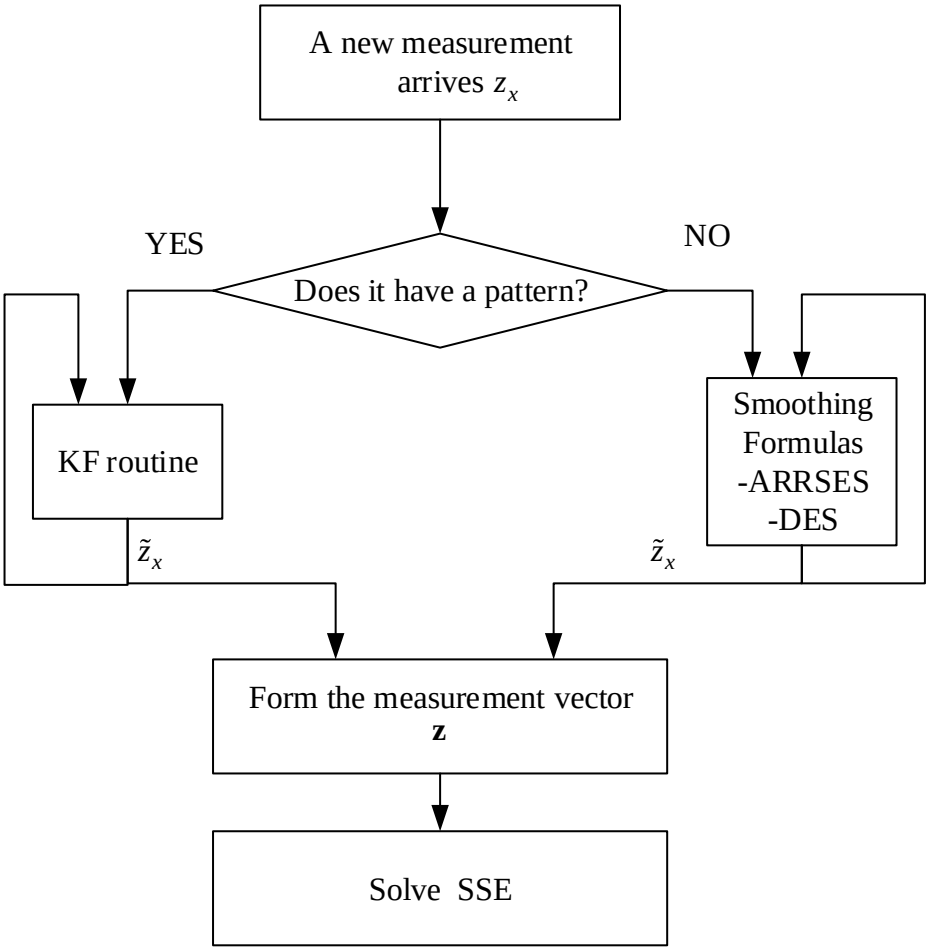

Figure 7.4: Semi-Dynamic State Estimation

7.7 Measurement Test

One aspect related with the dynamic SE algorithms is their reaction to the sudden changes in the network. The algorithms must detect the abrupt changes in the network; otherwise it is very likely that the previous pattern will be followed by the algorithm. In order to avoid this phenomenon, the measurements must be compared with the estimated ones at the end of each time step to confirm that the obtained result is valid. Let us consider the j th measurement with the variance of σ_j^2. By using (4.2), the residual for this measurement r_j can be written as;

$$r_j = z_j - h_j\left(\hat{\mathbf{x}}_t\right) \tag{5.32}$$

If a measurement is ‘good’, then it should satisfy the inequality below;

$$r_j^2 < \left(3\sigma_j\right)^2 \tag{5.33}$$

According to Figure 6.1, the probability of satisfying (5.33) is 99.8 % for a single measurement. Therefore, the ratio of the 'good' measurements which satisfy (5.33) to the total number of measurements must be at least 99.8 %. Thus, the measurement test can be defined as follows;

$$\begin{aligned} &N_{bad} = 0 \\ &for \;\; j = 1 : N_{meas} \\ &\qquad r_j = z_j - h_j\left(\hat{\mathbf{x}}_t\right) \\ &\qquad if \; r_j^2 > \left(3\sigma_j\right)^2 \\ &\qquad\qquad N_{uns} = N_{uns} + 1 \\ &\qquad end \\ &end \end{aligned} \tag{5.34}$$

where

N_{meas} : The total number of all measurements

N_{bad} : The number of measurements which are not satisfied (i.e., 'bad' measurement)

Theoretically, N_{bad} cannot exceed 0.2 % of N_{meas}. However, in order to avoid false triggering, this limit can be set to a bit upper level such as 5 % at the expense of sensitivity. Thus, based on (5.34) , if the number of bad measurements is greater than 5 %, it means there is a sudden change in the system. In that case, the entries of the covariance matrix $\tilde{\mathbf{P}}$ are inflated for the next 2 time steps to re adjust the unknowns to the new operation point. In case of a sudden change, the static SE algorithm with the most recent measurements can be performed and the results obtained by the static solver can be fed to the Predictor block to form the next forecast vector as the observed quantities.

7.8 Study Cases

The proposed dynamic and semi-dynamic estimators are tested on a standard IEEE test network and satisfactory results are obtained in terms of deviation from the true state. The solvers are tested for different scenarios to better evaluate the performance and quite satisfactory results are obtained. Also, the semi-dynamic state estimation is applied on a very large scale real distribution network.

The results obtained by the two algorithms are compared with the results of the static SE. To have a healthy comparison, the two are presented in the figure with the load flow results. And to evaluate the performance of the algorithm, two criteria are investigated in the simulations:

- The peak difference of the node j compared to the load flow results:

$$Criteria-1: \quad \begin{cases} \max\left(\left|\dfrac{\bar{\mathbf{V}}_{\mathbf{LF}}(j,t)-\bar{\mathbf{V}}_{\mathbf{SSE}}(j,t)}{\bar{\mathbf{V}}_{\mathbf{LF}}(j,t)}\right|\times 100\right) & \forall t=1,2,3,...t_{\max} \\ \max\left(\left|\dfrac{\bar{\mathbf{V}}_{\mathbf{LF}}(j,t)-\bar{\mathbf{V}}_{\mathbf{DSE}}(j,t)}{\bar{\mathbf{V}}_{\mathbf{LF}}(j,t)}\right|\times 100\right) & \forall t=1,2,3,...t_{\max} \end{cases} \tag{5.35}$$

where j is the index of the chosen node, t is the time index. The matrices $\bar{\mathbf{V}}_{\mathbf{LF}}$, $\bar{\mathbf{V}}_{\mathbf{SSE}}$, and $\bar{\mathbf{V}}_{\mathbf{DSE}}$ are formed by the voltage phasors for all nodes obtained at each time instant for the load-flow, static SE, and dynamic SE. (5.35) indicates the percentage maximum error obtained for the node chosen at all time instants.

- The mean difference of the node j compared to the load flow results:

$$Criteria-2: \quad \begin{cases} \dfrac{1}{t_{\max}}\displaystyle\sum_{t=1}^{t_{\max}}\left|\dfrac{\bar{\mathbf{V}}_{\mathbf{LF}}(j,t)-\bar{\mathbf{V}}_{\mathbf{SSE}}(j,t)}{\bar{\mathbf{V}}_{\mathbf{LF}}(j,t)}\right|\times 100 & \forall t=1,2,3,...t_{\max} \\ \dfrac{1}{t_{\max}}\displaystyle\sum_{t=1}^{t_{\max}}\left|\dfrac{\bar{\mathbf{V}}_{\mathbf{LF}}(j,t)-\bar{\mathbf{V}}_{\mathbf{DSE}}(j,t)}{\bar{\mathbf{V}}_{\mathbf{LF}}(j,t)}\right|\times 100 & \forall t=1,2,3,...t_{\max} \end{cases} \tag{5.36}$$

(5.36) indicates the percentage mean error obtained for the node chosen at all time instants.

7.8.1 Study Case-1: IEEE 342 Node Distribution Network

This is the same network described in the Chapter 6.4.3. As aforementioned, this is heavily meshed network with several feeders connected in parallel. The parameters related to the network were presented in the Chapter 6.4.3.

7.8.1.1 Scenario-1:

In the first scenario, fast variation of the loads is investigated. In Figure 7.5, the loading level of the network in percentage is shown. In the first 50-time step, the loading of the network is reduced

from 100 % to 50 % gradually. During the next 50-time step, the network remains constant at 50 % loading. And finally in the last 50-time step, the loading increases from 50 % to 100 %.

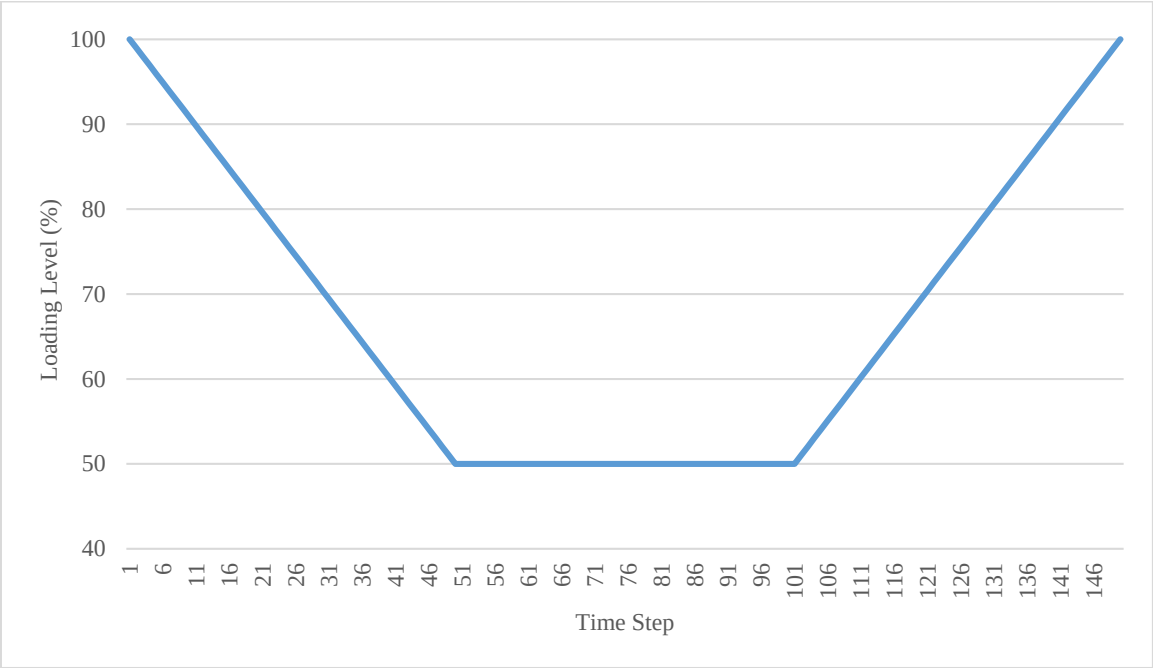

Figure 7.5: Load Profile for the Scenario-I

The standard deviation for the load real and reactive powers is chosen as 30 %. The voltage magnitude measurements are assumed to have a standard deviation of 10 %. To summarize, the measurements are assumed to be too noisy. The voltage magnitude is measured at 20 different buses. In the Predictor part, the ARRSES is chosen as the forecast technique. The Table 7.1 shows the comparison of the performance for the dynamic and static algorithms. The variation of the voltage magnitude over time is demonstrated below Figure 7.6-Figure 7.9 for different voltage levels in the network. The results suggest that the dynamic SE algorithm is 10 times better in terms of mean error (Criteria-2). In the graphs from Figure 7.6-Figure 7.9, there exists an offset on the magnitude. This is inherited from the ARRSES forecast technique which has an offset in the forecast.

Table 7.1: Evaluation of Performance

Node Name	Criteria-1		Criteria-2	
	SSE	DSE	SSE	DSE
S188b	4.247	0.304	1.525	0.167
P109a	4.184	0.273	1.513	0.181
S205c	4.108	0.319	1.521	0.166
P3b	4.032	0.282	1.487	0.207

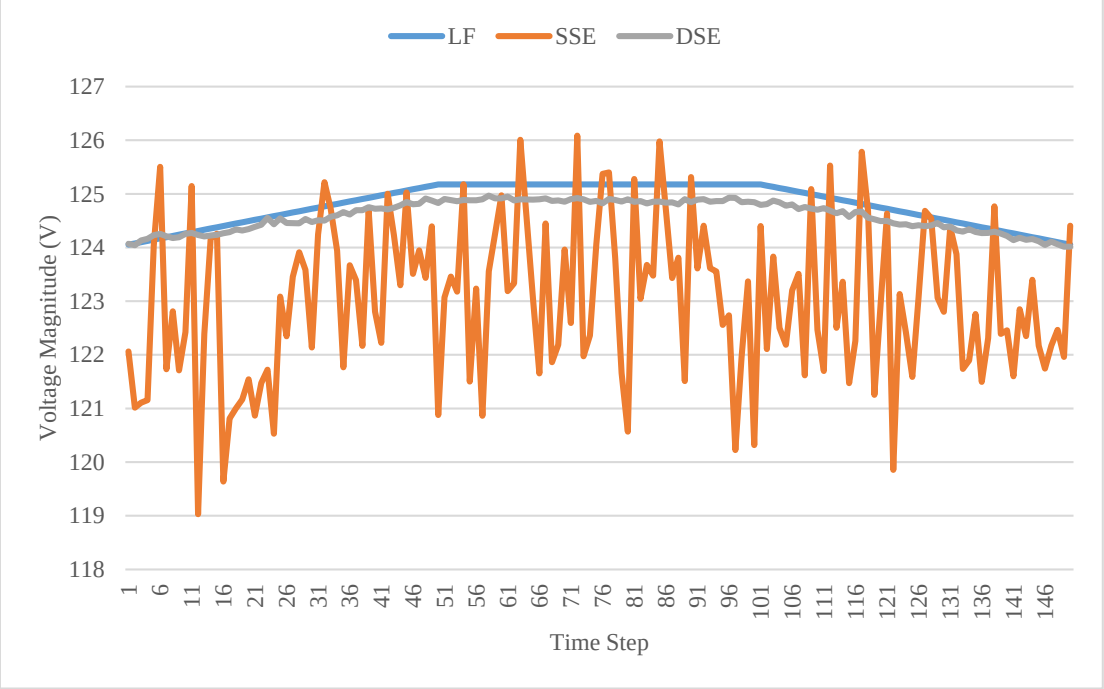

Figure 7.6: Voltage Magnitude at S188b

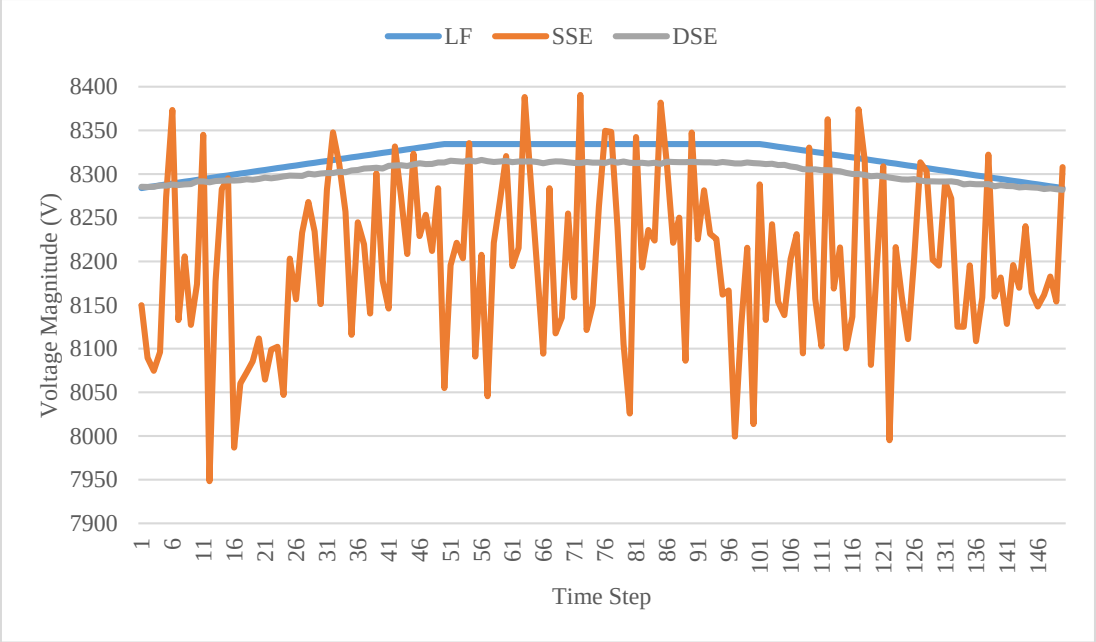

Figure 7.7: Voltage Magnitude at P109a

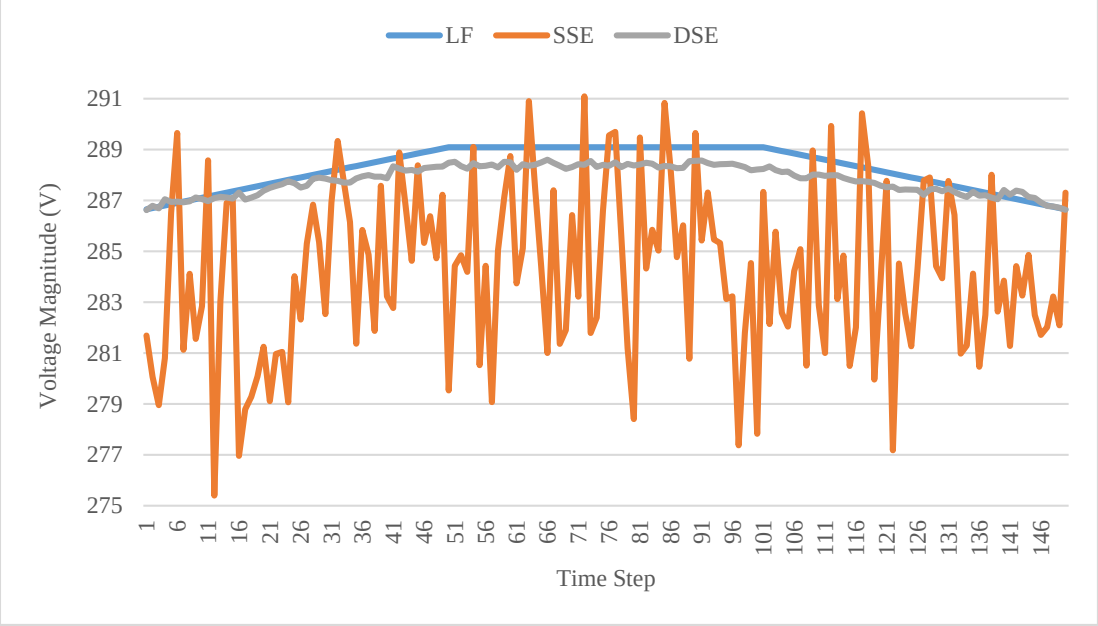

Figure 7.8: Voltage Magnitude at S205c

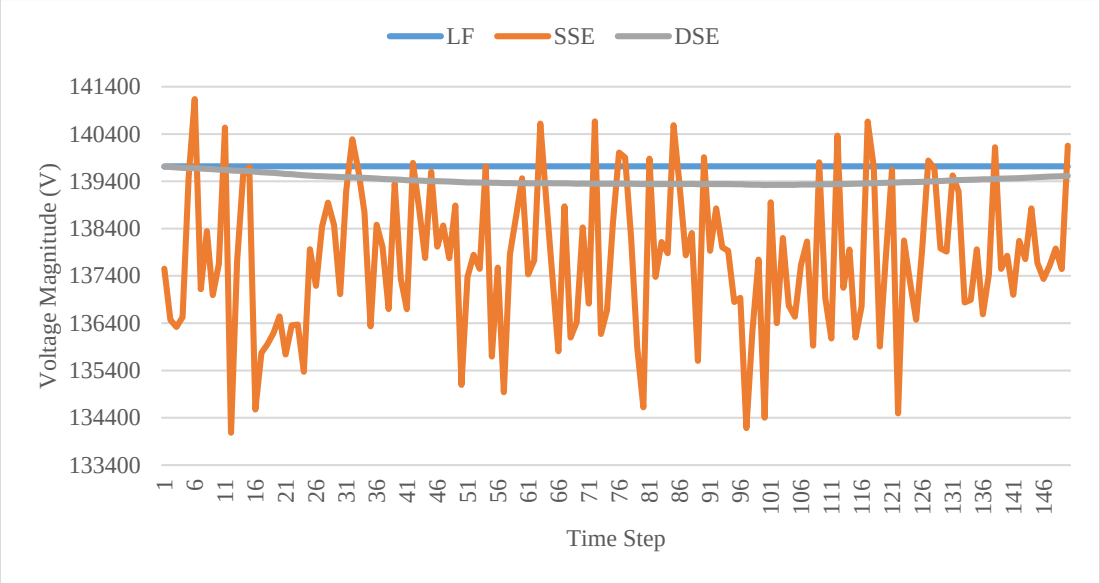

Figure 7.9: Voltage Magnitude at P3b

7.8.1.2 Scenario-2:

In the second scenario, the slow variation of the load profile of the network is investigated. As the loading of the network slowly increases, suddenly it changes to another level. In Figure 7.10, the percentage loading of the network is shown. Initially, the network is loaded at 50 % level. At the 50th time step, suddenly the loading level jumps to 100 % and continues to increase at the same rate until 105 % of loading level. This type of abrupt changes is rare, but still can occur in reality.

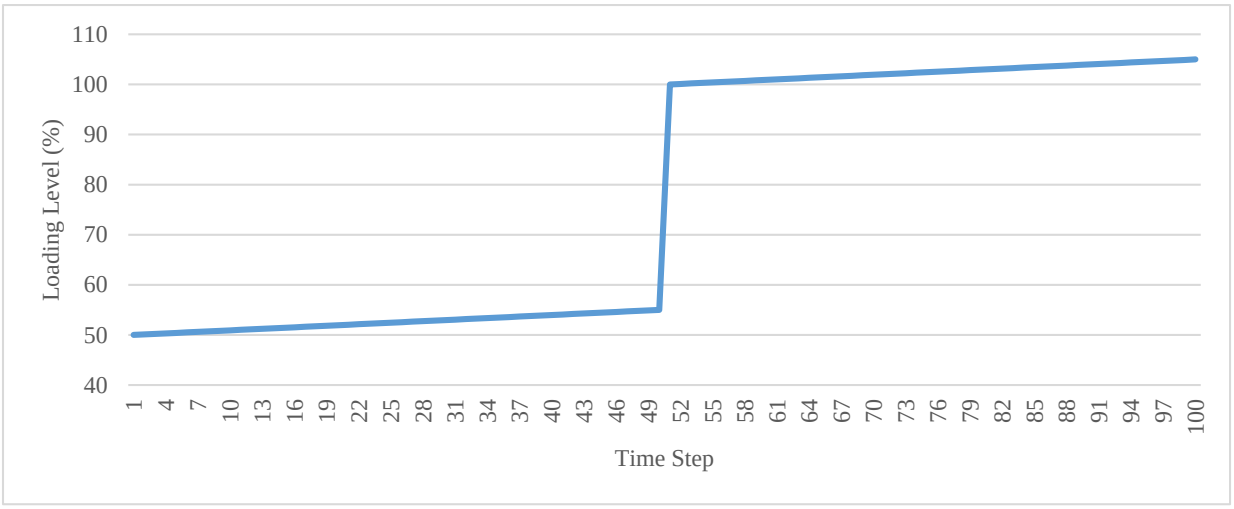

Figure 7.10: Load Profile for the Scenario-II

In this scenario, the voltage and load measurements are kept same as the ones in the Scenario-I. However, in the Predictor part, the forecast technique is chosen as the DES. The results for four nodes from different voltage levels are tabulated in Table 7.2 together with their variation over the time from

Table 7.2: Evaluation of Performance

Node Name	Criteria-1		Criteria-2	
	SSE	DSE	SSE	DSE
S188c	4.680	0.582	1.605	0.048
P109b	4.692	0.357	1.596	0.015
S196a	4.787	0.432	1.608	0.037
P4a	4.507	0.070	1.564	0.040

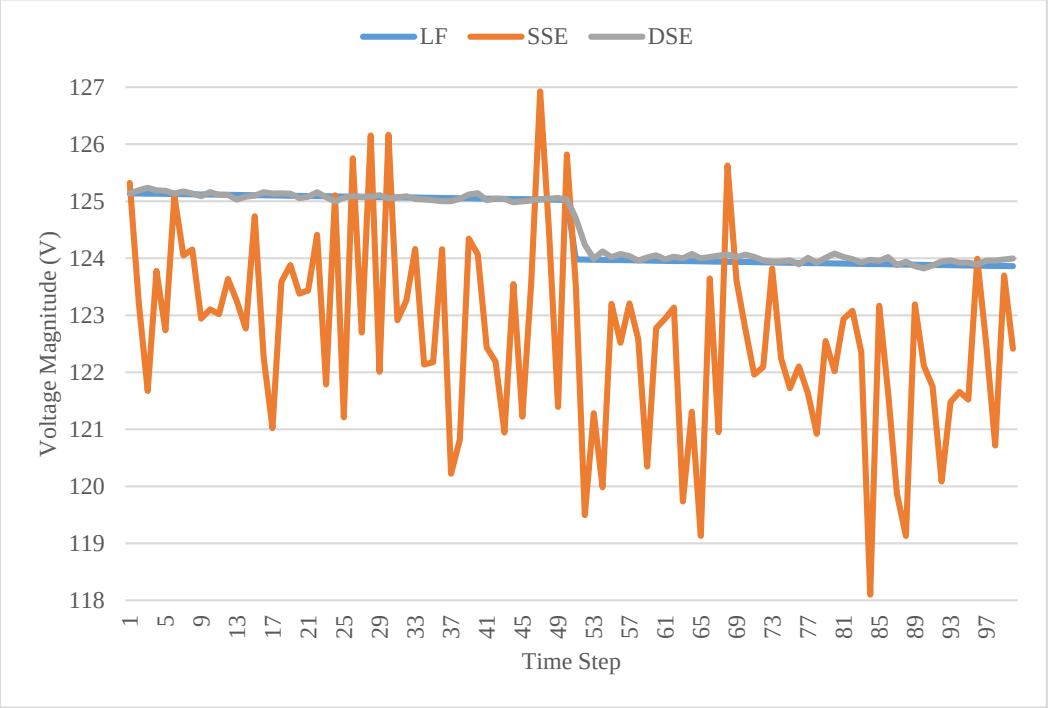

Figure 7.11: Voltage Magnitude at S188c

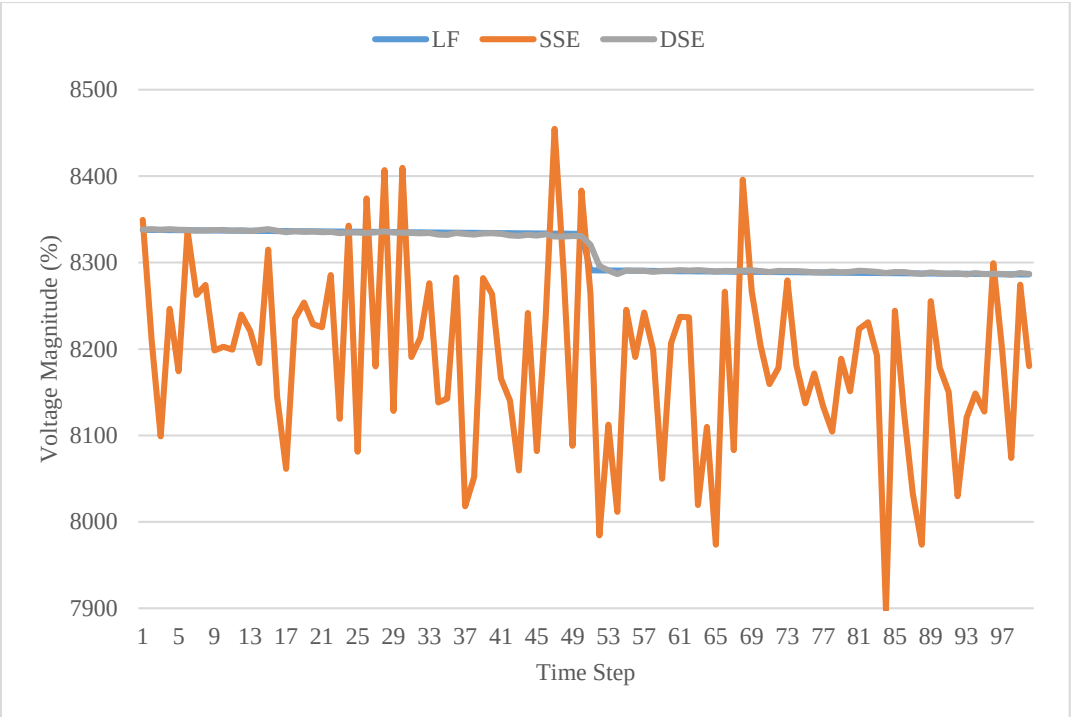

Figure 7.12: Voltage Magnitude at P109b

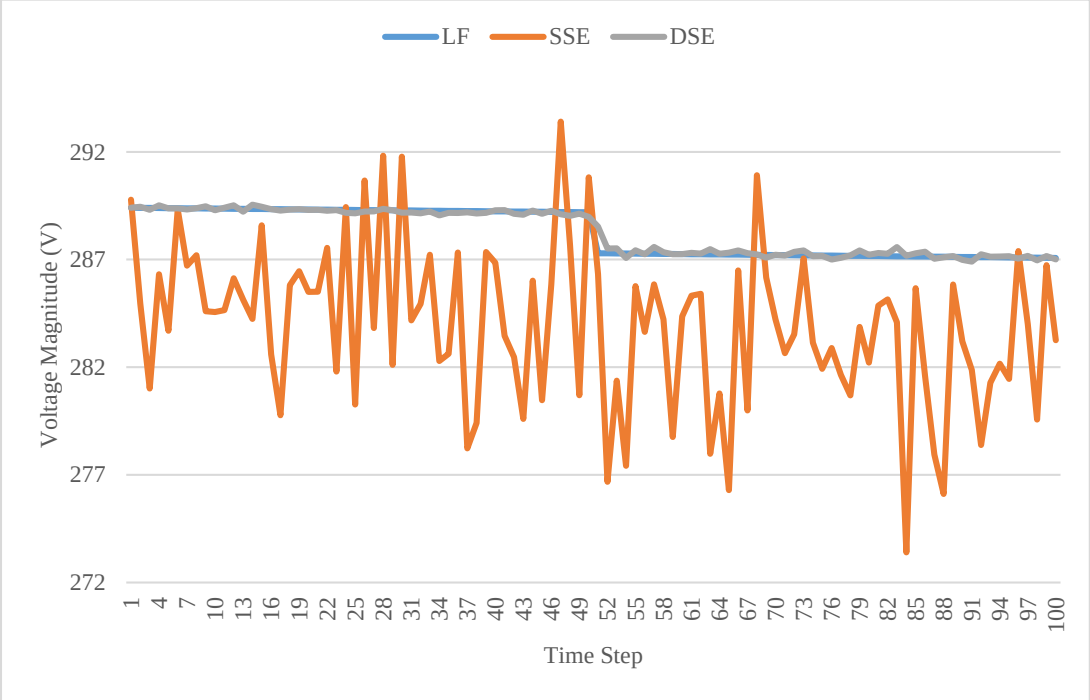

Figure 7.13: Voltage Magnitude at S196a

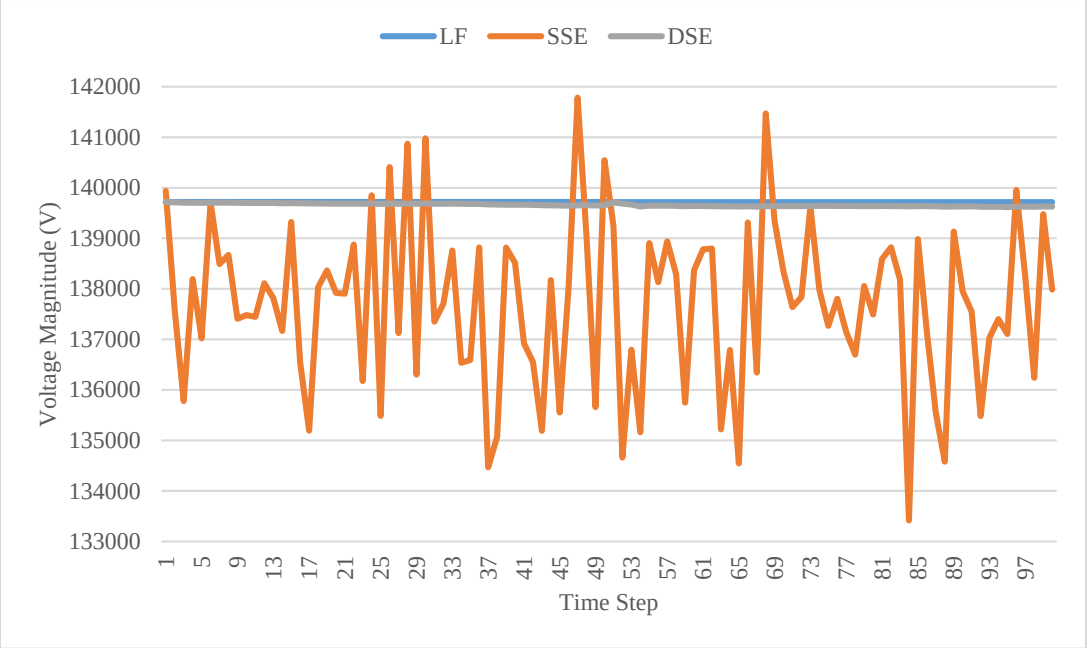

Figure 7.14: Voltage Magnitude at S196a

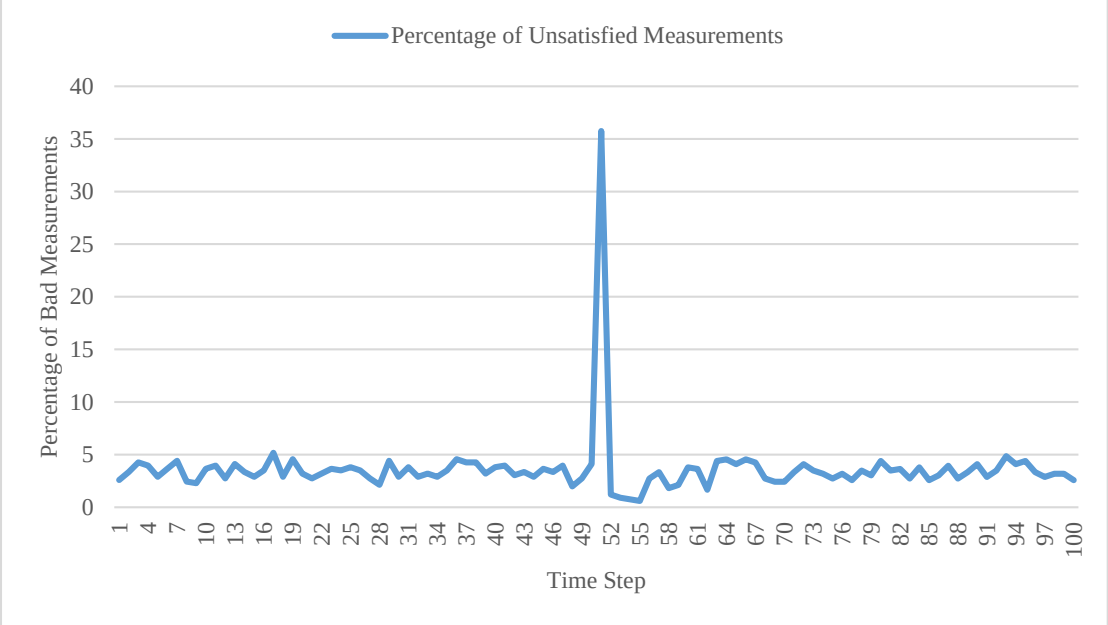

Figure 7.15: Measurement Test

The result of the measurement test is shown Figure 7.15. As can be seen from the graph, during the first 50-time step, the percentage of the bad measurement is less than 5 %. At the 50^{th} time instant, this number jumps to 35 % which is way higher than the limit. The following two steps, the elements of the covariance matrix for the unknowns $\tilde{\mathbf{P}}$ are assigned to reduce its effect on the

algorithm. After the 53rd time instant, the Predictor part is formed in the normal way as is before the occurrence of the sudden change and the percentage of the bad measurements is again less than 5 %.

7.8.2 Study Case-2: IEEE 34 Bus Test Case

In this study case, the modified version of the IEEE 34 Bus Test Case with the induction machines which is explained in [45] is investigated. Being a radial network, the variations in the measurements have more effect on the voltage profile.

Here, it is aimed to simulate the morning load pattern of a typical distribution network. The load pattern is represented with a sine wave as shown in Figure 7.16. In this study case, the loads are assumed to have 10 % standard deviation, and the voltage measurements are assumed to have 5 %. Based on the single line diagram given in Figure 4.10, the bus names where the voltage is measured are listed as follows; 808, 850, 822, 824, 854, 832 ,834, 838, 848.

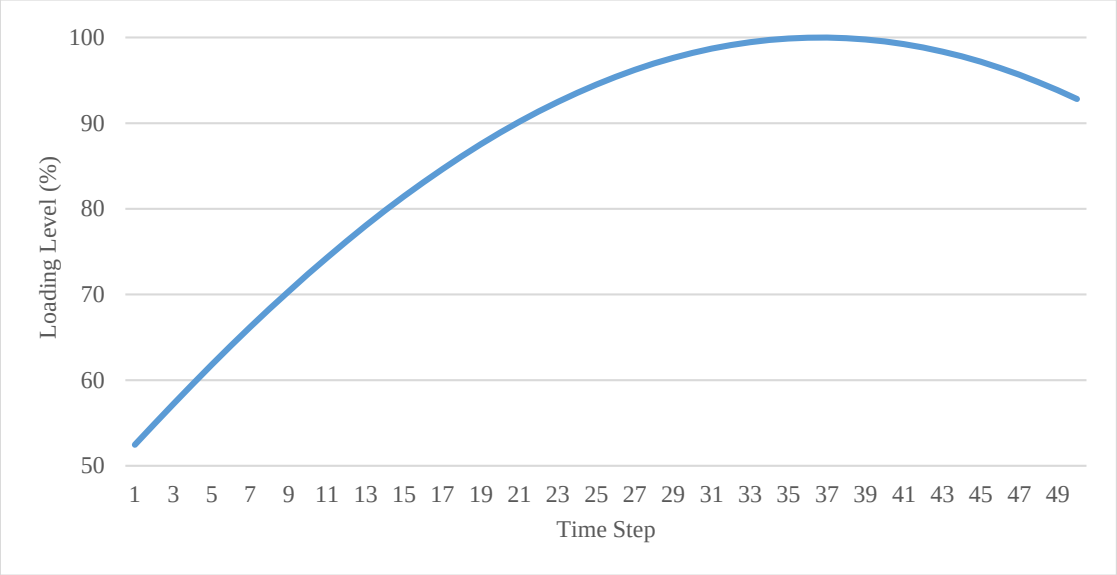

Figure 7.16: Morning Load Pattern

The evaluation of the performance of the SE algorithms in terms of the two criterion defined is tabulated in Table 7.3. In this study case, the network is radial, thus the oscillations in the measurements have a greater effect on the solver as can be observed from Figure 7.17 to Figure 7.20. Hence, the performance criteria are not as good as the ones obtained in the Study Case-1. The results obtained by the Dynamic SE is 2 times better than the ones obtained by the Static SE.

Table 7.3: Evaluation of Performance

Node Name	Criteria-1		Criteria-2	
	SSE	DSE	SSE	DSE
816c	0.705	0.331	0.290	0.106
822a	1.269	0.560	0.503	0.199
856b	1.204	0.428	0.469	0.150
890c	2.550	1.028	1.049	0.401

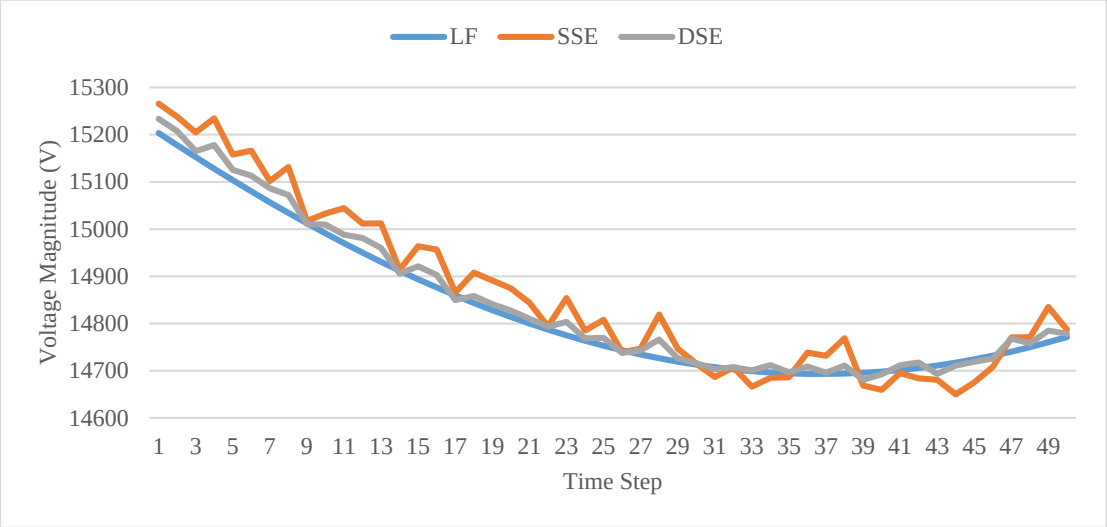

Figure 7.17: Voltage Magnitude at 816c

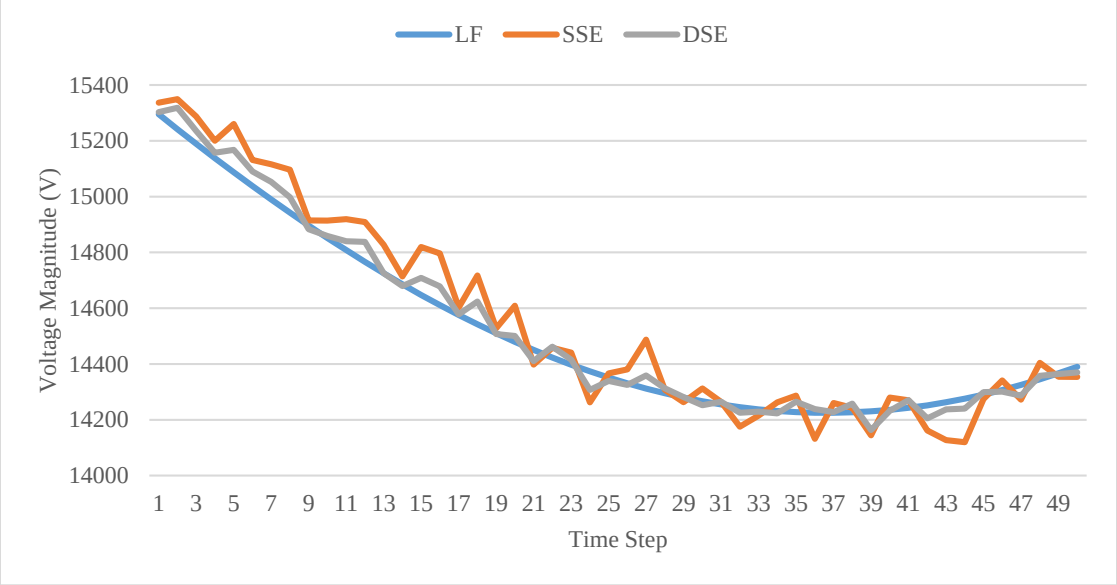

Figure 7.18: Voltage Magnitude at 816c

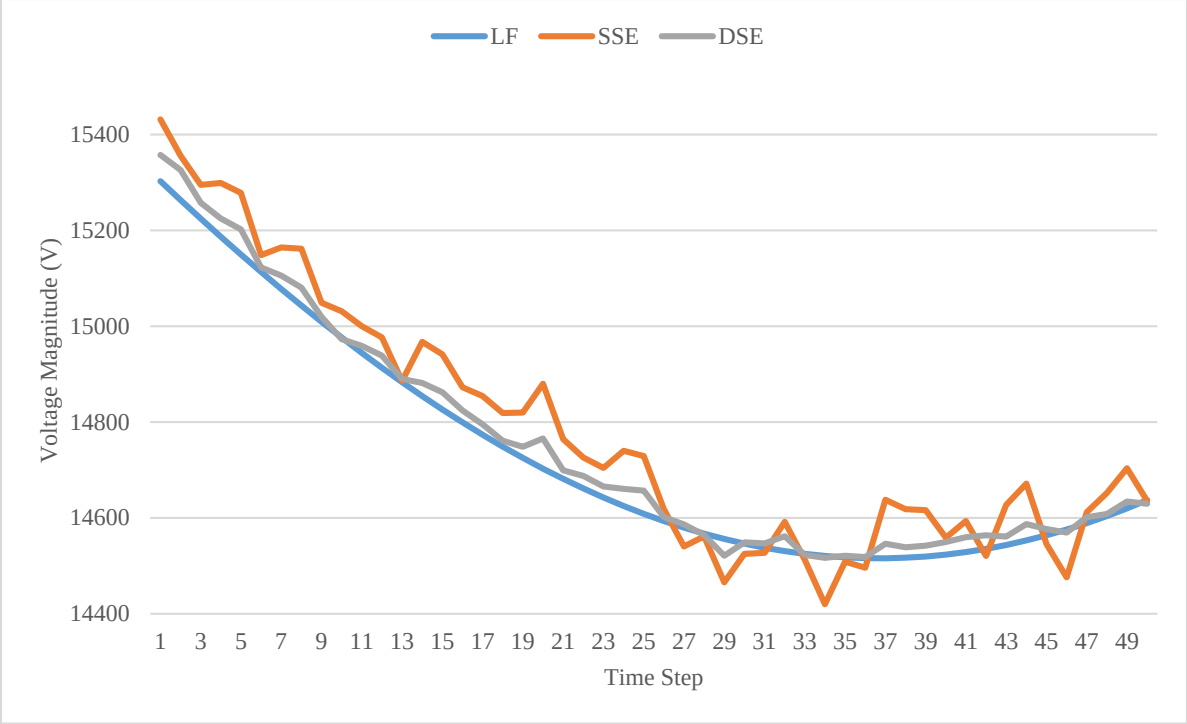

Figure 7.19: Voltage Magnitude at 856b

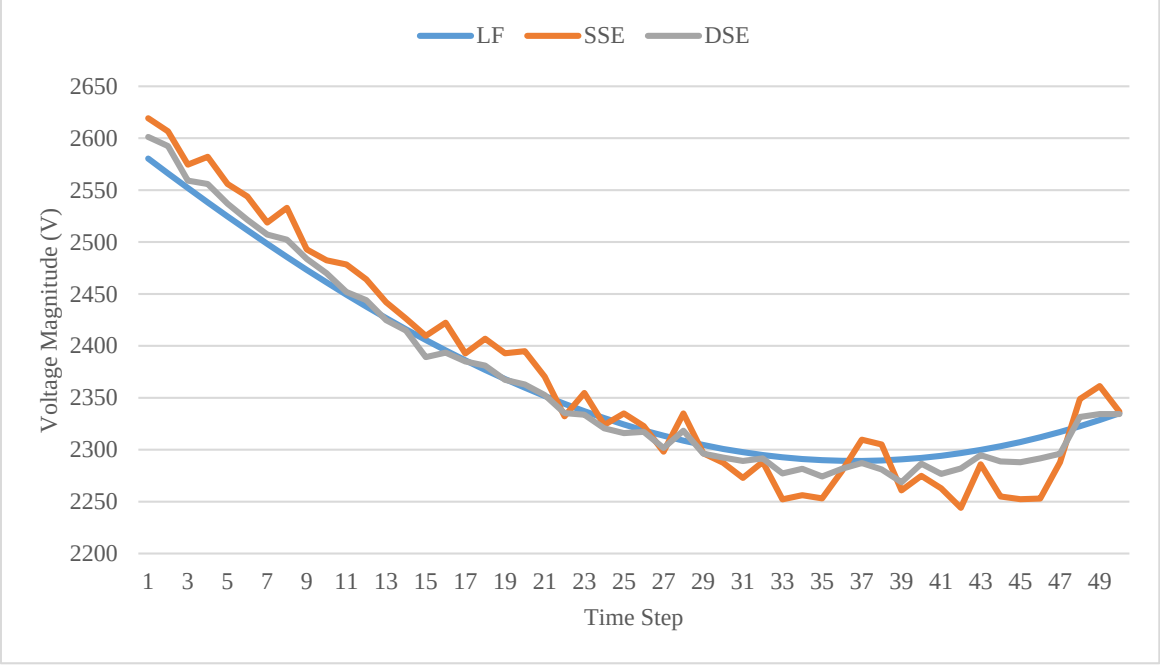

Figure 7.20: Voltage Magnitude at 890c

7.8.3 Study Case-3: Real Distribution Network

This network is the same one previously used in the section 6.4.4. However, the original network has been altered to have an unbalanced loading in the network. In this study case, each load is assigned one of the ten predefined load patterns. The aim of this study case is to evaluate the performance of the semi-dynamic state estimation algorithm on an extremely big distribution network.

Figure 7.21: Single Line Diagram of the Primary Distribution Network

In Figure 7.21, the feeders of the primary distribution network are demonstrated. On this network, the magnitude of voltage is measured at 105 different nodes of the network with the accuracy of 2 %. All load measurements have an accuracy of 30 % for both real and reactive power measurements. The approximate pattern of the loads is assumed to be known. Obtaining the load

pattern is out of scope of the study case. From Figure 7.22 to Figure 7.32, the voltage magnitudes at different buses are presented. The graphs are sorted in descending order for the mean error of the SSE. As can be observed from the figures, the DSE gives much better results for the nodes where the SSE has the greatest error. As the mean error of the SSE gets smaller (as the measured nodes get closer to the substation), the difference between the two algorithm vanishes and in some cases the SSE offers better solution. This is due to the fact that the aggregated error due to approximate load pattern model becomes significant compared to the randomly distributed measurement errors. This gives rise to a constant difference in the DSE results.

Table 7.4: Evaluation of Performance

Node Name	Criteria-1		Criteria-2	
	SSE	DSE	SSE	DSE
12783c	7.192	0.630	1.931	0.26
13091a	3.430	0.450	1.003	0.194
13774b	2.994	0.374	0.754	0.135
V7992a	1.413	0.340	0.332	0.148
V1474b	1.258	0.311	0.256	0.124
24M74colonM41745b	0.463	0.381	0.136	0.147
12977c	0.413	0.324	0.131	0.127
24M97colonV5150a	0.313	0.315	0.099	0.125
24M89colonM48458b	0.302	0.301	0.090	0.117
24M98colonM13634b	0.293	0.297	0.088	0.116
24M91colonM48520c	0.237	0.294	0.087	0.117

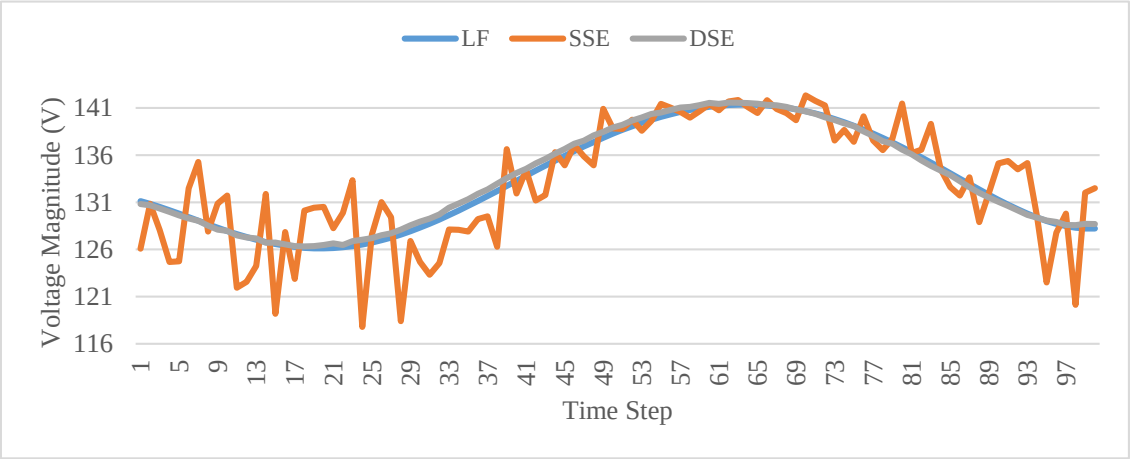

Figure 7.22: Voltage Magnitude at 12783c

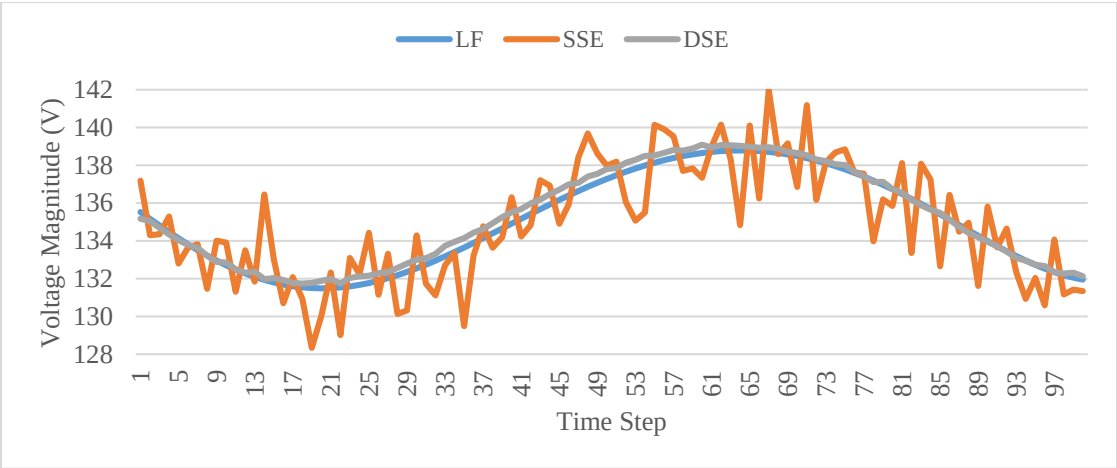

Figure 7.23: Voltage Magnitude at 13091a

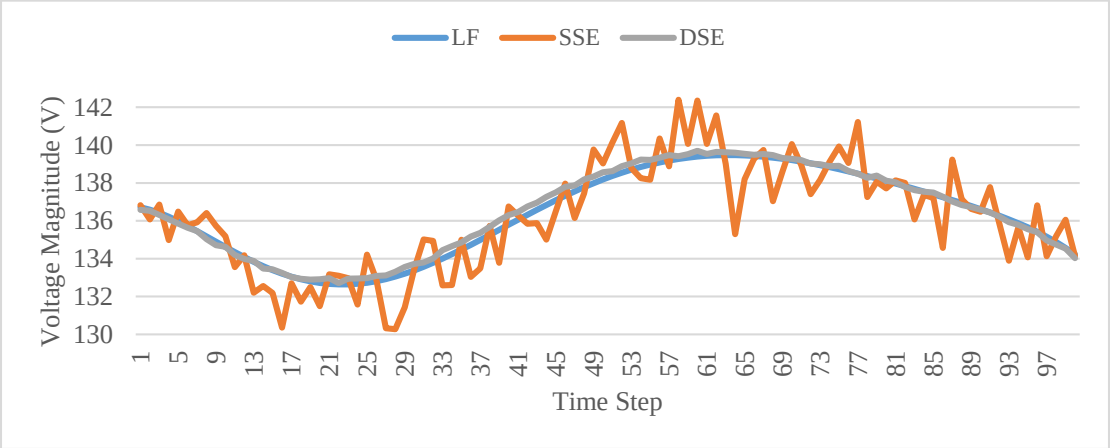

Figure 7.24: Voltage Magnitude at 13774b

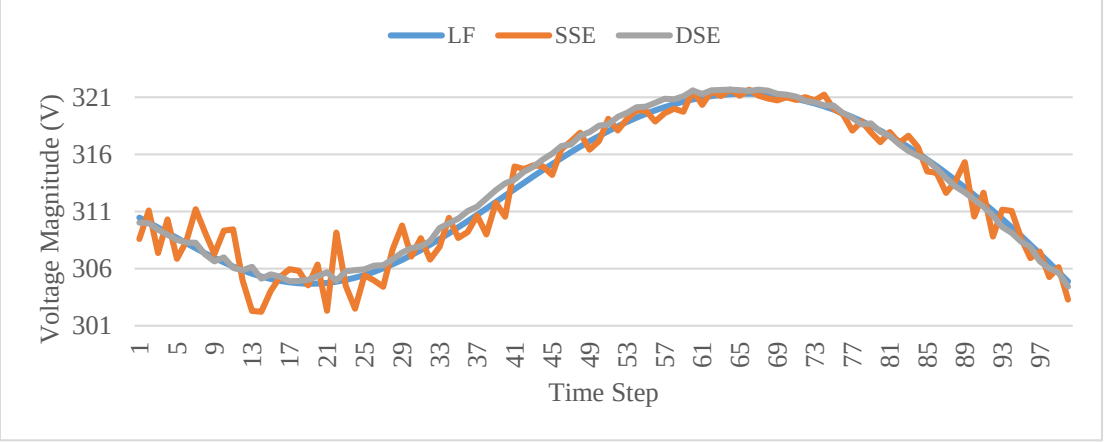

Figure 7.25: Voltage Magnitude at V7992a

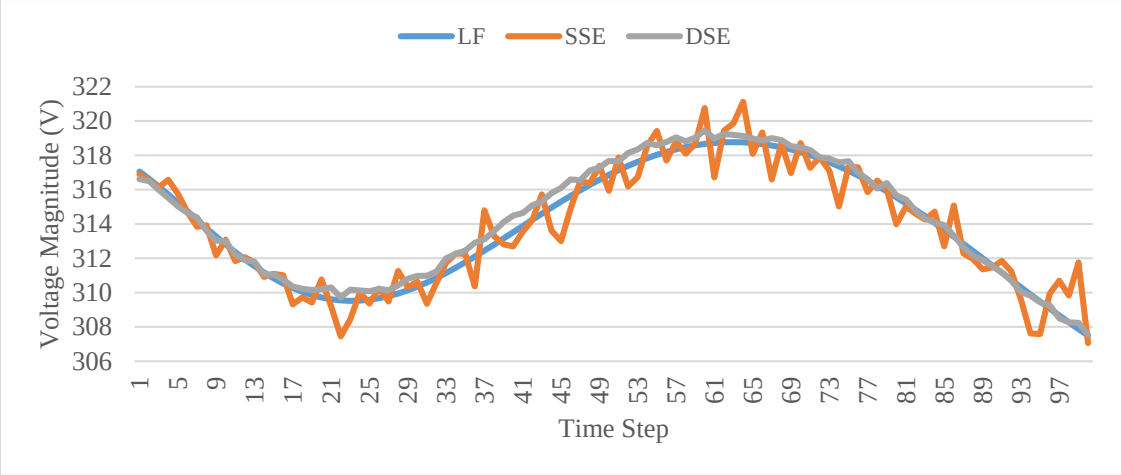

Figure 7.26: Voltage Magnitude at V1474b

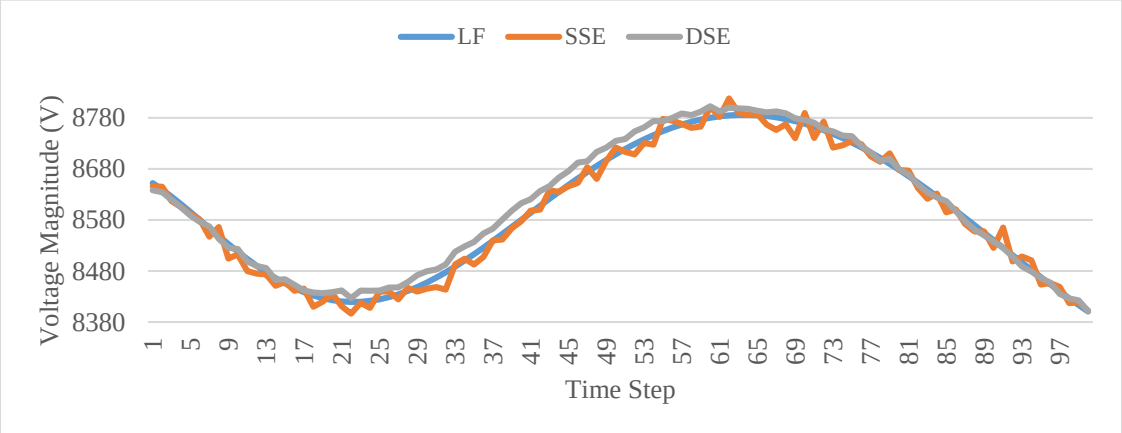

Figure 7.27: Voltage Magnitude at 24M74colonM41745b

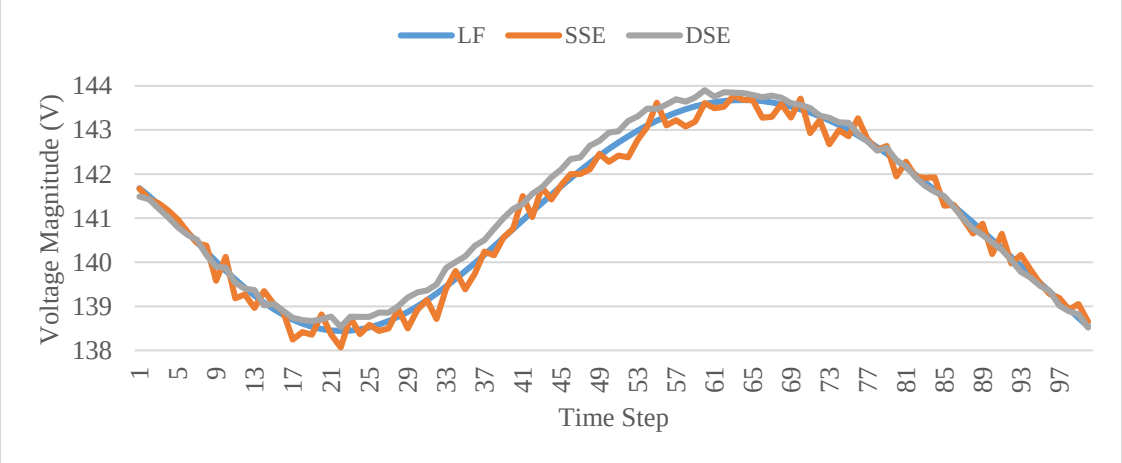

Figure 7.28: Voltage Magnitude at 12977c

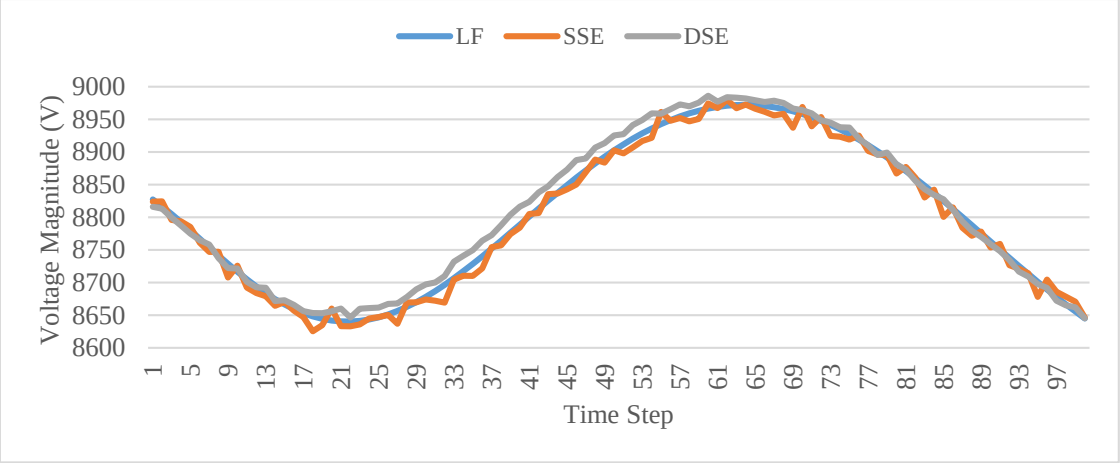

Figure 7.29: Voltage Magnitude at 24M97colonV5150a

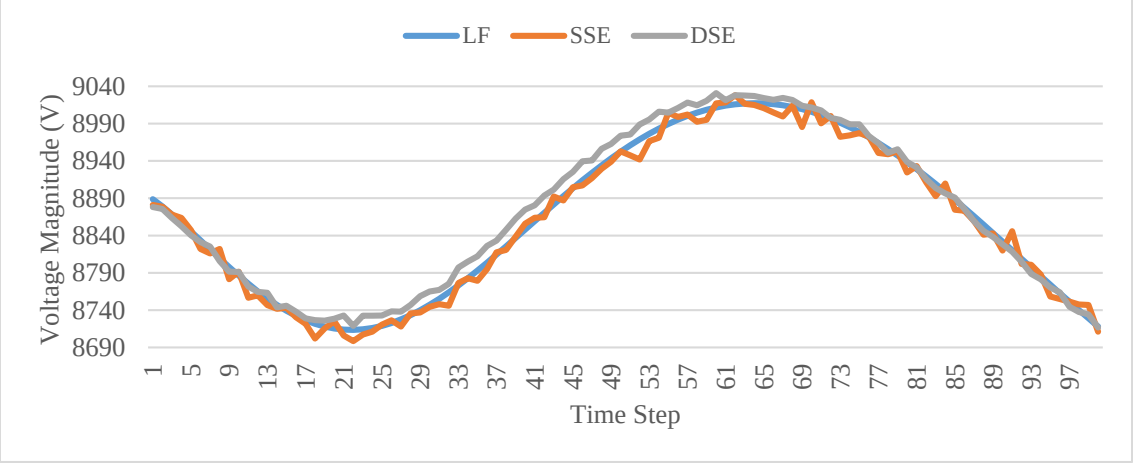

Figure 7.30: Voltage Magnitude at 24M89colonM48458b

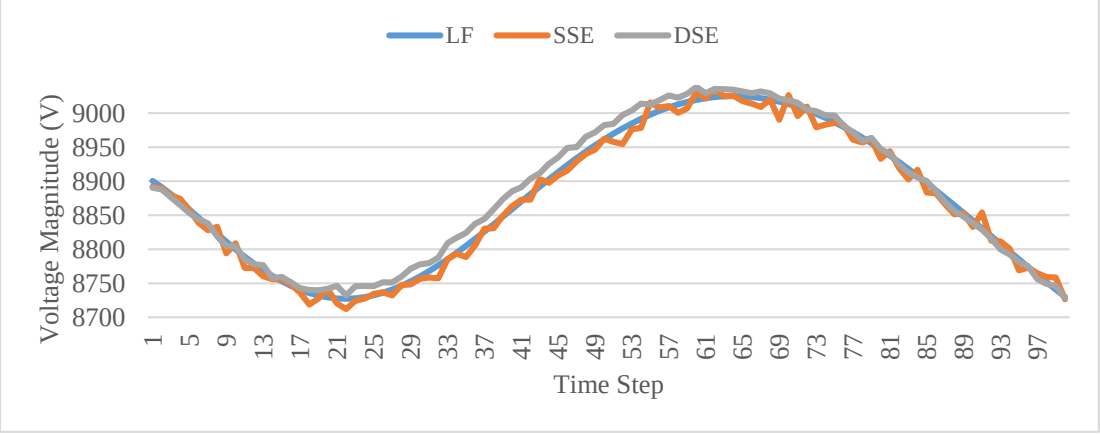

Figure 7.31: Voltage Magnitude at 24M98colonM13634b

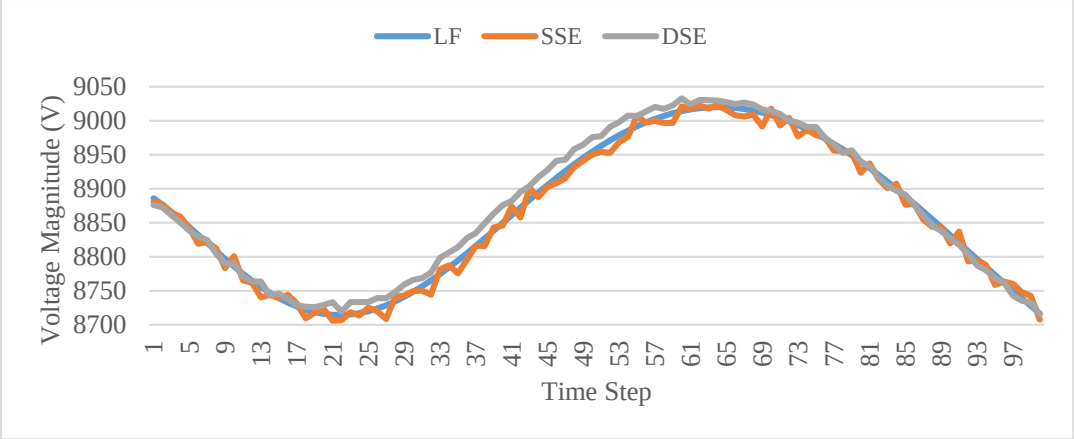

Figure 7.32: Voltage Magnitude at 24M91colonM48520c

7.9 Summary

In this chapter, two dynamic state estimation algorithms which are both constructed in Hachtel form are presented within MANA approach. The first proposed algorithm is a non Kalman, WLS based technique where the forecast values of the unknowns are included as measurements. There are certain advantages and disadvantages of the first algorithm. First of all, unlike the Kalman based techniques, the inversion of a full matrix is not needed, this makes the use of the sparse matrix techniques possible. Secondly, in the new technique, not all of the unknowns must be forecast. In other words, dependent state variables are excluded from being forecast in the predictor part. The main disadvantage of the first technique is that the formation of covariance matrix for the forecasts requires a prior statistical analysis and fine-tuning which is done automatically in the Kalman based methods. The second proposed algorithm, however, originates from the statistical state estimation and employs Kalman filter techniques in a different manner than the classical dynamic state estimators. In this method, the measurement patterns are used to form state transition function of the Kalman filtering technique. It is important to note that in the DSE problem, the trend of measurements is easier to obtain compared to the state variables. Especially in distribution networks, the load measurements usually have a daily pattern which makes possible to make such a hypothesis. Therefore, the second approach is more applicable to real distribution networks.

CHAPTER 8 CONCLUSION AND RECOMMENDATIONS

In this thesis, various electrical components that are omnipresent in modern distribution networks are modeled for load flow studies, and an alternative dynamic state estimation algorithm is proposed.

In Chapter-3, the step voltage regulators are discussed. By taking into account the physical limits of these devices, a new model is presented within the MANA approach. The proposed technique is a generic one such that the voltage transformation ratio is considered as the new unknown, rather than the turns ratio of the transformer, which has in fact the same value for the wye grounded step voltage transformers. The results obtained suggest that this method gives satisfactory results as far as the bandwidth of the regulator is concerned. Different regulator types can be modeled in a similar way; such as type-A or type-B autotransformers. This may be important step while performing the short circuit analysis of a network, as the zero sequence impedances of the step voltage regulator and type-A/B autotransformers are different.

In Chapter-4, the induction machines are investigated and integrated into the MANA approach. The model used can represent both double and single squirrel cage induction machines. The machines are simply inserted into the admittance matrix as an impedance. Also, it is important to note that there is no assumption on the reactive power of the machine in the algorithm. The constraint is defined as the real power absorbed by the machine and the slip of the machine which is the unknown representing the induction machine, is calculated iteratively. The three by three impedance matrix of the machine is obtained from the Steinmetz equivalent circuit directly for positive and negative sequences. Here, it should be once again noted that the zero sequence impedance of the machine is infinite because in the model, it is assumed that the connection of the machine is either delta or wye ungrounded. The two study cases show that the obtained results perfectly match to the published ones. However, the speed of convergence is much faster compared to the classical circuit analysis tools. It is also shown that this approach can be used to directly initialize its time-domain counterpart for the simulation of electromagnetic transients. The accuracy of the simulation in time-domain is a potent way to validate load-flow solutions.

In Chapter-5, the wind turbine generators are discussed and a current source based model is developed for these devices. The control circuitry of ECGs is presented for the Type-III and Type-IV wind turbine generators. It is observed that, in generic transient models such as the ones in

EMTP-RV, the injected power is controlled by adjusting the positive sequence component of the terminal current of the generators. Therefore, the constraints defining the mode of operation are defined for the positive sequence components. In the model presented, the generators act as a constant impedance for negative and zero sequence voltages that appear at its terminals. This new model is compared with the existing model and with the time simulations by using two test cases. In the balanced case, the difference is negligibly small for the existing and new model, as expected. On the other hand, in the unbalanced test case, the error between the existing model and time simulation is as great as 0.16 % while the one between the new model and the time simulation is around 0.04 %. This validates the initial assumption that the classical synchronous generator models are not accurate enough to model the electronically coupled generators. In this method, in order to be able to do the load flow analysis, the negative and zero sequence admittance of the generators must be specified. As a future work, the dependency between voltage and current sequence components can be investigated for other types of ECG models. In the study cases, this value is obtained from EMTP-RV simulations.

In Chapter-6, the impact of the load power factor on the SE analysis is discussed. In SE, the load measurements are formed by considering real and reactive powers independently. That is to say, the relation between the real and reactive powers for a load is ignored. The hypothesis assumed in this chapter is that the power factor measurement (pseudo-measurement) should have more precision than the power measurements. Hence, adjusting the reactive power measurement in terms of the power factor will minimize the discrepancy between active and reactive power measurements in SE, and this may improve the accuracy of the SE solution. Four test cases with different sizes are tested with two different approaches, i.e. with independent active and reactive power measurements, and with active and adjusted reactive power measurement using load power factor. It is observed that in the smallest network, the performance gain is not so much due to the small number of loads which makes the state estimation analysis almost a determined problem. However, it is seen that the size of the network has a considerable effect on the performance. The worst scenarios of the four tests confirm that efficiency of the idea.

In Chapter-7, two dynamic state estimation algorithms which are both constructed in Hachtel form are presented within MANA approach. In the first proposed algorithm, a non Kalman, WLS based technique where the forecast values of the unknowns are included as measurements is proposed. It has certain advantages and disadvantages. First of all, unlike the Kalman based techniques, this

technique does not require to deal with full matrices, which makes the use of the sparse matrix techniques possible. Secondly, in the new technique, thanks to the constraint equations, not all of the unknowns must be forecast. The main disadvantage of the first technique is that the formation of covariance matrix for the forecasts requires a prior statistical analysis and fine-tuning which is done automatically in the Kalman based methods and inaccurate tuning of the covariance matrix may have severe consequences. There are two possible outcomes of bad tuning: If the elements of the covariance matrix are extremely small, the algorithm tends to be unresponsive. In other words, the algorithm will not be affected by the measurements and will solely be dominated by the forecasts. This means that the state of the system will slowly change. In the second case, if the elements of the covariance matrix are too great, the algorithm will act like a static estimator and will be dominated by the measurements. The tuning refers to the correct choice of the covariance elements. In this work, the tuning is accomplished by means of statistical studies. The static state estimation for each network is performed for several times, and the difference between the true and estimated states are used to obtain the standard deviation of the unknowns. The results show that if the covariance matrix is well tuned, the dynamic state estimator is able to track accurately the true state of the network. As a future work of the first method, different techniques; such as machine learning, can be utilized to obtain the standard deviation of the unknowns. The second proposed algorithm, however, originates from the statistical state estimation and employs Kalman filter techniques in a different manner than the classical dynamic state estimators. In this method, the measurement trends are utilized in conjunction with the Kalman filtering technique. It is important to note that in the DSE problem, the trend of load measurements is easier to obtain compared to the state variables. Especially in distribution networks, the load measurements usually have a daily pattern which makes possible to claim such a hypothesis. The smoothed measurements through Kalman filters are fed to the static SE solver. In summary, the second approach is more applicable to real distribution networks and more robust as well. The second approach is applied to a very large scale urban distribution network with secondary details and improved results are obtained compared to the static SE with untreated measurements. This thesis not only proposes new approaches for the dynamic and static SE of distribution systems but demonstrates the solution of very large scale meshed distribution networks for the first time in the literature.

BIBLIOGRAPHY

[1] J. Mahseredjian, S. Dennetière, L. Dubé, B. Khodabakhchian, and L. Gérin-Lajoie, "On a new approach for the simulation of transients in power systems," *Electric Power Systems Research*, vol. 77, pp. 1514-1520, Sep 2007.

[2] J. Mahseredjian, "Multiphase Load-Flow Method," *Course Notes*, 2010.

[3] J. Mahseredjian, "Régimes transitoires électromagnétiques : simulation," *Techniques de l'ingénieur Problématiques communes des réseaux électriques : du fonctionnement au comptage*, vol. TIB266DUO, Feb. 2008.

[4] I. Kocar, J. Mahseredjian, U. Karaagac, G. Soykan, and O. Saad, "Multiphase Load-Flow Solution for Large-Scale Distribution Systems Using MANA," *IEEE Transactions on Power Delivery*, vol. 29, pp. 908-915, 2014.

[5] J. Mahseredjian, "Expandable modified augmenter nodal analysis," *Course Notes, Comportement des réseaux électriques*, 2012-2016.

[6] C. Haiyan, C. Jinfu, S. Dongyuan, and D. Xianzhong, "Power flow study and voltage stability analysis for distribution systems with distributed generation," in *Power Engineering Society General Meeting, 2006. IEEE*, 2006, p. 8 pp.

[7] A. Losi and M. Russo, "Dispersed generation modeling for object-oriented distribution load flow," *Power Delivery, IEEE Transactions on*, vol. 20, pp. 1532-1540, 2005.

[8] Y. Zhu and K. Tomsovic, "Adaptive power flow method for distribution systems with dispersed generation," *Power Delivery, IEEE Transactions on*, vol. 17, pp. 822-827, 2002.

[9] R. Stoicescu, K. Miu, C. O. Nwankpa, D. Niebur, and Y. Xiaoguang, "Three-phase converter models for unbalanced radial power-flow studies," *Power Systems, IEEE Transactions on*, vol. 17, pp. 1016-1021, 2002.

[10] Y.-B. Wang, C.-S. Wu, H. Liao, and H.-h. Xu, "Steady-state model and power flow analysis of grid-connected photovoltaic power system," in *Industrial Technology, 2008. ICIT 2008. IEEE International Conference on*, 2008, pp. 1-6.

[11] Z. Xiao-Ping, "Multiterminal voltage-sourced converter-based HVDC models for power flow analysis," *Power Systems, IEEE Transactions on*, vol. 19, pp. 1877-1884, 2004.

[12] L. M. Castro, C. R. Fuerte-Esquivel, and J. H. Tovar-Hernandez, "Solution of Power Flow With Automatic Load-Frequency Control Devices Including Wind Farms," *Power Systems, IEEE Transactions on*, vol. 27, pp. 2186-2195, 2012.

[13] L. Shenghu, "Power Flow Modeling to Doubly-Fed Induction Generators (DFIGs) Under Power Regulation," *Power Systems, IEEE Transactions on*, vol. 28, pp. 3292-3301, 2013.

[14] H. Nikkhajoei and R. Iravani, "Steady-State Model and Power Flow Analysis of Electronically-Coupled Distributed Resource Units," *Power Delivery, IEEE Transactions on*, vol. 22, pp. 721-728, 2007.

[15] M. Z. Kamh and R. Iravani, "A Unified Three-Phase Power-Flow Analysis Model For Electronically Coupled Distributed Energy Resources," *Power Delivery, IEEE Transactions on*, vol. 26, pp. 899-909, 2011.

[16] J. H. Teng, "Modelling distributed generations in three-phase distribution load flow," *Generation, Transmission & Distribution, IET,* vol. 2, pp. 330-340, 2008.

[17] A. E. Feijoo and J. Cidras, "Modeling of wind farms in the load flow analysis," *Power Systems, IEEE Transactions on,* vol. 15, pp. 110-115, 2000.

[18] D. Howard, "Short-Circuit Currents In Wind-Turbine Generator Networks," Ph. D., Electrical and Computer Engineering, Georgia Institute of Technology, 2003.

[19] F. Schweppe and J. Wildes, "Power System Static-State Estimation, Part I: Exact Model," *IEEE Transactions on Power Apparatus and Systems,* vol. 89, pp. 120-125, 1970.

[20] F. C. Schweppe and E. J. Handschin, "Static state estimation in electric power systems," *Proceedings of the IEEE,* vol. 62, pp. 972-982, 1974.

[21] A. Gjelsvik, S. Aam, and L. Holten, "Hachtel's Augmented Matrix Method - A Rapid Method Improving Numerical Stability in Power System Static State Estimation," *IEEE Power Engineering Review,* vol. PER-5, pp. 22-23, 1985.

[22] W. H. Kersting, *Distribution System Modeling and Analysis*, 3 ed.: CRC Press, 2012.

[23] I. Roytelman and S. M. Shahidehpour, "State estimation for electric power distribution systems in quasi real-time conditions," *IEEE Transactions on Power Delivery,* vol. 8, pp. 2009-2015, 1993.

[24] M. E. Baran and A. W. Kelley, "State estimation for real-time monitoring of distribution systems," *IEEE Transactions on Power Systems,* vol. 9, pp. 1601-1609, 1994.

[25] M. E. Baran and A. W. Kelley, "A branch-current-based state estimation method for distribution systems," *IEEE Transactions on Power Systems,* vol. 10, pp. 483-491, 1995.

[26] C. N. Lu, J. H. Teng, and W. H. E. Liu, "Distribution system state estimation," *IEEE Transactions on Power Systems,* vol. 10, pp. 229-240, 1995.

[27] L. Ke, "State estimation for power distribution system and measurement impacts," *IEEE Transactions on Power Systems,* vol. 11, pp. 911-916, 1996.

[28] R. C. Leou and C. N. Lu, "Improving feeder voltage calculation results with telemetered data," *IEEE Transactions on Power Delivery,* vol. 11, pp. 1914-1920, 1996.

[29] W. M. Lin and J. H. Teng, "Distribution fast decoupled state estimation by measurement pairing," *IEE Proceedings - Generation, Transmission and Distribution,* vol. 143, p. 43, 1996.

[30] A. M. Leite da Silva, M. B. Do Coutto Filho, and J. F. de Queiroz, "State forecasting in electric power systems," *IEE Proceedings C Generation, Transmission and Distribution,* vol. 130, p. 237, 1983.

[31] A. S. Debs and R. E. Larson, "A Dynamic Estimator for Tracking the State of a Power System," *IEEE Transactions on Power Apparatus and Systems,* vol. PAS-89, pp. 1670-1678, 1970.

[32] H. W. Sorenson, *Kalman Filtering: Theory and Application*, 1985.

[33] Available: http://www.emtp-software.com/

[34] P. A. N. Garcia, J. L. R. Pereira, and S. Carneiro, Jr., "Voltage control devices models for distribution power flow analysis," *Power Systems, IEEE Transactions on*, vol. 16, pp. 586-594, 2001.

[35] R. C. Dugan, "A perspective on transformer modeling for distribution system analysis," in *Power Engineering Society General Meeting, 2003, IEEE*, 2003, pp. 1-119 Vol. 1.

[36] L. V. Barboza, H. H. Zurn, and R. Salgado, "PICA 2001 Preview," *Power Engineering Review, IEEE*, vol. 21, pp. 17-18, 2001.

[37] A. Gómez-Expósito, E. Romero-Ramos, and I. Džafić, "Hybrid real–complex current injection-based load flow formulation," *Electric Power Systems Research*, vol. 119, pp. 237-246, 2// 2015.

[38] K. Imhof, F. Oesch, and I. Nordanlycke, "Modelling of tap-changer transformers in an energy management system," in *Power Industry Computer Application Conference, 1995. Conference Proceedings., 1995 IEEE*, 1995, pp. 378-384.

[39] W. H. Kersting, "Radial distribution test feeders," in *Power Engineering Society Winter Meeting, 2001. IEEE*, 2001, pp. 908-912 vol.2.

[40] (Jan., 2016). Available: http://ewh.ieee.org/soc/pes/dsacom/testfeeders/index.html

[41] R. F. Arritt and R. C. Dugan, "The IEEE 8500-node test feeder," in *IEEE PES T&D 2010*, 2010, pp. 1-6.

[42] B. Çetindağ, I. Kocar, U. Karaagac, and J. Mahseredjian, "Unbalanced Load-flow Solution Based Initialization of Induction Machines for Electromagnetic Transients," *IEEE Transactions on Power Systems*, submitted on October, 2016.

[43] A. E. Fitzgerald, C. Kingsley, and S. D. Umans, *Electric Machinery*: McGraw-Hill, 2003.

[44] R. C. Dugan, "Induction Machine Modeling for Distribution System Analysis - Test Case Description," in *2005/2006 IEEE/PES Transmission and Distribution Conference and Exhibition*, 2006, pp. 578-582.

[45] R. C. Dugan and W. H. Kersting, "Induction machine test case for the 34-bus test feeder - description," in *Power Engineering Society General Meeting, 2006. IEEE*, 2006, p. 4 pp.

[46] K. C. Divya and P. S. N. Rao, "Models for wind turbine generating systems and their application in load flow studies," *Electric Power Systems Research*, vol. 76, pp. 844-856, 2006.

[47] U. Eminoglu, B. Dursun, and M. H. Hocaoglu, "Incorporation of a new wind turbine generating system model into distribution systems load flow analysis," *Wind Energy*, vol. 12, pp. 375-390, 2009.

[48] A. E. Feijoo and J. Cidras, "Modeling of wind farms in the load flow analysis," *IEEE Transactions on Power Systems*, vol. 15, pp. 110-115, 2000.

[49] M. Z. Kamh and R. Iravani, "A Unified Three-Phase Power-Flow Analysis Model For Electronically Coupled Distributed Energy Resources," *IEEE Transactions on Power Delivery*, vol. 26, pp. 899-909, 2011.

[50] M. Z. Kamh and R. Iravani, "Three-Phase Steady-State Model of Type-3 Wind Generation Unit 2014;Part I: Mathematical Models," *IEEE Transactions on Sustainable Energy,* vol. 2, pp. 477-486, 2011.

[51] T. Athay, R. Podmore, and S. Virmani, "A Practical Method for the Direct Analysis of Transient Stability," *IEEE Transactions on Power Apparatus and Systems,* vol. PAS-98, pp. 573-584, 1979.

[52] L. Monjo, H. Kojooyan-Jafari, F. Córcoles, and J. Pedra, "Squirrel-Cage Induction Motor Parameter Estimation Using a Variable Frequency Test," *IEEE Transactions on Energy Conversion,* vol. 30, pp. 550-557, 2015.

[53] R. Hoffman, "Practical State Estimation for Electric Distribution Networks," in *2006 IEEE PES Power Systems Conference and Exposition*, 2006, pp. 510-517.

[54] R. F. Arritt and R. C. Dugan, "Distribution system analysis and the future Smart Grid," in *Rural Electric Power Conference (REPC), 2011 IEEE*, 2011, pp. B2-1-B2-8.

[55] G. T. Heydt, "The Next Generation of Power Distribution Systems," *IEEE Transactions on Smart Grid,* vol. 1, pp. 225-235, 2010.

[56] Y. F. Huang, S. Werner, J. Huang, N. Kashyap, and V. Gupta, "State Estimation in Electric Power Grids: Meeting New Challenges Presented by the Requirements of the Future Grid," *IEEE Signal Processing Magazine,* vol. 29, pp. 33-43, 2012.

[57] L. Whei-Min, T. Jen-Hao, and C. Shi-Jaw, "A highly efficient algorithm in treating current measurements for the branch-current-based distribution state estimation," *IEEE Transactions on Power Delivery,* vol. 16, pp. 433-439, 2001.

[58] J. H. Teng, "Using voltage measurements to improve the results of branch-current-based state estimators for distribution systems," *IEE Proceedings - Generation, Transmission and Distribution,* vol. 149, p. 667, 2002.

[59] L. Whei-Min and T. Jen-Hao, "State estimation for distribution systems with zero-injection constraints," *IEEE Transactions on Power Systems,* vol. 11, pp. 518-524, 1996.

[60] F. Therrien, I. Kocar, and J. Jatskevich, "A Unified Distribution System State Estimator Using the Concept of Augmented Matrices," *IEEE Transactions on Power Systems,* vol. 28, pp. 3390-3400, 2013.

[61] S. Naka, T. Genji, T. Yura, and Y. Fukuyama, "A hybrid particle swarm optimization for distribution state estimation," *IEEE Transactions on Power Systems,* vol. 18, pp. 60-68, 2003.

[62] I. Kocar, J. S. Lacroix, and F. Therrien, "General and simplified computation of fault flow and contribution of distributed sources in unbalanced distribution networks," in *Power and Energy Society General Meeting, 2012 IEEE*, 2012, pp. 1-8.

[63] J. S. Lacroix, I. Kocar, and M. Belletete, "Accelerated Computation of Multiphase Short Circuit Summary for Unbalanced Distribution Systems Using the Concept of Selected Inversion," *Power Systems, IEEE Transactions on,* vol. 28, pp. 1515-1522, 2013.

[64] R. C. Dugan and T. E. McDermott, "An open source platform for collaborating on smart grid research," in *Power and Energy Society General Meeting, 2011 IEEE*, 2011, pp. 1-7.

[65] A. Abur and A. G. Expósito, *Power System State Estimation: Theory and Implementation*: Taylor & Francis, 2004.

[66] R. Singh, R. A. Jabr, and B. C. Pal, "Choice of estimator for distribution system state estimation," *IET Generation, Transmission & Distribution,* vol. 3, pp. 666-678, 2009.

[67] F. C. Aschmoneit, N. M. Peterson, and E. C. Adrian, "State estimation with equality constraints," in *PICA Conference Proceedings*, 1977, pp. 427-430.

[68] R. R. Nucera and M. L. Gilles, "A blocked sparse matrix formulation for the solution of equality-constrained state estimation," *IEEE Transactions on Power Systems,* vol. 6, pp. 214-224, 1991.

[69] F. L. Alvarado and W. F. Tinney, "State estimation using augmented blocked matrices," *IEEE Transactions on Power Systems,* vol. 5, pp. 911-921, 1990.

[70] L. Holten, A. Gjelsvik, S. Aam, F. F. Wu, and W. H. E. Liu, "Comparison of different methods for state estimation," *IEEE Transactions on Power Systems,* vol. 3, pp. 1798-1806, 1988.

[71] K. Schneider, P. Phanivong, and J. S. Lacroix, "IEEE 342-node low voltage networked test system," in *2014 IEEE PES General Meeting | Conference & Exposition*, 2014, pp. 1-5.

[72] A. M. L. d. Silva, M. B. D. C. Filho, and J. M. C. Cantera, "An Efficient Dynamic State Estimation Algorithm including Bad Data Processing," *IEEE Transactions on Power Systems,* vol. 2, pp. 1050-1058, 1987.

[73] S. G. Makridakis, S. C. Wheelwright, and R. J. Hyndman, *Forecasting: Methods and Applications*: Wiley, 1998.

[74] D. M. Falcao, P. A. Cooke, and A. Brameller, "Power System Tracking State Estimation and Bad Data Processing," *IEEE Transactions on Power Apparatus and Systems,* vol. PAS-101, pp. 325-333, 1982.

[75] P. S. Kalekar, "Time series forecasting using holt-winters exponential smoothing," *Kanwal Rekhi School of Information Technology,* vol. 4329008, pp. 1-13, 2004.

[76] C. C. Holt, "Forecasting seasonals and trends by exponentially weighted moving averages," *International Journal of Forecasting,* vol. 20, pp. 5-10, 1// 2004.

[77] R. E. Kalman, "A new approach to linear filtering and prediction problems," *Journal of basic Engineering,* vol. 82, pp. 35-45, 1960.

[78] G. Bishop and G. Welch, "An introduction to the kalman filter," *Proc of SIGGRAPH, Course,* vol. 8, p. 41, 2001.

[79] T. Lefebvre, H. Bruyninckx, and J. De Schutter, "Kalman filters for non-linear systems: a comparison of performance," *International journal of Control,* vol. 77, pp. 639-653, 2004.

APPENDICES

APPENDIX-A: PARAMETERS OF INDUCTION MACHINE TEST CASE

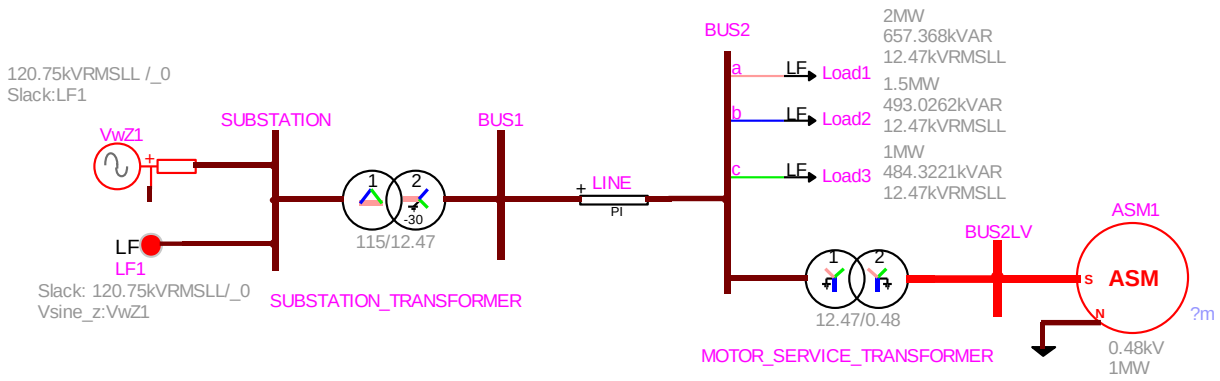

The source parameters:

Voltage	$115\angle 0°\ kV$
R_1	0.16038 Ω
X_1	0.64151 Ω
R_0	0.16977 Ω
X_0	0.50932 Ω

The substation transformer parameters:

Voltages	$115kV/12.47kV$
Connection	Delta-Wye Grounded
Apparent Power Rating	12 MVA
X	10 %
R	1 %

The line parameters:

Rmatrix(ohms/kft.)

$$\begin{bmatrix} 0.086846 & 0.029831 & 0.028888 \\ 0.029831 & 0.088797 & 0.029831 \\ 0.028888 & 0.029831 & 0.086846 \end{bmatrix}$$

Xmatrix (ohms/kft.)

$$\begin{bmatrix} 0.202545 & 0.084721 & 0.071916 \\ 0.084721 & 0.196145 & 0.084721 \\ 0.071916 & 0.084721 & 0.202545 \end{bmatrix}$$

Cmatrix (nF/kft) $\begin{bmatrix} 2.74 & -0.7 & -0.34 \\ -0.7 & 2.96 & -0.71 \\ -0.34 & -0.71 & 2.74 \end{bmatrix}$

The length of the line is 2 miles.

The load parameters:

Load-1	2000 kW at 0.95 PF (lag.)
Load-2	1500 kW at 0.95 PF (lag.)
Load-3	1000 kW at 0.9 PF (lag.)

The motor service transformer parameters:

Voltages	$12.47 kV / 480 V$
Connection	Wye Gr.-Wye Gr.
Apparent Power Rating	1 MVA
X	5 %
R	1 %

The machine parameters:

Nominal Voltage	480 V
Apparent Power Rating	1.2 MVA
Connection	Delta
R_s	0.0053 pu
X_s	0.106 pu
R_r	0.007 pu
X_r	0.12 pu
X_m	4 pu

APPENDIX-B: MACHINE PARAMETERS OF INDUCTION MACHINE TEST CASE FOR IEEE 34 NODE TEST FEEDER

Rated Voltage	480 V
Nominal Apparent Power	660 kVA
Stator Resistance (r_s)	0.0053 pu
Stator Reactance (x_s)	0.106 pu
Rotor Resistance (r_r)	0.007 pu
Rotor Reactance (x_r)	0.12 pu
Magnetizing Branch Reactance (x_m)	4 pu